

# Electrospray-assisted synthesis methods of nanostructured materials for Li-ion batteries

## Proefschrift

ter verkrijging van de graad van doctor  
aan de Technische Universiteit Delft  
op gezag van de Rector Magnificus,  
Prof. ir. K.C.A.M. Luyben,  
voorzitter van het College voor Promoties,  
in het openbaar te verdedigen op

woensdag, 10 november 2010 om 15:00 uur

door

Mario VALVO

Laurea in Fisica  
Università degli studi di Catania

VIII Master universitario internazionale per micro e nano-tecnologie  
Istituto Universitario di Studi Superiori di Pavia

geboren te Enna, Italië

Dit proefschrift is goedgekeurd door de promotor:  
Prof. dr. S.J. Picken

Samenstelling promotiecommissie:

Rector Magnificus	Voorzitter
Prof. dr. S.J. Picken	Technische Universiteit Delft, promotor
Prof. dr. D. Guyomard	Université de Nantes
Prof. dr. F.M. Mulder	Technische Universiteit Delft
Prof. dr. M. Gaberscek	Kemijski inštitut NIC Ljubljana
Prof. dr. P.H.L Notten	Technische Universiteit Eindhoven
Dr. ir. J.C.M. Marijnissen	Technische Universiteit Delft
Dr. E.M. Kelder	Technische Universiteit Delft
Prof. dr. A. Schmidt-Ott	Technische Universiteit Delft, reserve

Copyright © 2010 by Mario Valvo  
Cover design by Mario Valvo

ISBN 978-90-5335-343-1

All rights reserved. Parts of this thesis are published in scientific journals and copyright is subject to different terms and conditions.

# Electrospray-assisted synthesis methods of nanostructured materials for Li-ion batteries

## Thesis

presented for the degree of doctor  
at Delft University of Technology  
under authority of the Vice-Chancellor,  
Prof. ir. K.C.A.M. Luyben,  
Chairman of the Board of Doctorates,  
to be defended in public in the presence of a committee on

Wednesday, November 10<sup>th</sup>, 2010 at 15 o'clock

by

Mario VALVO

Degree in Physics  
Università degli studi di Catania

VIII International university master for micro and nano-technologies  
Istituto Universitario di Studi Superiori di Pavia

born in Enna, Italy

This thesis is approved by the promotor:  
Prof. dr. S.J. Picken

Composition of Examination Committee:

Rector Magnificus	Chairman
Prof. dr. S.J. Picken	Delft University of Technology, promotor
Prof. dr. D. Guyomard	University of Nantes
Prof. dr. F.M. Mulder	Delft University of Technology
Prof. dr. M. Gaberscek	National Institute of Chemistry Ljubljana
Prof. dr. P.H.L Notten	Eindhoven University of Technology
Dr. ir. J.C.M. Marijnissen	Delft University of Technology
Dr. E.M. Kelder	Delft University of Technology
Prof. dr. A. Schmidt-Ott	Delft University of Technology, reserve

Copyright © 2010 by Mario Valvo  
Cover design by Mario Valvo

ISBN 978-90-5335-343-1

All rights reserved. Parts of this thesis are published in scientific journals and copyright is subject to different terms and conditions.

To my beloved Family and Friends

*“Costruire una batteria per alimentare il sogno della ragione umana...”*  
(Mario Accolla)



# Table of contents

<b>Preface and outline of the thesis</b>	<b>i</b>
<b>Nomenclature</b>	<b>v</b>
<b>1 Introduction</b>	<b>1</b>
1.1 Time to change (and re-charge) the batteries	2
1.2 Rechargeable (Li-ion) batteries: basic principles	6
1.2.1 Materials for positive electrodes	8
1.2.2 Materials for negative electrodes	8
1.3 Reaction mechanisms of Li in negative electrodes	10
1.4 The renaissance of Li alloys: Sn and Si	14
1.5 Transition metal oxides: a turning point?	18
1.6 Outlook	21
1.7 References	22
<b>2 Electrohydrodynamic atomization – Theory and Applications</b>	<b>25</b>
2.1 Introduction to Electrohydrodynamic Atomization	26
2.1.1 Dripping, microdripping and spindle modes	29
2.1.2 Cone-jet Mode: a preliminary introduction	30
2.1.3 Cone-jet related modes	33
2.2 EHDA in the cone-jet mode	34
2.2.1 Characteristics of the cone-jet and its break-up	36
2.2.2 Parameters influencing the spraying process	39
2.2.3 Scaling laws for current and droplet size	40
2.3 EHDA-based techniques	42
2.3.1 Thin film electrodes for Li-ion batteries by ESD and ESP	43
2.3.2 Application of electrospun fibers to Li-ion batteries	44
2.4 Outlook	45
2.5 References	45

<b>3</b>	<b>Metallic and metallic-like powders via Electrostatic Spray Reductive Precipitation</b>	<b>51</b>
3.1	Coupling EHDA with chemical reactions in liquids	52
3.2	Experimental details	53
3.2.1	Precursor solutions	54
3.2.2	Aerosol generation and chemical reactions	54
3.2.3	Particle collection and measurements	56
3.3	Results and discussion	56
3.4	Investigation of other as-formed particles	66
3.5	Conclusions	68
3.6	References	69
<b>4</b>	<b>Nanostructured Sn/SnO<sub>x</sub> powders for negative electrodes</b>	<b>71</b>
4.1	Introduction	72
4.2	Experimental	73
4.3	Results and discussion	75
4.3.1	Structure characterization	76
4.3.2	Electrochemical characterization of SnO <sub>x</sub> /Sn	80
4.3.3	Electrochemical characterization of Sn, SnO and SnO <sub>2</sub>	85
4.4	Conclusions	87
4.5	References	88
<b>5</b>	<b>One-step synthesis and assembly of coated nanocomposite layers</b>	<b>91</b>
5.1	Introduction	92
5.2	Experimental	95
5.2.1	Precursor solutions and suspensions	96
5.2.2	Aerosol generation and electrode coating	96
5.2.3	Characterization and electrochemical tests	99
5.3	Results and discussion	99
5.4	Conclusions and outlook	129
5.5	References	130



---

<b>6</b>	<b>Synthesis of gold nanoparticles by electro spraying into a reductive-surfactant solution</b>	<b>133</b>
6.1	Introduction	134
6.2	Experimental	135
6.3	Results and discussion	137
6.3.1	Scaling laws for electro spraying	137
6.3.2	Formation of the colloids	139
6.3.3	Stability of the colloids	146
6.4	Conclusions	147
6.5	References	148
	<b>Summary</b>	<b>151</b>
	<b>Samenvatting</b>	<b>157</b>
<b>A</b>	<b>Electrochemical aspects</b>	<b>163</b>
A.1	Nernst equation and thermodynamics of a cell	164
A.2	Effects of the current flow on a cell	165
A.3	Theoretical capacity of electrode materials	168
A.3.1	Errors on the practical capacity of the tested electrodes	170
A.4	Electro spraying: an 'atypical' electrolytic cell?	171
A.5	References	172
<b>B</b>	<b>Particle formation in liquid media</b>	<b>175</b>
B.1	Nanoparticles via homogeneous nucleation	176
B.2	Basic aspects of homogeneous nucleation	176
B.3	Growth of nuclei	181
B.3.1	Growth controlled by diffusion	182
B.3.2	Growth controlled by surface processes	183
B.4	Particle formation via aerosol drying	186
B.4.1	Evaporation of a pure liquid droplet	187
B.4.2	Evaporation of droplets containing dissolved solids	187
B.4.3	Onset of precipitation and crust formation	188
B.4.4	Drying and formation of solid particles	190
B.5	References	191

<b>C</b>	<b>Volume change and effects on energy density</b>	<b>193</b>
	C.1 Molar volume and relative volume change	194
	C.2 Calculation of energy density for Li-alloys	194
	C.3 Reference	198
	<b>Acknowledgements</b>	<b>199</b>
	<b>Publications</b>	<b>205</b>
	<b>Curriculum vitae</b>	<b>206</b>

# Preface and outline of the thesis

Nanostructured materials and their applications to various technological fields are literally booming during the last decades. This is not surprising, because the search for new materials with special properties is a key point to overcome the limitations posed by conventional materials and their current technological use. Nanostructures are interesting systems, since their properties often vary strongly from those of the bulk. Their reduced size influences the physical and chemical properties of the original materials. In particular, ‘trivial’ size effects can be distinguished from ‘true’ size effects. Trivial size effects account merely for an increase in the surface-to-volume ratio, while ‘true’ size effects are responsible for major physical and chemical changes in the materials, involving modifications of the local properties. Both effects are important in defining the behaviour of the ultimate materials and therefore they should be considered during the synthesis and the assembly of the nanostructures within the systems where they are employed.

In this thesis nanostructured materials were synthesized via an aerosol-assisted route, based on electro spraying of liquid precursors. Electro spraying, also referred to as Electrohydrodynamic Atomization (EHDA), is a powerful technique for the production of nearly-monodispersed, highly-charged droplets. The possibility of tailoring the droplet size, as well as coupling the process to different reactions mechanisms (i.e. pyrolysis, sol-gel, reduction, etc.) makes this technique an attractive candidate for the production of a wide variety of nanostructured functional materials. The nanostructured materials synthesized in this work are directly related to applications in Li-ion batteries. Even though it is beyond the scope of this thesis to give a summary of potential applications of the fabricated materials, it is important to stress that also other devices for energy conversion and storage, as well as for catalysis purposes, clearly can benefit from both the use of these nanostructured materials and the process methodologies that have been developed in this work. Therefore, the main focus of this thesis is related to the synthesis and deposition of nanostructured materials for negative electrodes in Li-ion batteries via electro spray-assisted methods. The electro spray process has been implemented in two slightly different contexts for the production of different nanostructures. The first one consists in the production of nanoparticles via an unconventional approach that combines charged aerosols with red-ox reactions in liquids, while the second one develops a single step process for a complete synthesis and assembly of nanocomposite coated electrodes by pyrolysis and/or deposition of precursor solutions and suspensions.

The structure of the thesis consists of six independent chapters that describe the main ideas developed in this work and that are summarized in the final

conclusions. Furthermore, few appendices providing some general background information and notes on the related topics have been included. A brief outline of the chapters is given below.

Chapter one provides a general overview on the challenges related to advanced Li-ion batteries, where a particular attention is devoted to negative electrode materials and their characteristic reaction mechanisms, along with the possibility of increasing Li storage capacities. Moreover, pros and cons related to the use of different types of materials and reactions mechanisms are addressed. Crucial issues concerning the mechanical stability of the materials are examined and some possible strategies are also suggested.

Chapter two describes the general theory of electrospraying and its modes of operation. The attractive features of generating charged, nearly-monodispersed droplets with tunable sizes, as well as the challenges related to the increase of their production rate are discussed. Besides, common approaches to produce nanostructured materials via electrospray-based techniques are mentioned, together with some specific applications related to Li-ion batteries.

Chapter three develops an alternative concept for electrospraying, e.g. charged precursor droplets are collected in a liquid bath where they can undergo further chemical reactions. In particular, the standard technique of chemical reduction via reductive precipitation of metal chlorides by sodium-boron-hydride is bridged to electrospraying. The underlying idea of the method is to extend a drop-wise addition of the precursors to a continuous process, where charged precursor droplets with micrometric sizes are directly supplied to the reductive bath. In this way, the amount of precursor that is released for the formation of the precipitated particles can be in principle adjusted via a preliminary analysis of the average droplet size. Accordingly, this novel method can promote a continuous formation of small nanoparticles in a dynamic process driven by electrostatic forces. Tin nanoparticles were chosen as a major example of synthesized materials for this investigation since they can be applied to Li-ion battery negative electrodes.

Chapter four focuses on the characterization and electrochemical testing of Sn nanopowders synthesized via the combined approach of electrospray and chemical reduction described in chapter three. Their electrochemical behaviour as negative electrodes is compared to those of Sn-based commercial powders having different stoichiometries and mesh sizes. The structure of the obtained Sn nanopowders, their oxidation, due to the limitations imposed by the current process (i.e. exposure to air), and their impact on the ultimate electrode performances are discussed.

Chapter five provides a new direction for the use of electrospraying in the context of direct synthesis and assembly of nanocomposite negative electrodes for Li-ion batteries. It offers some key ideas on possible shortcomings deriving from the conventional electrode fabrication, where the active materials (i.e. nanopowders) need

to be processed in multi-step processes with polymeric binders/additives in order to cast laminated electrodes. Consequently, limitations in the electrochemical performances for this type of electrodes can easily arise from inhomogeneous dispersion of the active nanoparticles with the inactive components in the slurries to be cast or unsuitable matching of their electrical and mechanical properties in the resulting composite coatings. Electro spray pyrolysis of precursor solutions containing dissolved precursor salts together with conventional binders (i.e. PVdF) is presented as an effective approach for direct synthesis and deposition of nanocomposite electrodes in a single step process. In this way, the nanoparticles generated via pyrolysis of the metal precursors are in intimate contact with the binder contained in the emitted droplets during the electro spray process. The reacted droplets are at the same time directly driven on selected areas to form nanocomposite coated electrodes. Different PVdF/oxide materials employing Sn, Co and Fe precursors have been synthesized and assembled via this straight approach at low temperatures. Structural and electrochemical characterizations of the resulting electrodes are presented. The impact of the approach and its effects on the dispersion of the active nanoparticles in the composite remnants are discussed. Finally, a similar process relying on electrode deposition from concentrated suspensions of PVdF/Si nanoparticles is also considered as possible route.

Chapter six discusses the synthesis of other metal nanoparticles (i.e. Au) for possible applications in catalysis via a route very similar to that described in chapter three. In this case, electro spray of gold precursor solutions with different concentrations has been directly performed into a reductive-surfactant solution, where Au nanoparticles are directly generated and stabilized by a capping agent released in the reduction process. In particular, this method can provide a one-step approach for a quick and continuous preparation of quasi-spherical and anisotropic Au particles at room temperature under air.



# Nomenclature

$\alpha_s$	symmetry factor
$\alpha_T$	Taylor cone half-angle
$\gamma$	surface tension
$\Gamma$	successful jump frequency of the growth species
$\epsilon_0$	permittivity of the vacuum
$\epsilon_r$	relative permittivity
$\eta$	overpotential
$\eta_{CT}$	charge transfer overpotential
$\eta_{MT}$	mass transfer overpotential
$\kappa$	electrical conductivity
$\lambda$	wavelength
$\mu$	viscosity
$\mu_v$	chemical potential per unit volume
$\mu_s$	chemical potential per unit surface
$\rho$	density
$\rho_d$	density of a liquid droplet
$\rho_p$	density of a solid particle
$\sigma_n$	normal electric stress
$\sigma_t$	tangential electric stress
$\tau_e$	electrical relaxation time
$\tau_h$	hydrodynamic time
$\tau_j$	characteristic time for jet formation
$\tau_l$	characteristic time for liquid supply
$\tau_p$	characteristic time for jet or meniscus deformation
$\tau_d$	characteristic time for droplet formation
$\phi$	Fuchs correction factor
$\Sigma$	supersaturation

## Nomenclature

---

$\Omega$	atomic volume
$a$	droplet radius
$a_{prod}$	activity of the products
$a_{react}$	activity of the reactants
$a_s$	activity coefficient of the solvent at the droplet surface
$d_d$	droplet diameter
$d_{gs}$	diameter of the growth species
$d_p$	particle diameter
$d_j$	jet diameter
$e$	electron charge
$f$	mass fraction of the material in solution
$g$	local acceleration due to gravity
$i$	current flowing in an electrochemical cell
$i_A$	anodic current flowing in an electrochemical cell
$i_C$	cathodic current flowing in an electrochemical cell
$i_0$	exchange current in an electrochemical cell
$k_B$	Boltzmann constant
$\ell$	diffusion length
$\ell_g$	gas mean free path
$m$	mass
$m_c$	mass of the droplet for its critical solute concentration
$m_d$	mass of the droplet
$m_{dm}$	mass of the dry matter
$n$	number of transferred electrons (charges)
$n_{sp}$	number of growth species per unit volume
$p_d$	partial pressure of the vapor at the surface of the droplet
$p_{sat}$	saturation vapor pressure
$p_\infty$	ambient partial pressure of the vapor
$q_R$	Rayleigh limiting charge
$r$	radius
$r^*$	critical radius



---

$r_0$	initial radius of the nucleus
$r_n$	radius of the nozzle
t	time
$t_{\text{exp.}}$	duration of the experiment
$t_d$	characteristic time for diffusion
$w_c$	thickness of the solid crust
$x_s$	solute mole fraction at the surface of the droplet
C	concentration of the solute
$C_0$	initial concentration
$C_e$	equilibrium concentration
$C_l$	concentration in the bulk of a liquid
$C_{\text{prec.}}$	precursor concentration
$C_s$	concentration on the surface of a solid particle
$C_{\text{sp.}}$	specific capacity
$C_{\text{th}}$	theoretical capacity
D	diffusion coefficient
$D_i$	inner diameter of the nozzle
$D_o$	outer diameter of the nozzle
$D_s$	diffusion coefficient of the solute in the liquid
$D_v$	diffusion coefficient of vapor in air
E	electric field
$E^\circ$	standard reduction potential (referred to a SHE)
$E_i$	electrode potential upon current flow
$E_{\text{th}}$	thermodynamic reduction potential
$E_{\text{tip}}$	effective field strength at the tip of the electrified nozzle
$E_{\text{on}}$	electric field corresponding to the onset of electrospray
$E_n$	normal component of the electric field
$E_t$	tangential component of the electric field
F	Faraday's constant
$F_{\text{prec.}}$	mass flow rate of the precursor
G	Gibbs free energy

## Nomenclature

---

$G^*$	critical Gibbs free energy
$G^\circ$	standard Gibbs free energy
$G_v$	Gibbs free energy per unit volume of the solid phase
$I$	current intensity
$L$	characteristic distance travelled by the droplets
$M_m$	molar mass
$N_A$	Avogadro's number
$P_\gamma$	pressure caused by surface tension
$P_e$	electrostatic pressure
$P_{th}$	probability for a thermodynamic fluctuation
$R$	ideal gas constant
$R_{int}$	internal resistance of a cell
$R_c$	radial coordinate of the surface of the crust
$R_{CT}$	charge transfer resistance
$R_{MT}$	charge transfer resistance
$R_N$	rate of nucleation
$R_j$	radial characteristic length of the jet
$Q$	flow rate
$Q_{tot}$	total amount of electrical charge
$T$	temperature
$T_d$	temperature of the vapor at the surface of the droplet
$T_\infty$	ambient temperature of the vapor
$V$	potential
$V_{ch}$	cell voltage during charge
$V_d$	cell voltage during discharge
$V^\circ$	standard cell voltage
$V_m$	molar volume
$V_n$	effective voltage applied to the nozzle
$V_{on}$	voltage corresponding to the onset of electrospray
$V_{th}$	thermodynamic voltage of a cell
$V_{UC}$	volume of a unit cell

---

Z            number of atoms/molecules per unit cell

## Abbreviations

AAS	Atomic Absorption Spectroscopy
AFM	Atomic Force Microscopy
CB	Carbon Black
CCEC	Controlled-Current Electrolytic Cell
CV	Cyclic Voltammetry
CVD	Chemical Vapor Deposition
DDA	Dodecylamine
DDAM	Dodecylaminomethanol
DMC	Di-methyl Carbonate
DMSO	Di-methyl Sulfoxide
EC	Ethylene Carbonate
EDS	Energy Dispersive Spectroscopy
EDX	Energy Dispersive X-Rays (Analysis)
EHDA	Electrohydrodynamic Atomization
ES	Electrospray
ESD	Electrostatic Spray Deposition
ESP	Electrostatic Spray Pyrolysis
ESRP	Electrostatic Spray Reductive Precipitation
EV	Electric Vehicle
FA	Formaldehyde
FDM	Fused Deposition Modeling
FT-IR	Fourier Transform-Infrared Spectroscopy
GC-MS	Gas Chromatography-Mass Spectrometry
HEV	Hybrid Electric Vehicle
IPA	Iso-propyl Alcohol
JCPDS	Joint Committee on Powder Diffraction Standards
LACVP	Laser Assisted Chemical Vapour Pyrolysis

## Nomenclature

---

M.W.	Molecular Weight
NMP	N-Methylpyrrolidone
NMR	Nuclear Magnetic Resonance
OCV	Open Circuit Voltage
PAN	Polyacrylonitrile
PDF	Powder Diffraction File
PVA	Poly-vinyl-Alcohol
PVD	Physical Vapor Deposition
PVdF	Polyvinylidene Fluoride
PVP	Poly-vinyl-pyrrolidone
RP	Reductive Precipitation
RT	Room Temperature
SAED	Selected Area Electron Diffraction
SEI	Solid Electrolyte Interphase
SEM	Scanning Electron Microscopy
SHE	Standard Hydrogen Electrode
TEM	Transmission Electron Microscopy
TMO	Transition Metal Oxides
UV-Vis.	Ultraviolet-Visible (spectroscopy)
VLS	Vapour-Liquid-Solid (growth)
VS	Vapour-Solid (growth)
Wt.	Weight
XRD	X-Rays Diffraction

# Chapter 1

## Introduction

*Porta itineris dicitur longissima esse.  
(Latin proverb)*

This chapter gives a general overview of the Lithium-ion battery technology, with a primary focus on negative electrodes. The challenges related to the use of alternative materials to enhance the performances of advanced Li-ion battery electrodes are discussed, as well as the issues arising from the various electrochemical mechanisms responsible for Li storage. Nanostructured materials are introduced in this context as potential candidates to address the intrinsic shortcomings of bulk structures during electrochemical processes. Particular attention is devoted to the possibility of increasing both gravimetric and volumetric energy densities by using Li-alloys or transition metal oxides, as well as to the volume change the negative electrode has to endure upon Li up-take and removal. The chapter also highlights the importance of selecting and developing suitable routes for the synthesis of various nanomaterials, in order to effectively exploit their properties in coated electrodes, in combination with binders and additives.

## 1.1 Time to change (and re-charge) the batteries

Batteries are electrochemical devices that enable the conversion of chemical energy into electrical energy. The first battery, also known as ‘pila’, was invented in 1800 by the Italian physicist Alessandro Volta. Since then, a large variety of electrochemical cells with different features and shapes have been developed. In all cases, the various battery technologies share the same principle: they exploit chemical reactions between different materials to store and deliver electrical energy. Batteries represent a particular type of electrochemical cell. Strictly speaking, an electrochemical cell is a system that can convert electrical energy into chemical energy and vice versa (i.e. chemical energy into electrical energy) by redox reactions. Electrochemical cells can be divided in two categories: *i) galvanic cells* and *ii) electrolytic cells*. A galvanic cell can directly produce electricity via spontaneous redox reactions. These cells are also referred to as ‘primary batteries’ and constitute a power source that can be used to power electrical devices and once discharged cannot be re-utilized (i.e. recharged). On the other hand, electrolytic cells enable the transformation of electrical energy into chemical energy via forced redox reactions. Electrolysis has various technological applications, like gas production (i.e. H<sub>2</sub>, Cl<sub>2</sub>, etc.) and metal plating (i.e. electrodeposition). The electrolytic process is further exploited in the so-called ‘secondary batteries’. Secondary batteries, also commonly referred to as rechargeable batteries, can store and convert reversibly electrical and chemical energy, relying on both galvanic and electrolytic processes. In particular, a rechargeable battery works as an electrolytic cell during its charge and as a galvanic cell upon discharge. The big advantage of secondary batteries is that their underlying chemical reaction can be reversed. In this way they can be restored to their charged state by reversing the direction of the current flow that occurs during discharging. Consequently, they can be re-used easily hundreds or even thousands of times.

Four different types of rechargeable batteries currently dominate the industrial market, each of which has its own pros and cons when it comes to practical issues like application, durability, cost, safety and performance.

- Lead-acid (Pb-acid)
- Nickel-Cadmium (Ni-Cd)
- Nickel-metal-hydride (Ni-MH)
- Lithium-ion (Li-ion)

The first rechargeable battery, the lead-acid battery was invented in 1859 by the French physicist Gaston Planté. Nowadays lead-acid batteries take up about half the worldwide rechargeable-battery market. They are extremely cost-effective power sources that are found in virtually all cars and are also used in large back-up systems.

Yet, they cannot store much energy for a given weight or volume, compared to more recent technologies.

Nickel-Cadmium batteries were first introduced in 1899 by Waldemar Jungner from Sweden. They were adopted in all applications where more power was needed. After the 1960s, Ni-Cd batteries became popular power sources for portable electronics, electric razors, toys and, more in general, for devices where large surge currents are required.

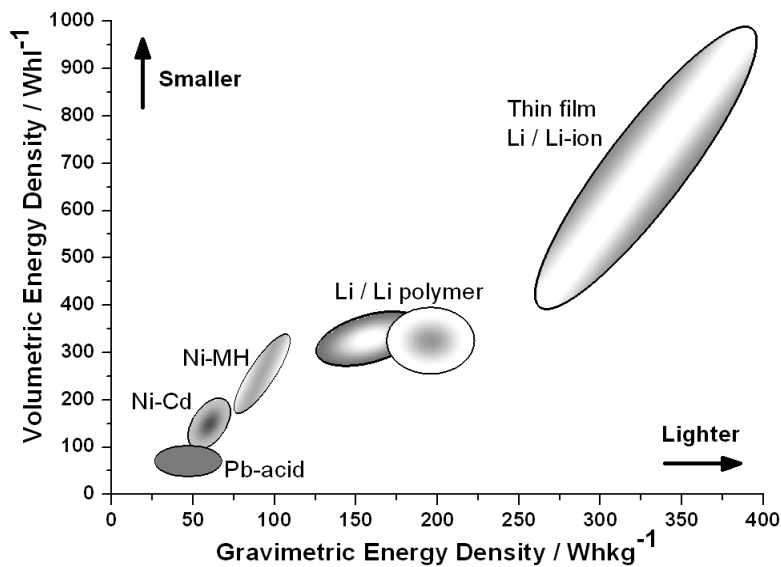
Ni-metal-hydride batteries appeared on the market in 1989 as an evolution of the 1970s' Nickel-hydrogen batteries, which were only used in space applications (e.g. in satellites). Ni-MH technology was finally established by an American inventor, Stanford Ovshinsky, who created suitable metal-hydride alloys with disordered structures and specific compositions to meet the commercial requirements. Nevertheless, the early prototypes were actually produced by Percheron and van Vecht, in France and the Netherlands respectively. Ni-MH technology represents the first quantum leap in terms of energy stored per unit weight, with figures doubling those of lead-acid batteries. Not surprisingly, Ni-MH batteries in the '90s became the favourite choice for powering portable electronics, displacing Ni-Cd technology in many applications, and even providing a power source for hybrid-electric vehicles (HEV).

Li-ion batteries evolved from primary (i.e. non-rechargeable) lithium batteries, which appeared in the '70s for low-current applications, such as watches, hearing aids and pace-makers. Electrochemical reactions involving lithium are attractive, because Li is the lightest solid element on earth ( $M_m = 6.941 \text{ g mol}^{-1}$ ;  $\rho = 0.534 \text{ g cm}^{-3}$ ) and is also the most reducing metal in nature ( $E^\circ = -3.04 \text{ V}$ ), which makes it an excellent candidate for batteries with a high energy density.

Most of the first lithium batteries employed metallic Li in combination with  $\text{MnO}_2$ , and a non-aqueous electrolyte. In 1975 other pioneering studies by Whittingham were performed on rechargeable lithium batteries [1], where the metallic lithium constituted the negative electrode and a layered  $\text{Li}_x\text{TiS}_2$  structure was used as the positive electrode in a non-aqueous electrolyte. The critical issue of these batteries concerned their stability. Repeated charge and discharge resulted in the formation of dendrites on the lithium electrode, which caused short circuits through the separator. This intrinsic drawback, together with the reactivity of metallic lithium posed severe limitations to widespread and safe use of these cells. The risk of explosions and bursting into flames, accompanied by release of toxic fumes, was simply too high for these batteries to enter the market.

A real breakthrough in Li technology occurred in the '80s. On the one hand, metallic lithium was replaced by intercalation compounds containing lithium [2-5], on the other hand, graphite [6], and more in general carbonaceous materials [7, 8], were found to accept and electrochemically release Li in a reversible fashion. The

systems constituted by the combination of these materials were referred to as “Li-ion batteries”, because the lithium was merely present in its ionic form. Most of the research that resulted in a fast development of these cells, making use of polymer electrolytes was carried out by the French and Italian groups led by Armand and Scrosati respectively [9-12]. The first commercial Li-ion battery was released in 1991 by Sony. It was made of layered lithium cobalt oxide as the positive electrode, graphite as the negative electrode and a polymer electrolyte as Li-ion conductor. In the following years several improvements were introduced in the technology as well as in the materials allowing Li-ion batteries to start dominating the market of power sources for portable electronics. The reason for this rapid ‘battery change’ is evident by looking at the plot shown in Fig. 1.1, which compares the various rechargeable battery technologies in terms of gravimetric and volumetric energy densities.

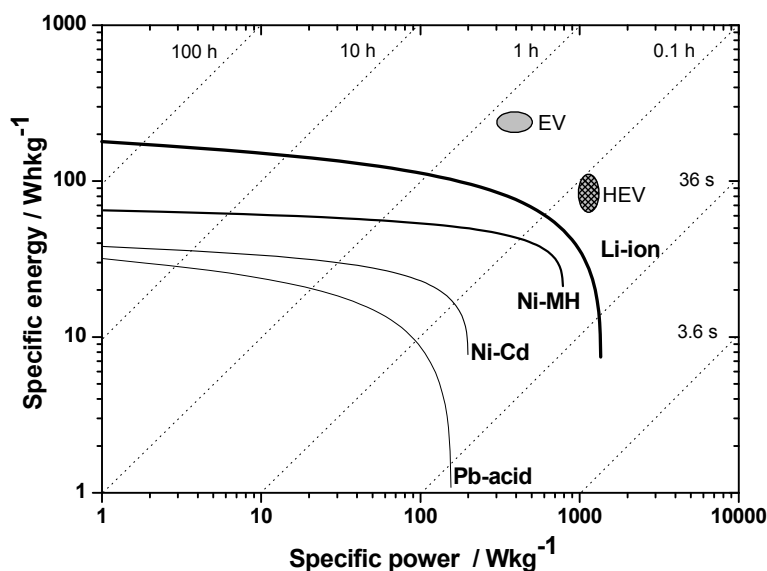


**Fig. 1.1.** Battery scenario comparing different technologies for rechargeable cells in terms of volumetric and gravimetric energy densities. Please note that thin film Li-ion batteries represent the latest technology in the plot, as far as their development is concerned.

Li-ion batteries outperform the other technologies, providing more compact and lighter power sources. Another important feature that contributed to their widespread use is that, unlike other rechargeable cells, they do not suffer from any memory effect (i.e. the loss in capacity when a battery is recharged without being fully depleted) and they have a longer ‘shelf life’ (i.e. a longer characteristic time of self-discharge). All these factors made the mobile-phone revolution possible. However, Li-ion batteries now have to face the major ‘mobility challenge’: powering electric vehicles (EV). Electrification of cars is soon expected, especially considering the global climate change and the rise in the oil price. When it comes to this task, the success of current Li-ion battery technologies is not guaranteed. Indeed, as shown in Fig. 1.2 Li-ion



batteries are still quite far from the requirements for EV. Applications to HEV are expected to rapidly increase in these years, especially if the technology and the materials become cheaper than those of Ni-MH batteries.



**Fig. 1.2.** Ragone plot comparing different types of rechargeable batteries. The two bubbles refer to the requirements needed for powering electric vehicles (EV) and hybrid electric vehicles (HEV), respectively. Note also that the various time intervals, in which the energy is being delivered, are indicated by the dotted lines.

Significant improvements in terms of both gravimetric and volumetric energy densities, as well as power delivery are still needed in order to conveniently meet the EV requirements. Fully re-charging an EV battery pack in a reasonable amount of time is at the moment one of the main issues that limit the spreading of commercial EV. Another major problem concerns their safety, since Li-ion batteries tend to become unstable if overheated, overcharged or pierced. A noteworthy example is offered, in this respect, by the laptop batteries that Sony had to withdraw from the market in 2006, due to a manufacturing defect that in some cases resulted in explosions and fire. Needless to say that a similar situation in a faulty car module, with much more energy stored, is extremely dangerous. Not surprisingly, car companies are very cautious and have not embarked on EV technology, due to the huge risks involved.

Luckily enough, there is room for improvement in the materials and the entire Li-ion technology, as well as in the design of suitable cells architectures. It is important to bear in mind that the battery technologies have evolved very slowly over the years, and that they cannot keep up with Moore's law, similarly to semiconductors, due to their intrinsic nature of active systems, which add further complexity. Nevertheless, advanced engineering and convenient combination of the materials ultimately determine the characteristics of the batteries. Therefore, specific

energy and power densities, safety, durability and cost could no longer be an issue in the near future. To achieve this there is a strong belief among the researchers that developing novel nanostructured electrodes can address all the current shortcomings.

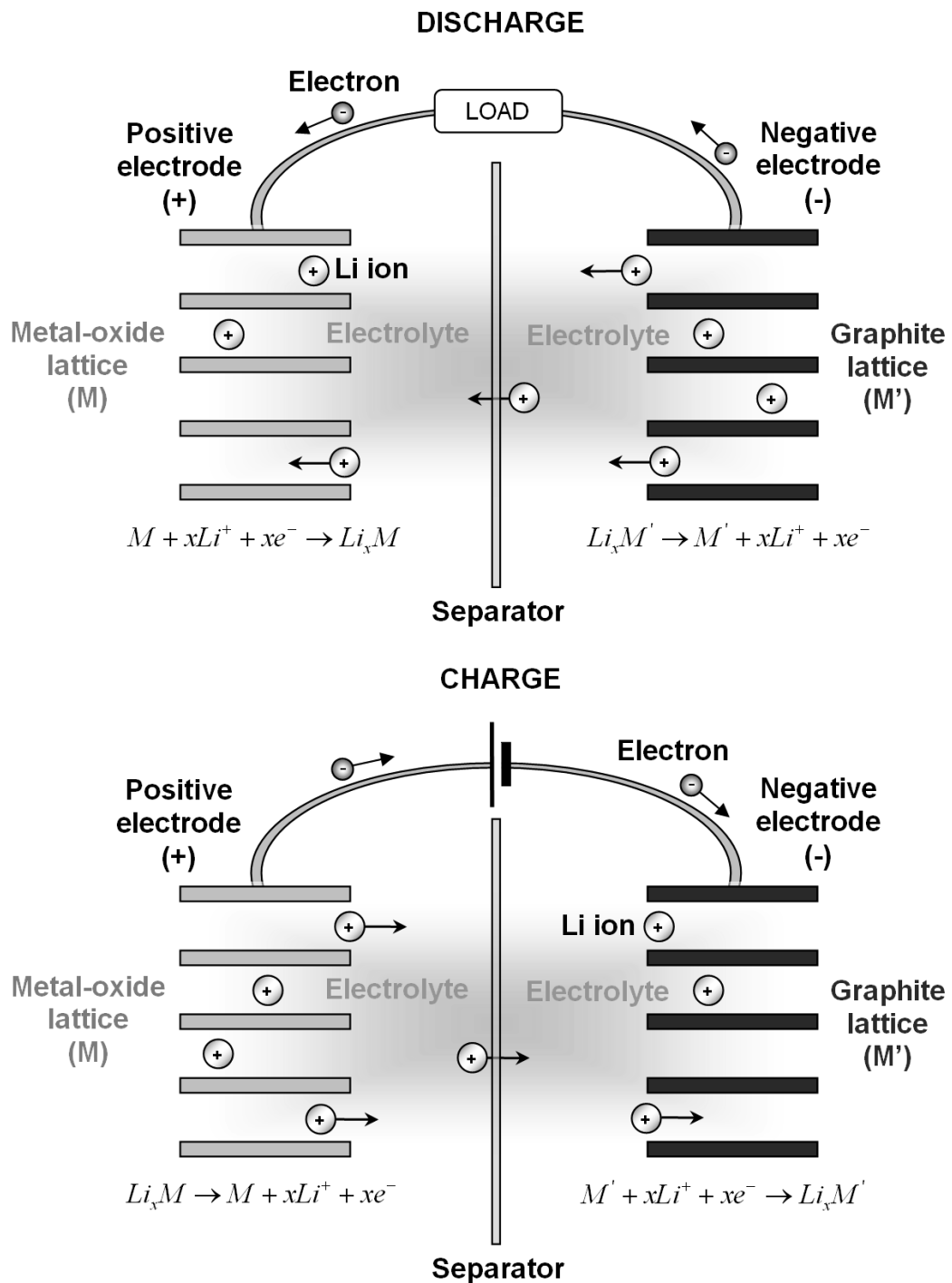
## 1.2 Rechargeable (Li-ion) batteries: basic principles

In general, a (Li-ion) battery is made up of a positive electrode and a negative electrode kept apart by a separator soaked in a conductive electrolyte that allows ( $\text{Li}^+$ ) ions, but not electrons to travel between them. The electrolyte can be a solid-state compound, an ion-conductive polymer or a (non-aqueous) liquid.

As positively charged ions travel from the negative electrode to the positive electrode through the electrolyte, an equal number of electrons must make the same journey through an external circuit, producing an electric current that does useful work. This process of discharge is shown in Fig. 1.3 for a Li-ion battery, together with the subsequent step of charging. Recharging a (Li-ion) battery involves external work which forces the electrochemical reaction in the opposite direction and this is achieved by reversing the direction of the current flow through the external circuit.

Li-ion batteries typically employ intercalation materials like Li-metal oxides as positive electrodes and carbonaceous materials (i.e. graphite) as negative insertion hosts, separated by a polymeric separator soaked in a liquid electrolyte. Usually this is a non-aqueous electrolyte based on lithium salts (i.e.  $\text{LiPF}_6$ ) dissolved in an organic solvent mixture (i.e. ethylene carbonate/dimethyl carbonate). It is important to note that the current electrode materials do not alter their crystal lattice upon accepting and releasing Li, and their structures are only slightly strained or distorted. This contributes to the stability of the system. However the presence of the liquid electrolyte is a major concern. Flammability of the organic solvents and a limited range of operational temperatures for the electrolytes are crucial issues that severely restrict the use of Li-ion batteries.

Electrode-electrolyte interfaces play a fundamental role in electrochemistry and for Li-ion batteries there are no exceptions. In particular, it is known that together with redox reactions also electrolyte degradation occurs, which generally results in the formation of the so-called Solid Electrolyte Interphase (SEI). The formation of an SEI layer is often viewed as a mechanism to prevent further degradation of the electrode or electrolyte. The formation of the SEI on negative electrodes during Li uptake has been documented by various studies, while its presence on positive electrodes is often suggested but has not been proven in all cases [13].



**Fig. 1.3.** Schematic drawing of the working principle of a Li-ion battery. M and M' represent the active materials. In a charged Li-ion battery the graphite lattice is packed with Li ions in a high-energy state. Connecting a load causes its discharge, with Li ions transferred through the electrolyte and taking up residence in the metal-oxide lattice, while releasing energy in the process. Note that for each Li ion an electron must make the same journey through the external circuit, producing a current. Recharging the battery requires a forced reaction, by which the electrons are pushed in the opposite direction through the circuit and the lithium ions are driven back through the electrolyte into the graphite lattice.

### 1.2.1 Materials for positive electrodes

Typical materials for positive electrodes are intercalation compounds made from Li-metal oxides, which provide a source of lithium stable in air and with a relatively high potential. The first materials proposed were  $\text{LiNiO}_2$  and  $\text{LiCoO}_2$ , whose layered structures allowed Li to move back and forth between their alternating lattice planes.  $\text{LiNiO}_2$  possesses a slightly higher theoretical capacity (i.e.  $275 \text{ mAhg}^{-1}$ ) than  $\text{LiCoO}_2$  (i.e.  $274 \text{ mAhg}^{-1}$ ). The latter, however, is more stable when Li is removed from the lattice [14-16] which justifies its widespread use in commercial batteries.

An alternative material is  $\text{LiMn}_2\text{O}_4$ , which has some advantages over the layered structures, mainly in terms of production cost and toxicity [17]. Its three-dimensional cubic spinel structure also provides wider 3D-pathways for Li [18]. Nevertheless, it has also some intrinsic disadvantages: a lower theoretical capacity (i.e.  $148 \text{ mAhg}^{-1}$ ), structural changes [17], limited cycle life and poor storage ability at elevated temperatures, as well as possible dissolution of Mn at high potentials, related to electrolyte degradation [19, 20]. Some issues have been partly addressed by doping  $\text{LiMn}_2\text{O}_4$  with other elements (i.e. Mg, Ni, etc..) and  $\text{LiMg}_\delta\text{Ni}_{0.5-\delta}\text{Mn}_{1.5}\text{O}_4$  ( $\delta = 0.05, 0.07, 0.1$ ) represents an interesting material for high-voltage positive electrodes showing suitable characteristics [21-24]. Still, its performance is not optimal.

Another option is the olivine  $\text{LiFePO}_4$ , which yields a very stable potential almost up to its full capacity (i.e.  $170 \text{ mAhg}^{-1}$ ). The output voltage is not as high as in the previous case, but its stability at elevated temperatures (up to  $85 \text{ }^\circ\text{C}$ ) over long cycle life [25, 26] makes this compound extremely attractive for practical applications. Its main drawback is poor electrical conductivity, which makes it unsuitable for a normal cell. Further development of  $\text{LiFePO}_4$  by carbon coating [27] or even using non-coated nanoparticles makes it possible to fabricate operational electrodes that are currently used in commercial applications.

### 1.2.2 Materials for negative electrodes

One of the first materials to replace metallic lithium as the negative electrode in Li-ion batteries is graphite. Its planar structure can react reversibly with Li according to the following reaction:



The topotactic reaction of one Li with six atoms of carbon is responsible for a theoretical capacity of  $372 \text{ mAhg}^{-1}$ . This value is relatively high, especially compared to the capacity of positive electrodes, due to the fact that carbon is one of the lightest

elements ( $M_m = 12.011 \text{ gmol}^{-1}$ ;  $\rho = 2.266 \text{ gcm}^{-3}$ ). Moreover, lithiated  $\text{LiC}_6$  has a potential close to that of metallic Li, meaning that almost the full potential of Li can be exploited in a battery using graphite as the negative electrode [28, 29]. Carbon has several other advantages: fair electrical conductivity, structural stability, contained production cost, limited environmental impact and abundance in nature. However, advantages are never separated from disadvantages: carbon reacts with the electrolyte forming an SEI layer, which accounts for an irreversible capacity loss of about 15% [28, 30, 31]. Additionally,  $\text{LiC}_6$ , having a potential close to that of metallic Li, favors metal plating of lithium on the carbon when charged under high current densities. This circumstance is hazardous, because results in a similar scenario to that of metallic Li in secondary lithium batteries with the formation of dendrites.

Possible alternatives are materials like the spinel  $\text{Li}_4\text{Ti}_5\text{O}_{12}$ , which shows attractive characteristics in terms of extremely stable potential around 1.55 V versus metallic lithium up to about 90% of its theoretical capacity (i.e.  $175 \text{ mAhg}^{-1}$ ) [32]. Moreover, it has a negligible volume variation of the host lattice during Li uptake and removal (i.e.  $< 0.1\%$ ), resulting in a ‘zero strain’ material [33]. These features are extremely important for the safety and the cyclability of an entire Li-ion battery.

However, if the main goal is to increase the overall gravimetric and volumetric energy densities in advanced Li-ion batteries, other alternatives must be considered. Indeed, the practical values for the overall capacity in Li-ion batteries are ultimately limited by the positive materials. The real breakthrough should come from the discovery of new Li-rich sources for positive electrodes, which could provide much higher capacities than those mentioned above. Still, this turning point seems quite far and at the moment the capacity issue can be addressed differently. One way is to adopt other materials for negative electrodes, which are able to accept much more Li than graphite, thus enhancing the storage capacity. This means that a reduced amount of negative electrode material is needed to obtain a definite capacity value, and more material on the positive side can be added at the same time to match the needed energy density figures.

A first class of materials is represented by the so-called *lithium-metal alloys*. As from the early ‘70s it was demonstrated that lithium can undergo electrochemical alloying reactions with several other metallic or semi-metallic elements [34, 35]. These electrochemical reactions are feasible at room temperature in a non-aqueous electrolyte. More important, the as-formed alloys with Li are exactly the same as those prepared by metallurgical ways. In this sense, the ‘driving force’ for Li alloying is not thermal but electrochemical and monitoring the behaviour of these electrodes in a lithium cell can be viewed as a way to ‘electrochemically screen’ a lithium-metal (i.e. Li-M) phase diagram at room temperature [36]. Nevertheless, the nature of the reaction itself is totally different from the topotactic intercalation/insertion mechanisms mentioned so far. Alloying and de-alloying of Li with other metals imply

reconstitution reactions, which strongly affect the crystal structure of the pristine materials. In most cases, large volume changes and lattice alterations of the host materials are involved during uptake and removal of Li. This fact severely compromises the stability of these electrodes and results in a very poor cycling behaviour, which will be discussed later. Despite these drawbacks, the huge theoretical capacities (i.e. up to  $4200 \text{ mAhg}^{-1}$ ) expected for the formation of some Li-rich alloys or intermetallics are very appealing and justify the revival for this class of negative electrodes for possible applications to HEV and EV.

The latest class of alternative materials to carbon comprises some *transition metal oxides* (TMO). This approach was proposed for the first time about ten years ago [37, 38] and it implies a different reaction pathway, through which high capacities can be achieved by reversibly storing Li in the form of  $\text{Li}_2\text{O}$  by a mechanism termed ‘conversion’. This circumstance is extremely interesting, since under normal conditions it is not possible to extract Li from  $\text{Li}_2\text{O}$ . The very nature of the electrochemical reaction of Li with TMO is responsible for the formation of a complex nanostructured system in which non-active metal nanoparticles are interdispersed in an *active* matrix of  $\text{Li}_2\text{O}$ . However, also these materials suffer from a number of shortcomings, like a limited cycle life due to volume changes of the host and a big hysteresis in their characteristic voltage profiles.

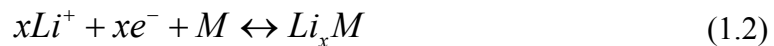
The different types of reactions that negative electrode materials can undergo with Li are further discussed in the following paragraph, stressing their intrinsic features and their possible roles in an advanced battery design.

### 1.3 Reaction mechanisms of Li in negative electrodes

The electrochemical reaction of Li can follow several different pathways, depending on the nature of the host material and its crystalline structure. A list of all the possible types of reactions with single elements or binary compounds is here reported.

#### *I – Insertion*

This is the typical reaction that graphite undergoes with lithium, where lithium is inserted between adjacent graphene sheets. The lithium is reversibly stored in the active material,  $M$ , according to the general reaction:

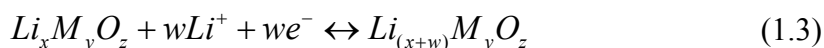


which reduces to eq. (1.1) when  $M$  is taken as  $6C$  and  $x$  equals  $1$ . This reaction has the big advantage of not involving any structural change into the host lattice of the graphite. It accounts only for a minimal volume variation during the electrochemical

process, which is negligible in terms of strain. The fair electrical conductivity of carbon and the high reversibility of the process are basically the keys of the practical success of this material in commercial batteries. In this respect, *if* suitable materials for positive electrodes (i.e. with theoretical capacities close to  $400 \text{ mAhg}^{-1}$  and voltages possibly higher than 4 V) were to be found, then there would be no need to replace graphite with other materials in advanced Li-ion batteries. The issues mentioned in the previous sub-paragraph could probably be addressed with proper engineering of the entire cell and its parts.

### *II – Intercalation*

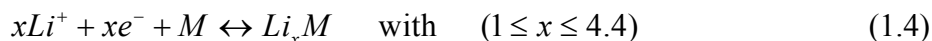
This type of reaction has already been mentioned for Li-rich metal oxides, where the lithium ions remain in their oxidation state of  $\text{Li}^+$ . Only the host material changes its oxidation state, according to the general mechanism:



where  $M$  is the metal,  $O$  is the oxygen and the subscripts refer to the stoichiometry. In the case of a negative electrode, this reaction can be considered for the spinel  $\text{Li}_4\text{Ti}_5\text{O}_{12}$ , which can accept lithium yielding  $\text{Li}_7\text{Ti}_5\text{O}_{12}$  as final product. The advantage of intercalation is that it does not destroy the host lattice and usually only limited volume changes take place. For  $\text{Li}_4\text{Ti}_5\text{O}_{12}$  this situation is rather special, since negligible volume variations occur and its potential of reaction is far from that of metallic lithium, increasing the safety of the electrochemical process in a whole cell. This material and its characteristic reaction is clearly the one of the first choices for Li-ion batteries which can safely handle high current densities, but with limited voltage outputs and ultimately with reduced energy densities. Moreover, the capacity of this spinel material is negatively affected by a limited stability in acidic environments [39].

### *III – Alloying with a single active component*

The general reaction of Li alloying with a single active element,  $M$ , is as follows:

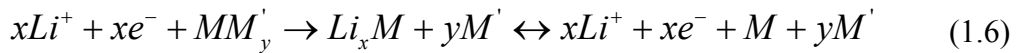
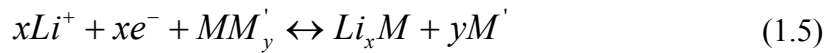


where  $x$  refers to the number of lithium atoms per unit  $M$ . Alloying of Li occurs with several metals, semi-metals and semiconductors (i.e. Al, Si, Ge, Sn, Sb, etc.) resulting in a remarkable Li storage capacity. Furthermore, it offers a wide choice for tuning the potential of the reactions with respect to that of metallic Li [35, 40]. However, there is a price to pay for these attractive characteristics, namely their limited mechanical stability. It is interesting to observe that most of the metals and semi-

metals that alloy with Li show values of their atomic radii which are relatively close to that of metallic lithium (i.e. 1.45 Å). The reaction often involves a complete change of the structure of the host materials, due to the different nature of the chemical bonds (i.e. metallic). In most of the cases several structure changes are involved at different states of charge and discharge, with the formation of intermetallic compounds. Sn and Si, for example, can undergo the formation of up to six different intermediate phases. Including a vast amount of Li necessarily implies large volume changes, which directly affect the stability of the host materials. Repeated alloying and de-alloying causes fragmentation of the host material, which undergoes extended cracking and loss of electrical contact between the electrode parts. Additionally, the electrical conductivity of most Li-alloys hinders an efficient transport of the electrons exchanged in the electrochemical reaction. These drawbacks represent the main obstacle for incorporation of Li-alloys in advanced negative electrodes with high gravimetric and volumetric capacities. Engineering of the host particles, of their mutual contact in a composite electrode, as well as their assembly on the current collector, could hold the key for a breakthrough in these applications.

#### *IV – Alloying with one active component and displacement of the inactive one*

Li alloying with binary (intermetallic) compounds (i.e.  $MM'$ ) may follow also other pathways. In this case  $M'$  represent an element which does not react with Li and it is separated during the electrochemical processes, according to the following reactions:

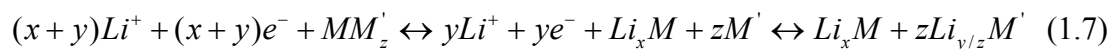


where in the first case  $M'$  is displaced reversibly, in order to re-form  $MM'$ , while in the second case it is irreversibly displaced after the initial reaction and remains isolated upon subsequent cycling [41]. As a result, a finely inter-dispersed composite of a lithiated phase in an un-reacted (non-lithiated) matrix is obtained (i.e.  $Sn_2Fe$  or  $Ni_xSn$  where Fe and Ni are inactive). On the one hand, the presence of the inactive component reduces the theoretical capacity compared to that of the pure active metals. On the other hand, the presence of a non-reactive phase stabilizes the composite material, as the volume changes are somehow “buffered” by the inactive component which ‘dilutes’ the reactive phase [41]. In the case of Sn this mechanism prevents aggregation of Sn into larger grains, which are more prone to undergo cracking and consequently loss of capacity. Moreover, when the inactive component has a good electrical conductivity its inter-dispersion promotes the transport of the electrons, providing a conductive network that is not damaged by the electrochemical reaction. Therefore, this type of alloys has also potential for applications in advanced negative electrodes, provided that a good tradeoff for their features is reached.



*V – Displacement and alloying with both active components*

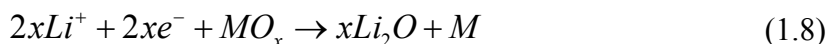
A binary compound can also have both materials active towards Li according to:



where one component starts alloying with Li, with the simultaneous displacement of the other one, which reacts with Li at a later stage. As a result, a composite of two finely inter-dispersed lithiated phases is obtained. SnSb is a typical example, where Sb starts alloying with Li in order to form  $Li_3Sb$  and then later  $Li_xSn$  is formed. Since both materials are active, the theoretical capacity of these compounds is high, close to that of the pure elements. The volume change obviously remains an issue, though a sort of “buffer” effect is present also in this case. In fact, the components react one after each other and therefore the inactive phase buffers the active one. Also in this case, a sort of barrier against aggregation of Sn is present [41]. However, the conductive network of these electrodes is not as good as the previous case, as both materials are damaged by repeated alloying with Li. Therefore, also these materials are interesting, but the mentioned issues need to be properly addressed in an advanced negative electrode.

*VI – Irreversible conversion and alloying with a displaced component*

A different reaction can also occur in presence of metal oxides like, for example, SnO or SnO<sub>2</sub>. The general mechanism in this case involves two separate steps [42]:

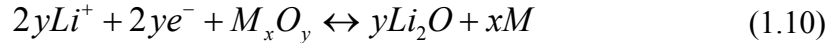


where Li initially reacts with the oxygen irreversibly, in order to form inactive  $Li_2O$  and displaces at the same time the active metal (1.8). This reaction is referred to as ‘conversion’. The active metal can further alloy with Li according to (1.9). It is important to observe that these two steps account for a huge storage of Li. Unluckily, only the Li stored in the alloy is reversible. A small fraction of Li can be extracted from  $Li_2O$  when small particles are present [43]. However, the presence of  $Li_2O$  is not completely detrimental, because it acts as a sort of inactive ‘buffer matrix’ for the displaced metal undergoing alloying, and it provides fair ionic conductivity for  $Li^+$  ions. On the other hand, the electronic conductivity of such materials is rather poor and electrons can only flow through the segregated metal (alloy). Despite all these limitations, the materials reacting with this mechanism have been considered extremely attractive. In particular, tin-based amorphous oxides have been proposed for more than ten years as possible candidates to replace graphite in commercial batteries [44, 45]. However, the severe capacity loss from eq. (1.8) and the limited

stability upon cycling have up to now prevented their practical usage. Still, some researchers believe that these materials are not out-of-date and solutions to these problems will be found.

#### *VII – Reversible conversion with transition metal oxides*

The last type of reaction that Li undergoes with some transition metal (i.e. Co, Fe, Cu, Ni, Ru, etc..) oxides is a (almost) fully-reversible conversion:

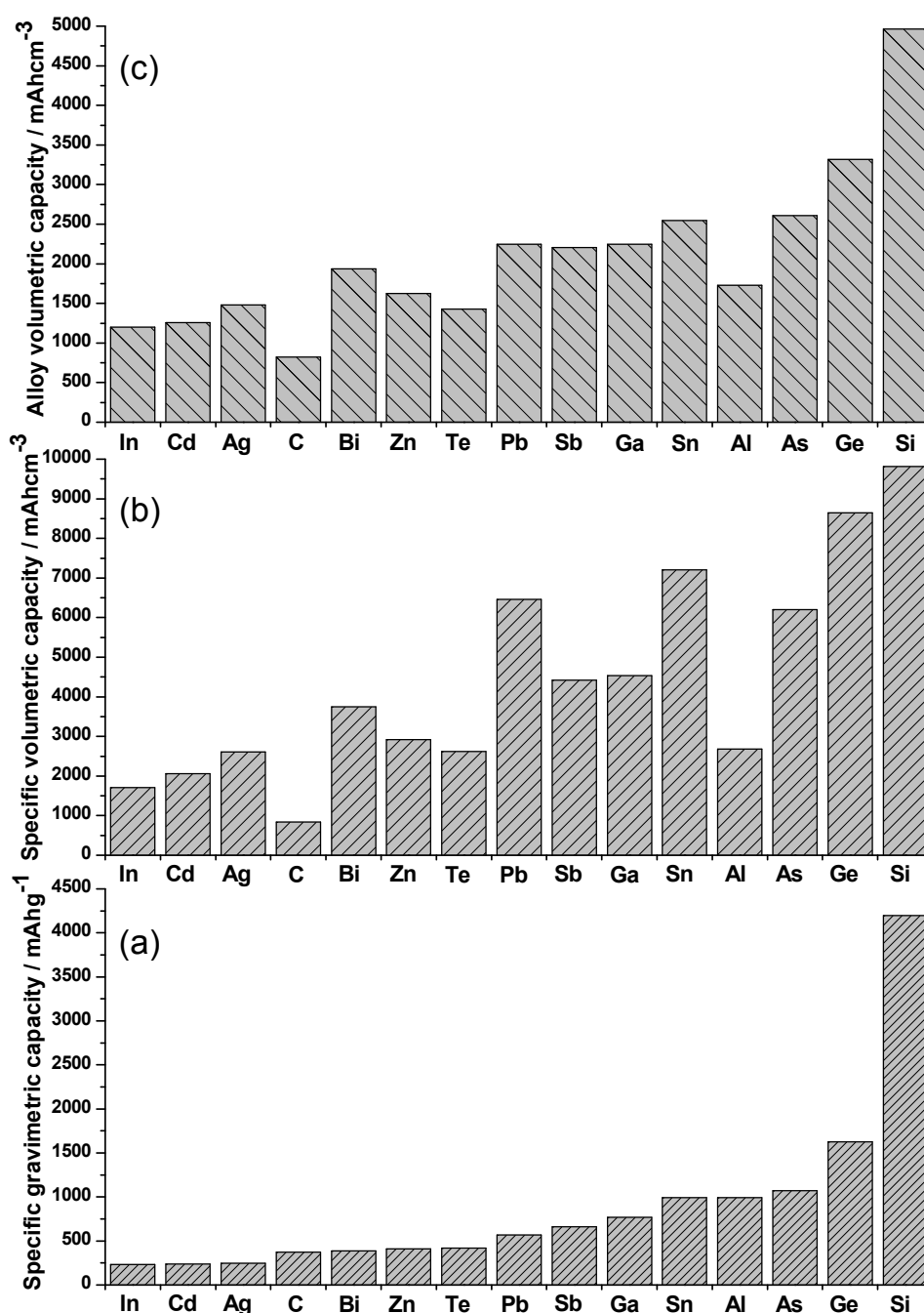


where the transition metal  $M$  is displaced and does not react with Li. The whole process results in the formation of extremely small metal dots (i.e. 1-2 nm) embedded in an *active* matrix of  $Li_2O$  [37]. In particular, it is believed that the electrochemically-driven size confinement of the metal particles enhance their electrochemical activity towards the formation/decomposition of  $Li_2O$ . This situation is particularly favourable, since it enables oxygen to be a *reversible* storage medium in such systems. Moreover, the transfer of electrons should not be an issue, due to the extended electrical-conducting network provided by the metal dots. This reaction is therefore unusual and extremely attractive for its ability to reversibly store a remarkable amount of Li. The dynamics of this reaction has been thoroughly studied, providing interesting insights on further mechanisms of charge storage occurring between the neighbouring M- $Li_2O$  nano-phases [46]. Interfacial storage of charge in a capacitor-like mode (i.e.  $e^-$  on M and  $Li^+$  on  $Li_2O$ ) accounts for an extra capacity, which is sensitive to the extended interface of the materials. The charge stored in this way can be quickly released, so that this mesoscopic system forms a bridge between batteries and capacitors [47, 48]. All these materials, however, suffer from volume changes and limited stability upon repeated cycling. Their characteristic voltage profiles show also noticeable hysteresis between charge and discharge, which is not desirable for practical applications. Nonetheless, transition metal oxides can meet the requirements for advanced negative electrodes. The development of novel synthesis and assembly techniques for these materials is crucial for bringing this technology a step further toward commercial applications.

## **1.4 The renaissance of Li alloys: Sn and Si**

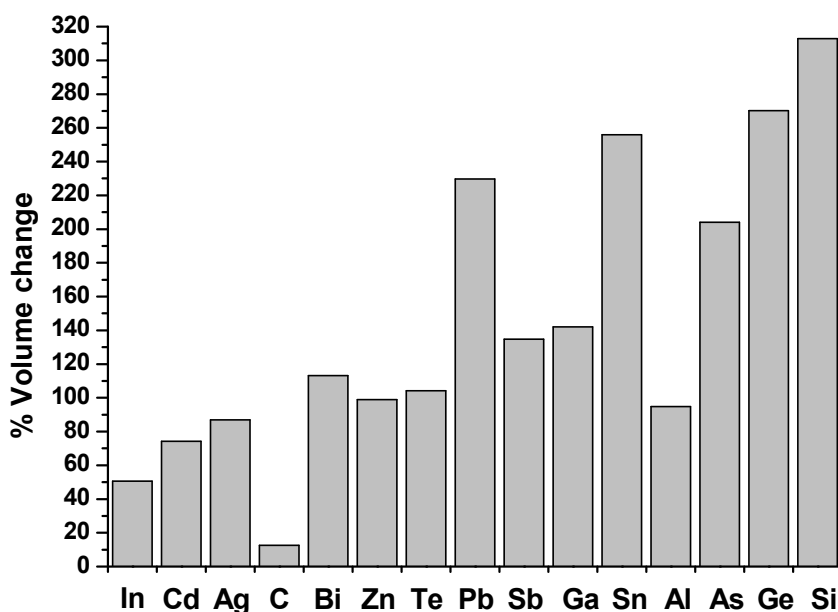
Among several Li alloys there are a few promising candidates in order to replace carbonaceous materials for applications where higher energy densities are required.

Fig. 1.4 presents a scenario for theoretical gravimetric and volumetric capacities of a number of elements alloying with Li, as well as the volumetric capacity of the alloys.



**Fig. 1.4.** Bar graphs for specific theoretical capacities of a number of elements alloying with lithium. Theoretical gravimetric capacity (see appendix A – eq. A. 25) of the elements (a). Theoretical volumetric capacities referred to the element densities (b). Theoretical volumetric capacities referred to the alloy densities (c). Please note that all the values are referred to the maximum amount of Li that can be theoretically stored in the alloy. The relevant properties of the materials are taken from JCPDS–International Centre for Diffraction Data.

Clearly Si, Ge, As and Sn show the best characteristics in terms of Li storage. However, it should be also taken into account that As is extremely toxic and Ge is expensive. Therefore, Si and Sn are the most convenient choices in terms of abundance, costs and impact on the environment, being Si the ‘ideal’ candidate for its attractive properties. Nevertheless, both materials suffer from severe volume changes, which directly affect their mechanical stability during cycling (Fig. 1.5).

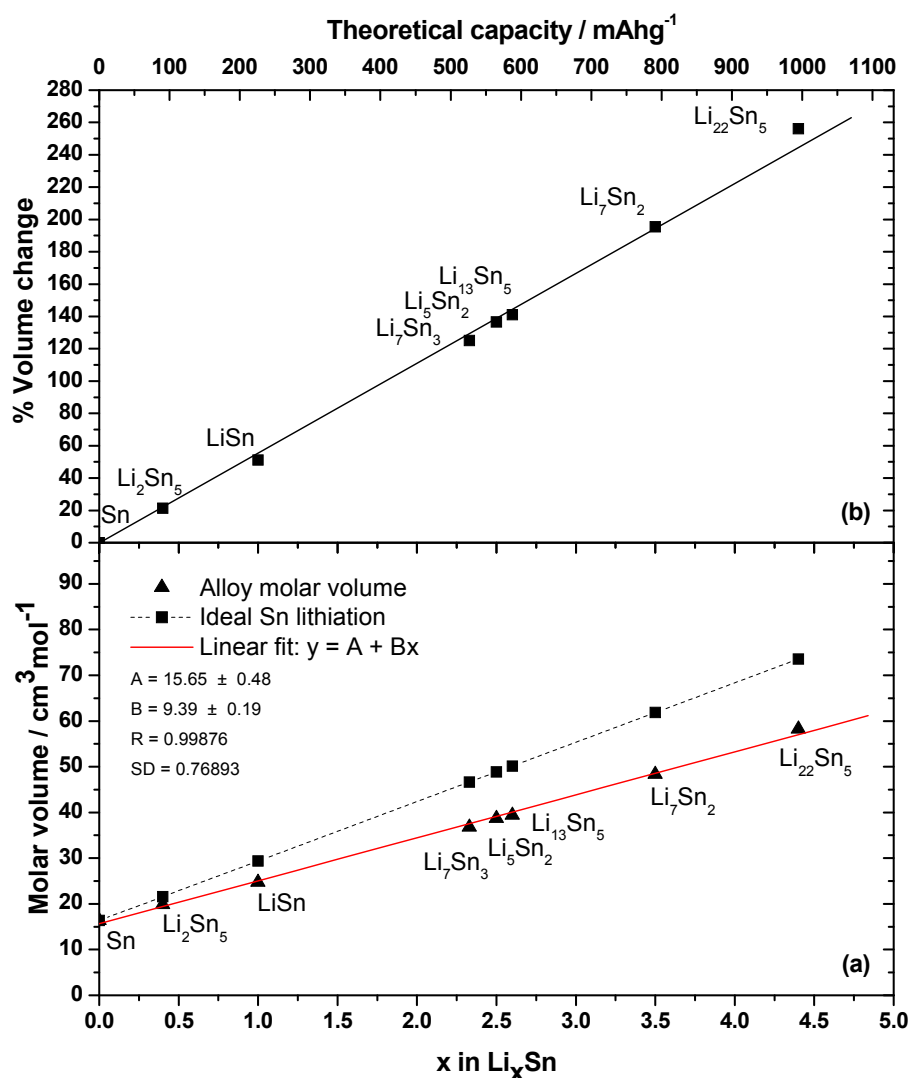


**Fig. 1.5.** Bar graph showing the theoretical volume change for a number of Li alloys. The variation is calculated between the final volume of the fully-lithiated alloy and the initial volume of the bare element (see appendix C – eq. C.1). The relevant data for the calculations are taken from JCPDS–International Centre for Diffraction Data.

From Fig. 1.5 it is noted that Si and Sn in their fully-lithiated states (i.e.  $Li_{4.4}M$ , where  $M$  is Si or Sn) undergo huge volume changes, especially compared to that of graphite. In particular, the theoretical volume changes are calculated assuming ideal crystalline structures for both the unlithiated host and the final Li alloy. Despite this evident limitation, Sn and Si have potential for practical applications and this fact is justified by their large theoretical capacities. Indeed, even exploiting a limited capacity, lower than the theoretical one, it is still much higher than carbon. In this way, reduced volume changes due to limited lithiation can be handled more effectively and suitable approaches can be applied to address this issue.

Fig. 1.6 shows the variation of the molar volume and the related volume change upon increasing Li content in the crystalline Li-Sn alloy. In particular, it can be observed that the variations are linear with the amount of Li. This fact is shown here for Sn, since it is a material that has been investigated extensively in this work.

However, analogous conclusions can be also drawn for Si, since this behavior represents a more general property of Li alloys [49].



**Fig. 1.6.** Plots showing the variation of the molar volume versus the lithium content in crystalline tin alloys (a) and their respective volume changes (b). The dotted line in (a) represents the ideal evolution of the molar volume of a lithiated Sn host, where no lattice restructuring is involved (i.e. the molar volume of crystalline Li has been merely added to that of Sn in the indicated proportions). The relevant data are taken from JCPDS–International Centre for Diffraction Data.

Even though these calculations are performed on a theoretical basis, it still provides valuable information that can be used in the development of advanced electrodes. Indeed, graphs like those of Fig. 1.6 represent general guidelines on how to tune the properties of the selected materials in practical systems, where other components are also involved (i.e. binders and additives). In particular, Sn and Si need a careful matching of their physical-chemical properties in effective electrode structures.

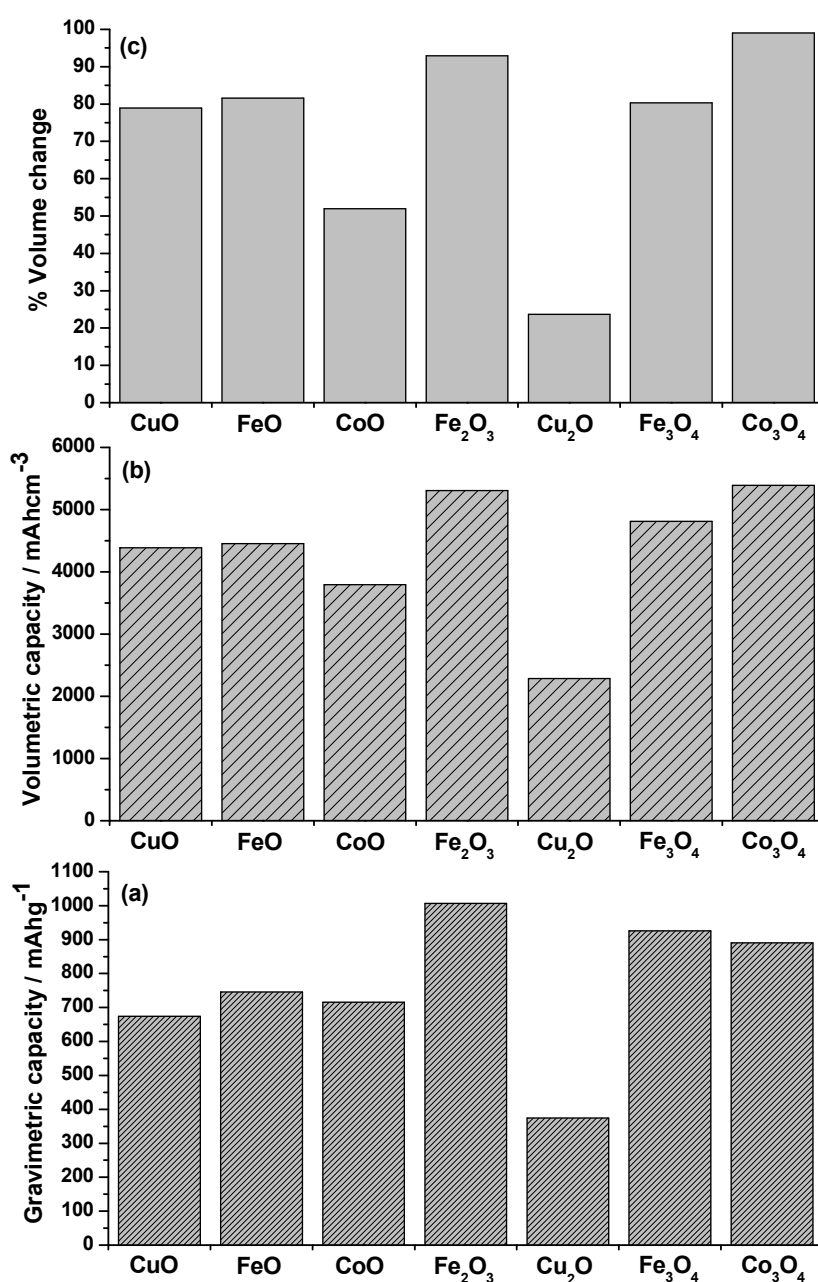
Moreover, the dependence of the volumetric energy density of Li alloys on the amount of Li introduced in their hosts is also another factor that should not be neglected for an effective electrode design (see Appendix C).

The above considerations are general and have been applied to bulk crystalline alloys, however, it is important to observe that these materials can be also obtained and manipulated in different forms. In particular, the use nanoparticles is effective in limiting the strain suffered by the materials during repeated cycling. For example, Sn can be cycled in the form of small dots, provided that a matrix prevents its agglomeration, which finally results into breakage and loss of electrical contact [50]. However, both Sn and Si are also difficult to handle when their size approaches the nanoscale. Indeed, they easily undergo immediate oxidation, with the formation of oxides that are not reversible and are electrochemically-inactive. The shrinkage of their size is also responsible for easier degradation of the electrolyte, due to higher reactivity of the particles. In this sense, the use of (nano)composites in a matrix is beneficial for enhancing the stability of both electrode and electrolyte. Moreover, when the major shortcomings are related to anisotropic volume changes, due to the phase transitions between different crystalline lattice structures, the use of amorphous particles has a positive impact on the cycle performance. Indeed, the absence of phase transitions and the feature of isotropic volume changes enhance the cycle life of the electrodes, provided that the particles remain in their amorphous state.

From the above it is clear that the use of suitable electrode architectures, thin films, porous layers and especially the use of dedicated binders and electrode processing are crucial for bringing Sn and Si closer to commercial applications.

## 1.5 Transition metal oxides: a turning point?

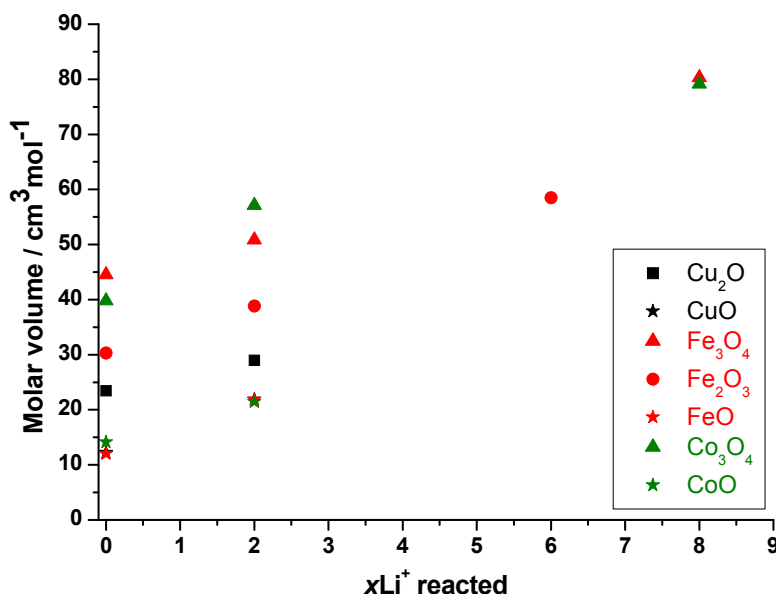
Transition metal oxides (TMO) are also attractive candidates, because high capacities and good cycle performances can be retained upon prolonged cycling, provided that the materials are in the form of nanostructures. The mechanism of reaction differs from Li-alloying and involves in-situ formation and decomposition of  $\text{Li}_2\text{O}$ , accompanied by the reduction and oxidation of tiny metal nanoparticles. In particular, the surface reactivity of the metal nanoparticles and their interfacial storage effects with  $\text{Li}_2\text{O}$  are key points to improve the performances for this class of negative electrodes. However, a careful fabrication of electrodes containing these nanostructures is still a primary issue. This is one of the first points that must be addressed, since also in this case, a high storage of Li unavoidably implies major structural changes which threaten the mechanical stability of the entire electrode structure. Fig. 1.7 shows some bar graphs for the theoretical storage capacities and the related volume changes of a number of crystalline transition metal oxides.



**Fig. 1.7.** Bar graphs of relevant storage characteristics for a number of transition metal oxides. Theoretical gravimetric capacities (see appendix A – eq. A. 25) of the considered metal oxides (a). Theoretical volumetric capacities referred to the characteristic density of the metal oxides (b). Theoretical volume changes for the reacted metal oxides. The variation is calculated between the final volume of the fully-lithiated materials and the initial volume of the bare metal oxides (see appendix C – eq. C.1). The relevant properties of the materials are taken from JCPDS–International Centre for Diffraction Data. Note that only ideal crystalline structures have been considered for the calculations and that the final volume of the fully-reacted materials does not account for any lattice restructuring.

It can be seen from Fig. 1.7 that the theoretical capacities of Cu, Fe and Co oxides are not really far from those of Li alloys, with the exceptions of Si and Ge (see Fig. 1.4).

Interestingly, the theoretical volume changes are not as severe as those of most Li-alloys, where 99% is the maximal variation in the case of  $\text{Co}_3\text{O}_4$  undergoing full reaction with Li. In any case, these volume changes cannot be neglected, since they have to be accommodated by the whole electrode structure, which needs to maintain integrity upon cycling. The ideal evolution of the molar volume of the crystalline transition metal oxides reacted with lithium is schematically presented in Fig. 1.8.



**Fig. 1.8.** Plot showing the theoretical variations for the molar volume of a number of crystalline transition metal oxides upon reaction with Li. Note that the indicated values are calculated on the basis of equation (1.10), where the molar volumes of the involved crystalline species (i.e. metals, transition metal oxides and lithium oxide) are considered without any lattice restructuring and are taken from JCPDS–International Centre for Diffraction Data. Note also that the reported values for  $\text{Fe}_2\text{O}_3$ ,  $\text{Fe}_3\text{O}_4$  and  $\text{Co}_3\text{O}_4$  take into account possible intermediate reactions where FeO and CoO are initially produced together with  $\text{Li}_2\text{O}$ .

Even though the data reported in Fig. 1.8 merely account for hypothetical crystalline structures, it is instructive to observe that in most of the cases a linear trend for the variations of the molar volume upon lithiation can be expected. This information can be regarded as a starting point for evaluating possible limitations that could arise during electrode fabrication, where the mechanical, chemical and electrical properties of these active materials need to be matched to those of the entire electrode assembly. Moreover, a comparison between Fig. 1.8 and 1.6a helps visualizing the difference in the storage mechanisms (i.e. TMO *vs.* Li-alloys) from another perspective. Indeed, the medium for storing Li here is oxygen, and one could compare for example the case of bare CoO and Sn, which show comparable molar volumes. In this particular case, an eventual uptake of two moles of Li has clearly a different impact on the molar volume of these hosts. In the case of CoO the final molar volume of the reacted



products (i.e. Co and  $\text{Li}_2\text{O}$ ) is clearly lower than that of an equivalent  $\text{Li}_x\text{Sn}$  alloy. In terms of volume changes, a fully-reacted CoO host undergoes ideally an expansion of roughly 50% (see Fig. 1.7c), while a “half-reacted” Sn alloy yields about 100% expansion (see Fig. 1.6b). This consideration suggests that reversible storage of Li in oxygen, catalyzed by the in-situ generated transition metal nanoparticles can be a valuable approach to achieve a tradeoff in terms of amount of Li stored and build-up of mechanical stress for advanced electrodes.

The reaction mechanism of TMO is atypical, because it is only the oxygen that reacts *reversibly* with Li, while none of the reduced *3d* metals undergoes Li alloying. This peculiarity of in-situ formation of a nanocomposite Metal/ $\text{Li}_2\text{O}$  brings about another striking phenomenon, which further contributes to Li storage. Indeed, these two adjacent nano-phases cannot individually store lithium. On the one hand the structure of the metal does not allow  $\text{Li}^+$ , only  $e^-$  can be accepted; while on the other hand  $\text{Li}_2\text{O}$  is an insulator which does not accept  $e^-$ , but  $\text{Li}^+$  can be easily accommodated in its lattice defects. Interestingly, the synergy of these two separate mechanisms on the nanoscale accounts for an extra storage, which for Ru/ $\text{Li}_2\text{O}$  has been shown to reach about a monolayer of  $\text{Li}^+$  per boundary [48]. Therefore, achieving tailored extended interfaces in this type of nanomaterials, where the ratio surface atoms/bulk atoms is enhanced, can in principle constitute a turning point for boosting Li storage via this pseudo-capacitive effect. In particular, when the metal dots are so small that the space-charges overlap with  $\text{Li}_2\text{O}$ , this mechanism forms an intermediate between a supercapacitor and a battery electrode. Indeed it may offer a reasonable compromise between the rate of discharge and the delivered capacity [48].

Finally, the shortcomings related to limited cycle life and impractical voltage profiles could be addressed via direct synthesis of TMO nanostructures and defect engineering (i.e. homogeneous and/or heterogeneous doping), respectively.

## 1.6 Outlook

The scenario presented in this chapter gives only a ‘first flavor’ of the major challenges in the Li-ion battery field and also the description of the various approaches for the negative electrodes is clearly not exhaustive. Still, from the considerations developed so far it emerges that the typology of the selected materials is of utmost importance to enhance energy densities, power densities, cycle life and safety. Unfortunately at the moment these features cannot be obtained all at once with the use of conventional materials. In this respect, nanostructured materials can be considered the most promising way to overcome the current limitations and to achieve these goals. Nevertheless, it is important to recognize the impact of the nanomaterials on the electrode structure and performance, as well as to deal with the

pros and cons related to their size effects. In particular, the control of the size, size distribution, composition, crystallinity and morphology of the nanostructures represents a crucial issue that should be directly addressed during their synthesis. Conventional synthesis routes might be adapted and developed in such a way that the produced nanomaterials can be easily generated and conveniently used in electrode structures.

In the following chapters electro spraying is presented as a versatile method for the synthesis of nanostructured materials and specifically for applications to Li-ion battery negative electrodes. Novel approaches for electro spraying and advanced methodologies of synthesis and assembly will be discussed as well.

## 1.7 References

- [1] M. S. Whittingham, F. R. Gamble Jr, *Materials Research Bulletin* **1975**, *10*, 363.
- [2] M. M. Thackeray, W. I. F. David, P. G. Bruce, J. B. Goodenough, *Materials Research Bulletin* **1983**, *18*, 461.
- [3] M. M. Thackeray, P. J. Johnson, L. A. de Picciotto, P. G. Bruce, J. B. Goodenough, *Materials Research Bulletin* **1984**, *19*, 179.
- [4] M. M. Thackeray, W. I. F. David, J. B. Goodenough, *Materials Research Bulletin* **1982**, *17*, 785.
- [5] M. G. S. R. Thomas, P. G. Bruce, J. B. Goodenough, *Solid State Ionics* **1985**, *17*, 13.
- [6] R. Yazami, P. Touzain, *Journal of Power Sources* **1983**, *9*, 365.
- [7] R. Kanno, Y. Takeda, T. Ichikawa, K. Nakanishi, O. Yamamoto, *Journal of Power Sources* **1989**, *26*, 535.
- [8] M. Mohri, N. Yanagisawa, Y. Tajima, H. Tanaka, T. Mitate, S. Nakajima, M. Yoshida, Y. Yoshimoto, T. Suzuki, H. Wada, *Journal of Power Sources* **1989**, *26*, 545.
- [9] M. Armand, *Solid State Ionics* **1983**, *9-10*, 745.
- [10] M. Armand, *Advanced Materials* **1990**, *2*, 278.
- [11] B. Scrosati, *Journal of the Electrochemical Society* **1989**, *136*, 2774.
- [12] B. Scrosati, *Journal of the Electrochemical Society* **1992**, *139*, 2776.
- [13] K. Xu, *Chemical Reviews* **2004**, *104*, 4303.
- [14] W. Ebner, D. Fouchard, L. Xie, *Solid State Ionics* **1994**, *69*, 238.
- [15] C. H. Lu, P. Y. Yeh, *Journal of the European Ceramic Society* **2002**, *22*, 673.
- [16] H. Arai, S. Okada, Y. Sakurai, J. I. Yamaki, *Journal of Power Sources* **1997**, *68*, 716.
- [17] A. Yamada, M. Tanaka, K. Tanaka, K. Sekai, *Journal of Power Sources* **1999**, *81-82*, 73.
- [18] M. M. Thackeray, L. A. de Picciotto, A. de Kock, P. J. Johnson, V. A. Nicholas, K. T. Adendorff, *Journal of Power Sources* **1987**, *21*, 1.

- [19] H. Yamane, M. Saitoh, M. Sano, M. Fujita, M. Sakata, M. Takada, E. Nishibori, N. Tanaka, *Journal of the Electrochemical Society* **2002**, 149.
- [20] S. Ma, H. Noguchi, M. Yoshio, *Journal of Power Sources* **2001**, 97-98, 385.
- [21] C. Locati, U. Lafont, L. Simonin, F. Ooms, E. M. Kelder, *Journal of Power Sources* **2007**, 174, 847.
- [22] F. G. B. Ooms, E. M. Kelder, J. Schoonman, M. Wagemaker, F. M. Mulder, *Solid State Ionics* **2002**, 152-153, 143.
- [23] F. G. B. Ooms, M. Wagemaker, A. A. Van Well, F. M. Mulder, E. M. Kelder, J. Schoonman, *Applied Physics A: Materials Science and Processing* **2002**, 74.
- [24] M. Wagemaker, F. G. B. Ooms, E. M. Kelder, J. Schoonman, G. J. Kearley, F. M. Mulder, *Journal of the American Chemical Society* **2004**, 126, 13526.
- [25] P. P. Prosinì, M. Carewska, S. Scaccia, P. Wisniewski, M. Pasquali, *Electrochimica Acta* **2003**, 48, 4205.
- [26] A. S. Andersson, J. O. Thomas, B. Kalska, L. Haggstrom, *Electrochemical and Solid-State Letters* **2000**, 3, 66.
- [27] M. M. Doeff, Y. Hu, F. McLarnon, R. Kostecki, *Electrochemical and Solid-State Letters* **2003**, 6.
- [28] R. Fong, U. von Sacken, J. R. Dahn, *Journal of the Electrochemical Society* **1990**, 137, 2009.
- [29] K. Sawai, Y. Iwakoshi, T. Ohzuku, *Solid State Ionics* **1994**, 69, 273.
- [30] K. Zaghib, K. Kinoshita, *Journal of Power Sources* **2004**, 125, 214.
- [31] K. Zaghib, G. Nadeau, K. Kinoshita, *Journal of the Electrochemical Society* **2000**, 147, 2110.
- [32] T. Ohzuku, A. Ueda, N. Yamamoto, Y. Iwakoshi, *Journal of Power Sources* **1995**, 54, 99.
- [33] S. Scharner, W. Weppner, P. Schmid-Beurmann, *Journal of the Electrochemical Society* **1999**, 146, 857.
- [34] A. N. Dey, *Journal of the Electrochemical Society* **1971**, 118, 1547.
- [35] J. O. Besenhard, M. Hess, P. Komenda, *Solid State Ionics* **1990**, 40-41, 525.
- [36] R. A. Huggins, *Journal of Power Sources* **1999**, 81-82, 13.
- [37] P. Poizot, S. Laruelle, S. Grugeon, L. Dupont, J. M. Tarascon, *Nature* **2000**, 407, 496.
- [38] P. Poizot, S. Laruelle, S. Grugeon, J. M. Tarascon, *Journal of the Electrochemical Society* **2002**, 149.
- [39] D. R. Simon, E. M. Kelder, M. Wagemaker, F. M. Mulder, J. Schoonman, *Solid State Ionics* **2006**, 177, 2759.
- [40] M. Winter, J. O. Besenhard, *Electrochimica Acta* **1999**, 45, 31.
- [41] M. Wachtler, M. Winter, J. O. Besenhard, *Journal of Power Sources* **2002**, 105, 151.
- [42] I. A. Courtney, J. R. Dahn, *Journal of the Electrochemical Society* **1997**, 144, 2045.
- [43] S. T. Chang, I. C. Leo, C. L. Liao, J. H. Yen, M. H. Hon, *Journal of Materials Chemistry* **2004**, 14, 1821.
- [44] Y. Idota, T. Kubota, A. Matsufuji, Y. Maekawa, T. Miyasaka, *Science* **1997**, 276, 1395.
- [45] R. A. Huggins, *Solid State Ionics* **1998**, 113-115, 57.

- [46] P. Balaya, H. Li, L. Kienle, J. Maier, *Advanced Functional Materials* **2003**, *13*, 621.
- [47] J. Jamnik, J. Maier, *Physical Chemistry Chemical Physics* **2003**, *5*, 5215.
- [48] J. Maier, *Nature Materials* **2005**, *4*, 805.
- [49] M. N. Obrovac, L. Christensen, D. B. Le, J. R. Dahn, *Journal of the Electrochemical Society* **2007**, *154*.
- [50] J. Yang, M. Winter, J. O. Besenhard, *Solid State Ionics* **1996**, *90*, 281.

# Chapter 2

## Electrohydrodynamic atomization – Theory and applications

*The expert is a person who has made,  
in a very restricted field,  
all the possible mistakes.  
(Niels Bohr)*

This chapter briefly introduces the fundamentals of Electrohydrodynamic Atomization (EHDA) and discusses some technological applications of this phenomenon. Particular attention is devoted to the description of EHDA in the so-called “cone-jet mode”, due to its relevance for production of nanoparticles. Electrostatic Spray Deposition (ESD) and Pyrolysis (ESP), together with Electrospinning are also described here as classical examples of EHDA-based techniques for the synthesis of advanced functional materials for Li-ion battery electrodes.

## 2.1 Introduction to Electrohydrodynamic Atomization

Electrohydrodynamic Atomization (EHDA), which is also often referred to as “Electrospraying” (ES), is a physical process that concerns the disruption of a liquid into a spray of charged droplets when it is subjected to an intense electric field. In particular, the atomization of the liquid is carried out through Rayleigh instabilities and Coulombic interaction of charges in the liquid with an external applied field. The result of this interaction includes both acceleration of the liquid and subsequent disruption into droplets, as well as build-up of charge and further break-up [1].

It is worth to note, however, that a liquid jet can also break-up into droplets without the presence of any electric force, while developing eventual charge (e.g paint spraying, where the atomization is accomplished by mechanical forces and charging by induction or ion transfer, resulting in charged aerosols). This circumstance must be distinguished from electrospraying, which accounts only for atomization by primarily electrical forces. Depending on the strength of the electric stresses on the liquid surface, relative to surface tension stress and the kinetic energy of the liquid jet leaving the nozzle, different “spraying modes” can be obtained [1].

It is well known that electrospraying is governed by intrinsic properties of the liquid and that it depends on the experimental parameters employed. Here the intrinsic properties are: surface tension, viscosity, density, electrical conductivity and permittivity. Whereas the experimental parameters can be seen as: liquid flow rate, applied voltage, nozzle diameter, etc. However, the generation of a certain spraying mode, although using the required characteristics, is still not straightforward. Indeed, the appropriate combination of parameters is generally not known a priori [1, 2] and at the moment no complete theory describes how the EHDA proceeds as a function of both internal and external conditions. Several interesting studies have been devoted to the classification of different spraying modes [1-16], providing geometric criteria for the characterization of the form of the liquid meniscus, the generated jet, and the droplet formation. These studies mainly focus on:

- Investigation of the characteristic droplet sizes and charges generated in various spraying modes with different solvents
- Observation of the spatial distributions of the aerosols (spray patterns) obtained under different spraying modes
- Evaluation of the droplet emission frequencies with increasing applied voltages and transitions between modes.

As a general criterion, spraying modes can be conveniently divided in two groups.

*I – Discontinuous modes*

This group comprises the modes in which only fragments of the liquid are ejected from a nozzle and that do not exhibit a continuous flow through the meniscus. These modes are called: dripping, microdripping, spindle, and intermittent-jet modes and will be discussed in more detail later on.

*II – Continuous modes*

This second group includes the modes in which the liquid leaves the outlet of the nozzle in the form of a long, continuous jet that disintegrates into droplets only over a certain distance from the tip of the capillary. This group comprises the cone-jet, simple jet, multi-jet and ramified-jet modes. The meniscus and the jet for this group can be stable, can vibrate, rotate around the nozzle axis or whip irregularly. A more detailed description follows in subsections 2.1.2 - 2.1.3 and a schematic drawing is shown later in Fig. 2.1b. The geometry of the meniscus and the jet, as well as the modes of spraying, can be further described by a combination of several characteristic *time constants* referring to specific physical processes [2, 17]. The most important ones concerning these spraying modes are reported in Table 2.1.


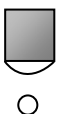






**Table 2.1.** The most relevant time constants for ES. (The symbols are explained in the nomenclature).

$\tau_e = \frac{\varepsilon_0 \varepsilon_r}{\kappa}$	Electrical relaxation time
$\tau_j = \frac{\mu D_i}{\gamma}$	Jet formation time
$\tau_h = \frac{LR_j^2}{Q}$	Hydrodynamic time
$\tau_l = \frac{\pi D_i^3}{4Q}$	Time for supply of the liquid to the nozzle
$\tau_\rho = \left( \frac{\rho D_i}{\gamma} \right)^{1/2}$	Jet or meniscus deformation time
$\tau_d = \left( \frac{\rho R_j^3}{\gamma} \right)^{1/2}$	Time for droplet formation by jet break-up

A list of the principal spraying modes and their peculiar characteristics is also reported in Table 2.2. A brief description of the principal modes is given in the following sections, with a separate discussion of the cone-jet mode and its variants.

Properties and applications of the aerosols obtained via atomization in the cone-jet mode are later considered, with a particular highlight for the production of functional materials and deposition of thin films. Challenges, potentialities and hurdles of the EHDA are addressed as well.

**Table 2.2.** Synoptic table of the principal spraying modes. The asterisk \* labels continuous modes.

Spraying mode	Shape of the liquid	Meniscus/jet	Spray pattern
1. Dripping 	Meniscus: hemispherical Droplets: spherical	Axially oscillating	Single large droplets with smaller satellites
2. Microdripping 	Meniscus: hemispherical Droplets: small, spherical	Axially oscillating	Series of small, uniform droplets
3. Spindle 	Meniscus: cone/hemisphere Droplets: elongated liquid relics (spindles)	Axially oscillating	Spindles disrupting into small droplets
4. Intermittent-jet 	Meniscus: cone/hemisphere Jet: linear and intermittent	Axially oscillating with almost regular jet emission	Fine droplets, with larger superimposed droplets
5. Cone-jet* 	Meniscus: cone (linear, concave, convex or skewed) Jet: straight linear	Axially stable with varicose or whipping motions for the jet	Fine, nearly-monosized droplets sprayed in a regular cone
6. Multi-jet* 	Meniscus: flattened cones Jet: linear, multiple	Axially stable, with enhanced whipping motions for the jets	Fine mist of nearly-monosized droplets with distinct directions
7. Simple-jet* 	Meniscus: slightly conical Jet: straight linear, thick	Axially stable, thick	Elongated jet, eventually breaking-up in small droplets and satellites
8. Ramified-jet* 	Meniscus: almost conical Jet: skewed, ramified in random directions	Central jet with sub-jets not stable and randomly distributed	Droplets sprayed irregularly around the capillary axis



### 2.1.1 Dripping, microdripping and spindle modes

#### *Dripping*

The so-called “dripping mode” does not differ much from the normal dripping of a liquid observed in the absence of an electric field that would have been applied to the nozzle. Usually the droplets are spherically-shaped and detach from the outlet of the capillary as the gravity and the electric forces overcome the surface tension. After the droplet detachment, the meniscus contracts back to a hemispherical-like shape. In general, the drop diameter remains greater than that of the nozzle, thus leading to the emission of large droplets at low frequencies ( $< 500$  Hz) [2, 5]. An increase of the applied voltage results in an augmented frequency of the emitted droplets. At the same time, elongation of the meniscus due to electrostatic forces results in the production of smaller satellite droplets.

#### *Microdripping*

The “microdripping mode” differs from the normal dripping mode because in this case the electric forces are sufficiently high to maintain a stable hemispherical or ellipsoidal meniscus, which does not contract after the droplet detachment. The name “microdripping” arises from the fact that the emission takes place drop by drop, as in the conventional dripping mode, and the droplets have a much smaller diameter than the capillary outlet section [2, 5]. This mode operates at low flow rates and produces droplets with narrow size distribution and frequencies up to a few kHz. The characteristic time for feeding the liquid through the capillary is much longer than the time related to the droplet formation, due to the electric forces, and no large fragment of liquid can be formed. The space charge due to the generated droplets in this case is also too weak to affect the generation process, because they are quickly removed by the electric field. The average size of the droplets can range from a few micrometers up to hundreds of micrometers. It has been suggested that the charge on the droplets can eventually approach half of the so-called ‘Rayleigh limit’ [2]. However, in most of the cases much lower charging values can be generally expected for the droplets ejected in this mode. The Rayleigh limit refers to the maximum amount of charge that can be carried by a charged droplet [18]. When the mutual repulsion of electric charges on a droplet exceeds the confining force of surface tension, then it shatters into smaller droplets. The limiting charge,  $q_R$ , for a liquid droplet of radius  $a$  is given by:

$$q_R = 8\pi\sqrt{\varepsilon_0\gamma a^3} \quad (2.1)$$

where  $\gamma$  is the surface tension of the liquid and  $\varepsilon_0$  is the permittivity of free space.

The ‘daughter’ droplets formed in this way are no longer monodispersed, but still highly charged.

### *Spindle*

The “spindle mode” is normally accomplished under higher flow rates and electric fields. In this case the liquid can be elongated in the direction of the electric field, taking the shape of a thick jet, which detaches as a large spindle-like fragment. The characteristic time for the liquid supply to the capillary is nearly equal to or shorter than the characteristic time for the jet formation [2]. Thus, the high electric field detaches a fragment of liquid before a continuous jet can be formed. The spindle mode operates at higher voltages than the dripping mode, and it differs from this last one because no regular droplets are ejected from the meniscus, but only elongated fragments of liquid. After its detachment, the spindle can disrupt into several small droplets of different sizes because of the electrostatic forces, while the meniscus contracts to its initial shape, and a new jet starts to be formed. Therefore, large primary droplets and several small satellites are the typical products of this spraying mode [5]. In particular, this property is used as a criterion to distinguish the spindle mode from the so-called “intermittent cone-jet mode”, which is later described and produces unstable cone-jets by a similar process of meniscus contraction.

## **2.1.2 Cone-jet Mode: a preliminary introduction**

One of the most interesting modes, which has been extensively investigated, is the so-called “cone-jet mode”. The very first observation of this phenomenon was reported by William Gilbert in his book “De Magnete” in 1600 and some interesting experiments were also performed around 1750 by Abbe’ Nollet. However, the first scientific description by Zeleny dates back to 1917 [19] and only in 1952 electrospray was reconsidered more carefully by Vonnegut and Neubauer [20, 21]. Later in 1964 the phenomenon was studied extensively by Taylor [22]. Since then, it has been often referred to as the “Taylor cone” (see Fig. 2.1 later on).

A Taylor cone forms when a liquid is slowly fed through a nozzle while a high voltage is applied between the nozzle and a counter electrode. The resulting electric field induces a surface charge on the droplet at the outlet of the nozzle. The interaction between the surface charge and the external field creates electric stresses at the liquid surface. If the electric field and the liquid flow rate are in an appropriate range, then the electric stresses can overcome the surface tension stress. As a result, the spherical shape of the droplet is changed to a conical one. Taylor was the first to describe the formation of the liquid cone. He balanced the outward electrostatic

pressure,  $P_e$ , with the inward pressure caused by the surface tension,  $P_\gamma$ , according to the following formula:

$$\frac{1}{2} \varepsilon_0 E^2 = \frac{\gamma}{r \tan \alpha_T} \quad (2.2)$$

where  $r$  is the radial coordinate,  $\varepsilon_0$  the permittivity of free space and  $\alpha_T$  the cone half-angle (i.e.  $49.3^\circ$ ). Taylor calculated the field between a conical surface and a special counter electrode to simplify the calculation. He assumed an equipotential cone surface and no pressure difference over the liquid surface. Moreover, he did not take into account any charge loss from the system. His assumptions were rather restrictive and his theory was too simple to adequately describe this phenomenon. In fact, Taylor's solution did not include either a liquid jet at the apex of the cone, or tangential stresses.

Successive works were carried out to improve Taylor's theory and to describe other processes involved in the formation of the cone and the emission of charged jet and droplets from its tip. It was recognized that the electric field induces a surface charge on the liquid. This causes a motion of the liquid inside the cone and also near its surface, where the liquid is strongly accelerated [23]. The fluid motion is in part directed downwards along the surface of the cone and in the jet and partly reverses upwards at the centre of the cone. The observed liquid flow inside the cone was explained in terms of the existence of an electrohydrodynamic shear stress [24, 25]. This shear stress, actually, is a characteristic of the cones, which must simultaneously carry surface charges and be subjected to a tangential electric field,  $E_t$  [26, 27]. The speed with which this charge accumulation takes place depends on the *electrical relaxation time*,  $\tau_e$ , of the charges in the liquid:

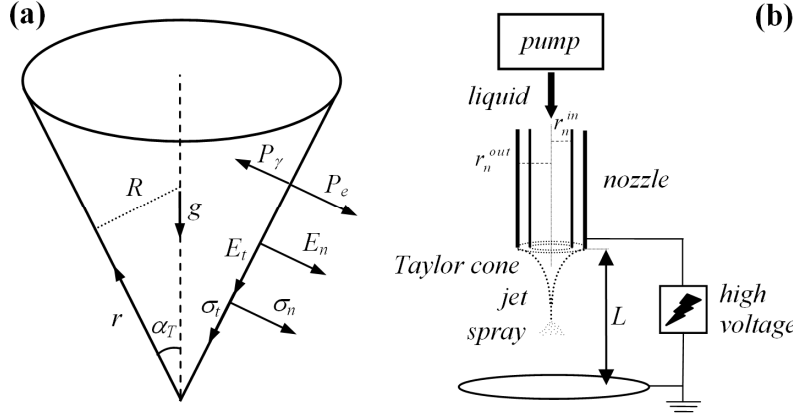
$$\tau_e = \frac{\varepsilon}{\kappa} \quad (2.3)$$

with  $\varepsilon = \varepsilon_0 \varepsilon_r$ , being  $\varepsilon_r$  the relative permittivity, and  $\kappa$  the electrical conductivity of the liquid. The charges at the liquid surface induce a normal electric field, causing a normal electric stress  $\sigma_n$  given by:

$$\sigma_n = \frac{1}{2} \varepsilon_0 E_n^2 - \frac{1}{2} (\varepsilon - \varepsilon_0) E_t^2 \quad (2.4)$$

where  $E_n$  and  $E_t$  are the normal and the tangential components of the electric field. The normal field stress opposes the pressure caused by the surface tension (Fig. 2.1a). Conversely, the tangential electric stress  $\sigma_t = \varepsilon E E_t$  is responsible for a downward longitudinal force, which stabilizes the cone surface. At a certain potential, the speed

of the charges moving towards the cone surface is equal to that of the charges removed by the liquid stripping in the jet, causing the onset of a “stable cone”.



**Fig. 2.1.** Simple drawing of a ‘mathematical’ Taylor cone subjected to normal and tangential electric stresses (a). The indicated parameters are mentioned in the text. Schematic drawing of a typical nozzle-disk configuration for the generation of Taylor cones and droplets via the cone-jet mode (b).

It has been calculated [28] that the electric field corresponding to the onset of EHDA from the liquid cone,  $E_{on}$ , is given by:

$$E_{on} = \left( \frac{2\gamma \cos \alpha_T}{\epsilon_0 r_n^{in}} \right)^{1/2} \quad (2.5)$$

where  $r_n^{in}$  is the inner radius of the electrified nozzle. The actual electric field strength  $E_{tip}$  at the tip of a nozzle with an outer wall radius  $r_n^{out}$ , which is placed at a distance  $L$  from a large disk electrode (see Fig. 2.1b), can be roughly evaluated by the approximate relationship:

$$E_{tip} = \left( \frac{2V_n}{r_n^{out} \ln(4L/r_n^{out})} \right)^{1/2} \quad (2.6)$$

where  $V_n$  is the potential applied to the nozzle.

A combination of equations (2.6) and (2.5) with  $\alpha_T = 49.3^\circ$  for the Taylor cone, and the assumption that  $r_n \approx r_n^{in} \approx r_n^{out}$ , yields the approximate voltage required at the nozzle tip for the onset of EHDA in the cone-jet mode [29]:

$$V_{on} \approx 2 \times 10^5 (\gamma r_n)^{1/2} \ln(4L/r_n) \quad (2.7)$$

This expression, however, gives only a rough estimation for the voltage, which is merely based on the knowledge of the liquid surface tension, the nozzle radius and

the distance from the electrode. It neglects the influence of other important parameters (i.e. conductivity, flow rate) and can be quite sensitive to the actual thickness of the rim of the nozzle and its wetting properties during electrospaying.

### 2.1.3 Cone-jet related modes

The cone-jet mode is related to different extents also to other types of modes that show various distinctive features.

#### *Intermittent cone-jet*

Sometimes the spindle mode and the intermittent cone-jet mode are grouped together into the so-called “pulsating-jet mode”. However these two modes produce different droplet size distributions. Indeed, the “intermittent cone-jet” mode produces a multitude of fine droplets with a superimposed, semi-periodic large droplet population. This mode corresponds to a transition regime that appears when the voltage is slightly lower than that needed to maintain a stable cone-jet. Therefore, the jet may be emitted only intermittently, while the apex of the meniscus takes on a pointed or rounded form in an alternating fashion [5]. Although the emission phases may occur at perfectly regular time intervals, the diameter of the jet varies during these emission phases, leading to a non-uniform size distribution for the ejected droplets.

#### *Multijet or multicone-jet*

This is an important variant of the cone-jet that usually develops from it by gradually increasing the applied voltage. Initially, the cone becomes skewed, leading to a single jet that is unstable and is typically replaced by two or three jets that are symmetrically distributed around the nozzle axis. The meniscus is rather flattened, with only small cones in correspondence of the emitted jets [2]. Sometimes even a larger number of jets and relatively higher flow rates can be simultaneously obtained (i.e. “rim-emission mode”). An advantage of this mode stems from the fact that in the cone-jet a reduction of the flow rate results in a decrease of the average droplet size, as it will be shown later. Therefore, for a fixed feeding rate, the sharing of the liquid flow between multiple jets yields both finer droplets and higher emission frequencies than in the cone-jet mode [5]. Increasing the number of the jets implies a decrease in their diameters. The diameter of the jets is generally smaller than a few tens of micrometers. The jets disintegrate due to “varicose instabilities” and “whipping motions” into small droplets, forming a fine mist around the capillary axis. The number of emission points increases with the applied voltage for a given flow rate, but up to a certain limit. As this limit number is exceeded, and the electrical forces

are too strong to stretch out smoothly the surface of the liquid into fine jets, the liquid is ejected in the form of large spindle-like fragments [2].

#### *Simple jet*

This mode differs from the cone-jet mode in the sharpness of the conical meniscus and it arises from dissimilar conditions. Indeed, the kinetic energy of the jet comes here mainly from the external pressure applied by the syringe pump, while for the cone-jet it originates from the electrical forces. Moreover, for the cone-jet the diameter of the cone base is generally determined by the outer diameter of the nozzle and the jet diameter mainly depends on the flow rate, while for the simple-jet the conical base is established by the inner diameter of the capillary. The jet diameter depends on the extra acceleration due to the electric field [5]. When the electric field is increased on a simple-jet, then the surface charge on the jet can exceed a certain threshold value. This occurrence causes the onset of the so-called “ramified-jet mode”.

#### *Ramified-jet*

In this mode the radial electrical forces cause the onset of several sub-jets, issuing from the surface of the simple-jet, and not from its apex. The ramifications are formed in random directions and these sub-jets are not stable. Ramified jets are rarely observed in the cone-jet mode because, when the voltage increases, the multi-jet mode appears before the electric field on the single jet reaches a sufficiently high value to produce them [2].

## **2.2 EHDA in the cone-jet mode**

The cone-jet and the multi-jet are by far the most interesting modes, due to their possible monodispersity, high charging and emission frequencies for the produced droplets. Depending on the liquid properties and the flow rates the average droplet size can range from a few nanometers with production frequencies up to  $10^9$  Hz to hundreds of micrometers with frequencies of about  $10^4$  Hz [30-34]. These features are particularly relevant for all the applications which demand narrow size distributions, as well as absence of coalescence for the generated droplets. The droplet size is smaller than those resulting from conventional atomizers and, at the same time, the surface charge enables much higher deposition efficiencies. Moreover, by using a configuration in which electro-sprayed droplets with two opposite polarities are directed towards each other it is possible to achieve *bipolar coagulation*. The coagulation occurs via the electrical attraction of the oppositely-charged droplets, yielding a quick mixing and eventual chemical reactions in the

newly generated drops [35-40]. In such a way, neutral reacted droplets and different products can be easily formed.

However, aerosol-based technology often requires high throughputs for most applications at an industrial scale level. In this respect, electrospray is a technique that suffers from limited production rates. Therefore, this shortcoming needs to be correctly addressed. Two different routes have been proposed in order to solve this issue: (i) *up-scaling* by extensive use of multiple jets in a linear array or rim-emission modes, with an increasing number of spraying points and (ii) *out-scaling* of the cone-jet mode, via multiplexed nozzle systems, which enable parallel electrospray [41, 42]. Both approaches exhibit advantages and disadvantages that should be taken into account, depending on the particular application or purpose.

For instance, up-scaling by multi-jet has the advantage of emitting on average smaller droplets at a higher frequency than the regular cone-jet. However, the higher voltage causes enhanced lateral electric forces, which generally have a negative influence on the monodispersity of the spray. It is worth noticing that for all the applications in which the uniformity of the droplets is not necessarily required, and only a large number of small drops are needed, multi-jet mode can represent an adequate tool for increasing the production by means of appropriate design of nozzles or spraying slits [43].

On the other hand, multiplexing has the advantage that the monodispersity of the droplets can be in principle easier to control, provided that the presence of neighboring nozzles does not destabilize the overall electrospray process. Moreover, the feeding of the liquid has to be maintained constant for all the nozzles, otherwise a discontinuity in their flows is likely to result in the production of droplets with different sizes. Despite these limitations, this approach is probably the most convenient, since the cone-jet mode has been extensively investigated and modeled [17, 44-53].

It is nowadays possible to achieve a discrete control on the droplets produced under such regime. In particular, the knowledge of the physical properties of the liquid to be sprayed, combined with a proper tuning of the experimental parameters enable the generation of charged droplets, whose size could be roughly tailored in advance, by applying the so-called “scaling laws” for EHDA in the cone-jet mode. They constitute a useful tool to assess the key parameters involved in the electrospraying process and their influence on the average droplet size and current flow.

The processes that govern EHDA in the cone-jet mode are presented in the following subsections. The influence of the main parameters on the spraying process and the droplet production are also briefly discussed together with the scaling laws for the current flowing through the cone-jet and the size of the emitted droplets.

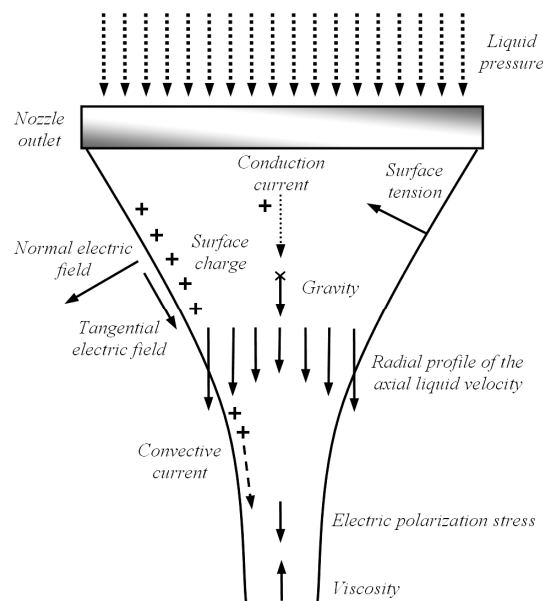
## 2.2.1 Characteristics of the cone-jet and its break-up

EHDA in the cone-jet mode can be generally described by four processes [51]:

1. Acceleration of the liquid in the Taylor cone combined with jet formation
2. Break-up of the jet into charged droplets
3. Evolution of the spray due to electrical interactions of the droplets
4. Electrical discharges in the surrounding atmosphere

The above processes are explained in more detail below.

1. The acceleration of the liquid is provided by the applied voltage. Under the influence of the electric field, free charges are induced on the surface of the liquid cone. These charges in a liquid are mainly constituted by ions. The presence of the surface charge influences the normal electric field inside the liquid. Indeed, the normal component of the electric field inside the liquid is much weaker than that outside the cone. The tangential component of the electric field accelerates the ions accumulated at the liquid surface towards the cone apex. In such a way, the ions progressively accelerate the surrounding liquid and a thin charged jet is emitted from the cone tip. This process and the resulting shape of the cone are the consequences of a balance of the pressure of the liquid, its surface tension, inertia, viscosity, gravity, and electric stresses at its surface. The role played by these factors is schematically represented in Fig. 2.2.

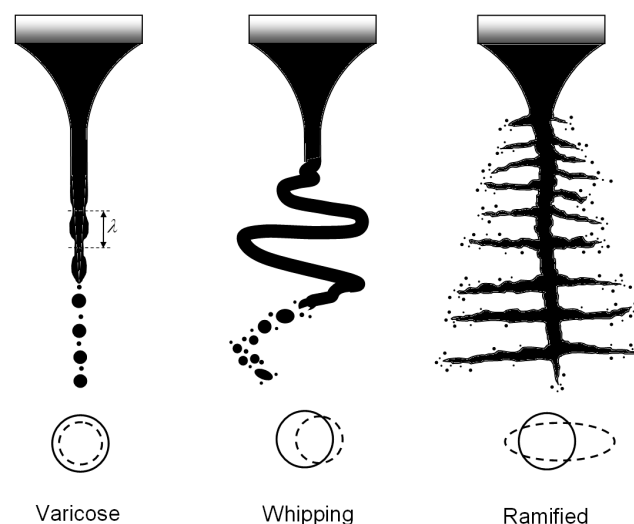


**Fig. 2.2.** Schematic drawing of different factors influencing the shape of the cone-jet.



It is clear from the picture that this description of the cone and the jet formation is more realistic and much more complicated than the one provided by Taylor. The simultaneous existence of *conduction* and *convection* currents is responsible for different charge transport mechanisms, which result eventually in non-flat profiles for the axial velocity of liquids with different viscosities and conductivities. In particular, charge convection governs the transport in the jet and contributes to a great extent to the kinetic energy of the ejected liquid.

2. The break-up of the jet produces charged droplets which generally carry up to 70 % of the limiting charge. In most of the cases, the break-up generates droplets with bimodal size distribution. This is explained by the jet that breaks up into primary droplets with a narrow size distribution and a minor population of smaller secondary droplets, arising from the filament between the primary droplets (see Fig. 2.3 – varicose). In some cases, even smaller satellite droplets are formed, due to the presence of this filament between a primary and a secondary droplet. The jet break-up can occur according to different modes, as schematically represented in Fig. 2.3.



**Fig. 2.3.** Different mechanisms responsible for the break-up of the jet.

The first one is called “axisymmetric” or “varicose break-up” where secondary droplets are present in a number comparable to that of primary droplets, as pointed out above. However, the volume fraction of the secondary droplets is much smaller. The generated droplets in the jet are highly charged, still the lateral electrical forces acting on them do not cause significant displacement from the capillary axis in the beginning. Rayleigh (1878) and Weber (1931) were the first to investigate the varicose instabilities produced in a liquid jet [54, 55]. Their descriptions were rather simple and they did not include the presence of an electric field. They could predict the wavelength  $\lambda$  of the fastest growing varicose instability and the effect of the

viscosity on this wavelength, which is often called the ‘dominant’ wavelength. Actually, the jet disrupts into droplets via instabilities with a wavelength close to the dominant one. The higher the viscosity, the longer the dominant wavelength produced. This fact results in a relatively larger volume fraction of secondary droplets, which, however, could not be described by their models. The dominant wavelength depended on the radius of the jet, which was assumed constant together with its velocity. Therefore, the acceleration of the jet and of the emitted droplets due to the electrical forces, as well as all the electrical effects were neglected.

A complete description of the jet-break up under the applied electric field has been carried out by Hartman, who modeled the entire phenomenon and investigated also the break-up by “whipping motions” [17, 51]. Indeed, these instabilities constitute a second mechanism, often referred as to “lateral kink break-up”. This mechanism normally occurs when the jet is slowed down by external forces (i.e. drag force of the surrounding gas), or when the jet is highly charged. In this case the cross-section of the jet is still circular, but it is laterally displaced, while being elongated. This break-up generates droplets which are generally not uniform in size. Finally, the “ramified-jet break-up” occurs only when the jet is extremely charged, and the electric stresses can overcome the surface tension of liquid jet. Consequently, the shape of the jet is modified, and its cross-section is no longer circular, being the liquid stripped from the lateral surface by the electric force.

3. The third process is then the evolution of the spray due to the interactions of the charged droplets. Electrical interactions among highly charged droplets are responsible for a size segregation effect. Smaller droplets will tend to move to the edge of the spray, while larger droplets will remain generally near its centre. Moreover, droplet fission can occur when evaporation of the liquid eventually causes the reaching of the Rayleigh limit, altering the droplet size distribution. Tang and Gomez showed that the droplet charge for EHDA in the cone-jet mode usually does not reach the Rayleigh limit [56]. However, increasing the flow rate enhances the charging of the droplets, which get closer to the Rayleigh limit. The evaporation rate of the liquid is not influenced by the charging process, as long as the droplets are larger than 0.1  $\mu\text{m}$ . Besides, the charge is not dissipated by evaporation, but only by impacts with ions and electrons from the surrounding gas [57].

4. Finally, also a fourth process should be considered: electrical discharges in the surrounding atmosphere [6, 25, 58]. Electrical discharges (i.e. corona discharge, streamers) interfere with the droplet production process. Important factors determining the occurrence of this phenomenon are for example the strength of the electric field, the shape of the meniscus/jet and the properties of the surrounding gas.

Clearly the shape of the capillary, the nozzle-electrode configuration and the liquid properties have a major influence [59].

## 2.2.2 Parameters influencing the spraying process

The *electrical conductivity*  $\kappa$  influences both the jet formation and the droplets size. It plays an essential role since it determines the electric tangential stresses acting on the cone surface [60]. If the conductivity is too low, about  $10^{-10}$ - $10^{-8}$   $\text{Sm}^{-1}$ , the liquid cannot be atomized, unless extra free charge is generated. For liquids with higher conductivities such as  $10^{-7}$ - $10^{-4}$   $\text{Sm}^{-1}$  a current can flow from the nozzle through the liquid and EHDA in the cone-jet depends mainly on the flow rate and the presence of eventual electrical discharges. Besides, the presence of ion species with characteristic mobility directly influences the current.

The *permittivity*  $\varepsilon$  determines the polarization, which weakens the electric field strength inside the liquid. Together with the conductivity it determines the characteristic time for charge transport inside the cone (see Table 2.1 earlier).

The *surface tension*  $\gamma$  plays a major role in the formation of a stable cone-jet, since it must be overcome by the electrical stresses. The higher the surface tension of a liquid, the higher the electric field required for its atomization. This, on its turn, results in higher currents, as well as in the onset of electrical discharges in the surrounding atmosphere that can destabilize the entire process.

The *viscosity*  $\mu$  influences the jet break-up process, as well as the radial profile of the axial velocity of the liquid in the jet formation and in the jet.

The *density*  $\rho$  has some importance in the acceleration of the liquid near the cone tip and it influences the shape of the cone due to effect of gravity on the pendant liquid meniscus.

The *flow rate* of the liquid,  $Q$  has a key role in EHDA. If it is too low, the atomization is not stable, since the cone cannot be continuously sustained. A minimum threshold value exists for the flow rate, above which the break-up and the droplet production are stable, resulting in a narrow size distribution [61]. However, increasing the flow rate above a certain value influences negatively the size distribution. If then it becomes too high, the EHDA cannot be properly established.

The *nozzle* also affects the spraying process. The shape of the nozzle and its wettability play an important role in determining the shape of the cone, the stability of the jet and the spraying modes that can be obtained. Moreover, the nozzle diameter affects the electric field lines, and therefore the current flowing through the cone. Smaller nozzle diameters sustain larger currents and generally need lower voltages for EHDA when compared to larger ones.

The *distance* between the nozzle and the counter electrode determines the geometry of the electric field lines. It affects the electric field strength for a fixed applied voltage and the time of flight for the emitted droplets. Increasing the distance from the nozzle implies a wider cross-section for deposition by the aerosol plume, so that larger area coverage can be achieved.

Finally, the *applied voltage* causes the onset of EHDA, which indeed is a field-driven process. The applied potential determines, for a fixed set of parameters, the spraying mode and the droplet production mechanism.

### 2.2.3 Scaling laws for current and droplet size

Several studies have been devoted to the analysis of the charged droplets produced in the cone-jet mode and different scaling laws have been proposed [17, 44, 47, 51, 61]. A large variety of equations depending on experimental constants have been adopted so far, indicating that the mathematical description of EHDA is complex. In particular, various equations based on dimensional analysis have been proposed for the calculation of the average droplet size,  $d$ , and the current flowing through the liquid,  $I$ , during the atomization process. Extensive measurements on the atomization of liquids with different physical properties have shown that basically two different (scaling) behaviors exist for these quantities. In particular, they are strongly dependent on the viscosity and the conductivity of the liquid. This is related to the different radial profiles of the axial velocity of the liquid in the cone-jet. The values assumed by a *dimensionless number*,  $\delta_\mu \delta^{1/3}$ , allow the separation between these two behaviors [61]:

$$\delta_\mu \delta^{1/3} = \left( \frac{\gamma^3 \epsilon_0^2}{\mu^3 \kappa^2 Q} \right)^{1/3} \quad (2.8)$$

This number represents the ratio of the change in the kinetic energy of the liquid jet in the axial direction and the change in viscous stress in the radial direction. Liquids with high conductivities and viscosities exhibit a flat profile for the axial velocity in the jet (i.e.  $\delta_\mu \delta^{1/3} < 1$ ) and behave differently from liquids with low conductivity and viscosity (i.e.  $\delta_\mu \delta^{1/3} > 1$ ). These last liquids exhibit a non-flat velocity profile, the velocity is higher near the surface of the jet than in its centre. Viscosity and electrical conductivity in liquids span a wide range and it is clear from eq. (2.8) that they strongly influence the radial profile of the axial velocities. In particular, flat profiles of the velocities are known to yield currents scaling as  $I \sim Q^{1/2}$ , while non-flat profiles generally follow  $I \sim Q^{1/4}$  [61].

Hartmann et al. investigated the process and derived independently a scaling law for the current, which was extended to cover all the Newtonian liquids with low conductivities and viscosities [51]. When  $\delta_\mu \delta^{d/3} < I$  then it results:

$$I \approx 2(\gamma\kappa Q)^{\frac{1}{2}} \quad (2.9)$$

This formula was then used to calculate the average droplet size for the different mechanisms of jet break-up (i.e. *varicose* and *whipping*),  $d_{d,v}$  and  $d_{d,w}$ :

$$d_{d,v} = c_d \left( \frac{\rho \varepsilon_0 Q^4}{I^2} \right)^{\frac{1}{6}} \quad (2.10)$$

$$d_{d,w} = \left( 0.8 \frac{288 \varepsilon_0 \gamma Q^2}{I^2} \right)^{\frac{1}{3}} \quad (2.11)$$

In eq. (2.10)  $c_d$  is a constant, which is approximately 2. Substituting eq. (2.9) in (2.10) and in (2.11) yields respectively:

$$d_{d,v} \approx \left( \frac{16 \rho \varepsilon_0 Q^3}{\gamma \kappa} \right)^{\frac{1}{6}} \quad (2.12)$$

$$d_{d,w} \approx \left( 0.8 \frac{72 \varepsilon_0 Q}{\kappa} \right)^{\frac{1}{3}} \quad (2.13)$$

It is worth pointing out that the actual jet break-up mechanism for a liquid is not known in advance and it needs to be observed by a high-speed camera. However, a simple criterion to determine which break-up mechanism is likely to occur relies on the calculation of the droplet size by both eq. (2.12) and (2.13). The expression that yields the smallest diameter is the one that determines which process occurs [17]. It should also be mentioned that the current depends on the electrode configuration and on the type of ions present. Furthermore, nozzles with narrow outlet diameters (i.e. < 1 mm) show intense electric field lines in the proximity of their tips, causing enhanced current flows and whipping of the jet. Real measurements can yield deviations from the scaling laws up to 30 %. Nevertheless, both formulas are very useful as a first estimate of the average droplet size, based on the knowledge of the physical properties of the liquid.

## 2.3 EHDA-based techniques

EHDA represents a simple and cost-effective technology that can be applied to several scientific fields and industrial processes. Mass spectrometry, painting, fine powders production, thin film deposition, drug delivery and crop spraying are just few examples [62-68]. These processes involve the deposition of droplets that carry solid particles or chemical substances. In particular, by superimposing pulsed DC voltage on the DC field it is also possible to control the droplet generation process and produce droplets on demand for manipulating tiny volumes of fluids (i.e. < 5 pL) [69-71].

Different reactions (i.e. pyrolysis, hydrolysis, condensation, etc.) can be also coupled to the electrospray in order to produce functional materials for ceramics, lithium batteries, solar cells, fuel cells, micro and nano-electronic devices [72-84].

Typically, Electrostatic Spray Deposition (ESD) and Pyrolysis (ESP) involve the use of a heat source in order to promote the evaporation of the solvent or to decompose the precursors and synthesize different materials at higher temperatures. These techniques are particularly attractive for the manufacture of thin films and coatings because they can be developed as continuous processes. Indeed, they can meet the requirements of high deposition rates, especially when compared to those accessible by other techniques such as Chemical Vapor Deposition (CVD) or Physical Vapor Deposition (PVD). The choice of the precursors, temperatures and solvents also influences the morphology of the deposited layers [65]. In fact, various textures can be obtained, ranging from dense layers to porous films [73, 79, 85, 86]. In particular, when pyrolysis is performed in order to produce particles from precursor solutions, the particle morphology is directly related to the drying history of the droplets [87]. Electrospray transport, evaporation and deposition have been investigated both theoretically and experimentally [88, 89]. Evaporation hardly influences the droplet transport. However, the droplet size and the salt concentration are strongly affected. In particular, the Rayleigh limit accounts for faster evaporation due to coulombic fission of the droplets. Moreover, the time of flight of the charged droplets influences the drying of the deposits and consequently affects the quality of the deposited film.

Another interesting technique that relates to EHDA is electrospinning of polymer fibers. It involves the ejection of a viscous polymeric solution or melt in the form of a charged jet from the outlet of the nozzle. Continuous drawing and solidification of the jet due to solvent evaporation lead to the generation of uniform, thin fibers. The main difference with conventional spinning processes is that the driving force for the fiber extrusion is not mechanical (i.e. stretching or pulling) but electrostatic. This distinctive feature enables the spinning of fibers with diameters that span from a few micrometers down to tens of nanometers, depending on the

rheological properties of the solution and other spinning parameters [90-94]. The presence of a polymer in the precursor solution does not necessarily imply electrospinning, but also electrospraying can occur. The rheological properties of the precursor solution, as well as the intrinsic characteristics of the polymer are extremely important in determining adequate viscosity, chain entanglement and interaction needed for electrospinning. In particular, viscosity alone is not sufficient to produce electrospinning. A minimum polymer concentration is needed for effective chain entanglement in order to avoid jet break-up and to prevent formation of irregular fiber diameters (i.e. 'beading') [95, 96].

### 2.3.1 Thin film electrodes for Li-ion batteries by ESD and ESP

Electrostatic Spray Deposition and Pyrolysis have been proposed in the early '90s for applications to Li batteries and micro-batteries [97]. Several studies have been carried out and promising results have shown the potential of these techniques for developing both positive and negative electrodes, as well as solid electrolytes [98-101]. The possibility of direct synthesis or deposition of nanostructured electrode materials onto current collectors is particularly attractive, especially for thin films, where no binders or electronically conductive additives are usually required for effective operation.

Thin film positive electrodes of  $\text{LiCoO}_2$ ,  $\text{LiCo}_x\text{Mn}_{2-x}\text{O}_4$ ,  $\text{LiNiO}_2$ ,  $\text{LiCo}_{0.5}\text{Ni}_{0.5}\text{O}_2$ ,  $\text{LiAl}_{0.25}\text{Ni}_{0.75}\text{O}_2$ ,  $\text{Li}_4\text{Ti}_5\text{O}_{14}$ ,  $\text{LiMn}_2\text{O}_4$ ,  $\text{LiNi}_{0.5}\text{Mn}_{1.5}\text{O}_4$  with different morphologies ranging from dense to porous layers have been obtained using various Li and metal precursors (i.e. acetates, nitrates) and solvents (i.e. ethanol, ethylene glycol, etc..) [76, 85, 102-111]. In most of the cases the precursor decomposition and reactions occur onto a heated substrate or while the droplets move towards the substrate. In particular, these synthesis processes can be carried out at lower temperatures (i.e. 250-500 °C) than conventional solid-state reactions. Often, a further thermal annealing is needed for full reaction and crystallization of the materials. Electrochemical tests demonstrate that these electrodes undergo  $\text{Li}^+$  intercalation/de-intercalation similar to conventional laminated electrodes and that porous structures favor efficient charge transfer.

Thin films of other metal oxides (i.e.  $\text{SnO}_2$ ,  $\text{Fe}_2\text{O}_3$ ,  $\text{CoO}$ ,  $\text{Cu}_2\text{O}$ ,  $\text{NiO}$ ,  $\text{ZrO}_2$ ,  $\text{Al}_2\text{O}_3$ ,  $\text{ZnO}$ ,  $\text{TiO}_2$ , etc..) have also been fabricated using the same approach [73-75]. In particular, nanostructured  $\text{SnO}_2$  and transition metal oxides (i.e.  $\text{M}_x\text{O}_y$ ) are receiving increasing attention as alternative negative electrodes [112-118]. Specific capacities much larger than those of carbonaceous materials can be achieved in such systems via alloying mechanisms or reversible conversion reactions, especially when they occur at the nanoscale. ESP can also address the issue related to their limited

cycling stability, due to severe volume changes of the host during up-taking and removal of Li. Three dimensional porous structures obtained by selection of particular substrates (i.e. nickel foams), temperatures and solvents proved to alleviate mechanical strains and provided optimal performances upon prolonged cycling [113, 119]. These systems with high surface areas constitute a groundbreaking approach to the fabrication of alternative negative electrodes for applications in thin-film batteries and micro-batteries.

However, the amount of active material that can be deposited in such a way is limited by the thickness of the deposited layers. Additionally, reticular and porous structures can be likely damaged or broken during the entire assembling of the battery. Finally, polymeric binders and conductive additives seem to be still crucial for the manufacture of thicker coated electrodes in conventional processes.

### **2.3.2 Application of electrospun fibers to Li-ion batteries**

Electrospinning of polymeric and ceramic nanofibers is interesting for a series of applications in Li-ion batteries. Polymer-fiber and gelled membranes [120-122], composite carbon nano-fibers [123], as well as composite hollow fibers by coaxial electrospinning are some examples of advanced materials that can be synthesized [124, 125]. The range of solvents, polymers and precursors that can be utilized is extremely wide. Moreover, fibers and hollow tubes exhibit ideal geometries to enhance the surface area of the electrodes and to accommodate at the same time the mechanical stresses induced by the electrochemical cycling. Several positive and negative electrode materials have been fabricated by such approach [126-129]. Polymers such as PAN, PVA, PVP etc. are typically dissolved together with the precursors and subsequently electro-spun as composite fibers. A thermal treatment under controlled atmosphere is generally required for precursor reaction (i.e. pre-oxidization) together with a complete burning or carbonization of the polymer at higher temperatures (i.e. 500-700 °C). Nanocomposite carbon/metal oxide fibers show good electrochemical performances and high rate capabilities [130, 131]. These structures are typically incorporated in coated electrodes with binders and conductive additives.

The mechanical strength of electrospun nanofibers and nanotubes, as well as the possibility for network-like architectures, are particularly favorable for novel negative electrodes. However, their entire fabrication and incorporation in coated electrodes have also shortcomings. An overall low throughput can be expected, as a result of the limited production rates for electrospinning and the extra time needed for subsequent thermal annealing at high temperatures. Additionally, the dispersion of the active nanofibers and nanotubes in laminated electrodes should be considered.



## 2.4 Outlook

EHDA is clearly an intriguing phenomenon that has attracted a great deal of attention due to its unique characteristics. Not surprisingly, the number of investigations and the related technological applications are expected to grow steadily in the forthcoming years. All the methods relying on EHDA share its versatility and limited costs for operation, which makes them ideal candidates for both scientific and industrial applications. Significant breakthroughs can be envisaged for the fabrication of nanostructured and functional materials via this approach. In particular, the challenges related to the synthesis and the assembly of nanocomposite materials for Li-ion batteries and fuel cells (i.e. electrodes, membranes and electrolytes) may be solved. The combination of theoretical studies and process engineering may eliminate shortcomings of existing processes and enable the development of the next generation of electrochemical devices with much enhanced performance.

## 2.5 References

- [1] J. M. Grace, J. C. M. Marijnissen, *Journal of Aerosol Science* **1994**, *25*, 1005.
- [2] A. Jaworek, A. Krupa, *Journal of Aerosol Science* **1999**, *30*, 873.
- [3] G. Joffre, B. Prunet-Foch, S. Berthomme, M. Cloupeau, *Journal of Electrostatics* **1982**, *13*, 151.
- [4] M. Cloupeau, B. Prunet-Foch, *Journal of Electrostatics* **1990**, *25*, 165.
- [5] M. Cloupeau, B. Prunet-Foch, *Journal of Aerosol Science* **1994**, *25*, 1021.
- [6] M. Cloupeau, B. Prunet-Foch, *Journal of Electrostatics* **1989**, *22*, 135.
- [7] L. De Juan, J. Fernandez De La Mora, *Journal of Colloid and Interface Science* **1997**, *186*, 280.
- [8] A. Gomez, K. Tang, *Physics of Fluids* **1994**, *6*, 404.
- [9] A. Jaworek, A. Krupa, *Journal of Aerosol Science* **1996**, *27*, 979.
- [10] A. Jaworek, A. Krupa, *Journal of Aerosol Science* **1996**, *27*, 75.
- [11] A. Jaworek, A. Krupa, *Experiments in Fluids* **1999**, *27*, 43.
- [12] G. H. Joffre, M. Cloupeau, *Journal of Electrostatics* **1986**, *18*, 147.
- [13] A. M. Ganán-Calvo, *Journal of Aerosol Science* **1994**, *25*, 309.
- [14] A. M. Ganán-Calvo, C. Pantano, A. Barrero, *Journal of Aerosol Science* **1996**, *27*.
- [15] A. G. Bailey, *Electrostatic Spray of Liquids*. Wiley, New York **1988**.
- [16] K. Tang, A. Gomez, *Journal of Colloid and Interface Science* **1996**, *184*, 500.
- [17] R. P. A. Hartman, D. J. Brunner, D. M. A. Camelot, J. C. M. Marijnissen, B. Scarlett, *Journal of Aerosol Science* **2000**, *31*, 65.

- [18] L. Rayleigh, *Philos. Mag.* **1882**, *14*, 184.
- [19] J. Zeleny, *Physical Review* **1917**, *10*, 1.
- [20] B. Vonnegut, R. L. Neubauer, *Journal of Colloid Science* **1952**, *7*, 616.
- [21] B. Vonnegut, R. L. Neubauer, *Journal of Colloid Science* **1953**, *8*, 551.
- [22] G. I. Taylor, *Proc.R.Soc.London, Ser.A* **1964**, *280*, 383.
- [23] I. Hayati, A. I. Bailey, T. Tadros, *Nature* **1986**, *319*, 41.
- [24] I. Hayati, A. I. Bailey, T. Tadros, *Journal of Colloid and Interface Science* **1987**, *117*, 205.
- [25] I. Hayati, A. Bailey, T. F. Tadros, *Journal of Colloid and Interface Science* **1987**, *117*, 222.
- [26] J. R. Melcher, G. I. Taylor, *Annual Review of Fluid Mechanics* **1969**, *1*, 111.
- [27] D. A. Saville, in *Annual Review of Fluid Mechanics*, Vol. 29, **1997**, 27.
- [28] D. P. H. Smith, *IEEE Trans. Ind. Appl.* **1986**, *1A-22*, 527.
- [29] M. G. Ikononou, A. T. Blades, P. Kebarle, *Analytical Chemistry* **1991**, *63*, 1989.
- [30] J. Fernandez De La Mora, J. Navascues, F. Fernandez, J. Rosell-Llompart, *Journal of Aerosol Science* **1990**, *21*.
- [31] J. Rosell-Llompart, J. Fernandez De La Mora, *Journal of Aerosol Science* **1994**, *25*, 1093.
- [32] G. M. H. Meesters, P. H. W. Vercoulen, J. C. M. Marijnissen, B. Scarlett, *Journal of Aerosol Science* **1990**, *21*.
- [33] G. M. H. Meesters, P. H. W. Vercoulen, J. C. M. Marijnissen, B. Scarlett, *Journal of Aerosol Science* **1991**, *22*.
- [34] G. M. H. Meesters, P. H. W. Vercoulen, J. C. M. Marijnissen, B. Scarlett, *Journal of Aerosol Science* **1992**, *23*, 37.
- [35] J. P. Borra, D. Camelot, J. C. M. Marijnissen, B. Scarlett, *Journal of Aerosol Science* **1996**, *27*.
- [36] D. M. A. Camelot, J. P. Borra, J. C. M. Marijnissen, B. Scarlett, *Journal of Aerosol Science* **1998**, *29*.
- [37] D. Camelot, J. C. M. Marijnissen, B. Scarlett, *Industrial and Engineering Chemistry Research* **1999**, *38*, 631.
- [38] D. Camelot, K. L. Chou, P. J. Kooyman, J. C. M. Marijnissen, B. Scarlett, J. P. Borra, *Journal of Aerosol Science* **1997**, *28*.
- [39] J. P. Borra, D. Camelot, K. L. Chou, P. J. Kooyman, J. C. M. Marijnissen, B. Scarlett, *Journal of Aerosol Science* **1999**, *30*, 945.
- [40] J. P. Borra, D. Camelot, J. C. M. Marijnissen, B. Scarlett, *Journal of Electrostatics* **1997**, *40-41*, 633.
- [41] W. Deng, A. Gomez, *Journal of Aerosol Science* **2007**, *38*, 1062.
- [42] W. Deng, J. F. Klemic, X. Li, M. A. Reed, A. Gomez, *Journal of Aerosol Science* **2006**, *37*, 696.

- [43] J. C. Almekinders, C. Jones, *Journal of Aerosol Science* **1999**, 30, 969.
- [44] J. F. De La Mora, I. G. Loscertales, *Journal of Fluid Mechanics* **1994**, 260, 155.
- [45] A. M. Ganan-Calvo, *Physical Review Letters* **1997**, 79, 217.
- [46] A. M. Ganan-Calvo, *Journal of Fluid Mechanics* **1997**, 335, 165.
- [47] A. M. Ganan-Calvo, *Journal of Aerosol Science* **1999**, 30, 863.
- [48] A. M. Ganan-Calvo, A. Barrero, C. Pantano-Rubino, *Journal of Aerosol Science* **1993**, 24.
- [49] R. P. A. Hartman, J. P. Borra, D. J. Brunner, J. C. M. Marijnissen, B. Scarlett, *Journal of Electrostatics* **1999**, 47, 143.
- [50] R. P. A. Hartman, J. P. Borra, J. C. M. Marijnissen, B. Scarlett, *Journal of Aerosol Science* **1996**, 27.
- [51] R. P. A. Hartman, D. J. Brunner, D. M. A. Camelot, J. C. M. Marijnissen, B. Scarlett, *Journal of Aerosol Science* **1999**, 30, 823.
- [52] R. P. A. Hartman, D. J. Brunner, J. C. M. Marijnissen, B. Scarlett, *Journal of Aerosol Science* **1998**, 29.
- [53] R. P. A. Hartman, J. C. M. Marijnissen, B. Scarlett, *Journal of Aerosol Science* **1997**, 28.
- [54] L. Rayleigh, *Proc. London Math. Soc.* **1878**, 11, 4.
- [55] C. Weber, *Z. Angew Math. und Mech.* **1931**, 11, 136.
- [56] K. Tang, A. Gomez, *Physics of Fluids* **1994**, 6, 2317.
- [57] S. E. Law, *IEEE Trans. Ind. Appl.* **1989**, 25, 1081.
- [58] J. P. Borra, R. Hartmann, J. Marijnissen, B. Scarlett, *Journal of Aerosol Science* **1996**, 27.
- [59] M. Cloupeau, *Journal of Aerosol Science* **1994**, 25, 1143.
- [60] A. Barrero, A. M. Ganan-Calvo, J. Davila, A. Palacios, E. Gomez-Gonzalez, *Journal of Electrostatics* **1999**, 47, 13.
- [61] A. M. Ganan Calvo, J. Davila, A. Barrero, *Journal of Aerosol Science* **1997**, 28, 249.
- [62] C. M. Whitehouse, R. N. Dreyer, M. Yamashita, J. B. Fenn, *Analytical Chemistry* **1985**, 57, 675.
- [63] T. Dulcks, F. W. Rollgen, *Journal of Mass Spectrometry* **1995**, 30, 324.
- [64] A. Jaworek, *Powder Technology* **2007**, 176, 18.
- [65] A. Jaworek, *Journal of Materials Science* **2007**, 42, 266.
- [66] J. C. Ijsebaert, K. B. Geerse, J. C. M. Marijnissen, B. Scarlett, *Journal of Aerosol Science* **1999**, 30.
- [67] K. Tang, A. Gomez, *Journal of Aerosol Science* **1994**, 25, 1237.
- [68] K. B. Geerse, J. C. M. Marijnissen, A. Kerssies, M. Van Der Staaij, B. Scarlett, *Journal of Aerosol Science* **1999**, 30.

- [69] U. Stachewicz, J. F. Dijksman, D. Burdinski, C. U. Yurteri, J. C. M. Marijnissen, *Langmuir* **2009**, *25*, 2540.
- [70] U. Stachewicz, J. F. Dijksman, J. C. M. Marijnissen, *Journal of Physics: Conference Series* **2008**, *142*.
- [71] U. Stachewicz, J. F. Dijksman, C. U. Yurteri, J. C. M. Marijnissen, *Applied Physics Letters* **2007**, *91*.
- [72] E. M. Kelder, O. C. J. Nijs, J. Schoonman, *Solid State Ionics* **1994**, *68*, 5.
- [73] C. Chen, E. M. Kelder, J. Schoonman, *Journal of the Electrochemical Society* **1997**, *144*.
- [74] C. H. Chen, M. H. J. Emond, E. M. Kelder, B. Meester, J. Schoonman, *Journal of Aerosol Science* **1999**, *30*, 959.
- [75] C. H. Chen, E. M. Kelder, J. Schoonman, *Thin Solid Films* **1999**, *342*, 35.
- [76] C. H. Chen, E. M. Kelder, M. J. G. Jak, J. Schoonman, *Solid State Ionics* **1996**, *86-88*, 1301.
- [77] I. W. Lenggoro, K. Okuyama, *Journal of Aerosol Science* **1997**, *28*.
- [78] D. Zaouk, Y. Zaatar, A. Khoury, C. Llinares, J. P. Charles, J. Bechara, *Microelectronic Engineering* **2000**, *51*, 627.
- [79] Y. Yu, J. L. Shui, S. Xie, C. H. Chen, *Aerosol Science and Technology* **2005**, *39*, 276.
- [80] S. N. Jayasinghe, M. J. Edirisinghe, D. Z. Wang, *Nanotechnology* **2004**, *15*, 1519.
- [81] M. J. Edirisinghe, S. N. Jayasinghe, *International Journal of Applied Ceramic Technology* **2004**, *1*, 140.
- [82] W. D. Teng, Z. A. Huneiti, W. Machowski, J. R. G. Evans, M. J. Edirisinghe, W. Balachandran, *Journal of Materials Science Letters* **1997**, *16*, 1017.
- [83] N. H. J. Stelzer, J. Schoonman, *Journal of Materials Synthesis and Processing* **1996**, *4*, 429.
- [84] P. H. Michael Bottger, Z. Bi, D. Adolph, K. A. Dick, L. S. Karlsson, M. N. A. Karlsson, B. A. Wacaser, K. Deppert, *Nanotechnology* **2007**, *18*.
- [85] C. H. Chen, E. M. Kelder, J. Schoonman, *Journal of Materials Science* **1996**, *31*, 5437.
- [86] J. L. Shui, Y. Yu, C. H. Chen, *Applied Surface Science* **2006**, *253*, 2379.
- [87] S. Nestic, J. Vodnik, *Chemical Engineering Science* **1991**, *46*, 527.
- [88] O. Wilhelm, L. Madler, S. E. Pratsinis, *Journal of Aerosol Science* **2003**, *34*, 815.
- [89] I. B. Rietveld, K. Kobayashi, H. Yamada, K. Matsushige, *Journal of Physical Chemistry B* **2006**, *110*, 23351.
- [90] D. Li, Y. Xia, *Advanced Materials* **2004**, *16*, 1151.
- [91] D. Li, J. T. McCann, Y. Xia, M. Marquez, *Journal of the American Ceramic Society* **2006**, *89*, 1861.

- [92] J. Doshi, D. H. Reneker, *Journal of Electrostatics* **1995**, *35*, 151.
- [93] S. V. Fridrikh, J. H. Yu, M. P. Brenner, G. C. Rutledge, *Physical Review Letters* **2003**, *90*.
- [94] D. Li, Y. Xia, *Nano Letters* **2003**, *3*, 555.
- [95] H. Fong, I. Chun, D. H. Reneker, *Polymer* **1999**, *40*, 4585.
- [96] S. L. Shenoy, W. D. Bates, H. L. Frisch, G. E. Wnek, *Polymer* **2005**, *46*, 3372.
- [97] A. A. van Zomeren, E. M. Kelder, J. C. M. Marijnissen, J. Schoonman, *Journal of Aerosol Science* **1994**, *25*, 1229.
- [98] C. H. Chen, E. M. Kelder, J. Schoonman, *Journal of Power Sources* **1997**, *68*, 377.
- [99] J. Zhang, L. B. Chen, C. C. Li, T. H. Wang, *Applied Physics Letters* **2008**, *93*.
- [100] Y. Yu, J. L. Shui, Y. Jin, C. H. Chen, *Electrochimica Acta* **2006**, *51*, 3292.
- [101] J. Schoonman, E. M. Kelder, *Journal of Power Sources* **1997**, *68*, 65.
- [102] K. Yamada, N. Sato, T. Fujino, C. G. Lee, I. Uchida, J. R. Selman, *Journal of Solid State Electrochemistry* **1999**, *3*, 148.
- [103] C. Chen, E. M. Kelder, P. J. J. M. Van Der Put, J. Schoonman, *Journal of Materials Chemistry* **1996**, *6*, 765.
- [104] C. H. Chen, A. A. J. Buysman, E. M. Kelder, J. Schoonman, *Solid State Ionics* **1995**, *80*, 1.
- [105] K. Dokko, N. Anzue, Y. Makino, M. Mohamedi, T. Itoh, M. Umeda, I. Uchida, *Electrochemistry* **2003**, *71*, 1061.
- [106] Y. Yu, J. L. Shui, C. H. Chen, *Solid State Communications* **2005**, *135*, 485.
- [107] K. Yamada, N. Sato, T. Fujino, M. Nishizawa, I. Uchida, *Electrochemistry* **1999**, *67*, 68.
- [108] M. Mohamedi, M. Makino, K. Dokko, T. Itoh, I. Uchida, *Electrochimica Acta* **2002**, *48*, 79.
- [109] J. L. Shui, G. S. Jiang, S. Xie, C. H. Chen, *Electrochimica Acta* **2004**, *49*, 2209.
- [110] M. Mohamedi, D. Takahashi, T. Itoh, M. Umeda, I. Uchida, *Journal of the Electrochemical Society* **2002**, *149*, A19.
- [111] F. Cao, J. Prakash, *Electrochimica Acta* **2002**, *47*, 1607.
- [112] Y. Yu, Y. Shi, C. H. Chen, *Nanotechnology* **2007**, *18*.
- [113] Y. Yu, C. H. Chen, J. L. Shui, S. Xie, *Angewandte Chemie - International Edition* **2005**, *44*, 7085.
- [114] L. Wang, H. W. Xu, P. C. Chen, D. W. Zhang, C. X. Ding, C. H. Chen, *Journal of Power Sources* **2009**, *193*, 846.
- [115] M. Mohamedi, S. J. Lee, D. Takahashi, M. Nishizawa, T. Itoh, I. Uchida, *Electrochimica Acta* **2001**, *46*, 1161.
- [116] P. Poizot, S. Laruelle, S. Grugeon, L. Dupont, J. M. Tarascon, *Nature* **2000**, *407*, 496.

- [117] C. Chen, N. Ding, L. Wang, Y. Yu, I. Lieberwirth, *Journal of Power Sources* **2009**, *189*, 552.
- [118] F. Badway, I. Plitz, S. Grugeon, S. Laruelle, M. Doll+©, A. S. Gozdz, J. M. Tarascon, *Electrochemical and Solid-State Letters* **2002**, *5*.
- [119] Y. Yu, L. Gu, A. Dhanabalan, C. H. Chen, C. Wang, *Electrochimica Acta* **2009**, *54*, 7227.
- [120] D. Bansal, B. Meyer, M. Salomon, *Journal of Power Sources* **2008**, *178*, 848.
- [121] C. Yang, Z. Jia, Z. Guan, L. Wang, *Journal of Power Sources* **2009**, *189*, 716.
- [122] S. W. Lee, S. W. Choi, S. M. Jo, B. D. Chin, D. Y. Kim, K. Y. Lee, *Journal of Power Sources* **2006**, *163*, 41.
- [123] M. Peng, D. Li, L. Shen, Y. Chen, Q. Zheng, H. Wang, *Langmuir* **2006**, *22*, 9368.
- [124] D. Li, Y. Xia, *Nano Letters* **2004**, *4*, 933.
- [125] D. Li, J. T. McCann, Y. Xia, *Small* **2005**, *1*, 83.
- [126] N. Yu, C. Shao, Y. Liu, H. Guan, X. Yang, *Journal of Colloid and Interface Science* **2005**, *285*, 163.
- [127] H. W. Lu, D. Li, K. Sun, Y. S. Li, Z. W. Fu, *Solid State Sciences*.
- [128] H. W. Lu, W. Zeng, Y. S. Li, Z. W. Fu, *Journal of Power Sources* **2007**, *164*, 874.
- [129] X. Fan, L. Zou, Y. P. Zheng, F. Y. Kang, W. C. Shen, *Electrochemical and Solid-State Letters* **2009**, *12*.
- [130] L. Wang, Y. Yu, P. C. Chen, D. W. Zhang, C. H. Chen, *Journal of Power Sources* **2008**, *183*, 717.
- [131] L. Wang, Y. Yu, P. C. Chen, C. H. Chen, *Scripta Materialia* **2008**, *58*, 405.

# Chapter 3

## **Metallic and metallic-like powders via Electrostatic Spray Reductive Precipitation**

*Si un hombre nunca se contradice,  
es porque nunca dice nada.  
(Miguel de Unamuno)*

This chapter introduces a novel application of electrospray for the synthesis of nanostructured powders in the liquid phase by coupling Electrohydrodynamic Atomization (EHDA) to chemical reactions. Electro spraying of metal chlorides precursor solutions is coupled to reductive precipitation in order to synthesize metallic and metallic-like particles in liquids. Tin precursors have been initially employed, due to their potential application in Li-ion battery negative electrodes. Nonetheless, this method enables the fabrication of a wide range of functional materials, whose application is not limited to electrochemical devices but extends to a variety of technological fields.

### 3.1 Coupling EHDA with chemical reactions in liquids

The number of investigations concerning the fabrication and manipulation of nano-structured functional materials is tremendously increasing during the last years. This is not surprising, since materials in the nanometric scale exhibit physical and chemical properties that are different from that of their bulk form, and for this reason they are interesting for the development of novel systems and devices [1, 2].

In this respect, metallic-like materials, e.g. metals, alloys, intermetallics, are a class of materials with potential applications in various fields, such as catalysis, Li-ion batteries or optoelectronics [3-5]. Some simple methods, which have been used to form metallic nanomaterials so far, are, for example, chemical reduction [6], high-energy ball-milling [7] and electrochemical deposition [8]. EHDA has also been proposed for the fabrication of nanoparticles of noble metals via pyrolysis in the gas phase [9].

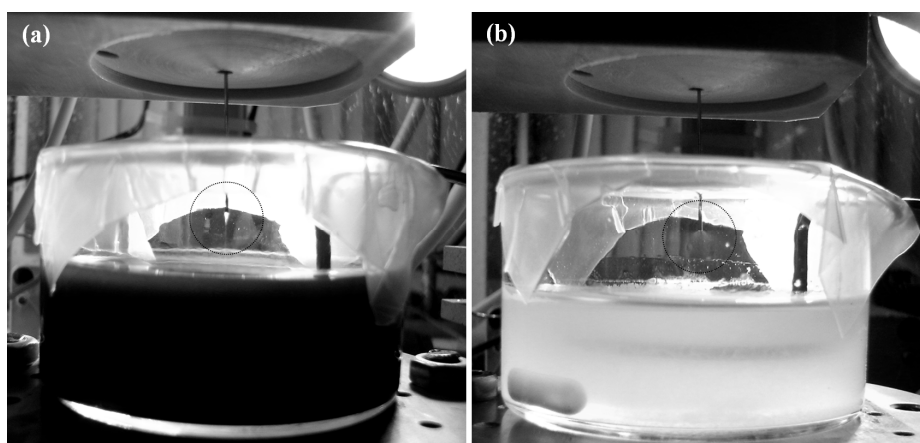
Electrospray (ES) is particularly attractive due to its versatility in dispersing liquids by electric fields [10], and by ‘DC-pulsed single event electrospraying’ it is even possible to dispense very small amounts of liquid in the form of charged droplets [11]. The possibility of using charged droplets from an electrospray source as precursors for chemical reactions in the liquid phase has some interesting features. On the one hand, the nature of the chemical reaction can be conveniently chosen and adapted to various purposes. On the other hand, the reactions that are carried out by a ‘drop-wise’ addition approach, for example, can be potentially carried out by means of micrometric or even sub-micrometric droplets, which exhibit a certain monodispersity. Finally, the charge present on the droplets is responsible for a self-dispersion of the generated aerosol, whose motion is determined by the applied electric field.

Among the modes of operation that can be selected for this kind of processes, the micro-dripping, the cone-jet and the multi-jet mode are the best choices, due to the quasi-homogeneous size distribution for the emitted droplets.

Herein EHDA is carried out in the cone-jet and multi-jet mode in order to form highly charged airborne precursor droplets, which are collected in a liquid bath where red-ox reactions can directly take place (Fig. 3.1). The process that has been developed employs red-ox reactions that involve chemical precipitation of metallic particles and it is referred to as Reductive Precipitation (RP).

RP of metal chlorides by  $\text{NaBH}_4$  is a well-known technique [12, 13] in materials chemistry, which enables the synthesis of fine particles of metals, alloys and intermetallics [14]. This method represents a “bottom-up” approach to the synthesis of fine metallic-like powders, which are often employed for Li-ion battery applications.





**Fig. 3.1.** EHDA in the cone-jet mode (a) and multi-jet mode (b) coupled reductive precipitation. The circles highlight the shape of the liquid meniscus at the outlet of the electrified nozzle.

Moreover, the size and the morphology of the precipitated materials can be influenced by several parameters, i.e. precursor concentrations, temperature, complexing agents etc. [15].

Although RP of metal chlorides by  $\text{NaBH}_4$  is a versatile technique, which can be carried out both in aqueous and organic solvents, achieving an effective control on the particle size and size distribution is not straightforward. It requires the use of proper surfactants or capping agents [15, 16] that often need to be removed for a practical use of the synthesized materials.

The atomization of the precursor solution via EHDA can be considered here as a “top-down” approach in order to produce micrometric droplets that carry a limited amount of precursor ions. These features are expected to help the formation of nanostructured metallic-like powders when bridging ES with RP by  $\text{NaBH}_4$ . Electrostatic Spray Reductive Precipitation (ESRP) can be regarded as a general synthesis method that combines physical and chemical routes, enabling the use of various precursors, solvents and reactants.

Tin-based nanostructured powders produced from chloride solutions are discussed here as an example, but it is stressed that this technique constitutes an alternative approach for producing a large variety of materials with applications in different technological fields.

## 3.2 Experimental details

The experimental procedure is described in the following sub-sections, which focus on the different steps involved in the entire process of synthesis and characterization.

### 3.2.1 Precursor solutions

Tin chloride dihydrate ( $\text{SnCl}_2 \cdot 2\text{H}_2\text{O}$ , M.W. = 225.63  $\text{g mol}^{-1}$  - J.T Baker) was dissolved in iso-propyl alcohol (IPA; 2-propanol - J.T Baker) in order to prepare 0.1 M solutions, corresponding to approximately 2.78 wt.% for the solute. IPA was preferred over de-ionized water as solvent for two reasons. Firstly, because its intrinsic properties facilitate a stable EHDA in the cone-jet mode using moderate voltages, and secondly because it is chemically stable towards the reducing agent  $\text{NaBH}_4$  (Fluka).

Physical properties of the precursor solution relevant for EHDA were measured: electrical conductivity ( $\kappa \approx 70 \mu\text{Sm}^{-1}$ ), surface tension ( $\gamma \approx 26.6 \text{ mNm}^{-1}$ ), specific gravity ( $\rho \approx 800 \text{ kgm}^{-3}$ ), viscosity ( $\mu \approx 2.58 \text{ mPa}\cdot\text{s}$ ), and relative permittivity ( $\epsilon_r \approx 18$ ). A second solution, used as reductive bath was prepared with  $\text{NaBH}_4$  in IPA. Each time, approximately 30% wt. excess on the stoichiometrical amount of  $\text{NaBH}_4$  needed for the reaction was added in order to ensure a complete reduction of the precursor metal ions. Both precursor and reductive solutions were thus separately prepared, then sealed and carefully stirred before starting the experiments.

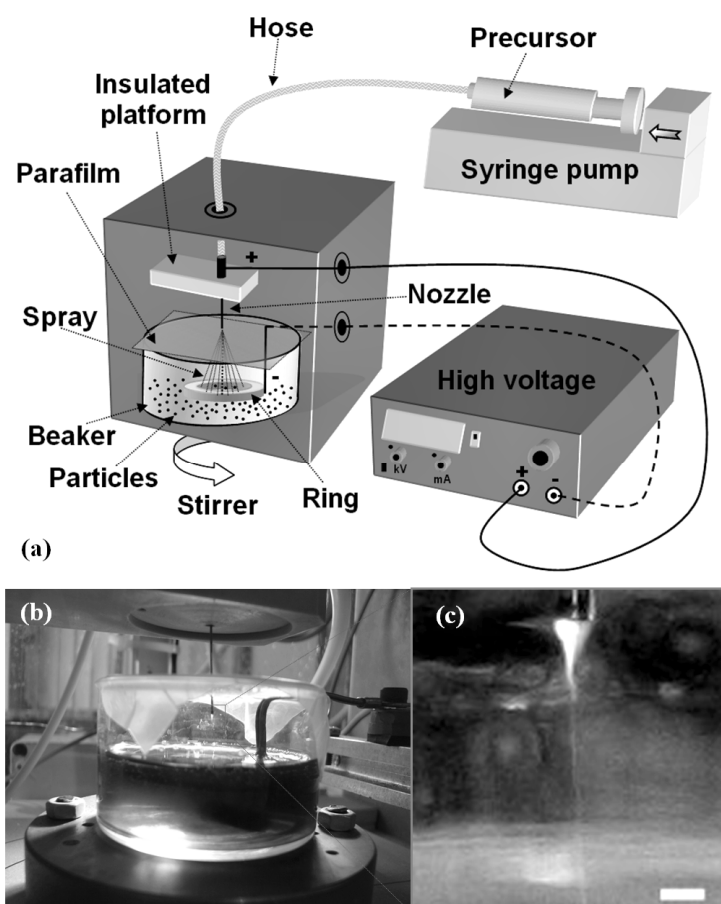
### 3.2.2 Aerosol generation and chemical reactions

All the experiments were carried out in air at room temperature (RT). The equipment used for EHDA is schematically represented in Fig. 3.2a.

It consists of a stainless steel nozzle (EFD Ultra, with  $D_i = 0.25 \text{ mm}$ ,  $D_o = 0.51 \text{ mm}$ ) mounted on a movable insulated platform and connected to the positive pole of a power supply (HCN 14-12500, FUG). A metal ring was used as grounded counter electrode, which was placed in the reductive bath. The ring was made of a tin alloy soldering wire in order to reduce possible contamination of other metals in the bath.

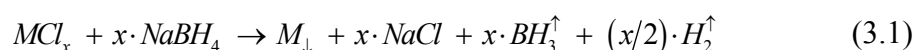
The relative distance between the tip of the nozzle and the grounded electrode was calibrated by a digital calliper. A typical distance of about 12 mm was used. A syringe pump (Kd Scientific model 100 series) and a 10 ml glass syringe (Fortuna Optima) were used to inject the precursor solution through the electrified nozzle with a controlled flow rate. A chemically resistant hose (Watson Marlow) was used as tubing for connecting the syringe to the nozzle. Low flow rates (about  $1.5 \text{ mlh}^{-1}$ ) were used in most cases. A higher flow rate of  $10 \text{ mlh}^{-1}$  was also employed to investigate its influence on the produced materials and for evaluating a possible enhancement of the production rate. The power supply provided the high voltage (i.e.  $0 \div 12.5 \text{ kV}$ ) between the nozzle and the counter-electrode. The shape of the liquid cone and the regime, where a stable jet was emitted from the tip of the cone, were observed with

the help of a halogen lamp. A magnetic stirrer (Variomag) was employed to homogenize the liquid suspension formed during the reaction process.



**Fig. 3.2.** Drawing of the set-up for EHDA-RP (a); EHDA-RP of Sn chloride (b); magnified detail of the cone-jet (c). The liquid cone and the thin jet emerging from its tip are clearly seen. Note that the solid bar in (c) corresponds roughly to the size of the outlet of the nozzle, i.e. 510  $\mu\text{m}$ .

Under the influence of the applied electric field, the charged aerosol formed by the jet break-up was attracted towards the grounded electrode, which was placed in the reductive bath. In this way, the small droplets containing the precursor metal ions were driven into this bath, where they were immediately reduced. The general reaction taking place to form the metal particles is the following:



where M refers to the metal precursor ions (in this case  $\text{Sn}^{++}$ ). It should be noted that this type of reaction involves also the formation of certain by-products, e.g. NaCl. This by-product needs to be washed off, in order to collect the particles in a pure form for further use.

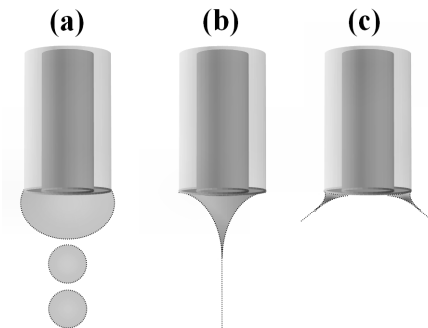
### 3.2.3 Particle collection and measurements

The suspension obtained in the way described above was stirred vigorously for about twenty minutes. Afterwards, centrifugation was carried out at 8000 rpm for 1 h in order to separate the particles from the liquid. The spun particles were carefully washed several times with technical ethanol, rinsed with acetone and finally dried and stored under vacuum at RT.

The morphology, size, and crystallinity of the particles were investigated by a Philips CM30T transmission electron microscope (TEM) operated at 300 kV, equipped with a LINK EDX probe (Oxford). The collected powders were also analyzed by a Philips XL20 Scanning Electron Microscope (SEM) and a Bruker (AXS D8 advance) X-ray diffractometer, with a Cu-K $\alpha$  radiation source.

## 3.3 Results and discussion

The atomization of the precursor solution was initially carried out at a constant flow rate of 1.5 mlh $^{-1}$  (i.e.  $4.2 \cdot 10^{-10}$  m $^3$  s $^{-1}$ ) with two different voltages, i.e. 2.0 and 9.0 kV. Then, the same precursor solution was pumped at a higher rate of 10 mlh $^{-1}$  (i.e.  $2.8 \cdot 10^{-9}$  m $^3$  s $^{-1}$ ) and was atomized by applying 3.3 and 10.5 kV.



**Fig. 3.3.** Schematic drawing of the liquid meniscus attached to a dripping nozzle under different voltage conditions: normal dripping, no applied voltage (a); onset of the cone-jet mode under the influence of an applied electric field (b); multi-jet mode obtained at higher voltages (c). Note that in the multi-jet mode the liquid meniscus is flattened and several jets can be present at the same time.

In all the experiments, the applied voltages were selected so that, for a given flow rate, the electric field generated under these conditions caused the onset of a stable cone-jet and the multi-cone jet mode respectively (Fig. 3.3b-c). A stable cone-jet mode, is often identified with the formation of the so-called “Taylor cone” [17].

The different processes taking place during EHDA exhibit various characteristic time constants [18, 19]. The electrical relaxation time ( $\tau_e$ ), the characteristic time for jet formation ( $\tau_j$ ), the hydrodynamic time ( $\tau_h$ ), and the

characteristic time for the supply of the liquid to the nozzle ( $\tau_l$ ) are here calculated from the experimental parameters for a description of the liquid cone and the emission of the jet from its apex. The characteristic size of the zone travelled by the liquid droplets,  $L$ , is approximately 10 mm (i.e. roughly the distance between the nozzle tip and the surface of the reductive bath) and the radial characteristic length of the jet,  $R_j$ , spans approximately from 40 to 50  $\mu\text{m}$ . The results for the calculated characteristic times are summarized in table 3.1.

**Table 3.1.** Overview of the calculated values for the characteristic times.

$Q$ [ $\text{m}^3\text{s}^{-1}$ ]	$L$ [mm]	$R_j$ [ $\mu\text{m}$ ]	$\tau_h = \frac{LR_j^2}{Q}$ [s]	$\tau_l = \frac{\pi D_i^3}{4Q}$ [s]	$\tau_e = \frac{\epsilon_0 \epsilon_r}{\kappa}$ [s]	$\tau_j = \frac{\mu D_i}{\gamma}$ [s]
$4.2 \cdot 10^{-10}$	$\approx 10$	$\approx 40$	$3.81 \cdot 10^{-2}$	$2.92 \cdot 10^{-2}$	$2.28 \cdot 10^{-6}$	$2.42 \cdot 10^{-5}$
$2.8 \cdot 10^{-9}$	$\approx 10$	$\approx 50$	$8.93 \cdot 10^{-3}$	$4.38 \cdot 10^{-3}$	$2.28 \cdot 10^{-6}$	$2.42 \cdot 10^{-5}$

A comparison of the calculated time constants clearly indicates that in all the cases results  $\tau_e \ll \tau_h$ . This means that it is possible to establish EHDA in the cone-jet mode [19]. It can also be noted that for both flow rates used is  $\tau_j \ll \tau_l$ , meaning that the jet can be readily emitted from the tip of the liquid cone. Under these conditions a regime of sufficient electrical shear stress is provided to the liquid in order to achieve a stable conical meniscus and a steady cone-jet emission.

At this point, the radial profile of the axial liquid velocity in the jet can be evaluated by considering a dimensionless number,  $\delta_\mu \delta^{1/3}$ , which gives information on the behaviour of the current and the droplet size of a liquid when subjected to EHDA.

$$\delta_\mu \delta^{1/3} = \left( \frac{\gamma^3 \epsilon_0^2}{\mu^3 \kappa^2 Q} \right)^{1/3} \quad (3.2)$$

Two different types of behaviour are known, which are strongly related to the viscosity and the electrical conductivity of the liquid [19]. The separation between these two types of behaviour is governed by the value of  $\delta_\mu \delta^{1/3}$ . Calculated values for  $\delta_\mu \delta^{1/3}$  yield respectively 0.347 and 0.184 for the two different flow rates employed (see table 3.2). In both cases the values are  $< 1$ , meaning that the radial profile of the axial liquid velocity in both jets is almost flat. This circumstance matches well with the use of a high conductivity solution and allows the application of the scaling law for the current,  $I$ , which flows through the liquid cone [20, 21]:

$$I = b(\gamma \kappa Q)^{1/2} \quad (3.3)$$

where  $b$  is a constant whose value is approximately 2.

Based on the knowledge of this current scaling law, two other scaling laws can be used for a preliminary evaluation of the average droplet diameter produced under different mechanisms of jet break-up [21]. In particular, for the so-called “varicose” break-up mode of the jet the droplet diameter is given by:

$$d_{d,v} = c \left( \frac{\rho \varepsilon_0 Q^4}{I^2} \right)^{\frac{1}{6}} \quad (3.4)$$

where  $c$  is a constant, which is close to 2, and  $\rho$  is the density of the solution. On the other hand, for a jet break-up in the “whipping mode”, the droplet diameter is calculated via the following equation:

$$d_{d,w} = \left( 0.8 \frac{288 \varepsilon_0 \gamma Q^2}{I^2} \right)^{\frac{1}{3}} \quad (3.5)$$

It is important to note that the actual mechanism of jet break-up for a certain liquid is not known a priori. Substitution of equation (3.3) in equations (3.4) and (3.5) enables the calculation of the average droplet size for these jet break-up mechanisms explicitly in terms of the experimental process parameters,  $\rho$ ,  $\gamma$ ,  $\kappa$ ,  $Q$ . The results are summarized in table 3.2.

**Table 3.2.** Calculated values for current and droplet size.

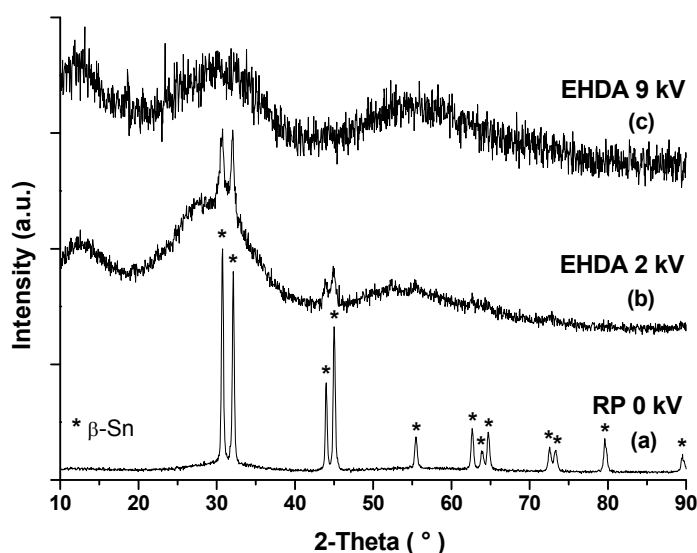
$Q$ [m <sup>3</sup> s <sup>-1</sup> ]	$\delta_\mu \delta^{\frac{1}{3}} = \left( \frac{\gamma^3 \varepsilon_0^2}{\mu^3 \kappa^2 Q} \right)^{\frac{1}{3}}$	$I$ [μA]	“Varicose” $d_{d,v}$ [μm]	“Whipping” $d_{d,w}$ [μm]
$4.2 \cdot 10^{-10}$	0.347	0.056	12.8	14.5
$2.8 \cdot 10^{-9}$	0.184	0.144	33.2	27.3

It can be seen that a lower flow rate yields a lower current intensity and a smaller droplet diameter for both break-up mechanisms. The break-up mechanism that is likely to take place can now be determined, using the following criterion: “the expression that gives the smallest droplet size is the appropriate one” [21]. Based on this assumption, it is seen from table 2 that the lowest flow rate yields likely a varicose break-up of the jet, producing an average droplet size of about 13 μm. On the other hand, the highest flow rate results in a jet break-up by whipping motions, with an average droplet size of about 27 μm. Conversely, it should be pointed out that a jet break-up in the whipping mode negatively influences the size distribution of the emitted droplets, which are no longer monodisperse, due to an increasing number of secondary droplets. In the present case, it should be taken into account that a more realistic value of the current is at least 15-20% higher than the expected values [21].

This is due to the fact that the outer diameter of the nozzle is rather narrow (i.e. less than 1 mm), and in such a case the application of a higher voltage for the atomization enhances considerably the current. As a result, the whipping of the jet increases [21].

Unfortunately, a similar discussion for the EHDA in the multi-jet mode is not possible, since scaling laws have not been derived yet. The mechanism of droplet formation is more complicated and eventually dominated by whipping motions of the jets. The electric forces heavily influence the generation and the transport of the highly charged droplets. Nevertheless, some qualitative considerations can be made. The fact that several cone-jets are present at the same time implies a sharing of the same liquid supply, resulting in a lower flow rate for each jet. Consequently, an average smaller droplet size is expected for a fixed flow rate, based on the cone-jet scaling laws. Moreover, the droplet emission frequency is much higher, and the number of produced droplets is further enhanced by disruption due to an earlier liquid evaporation and therefore exceeding the limiting charging, also known as the Rayleigh limit.

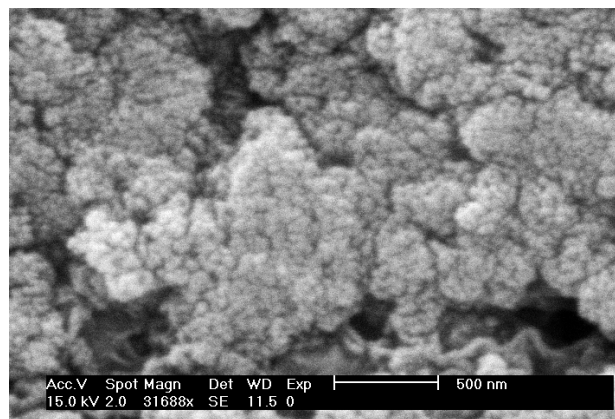
The above-mentioned conditions are now considered here for the production of the materials under study. Besides, reduction of the  $\text{SnCl}_2$  precursor in IPA was also carried out without applying any voltage, so as to include a reference sample for RP. The reduction conditions, therefore, were kept the same as the ones employed for the EHDA-produced samples. Fig. 3.4 shows the XRD spectra of the powders synthesized with a flow rate of  $1.5 \text{ mlh}^{-1}$  at RT but with different voltages, i.e. 0.0, 2.0, and 9.0 kV.



**Fig. 3.4.** XRD patterns of the synthesized powders. Metallic Sn is obtained by simple precipitation (0.0 kV) (a). Sn powders obtained by EHDA coupled to RP at 2.0 kV (b) and at 9.0 kV (c). The intensities of the spectra are normalized. The characteristic reflections of  $\beta$ -Sn are indicated by an asterisk (\*). No other peaks related to the reductive agent or reaction by-products are detected.

It is evident that the crystallinity of the collected materials is strongly influenced by the applied voltage. The material obtained by simple precipitation (Fig. 3.4a) displays diffraction peaks that match with the characteristic pattern of tetragonal tin,  $\beta$ -Sn, (JCPDS no. 04-0673). On the other hand, the XRD patterns of the powders produced by EHDA coupled to RP (Fig. 3.4b-c) exhibit a pronounced amorphous character, which increases with the applied voltage. Very broad peaks are seen at around  $27^\circ$  and  $53^\circ$  for the samples where EHDA was applied. These broad peaks have been observed earlier for Sn nanoparticles that showed  $\text{SnO}_2$  contamination [22, 23]. Besides, it was reported that the broad peak of weak diffraction observed around  $28^\circ$  is characteristic of SnO-containing glasses and it reflects a statistical distribution of the Sn-Sn distance in the matrix [24]. It is therefore believed, that a kind of oxidation of the tin occurs here as well. This oxidation is certainly not complete in the case of the sample prepared at 2.0 kV, where it is still possible to observe some diffraction peaks of  $\beta$ -Sn. In the case of the sample prepared at 9.0 kV the diffraction peaks of  $\beta$ -Sn have completely disappeared. This means that  $\beta$ -Sn diffracting domains are not detected any longer, but it does not necessarily mean that metallic tin is no longer present. From this preliminary analysis, it is noted that the application of high voltage is effective in decreasing the size of the crystallites of the powders and, at the same time, it favours the formation of an amorphous oxide phase, which coexists with the crystalline form of  $\beta$ -Sn.

The presence of small particles was confirmed by SEM analysis (Fig. 3.5), which shows a cauliflower-like morphology for the materials produced by the precursor atomization. Agglomeration of the particles is pronounced in the powders. The typical size of the individual spherical-like features observed in the image is around 40-50 nanometres.

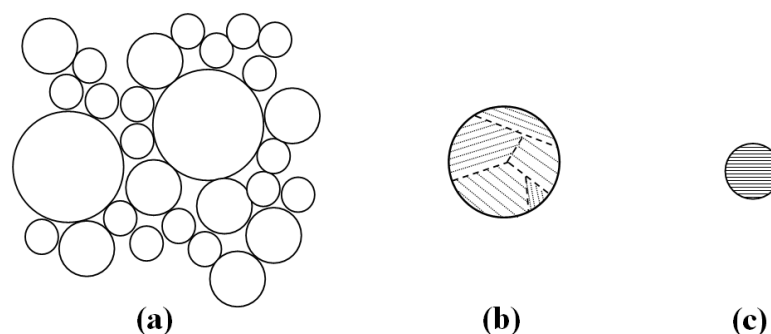


**Fig. 3.5.** SEM image of the typical morphology exhibited by the Sn powders synthesized via EHDA-RP process.

TEM analysis was carried out in order to investigate further the texture and the structure of the synthesized materials. The following definitions are adopted here:



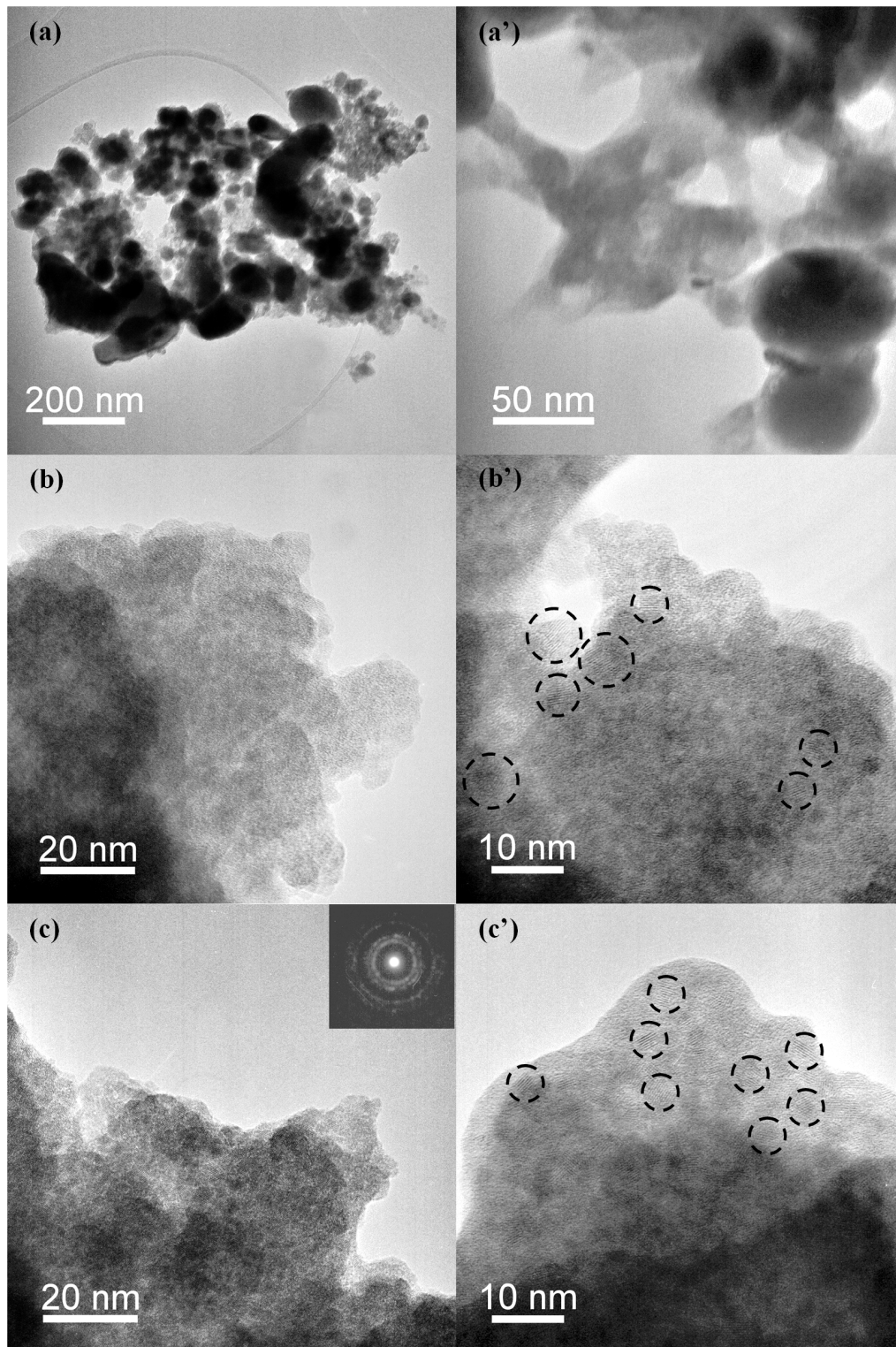
agglomerates are built up from primary particles, which, on their turn, can exhibit crystalline domains (i.e. crystallites), also often referred to as grains. If then the primary particles are in the nano-range they are called primary nanoparticles. In the case these primary nano-particles are single crystallites they are also referred to as “nanocrystals”. Fig. 3.6 presents a schematic drawing for this nomenclature.



**Fig. 3.6.** Drawing for the adopted nomenclature. (a) Agglomerate made up of primary particles; (b) primary particle containing different crystallites (grains); (c) primary particle consisting of one single crystallite, also referred to as “nanocrystal”.

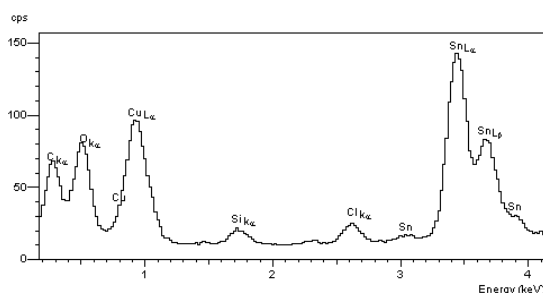
Fig. 3.7 depicts some TEM images of the agglomerated particles synthesized with different voltages. Fig. 3.7a-a' present two images with different magnifications of the powders produced by RP only. It can be observed that the particles resulting from this process are not monodisperse in size. Primary particles with inhomogeneous distribution are present and their minimal size is typically around 50 nm. On the other hand, the primary particles formed by EHDA coupled to RP are homogeneously-sized, as it can be noticed from the other images of Fig. 3.7. The powders synthesized with 2.0 and 9.0 kV exhibit a fluffy morphology (Fig. 3.7b-c) and their constitutive units display sizes below 10 nm. With higher magnification small nanocrystals are clearly seen in the micrographs (Fig. 3.7b'-c'). The Sn powders consist in both cases of agglomerated nanocrystals randomly oriented in an amorphous matrix. The inset in Fig. 3.7c represents the Selected Area Electron Diffraction (SAED) pattern of the sample synthesized with 9.0 kV. The observed diffraction rings confirmed the presence of the nanocrystalline Sn phase, which could not be inferred from the XRD spectrum (Fig. 3.4c), due to enhanced amorphization of the material and the simultaneous broadening of the line profiles, as a result of the reduced size of the crystallites.

Decreasing the size of the primary particles implies also an increase in the ratio of their surface atoms to bulk atoms. Consequently, the resulting primary nanoparticles are much more reactive than their micron-sized counterparts and they readily form surface oxides in contact with air. Indeed, it is reasonable to think that the observed amorphization of the powders is related to the formation of amorphous  $\text{SnO}_x$  ( $0 < x \leq 2$ ) during the collection of the produced materials.



**Fig. 3.7.** TEM micrographs of Sn powders produced with different voltages. RP of the tin precursor (0.0 kV) (a-a'). EHDA coupled to RP at 2.0 kV (b-b') and at 9.0 kV (c-c'). Nanocrystals are indicated by dotted circles. The inset in (c) of is a SAED showing the presence of crystalline tin.

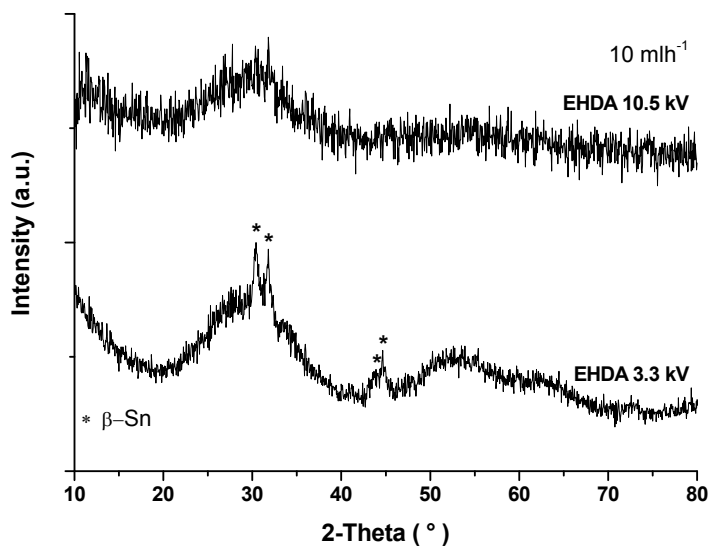
In that respect, it has been found that Sn metallic nanoparticles undergo a reaction forming a SnO<sub>2</sub>-like phase by air exposure [22] and, similarly, thin Sn films can be completely oxidized to SnO<sub>2</sub> at temperatures as low as 200 °C [25]. Elemental analysis was carried out by Energy Dispersive Spectroscopy (EDS) on the as-produced samples in order to evaluate the oxygen content for the particles just taken out from the suspension before centrifugation and washing (Fig. 3.8).



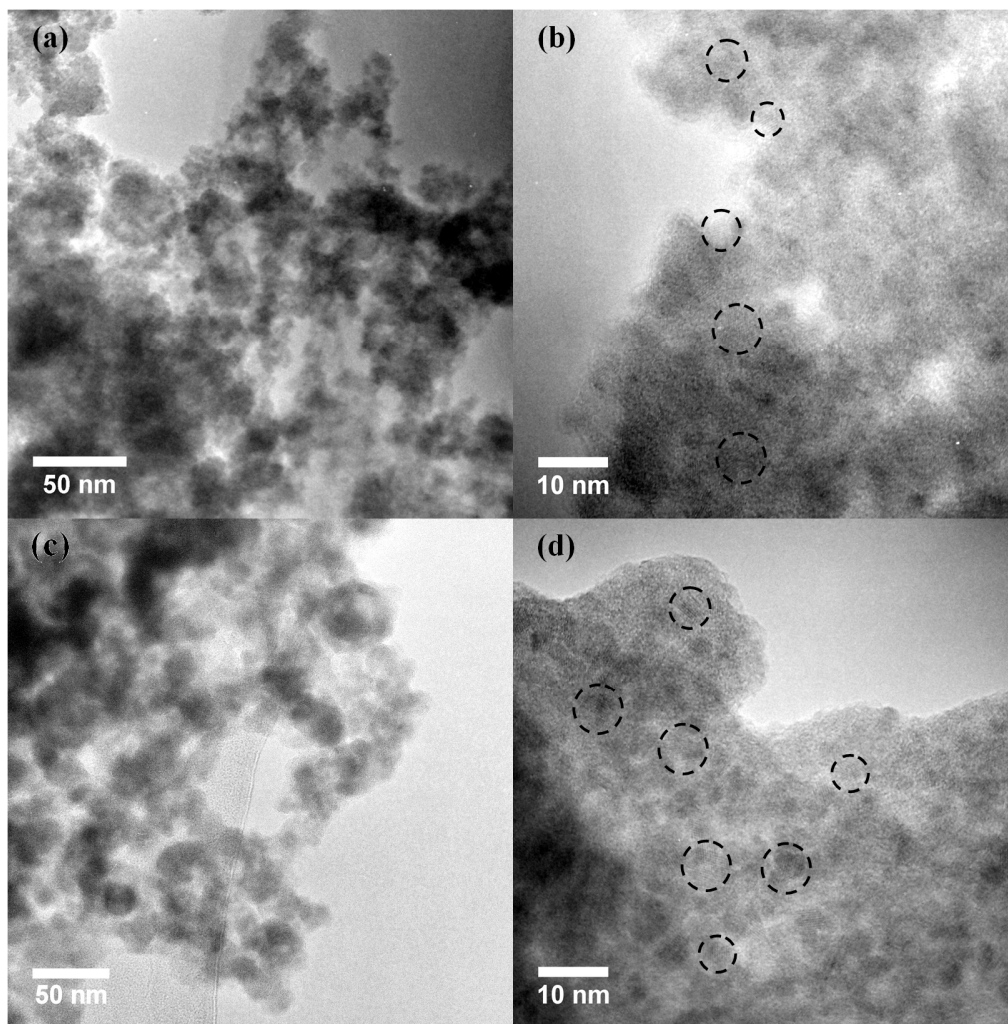
**Fig. 3.8.** Typical EDS spectrum for the as-produced samples. The other elements are due to sample preparation, reaction by-products and copper grid of the sample holder.

From the signals of the oxygen K-edge and the tin L-edge, an atomic ratio for Sn:O of about 1:2 has been estimated. This result matches well with previous observations of enhanced reactivity, indicating that even brief exposure to air leads to rapid oxidation of the materials.

Finally, a higher injection flow rate of 10 mlh<sup>-1</sup> was used in order to enhance the production rate via the EHDA-assisted process. In this case, almost 120 mg of pure Sn can be hypothetically precipitated in one hour according to the chemical reaction in eq. (3.1) and the concentration adopted for the precursor solution. It should be further mentioned that all the experimental parameters involved in the atomization process are interdependent. Therefore, a variation of one of the parameters generally affects the other ones. In the present case, a higher value for the flow rate, while keeping the other parameters unchanged, required a higher voltage in order to achieve the cone-jet mode. It was found that a minimum voltage of about 3.3 kV was needed. Interestingly, it was also possible to obtain a multi-jet mode by further increasing the applied voltage up to 10.5 kV. It should be noted, however, that under such conditions of high flow rate, intense electric field and elevated charging of the droplets electrical discharges (i.e. corona discharge) can occur, leading to generation of sparks in the surrounding air, which could be a safety issue. XRD and TEM analysis were also performed on these samples. The XRD patterns shown in Fig. 3.9 do not differ much from those obtained at 2.0 kV and 9.0 kV (viz. Fig. 3.4b-c). Hence, here too, an amorphous and a crystalline phase coexist. TEM images, as shown in Fig. 3.10, confirmed the XRD results of the coexisting phases.



**Fig. 3.9.** XRD spectrum of Sn powders produced with a flow-rate of  $10 \text{ mlh}^{-1}$ .



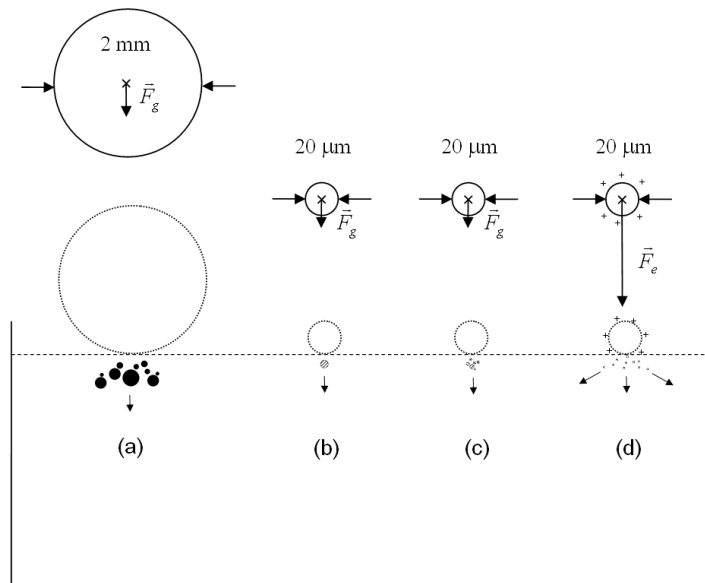
**Fig. 3.10.** TEM micrographs at different magnifications of Sn powders produced by EHDA coupled to RP with a flow rate of  $10 \text{ mlh}^{-1}$  at 3.3 kV (a)-(b), and at 10.5 kV (c)-(d).

Sn nanocrystals (dotted circles in Fig. 3.10b-d) are surrounded by an amorphous-like phase and an overall fluffy appearance is observed for the powders (Fig. 3.10a-c).

Apparently in this case, the flow rate does not seem to have a strong influence on the morphology and the composition of the materials, as long as a stable cone-jet mode or multi-jet mode can be maintained by properly adjusting the applied voltage. Therefore, even under this higher flow-rate regime, EHDA coupled to reductive precipitation allows the production of nanostructured powders, which display characteristics similar to those previously discussed.

Hence, under the experimental conditions given, by comparing the average droplet diameter with the size of the constitutive units of the powders, it appears that the formation of the primary particles is dominated by the chemical reaction of the precursor ions released by the charged micrometric droplets entering the reductive bath. Accepting a single precursor droplet with an average diameter of 13  $\mu\text{m}$  (see table 3.2), neglecting droplet fission, and assuming that the concentration of the dissolved salt remains constant at the onset of spraying (i.e. no solvent has been evaporated on the jet, due to the saturated vapours of the beaker), then its volume contains approximately  $1.2 \cdot 10^{-13}$  moles of  $\text{SnCl}_2$ . All the  $\text{Sn}^{2+}$  ions contained in the charged droplet can be reduced when entering the reductive bath. If the ions contained in a single droplet were to be reduced all together, in order to form ideally a single crystalline particle, a volume of almost  $2 \cdot 10^{-12} \text{ cm}^3$  would be found, on the basis of the molar volume of Sn (i.e.  $16.36 \text{ cm}^3 \text{ mol}^{-1}$ ). This volume corresponds roughly to a 'bulk' particle with a radius of almost 1  $\mu\text{m}$ , which can be taken as the maximum volume originated from such ideal process. However, the  $\text{Sn}^{2+}$  ions, are homogeneously dissolved inside a macroscopic, uncharged droplet. They are surrounded by counter ions, which are also determining the overall reaction rate. Dripping of a single macroscopic precursor droplet in the reductive bath causes in reality the formation of several microscopic particles which tend to agglomerate in the absence of stabilizing/capping agents, in order to minimize their overall exposed surface. Likewise, the generation of several nanoparticles from a micrometric precursor droplet can occur when it impinges on the surface of the reductive bath. Moreover, the charged electro sprayed droplets are further accelerated by the electric field, when compared to those resulting from a regular 'drop-wise' addition. The electrical forces are ruling out the droplet motion into the reductive bath and are also responsible for the accumulation of positive ions (i.e.  $\text{Sn}^{2+}$ ) on their surface, producing a local gradient in their concentration. These ions repel each other, causing an outward electrostatic pressure, which opposes the inward pressure due to the droplet surface tension. Such equilibrium is instable and the tendency of these micrometric droplets is to release their surface charge excess at the interface with the grounded reductive bath. In this respect, the surface charge is probably responsible for a quick dispersion and reaction of the precursor species in the reductive bath,

which could account for the monodispersity of the nanocrystals in the agglomerated powders. A schematic drawing is shown in Fig. 3.11, which summarizes the discussed scenarios for the droplets at the interface with the reductive bath and the formation of precipitated particles.



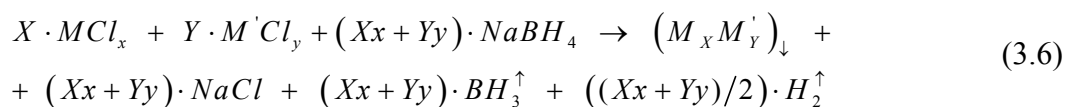
**Fig. 3.11.** Schematic drawing of possible scenarios for the reduction of precursor droplets at the interface with the reductive bath. (a) Macroscopic, uncharged droplet generating microscopic particles which tend to agglomerate; (b) micrometric, uncharged droplet generating an ideal single, crystalline (sub)-micrometric particle; (c) micrometric uncharged droplet generating nanoparticles which tend to agglomerate; (d) micrometric, charged droplet generating nanoparticles which tend to disperse.

Controlling the concentration of the precursor species, as well as their injection flow rate, represents the first step for tailoring the average diameter of the electro-sprayed droplets, as well as the maximum amount of precursor that can locally react to form smaller particles. Then, the surface charge excess on the droplets, as well as their acceleration due to the electric field can further influence their subsequent reactions and facilitate the dispersion of the as-formed particles.

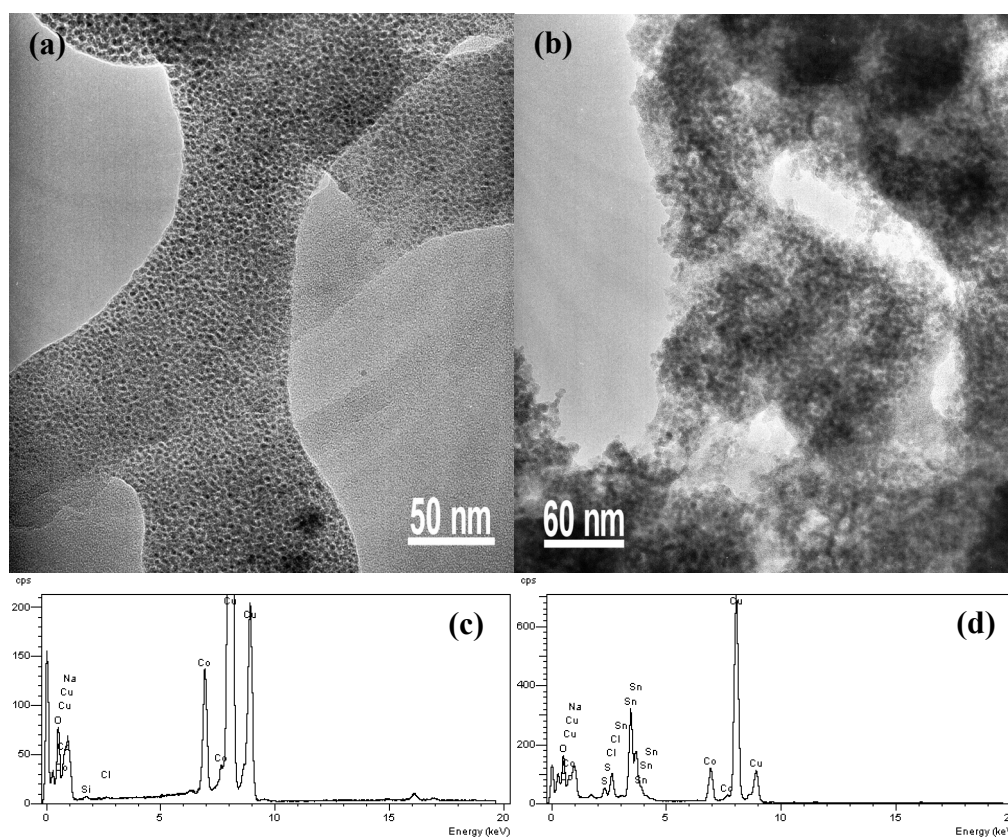
### 3.4 Investigation of other as-formed particles

Other metallic and metallic-like particles were produced by the same approach, using different precursors and solvents. Namely,  $\text{CoCl}_2$  (Aldrich) 0.1 M in IPA (J.T. Baker) and  $\text{CoCl}_2$  and  $\text{SnCl}_2 \cdot 2\text{H}_2\text{O}$  (0.05 M : 0.1 M) in di-methyl sulfoxide (DMSO - Acros), in order to produce particles with a Co-Sn composition (i.e.  $\text{CoSn}_2$  compound). Reductive baths with  $\text{NaBH}_4$  were prepared in the respective solvents, according to

the described preparation. The general reaction to form different metallic compositions is:



Where M and M' refer to the precursor metal ions. For CoSn<sub>2</sub>, note that  $x=2$ ,  $y=2$ ,  $X=1$ , and  $Y=2$ . An injection flow rate of 1.5 mlh<sup>-1</sup> was employed in both cases. Atomization of the precursors was performed at 9.0 kV in multi-jet mode. The process was carried out in a similar way to that described previously. The as-formed particles were investigated before centrifugation and washing by TEM and EDS.



**Fig. 3.12.** TEM micrograph of as-produced Co particles (a) and relative EDS spectrum (c). TEM image of as-formed particles with Co-Sn composition (b) and EDS spectrum (d). The intense Cu lines are due to the copper grid of the sample holder.

Irrespective of the difference in the solvents and the concentrations of the precursors, the as-formed particles with Co and Co-Sn compositions displayed similar characteristics, as shown in Fig. 3.12a and 3.12b. In Fig. 3.12a it is seen that small spherical primary particles with size of 2-5 nm were formed. The produced materials are amorphous and nanocrystals are not observed. Despite their agglomeration, the

single Co particles appear clearly separated from each other, as if embedded in a sort of 'matrix'. Their local composition was investigated by EDS (Fig. 3.12c), which indicated also in this case the presence of oxygen and other by-products.

Similarly, in Fig. 3.12b it can be observed that agglomerates of spherical particles are produced for the Co-Sn composition. The primary particles have sizes clearly below 10 nm and they are amorphous. The elemental analysis presented in Fig. 3.12d shows peaks for Co and Sn and their integrated signals are roughly in accordance with the stoichiometry expected for  $\text{CoSn}_2$ . Nevertheless, it cannot be excluded that the stoichiometry may vary throughout the sample, so as to form locally different compositions. Also in this case the presence of oxygen indicates the enhanced reactivity of the materials.

Coupling EHDA with RP proved a viable method to directly produce metallic and metallic-like nanoparticles in liquids. However, the quick oxidation and the surface contamination of the produced particles have to be taken into account. These issues represent the main obstacles for the collection and further manipulation of pure materials.

### 3.5 Conclusions

The method discussed so far represents a novel aerosol-assisted route for the synthesis of nanostructured powders in liquids. Electrohydrodynamic Atomization (EHDA) in the cone-jet and multi-jet mode has been successfully coupled to reductive precipitation by  $\text{NaBH}_4$ . In this way small metallic and metallic-like particles with different compositions have been generated. Application of EHDA proved very effective in reducing the size of the primary particles, which exhibited in all the circumstances an enhanced reactivity towards oxygen.

Although the experiments were carried out in air and the amount of the collected powders was initially rather limited, the results suggest that the technique has a potential for a larger production of various nanostructured materials with different characteristics and textures. The process requires the use of inert gas atmosphere and suitable solvents whenever the produced particles are prone to react immediately with oxygen or moisture. The synthesis can be extended to various types of nanoparticles by using different precursors, reductive agents and eventually stabilizers. The production rate, in principle, does not represent an issue, since the flow rates can be further enhanced by employing multiplexed-nozzle systems for a parallel atomization of the precursors. Finally, providing a constant flow for the reductive bath and an in-line separation unit for the solid particles would enable the development of a continuous production process.



### 3.6 References

- [1] J. Maier, *Nature Materials* **2005**, *4*, 805.
- [2] A. Stella, M. Nisoli, S. De Silvestri, O. Svelto, G. Lanzani, P. Cheyssac, R. Kofman, *Physical Review B - Condensed Matter and Materials Physics* **1996**, *53*, 15497.
- [3] C. T. Campbell, *Science* **2004**, *306*, 234.
- [4] S. A. Maier, M. L. Brongersma, P. G. Kik, S. Meltzer, A. A. G. Requicha, H. A. Atwater, *Advanced Materials* **2001**, *13*, 1501.
- [5] R. A. Huggins, *Journal of Power Sources* **1999**, *81-82*, 13.
- [6] J. Turkevich, P. C. Stevenson, J. Hillier, *Discussions of the Faraday Society* **1951**, *11*, 55.
- [7] O. Mao, R. A. Dunlap, I. A. Courtney, J. R. Dahn, *Journal of the Electrochemical Society* **1998**, *145*, 4195.
- [8] M. T. Reetz, W. Helbig, *Journal of the American Chemical Society* **1994**, *116*, 7401.
- [9] J. Van Erven, R. Moerman, J. C. M. Marijnissen, *Aerosol Science and Technology* **2005**, *39*, 941.
- [10] I. Hayati, A. I. Bailey, T. Tadros, *Nature* **1986**, *319*, 41.
- [11] U. Stachewicz, J. F. Dijkstra, C. U. Yurteri, J. C. M. Marijnissen, *Applied Physics Letters* **2007**, *91*.
- [12] H. I. Schlesinger, H. C. Brown, A. E. Finholt, J. R. Gilbreath, H. R. Hoekstra, E. K. Hyde, *Journal of the American Chemical Society* **1953**, *75*, 215.
- [13] L. Zhang, A. Manthiram, *Journal of Materials Chemistry* **1996**, *6*, 999.
- [14] J. Yang, M. Wachtler, M. Winter, J. O. Besenhard, *Electrochemical and Solid-State Letters* **1999**, *2*, 161.
- [15] M. Wachtler, M. Winter, J. O. Besenhard, *Journal of Power Sources* **2002**, *105*, 151.
- [16] Y. Wang, J. Y. Lee, T. C. Deivaraj, *Journal of the Electrochemical Society* **2004**, *151*.
- [17] G. I. Taylor, *Proc.R.Soc.London, Ser.A* **1964**, *280*, 383.
- [18] A. Jaworek, A. Krupa, *Journal of Aerosol Science* **1999**, *30*, 873.
- [19] A. M. Ganan Calvo, J. Davila, A. Barrero, *Journal of Aerosol Science* **1997**, *28*, 249.
- [20] R. P. A. Hartman, D. J. Brunner, D. M. A. Camelot, J. C. M. Marijnissen, B. Scarlett, *Journal of Aerosol Science* **1999**, *30*, 823.
- [21] R. P. A. Hartman, D. J. Brunner, D. M. A. Camelot, J. C. M. Marijnissen, B. Scarlett, *Journal of Aerosol Science* **2000**, *31*, 65.
- [22] M. Noh, Y. Kim, M. G. Kim, H. Lee, H. Kim, Y. Kwon, Y. Lee, J. Cho, *Chemistry of Materials* **2005**, *17*, 3320.

- [23] C. S. Yang, Q. Liu, S. M. Kauzlarich, B. Philips, *Chemistry of Materials* **2000**, *12*, 983.
- [24] Y. Idota, T. Kubota, A. Matsufuji, Y. Maekawa, T. Miyasaka, *Science* **1997**, *276*, 1395.
- [25] E. P. Domashevskaya, S. V. Ryabtsev, Y. Yurakov, O. A. Chuvenkova, V. M. Kashkarov, S. Y. Turishchev, S. B. Kushev, A. N. Lukin, *Thin Solid Films* **2007**, *515*, 6350.

# Chapter 4

## Nanostructured Sn/SnO<sub>x</sub> powders for negative electrodes

*The trouble with our times is that  
the future is not what it used to be.  
(Paul Valery)*

This chapter discusses the use of Sn-based materials as negative electrodes for Li-ion batteries. The electrochemical performances of nanostructured Sn/SnO<sub>x</sub> powders obtained via Electrostatic Spray Reductive Precipitation are compared to those of commercial Sn-based materials having different compositions and size. The influence of the particle size, as well as the issues connected to the surface area of the nanostructured powders and their effective dispersion in the coated electrodes are addressed.

## 4.1 Introduction

Sn and Sn-based composites are interesting materials for advanced Li-ion battery negative electrodes. The reversible reaction of metallic Sn with Li yields gravimetric capacities as high as 993 mAhg<sup>-1</sup>, which outperform commercial electrodes based on carbonaceous materials (i.e. 372 mAhg<sup>-1</sup> for graphite). Moreover, the formation of lithium-tin alloys is associated with electrochemical potentials versus Li/Li<sup>+</sup> that are considerably higher than that of lithiated graphite [1, 2]. This difference in potentials is favourable for practical purposes, since it improves the safety of the host, which is less prone to undergo deposition of metallic lithium [3].

Although these attractive features have initiated a number of studies on Sn-based hosts [1-8] as alternative negative electrodes for Li cells, a major drawback has hindered their use for practical applications in rechargeable Li-ion batteries. A severe volume change of the host material (i.e. up to about 250% with respect to the unstrained β-Sn lattice) during uptake and removal of Li ions is responsible for extended cracking and pulverization of these electrodes upon repeated cycling. In particular, bulk and coarse-grained Sn materials undergo loss of electrical contact with the current collector after few cycles, leading to early failure of the cell [9]. In this respect, the use of Sn-based nanoparticles and nanocomposites offers an effective way to enhance the mechanical stability of these materials upon prolonged cycling. On the one hand, employing reactive phases finely dispersed in less-active or inert phases - as in multiphases or composite electrodes - has the beneficial effect of buffering the volume changes during electrochemical cycling, and alleviating the stresses arising from this process [5]. On the other hand, reducing the size of the host particles results in a better acceptance of the induced local strain and it also favours the reaction kinetics, due to shorter migration lengths for lithium.

Nevertheless, decreasing the size of the primary particles to few nanometres, while retaining a homogeneous size distribution, still seems to be a crucial issue for most of the synthesis methods applied so far. For example, high-energy ball milling and reductive precipitation are easy techniques that have been extensively employed for the synthesis of metallic, intermetallic and alloyed Sn fine powders [9-13]. These methods have advantages and drawbacks that are characteristic for the type of the approach used (i.e. top-down vs. bottom-up) and for the environment in which the process is carried out (i.e. dry vs. wet).

Reductive precipitation of Sn chlorides by NaBH<sub>4</sub> constitutes an interesting alternative to mechanic-milling, since its bottom-up approach should provide an easier route to nano-particles formation. Despite that, in most of the cases, small nanoparticles with homogeneous size distribution cannot be directly achieved via this simple reduction process [13, 14]. Therefore, the use of suitable surfactants or capping agents during the synthesis becomes a prerequisite [14].

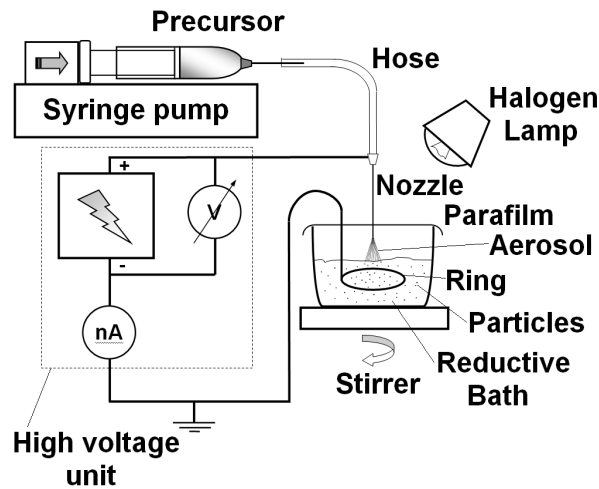
An advanced method to carry out reductive precipitation of metal chlorides by  $\text{NaBH}_4$  has been discussed in the previous chapter. The concept underlying this technique is the use of an electrospray for atomizing the liquid precursors in the form of charged aerosols. Electro spraying, which is also more precisely referred to as Electrohydrodynamic Atomization (EHDA), is a powerful technique which uses high electric fields for dispersing liquids. Nowadays this method is being increasingly applied to modern materials technologies and to nanotechnology [15-18]. Herein, electrospray provides a top-down approach, through which the size of the droplets containing the metal precursors can be typically reduced to few tens of microns or less, prior to their contact with the reductive agent. In this way, a discontinuous dripping of the liquid (i.e. drop-wise addition) can be easily converted into a continuous flow of highly charged droplets or micro-jets, in order to achieve a higher dispersion into the reductive bath.

The atomization of the precursors allowed the production of finely-dispersed materials and Sn nanostructured powders were obtained by coupling EHDA to Reductive Precipitation of Sn(II) chloride. This process is hereafter referred to as Electrostatic Spray Reductive Precipitation (ESRP) for simplicity.

The electrochemical behaviour of the synthesized materials has been tested in coin cells versus metallic Li. Their cycling performances have been compared to those of micrometric commercial Sn powders, which are taken here as reference. Since the produced nanopowders have undergone air exposure and consequently oxidation, other commercial Sn-based powders with different mesh size and compositions (i.e. oxygen content) have been considered for electrochemical comparison as well, e.g. SnO and  $\text{SnO}_2$ . In particular, the electrochemical analysis of these commercial samples is reported at the end of this chapter.

## 4.2 Experimental

Tin nanoparticles were synthesized by electro spraying a Sn precursor (0.1 M solution of  $\text{SnCl}_2 \cdot 2\text{H}_2\text{O}$  in isopropyl alcohol – IPA) into a reductive bath, where  $\text{NaBH}_4$  was used as reductive agent in IPA. The physical properties of the precursor solution, the details about the preparation and the reaction were mentioned in the previous chapter. The precursor solution was pumped at a constant flow rate of  $3.5 \text{ mlh}^{-1}$  through an electrified capillary. Different voltages, i.e.  $\sim 3\text{kV}$  and  $\sim 9\text{kV}$ , were applied between a stainless steel nozzle (EFD ultra, i.d.  $250 \mu\text{m}$ ) and a ring made of Sn soldering wire, which was dipped in the reductive bath, in order to achieve EHDA in the so-called “cone-jet” and “multi-jet” modes, respectively [19]. A schematic drawing of the experimental setup is depicted in Fig. 4.1.



**Fig. 4.1.** Schematic drawing of the equipment for Electrostatic Spray Reductive Precipitation.

Powder production and collection were carried out in air at room temperature (RT) following the procedure described previously. Definitions of particles and agglomerates that constitute the powders are given in the previous chapter as well. Different techniques were employed to investigate the crystallinity, the morphology and the structure of the produced powders. In that regard, X-Rays Diffraction (XRD) was performed on a Bruker (AXS D8 Advance) X-ray diffractometer with a Cu-K<sub>α</sub> radiation source ( $\lambda = 1.5418 \text{ \AA}$ ) between 10° and 85°. Transmission Electron Microscopy (TEM) and Scanning Electron Microscopy (SEM) were carried out on a Philips CM30T Transmission Electron Microscope operated at 300 kV and a Philips XL20 Scanning Electron Microscope, respectively. Further imaging of the produced materials was carried out via Atomic Force Microscopy (AFM) on a NT-MDT NTEGRA Scanning Probe Microscope in semi-contact mode, using a micro-fabricated Si cantilever and tip (NT-MDT, Silicon: NSG 03).

Sn-based commercial materials employed for comparison were purchased from Aldrich. In particular, Tin powders -325 mesh (i.e. 44  $\mu\text{m}$ ) were taken as reference. Tin nanosized activated powders, tin(II) oxide (10  $\mu\text{m}$ ), tin(IV) oxide -325 mesh (i.e. 44  $\mu\text{m}$ ) and Tin(IV) oxide nanopowders were also tested electrochemically. Table 4.1 lists the investigated samples.

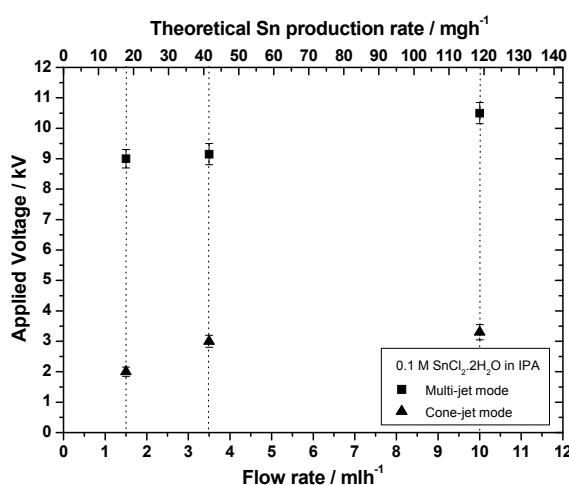
**Table 4.1.** Overview of the samples

ESRP	Sn/SnO <sub>x</sub> ~3 kV Sn/SnO <sub>x</sub> ~9 kV
Commercial	Sn -325 mesh (44 $\mu\text{m}$ ) Sn 'nano'
	SnO (10 $\mu\text{m}$ )
	SnO <sub>2</sub> -325 mesh (44 $\mu\text{m}$ ) SnO <sub>2</sub> 'nano'

Electrochemical measurements were performed on CR2320-type coin cells assembled in a He-filled glove box. Composite electrodes were prepared by casting a slurry of dry active powders with Carbon Black (CB) and Polyvinylidene Fluoride (PVdF) in a 3:1:1 weight ratio in N-Methylpyrrolidone (NMP) onto a thin copper foil (Akashi – 0.018 mm), followed by drying in a convection oven around 100°. Before usage, the electrodes were roller-pressed and circular disks of 14 mm diameter were punched out and weighed. The coated electrodes were dried under vacuum before assembling in coin cells, having metallic lithium as reference and counter electrode and a 1 M LiPF<sub>6</sub> solution in EC:DMC (2:1 by wt.) as electrolyte. The cells were discharged and charged in different voltage ranges versus Li/Li<sup>+</sup>. In order to avoid any confusion, discharge is here defined as Li uptake by the host Sn-based material, while charge refers to the Li release by the reacted intermetallic/alloy. It is also worth noting that when a Sn-based material is used in a Li-ion battery assembly it acts as the negative electrode rather than the positive, as it is the case here. Galvanostatic tests were performed with a Maccor (S-4000) cyler at a constant gravimetric current density of 113 mA g<sup>-1</sup>. The final tests were performed with the same current density, apart from their first cycle, which was carried out at a lower current density of 23 mA g<sup>-1</sup>.

### 4.3 Results and discussion

The used flow rate of 3.5 mlh<sup>-1</sup> for the SnCl<sub>2</sub> precursor enabled a reasonable production rate for the precipitated materials (i.e. ideally ≈ 40 mg h<sup>-1</sup>), based on the reaction reported in eq. (3.1). Fig. 4.2 shows a comparison of the flow rates employed so far, together with the required voltages for atomization and the theoretical Sn production rates (see chapter 3).

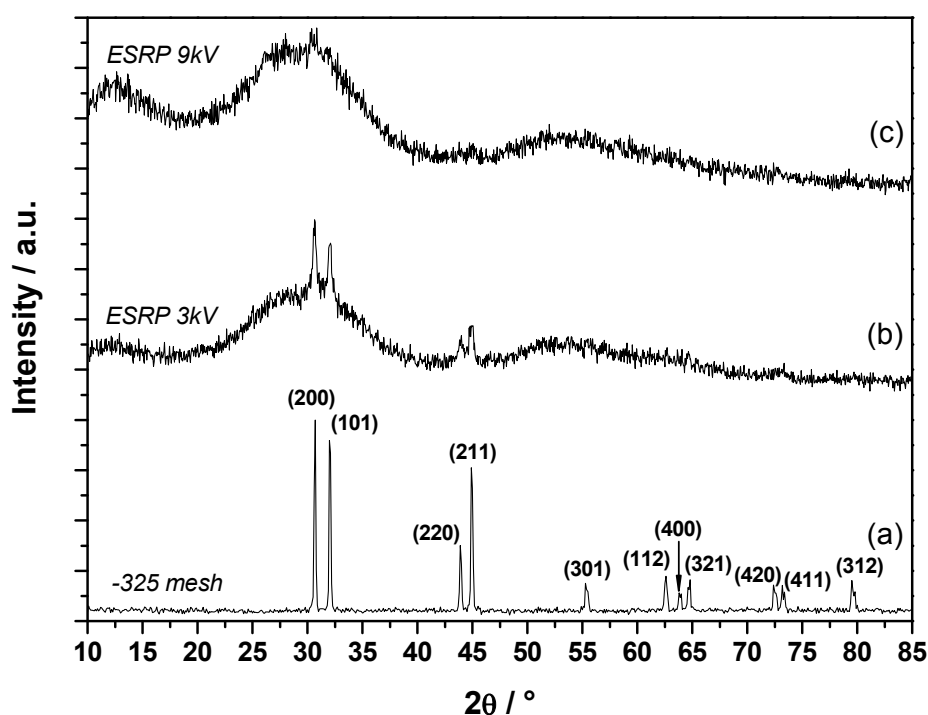


**Fig. 4.2.** Applied voltage required for the atomization of the SnCl<sub>2</sub> precursor pumped at different flow rates. The theoretical production rate is calculated on the basis of the chemical reaction of eq. (3.1).

The flow rate of 3.5 mlh<sup>-1</sup> was employed here because it constituted a tradeoff between the feeding of the species and the applied voltage, enabling the synthesis and the collection of an adequate amount of powders for the preparation of coated electrodes.

### 4.3.1 Structure characterization

The materials produced in this way via ESRP were analysed by XRD. The results are shown in Fig. 4.3, where micrometric Sn powders (Aldrich, -325 mesh) are included as reference material.



**Fig. 4.3.** XRD patterns of the materials obtained via ESRP with different voltages (a)-(b) and micrometric commercial Sn powders (c). The intensities of the spectra are normalized. The characteristic diffractions peaks of  $\beta$ -Sn are indexed.

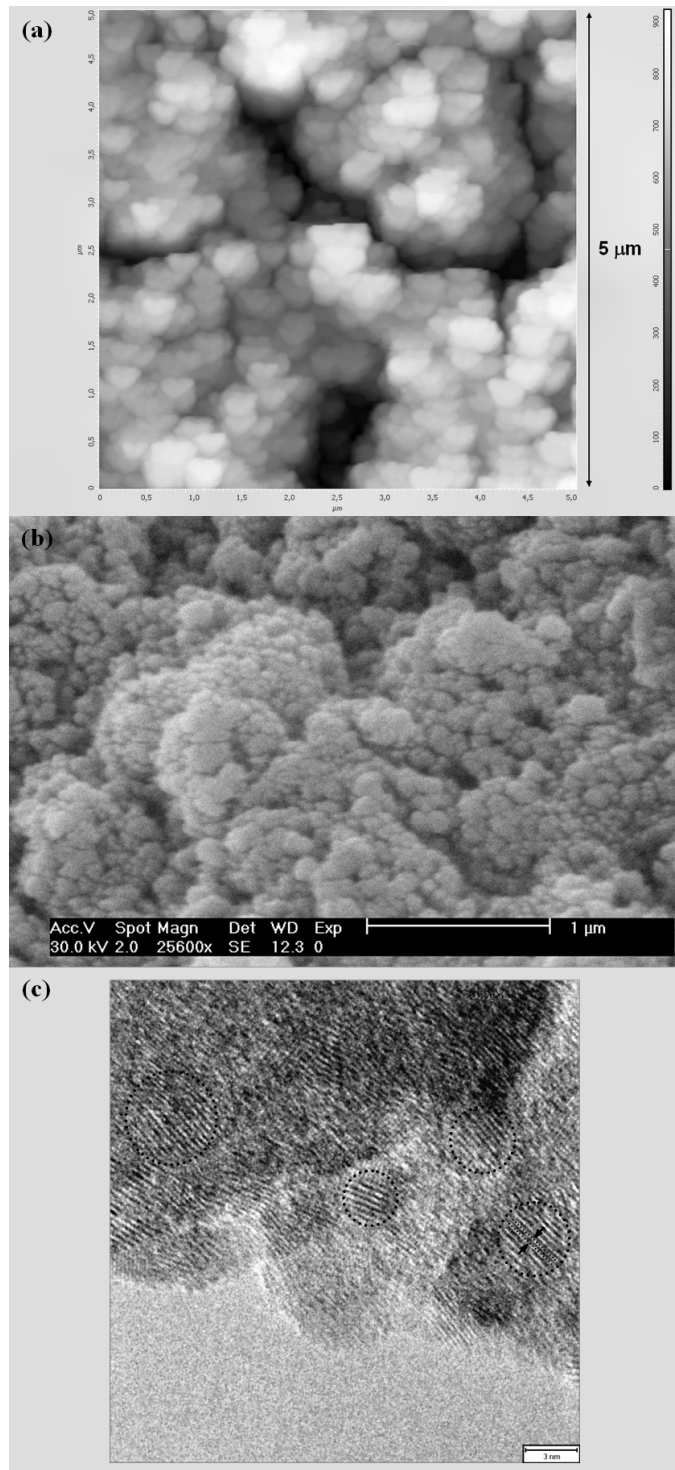
Employing a high voltage has a clear influence on the diffraction pattern of the produced materials. The applied electric field is effective in reducing the size of the materials, as indicated by an increased broadening of the characteristic diffraction peaks when compared to those of the commercial powders. In particular, the most intense peaks in Fig. 4.3b match with the characteristic reflections of the  $\beta$ -Sn lattice structure (JCPDS No. 04-0673). No crystalline impurities related to reaction by-products or to crystalline tin oxides are detected for the produced powders. However, both of them show broad peaks around  $\sim 27^\circ$  and  $\sim 53^\circ$  in their diffraction patterns.



This feature becomes more pronounced with increasing the applied voltage, with a simultaneous vanishing of the sharp characteristic peaks. These broad diffractions are associated with SnO<sub>2</sub> contamination of the nanoparticles [20]. Reducing the size of the particles implies an enhanced surface reactivity, and it is not surprising that the materials have undergone oxidation during collection and manipulation. Interestingly, a similar diffraction pattern is displayed by composite Sn-based amorphous oxides [6, 21] and the broad weak diffraction around 28° has been related to a distribution of Sn-Sn atomic distances in a glass matrix. [6]. From these results, it can be concluded that increasing the voltage for the atomization, for a fixed flow rate, results in a higher tendency for oxidation and amorphization for the collected materials. Here, a nanocomposite material is expected, in which a crystalline tin phase is coexisting with an amorphous oxidic phase, as suggested by Fig. 4.3b. A slight decrease in the average size of the crystallites can also contribute to the observed pattern of Fig. 4.3c. Indeed, the most intense diffraction peaks associated to the Sn (200) and (101) planes have practically vanished in this spectrum. However, this fact alone does not imply the absence of the Sn crystallites. Even a small reduction in their average size implies a larger contribution by the surrounding amorphous part, which is responsible for the observed diffraction pattern.

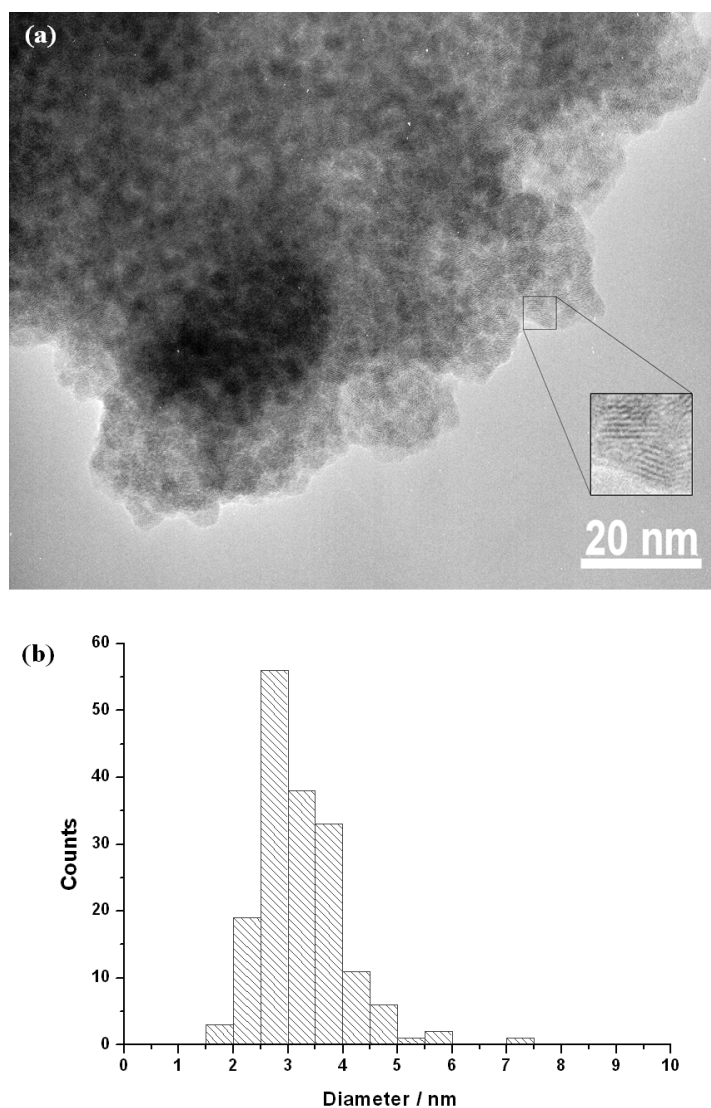
Conversely, powders produced via reductive precipitation by NaBH<sub>4</sub> show generally large surface areas, which cause easier contamination by oxidic and hydroxylic impurities [13]. Typical morphologies for the materials resulting from ESRP confirm that extended surface areas are expected for these products, and that they can play a key role in their electrochemical behaviour.

Fig. 4.4 presents the typical morphology observed for the materials synthesized via ESRP at ~3 kV, monitored by AFM, SEM and TEM. From the pictures of Fig. 4.4a-b it is seen that the powders are composed of continuous interconnections between the agglomerated particles. An overall fluffy morphology is observed for the exposed surface of the materials, and no big bulky particles are detected. From the SEM micrograph (Fig. 4.4b) it is also noted that the agglomerates have a rounded shape and their typical size is tens of nanometres. These agglomerates, on their turn, are further divided into crystalline domains with different sizes, surrounded by an amorphous phase, as it is shown by the TEM micrograph in Fig. 4.4c (dotted circles). In particular, the number of lattice fringes observed for the single crystallites is typically about 8–15. The spacing between the fringes is approximately 2.8 – 3.0 Å, matching with the typical crystallographic orientations (200) and (101) for the lattice of β-Sn ( $d_{200} = 2.915 \text{ \AA}$ ,  $d_{101} = 2.793 \text{ \AA}$ ).



**Fig. 4.4.** Typical morphology for Sn powders synthesized via ESRP at ~3 kV. AFM scan (5x5 μm) (a) and SEM micrograph (b). Au was sputtered onto the sample to allow clearer SEM imaging. TEM micrograph at high magnification showing the inner structure of the agglomerates (c). Note that the scale bar in the inset is 3 nm.

The typical structure of the materials obtained via ESRP at  $\sim 9$  kV is presented in Fig. 4.5. From Fig. 4.5a-b it is observed that the primary particles have sizes well below 10 nm. They are spherically-shaped and show a homogeneous distribution, with an average size of about 3 nm. Crystalline domains are observed throughout the image. In the magnified inset of the picture, a few Sn nanocrystals are clearly seen embedded in an amorphous-like structure.



**Fig. 4.5.** TEM micrograph of the powders produced via ESRP at  $\sim 9$  kV (a). Size distribution for 170 measured particles (b).

Approximately 6–8 lattice fringes appear distinct in the magnified detail. Comparing this outcome with the XRD pattern of Fig. 4.3c, it can be concluded that the primary particles are made up of one crystalline domain (i.e. a single crystallite, referred to as a nanocrystal). Hence, the presence of very small crystallites, combined with the amorphous oxide contamination of the particles, is responsible for the broad humps

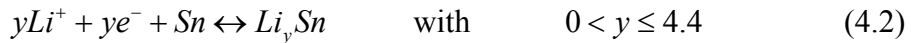
observed in the diffraction pattern. Therefore, this leads to the conclusion that nanocomposite materials are the result of the ESRP process under these experimental conditions. In particular, Sn nanocrystals of few nanometres are surrounded by an amorphous oxide phase (i.e. SnO<sub>x</sub>). As already mentioned, a Sn-based nanocomposite material is expected to enhance the stability during cycling.

### 4.3.2 Electrochemical characterization of SnO<sub>x</sub>/Sn

In a composite SnO<sub>x</sub>/Sn ( $1 \leq x \leq 2$ ) electrode the electrochemical reactions of Li ions with the oxidic phase and metallic tin take place at different potentials during the first discharge, with the initial irreversible formation of Li<sub>2</sub>O, according to the following reaction [22]:



In general, it is known that most of the Li<sub>2</sub>O is formed during the first cycle and that only a negligible amount of it can be recycled in the following cycles as the particle size is in the micrometer-scale range [22]. Hence, the Li<sub>2</sub>O is irreversible in such systems. Then, Sn can reversibly react with Li according to the following reaction:

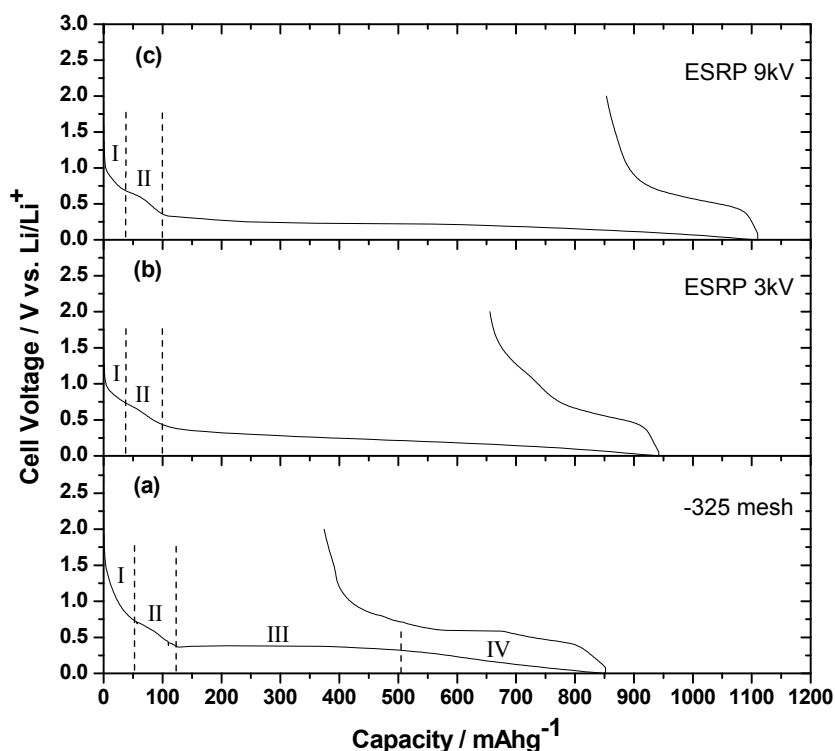


The conversion reaction (4.1) is responsible for the formation of Sn clusters, which agglomerate and grow upon prolonged cycling, leading to loss of capacity [21].

Here Sn nanocrystals are created during the synthesis process, and they are in intimate contact with the Li<sub>2</sub>O phase formed upon the first discharge. The presence of Li<sub>2</sub>O in this case has a negative influence on the reversible capacity, but it can also have some beneficial effects. First of all, it acts as a buffering matrix alleviating the strain related to the volume changes. Secondly, it constitutes a fair ionic conductor, promoting the transport of Li ions to and from the Sn nanocrystals during discharge and charge. Finally, it could also lead to different mechanisms for Li storage, since Sn nanoparticles with size smaller than 10 nm could activate the transformation of Li<sub>2</sub>O into Li<sup>+</sup>, promoting a partial reversibility of the oxide [23]. Moreover, the reversibility of Li<sub>2</sub>O has been demonstrated earlier for transition metal oxides (i.e. M<sub>x</sub>O<sub>y</sub> with M=Co, Fe, Cu, Ni, Ru, etc...) [24-26].

Fig. 4.6 shows the first discharge-charge profiles for the electrodes containing the synthesized materials and the commercial Sn micrometric powders. The commercial powders show a discharge capacity of 852 mAhg<sup>-1</sup>, which corresponds roughly to an uptake of 3.8 Li per unit Sn. The main feature observed in Fig. 4.6a is

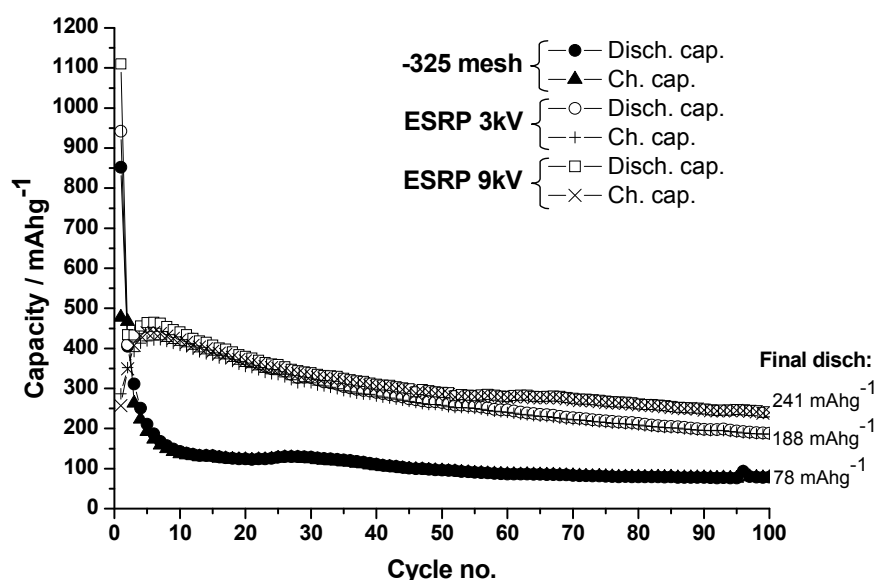
the distinctive potential plateau around 0.4 V (region III) followed by a tail, indicating the formation of the Li-rich Sn alloy (region IV).



**Fig. 4.6.** Voltage profiles for the first cycle of discharge-charge at  $113 \text{ mA g}^{-1}$  between 0.0 and 2.0 V. (a) Commercial powders; (b) powders synthesized at  $\sim 3 \text{ kV}$  and (c)  $\sim 9 \text{ kV}$ . The indicated regions refer to different stages during the discharge. Region I accounts for the initial stage of the discharge process and the early formation of the SEI layer; region II corresponds to the growth of the SEI film and the first lithiation of the host; region III indicates a characteristic plateau associated to the  $\text{Li}_y\text{Sn}$  formation; region IV is associated with the formation of a Li-rich Sn alloy.

A slant part at higher voltages is also observed for all the materials during the early stages of the discharge (region I). No definite plateaus are detected for the produced materials related to the reduction of the oxide (i.e. around 0.9-1.0 V), and the slight bending of the curves can be associated to the growth of the Solid Electrolyte Interphase (SEI) at the initial stage of the lithiation process (region II). It can be also noted that the capacity resulting from this part of the curve is comparable for all the materials. However, the final discharge capacities of (a), (b) and (c) in Fig. 4.6 are clearly different. In the last case the amount of Li stored exceeds the theoretical value expected for the  $\text{Li}_{4.4}\text{Sn}$  alloy, indicating extra storage probably due to surface effects and the amorphous oxide. The reversible capacity of the synthesized materials is negatively influenced by the presence of large surface areas, as it is observed in Fig. 4.6b-c. Indeed, the small size of the particles causes easier surface contamination by impurities. This fact and the observed amorphous oxide around the nanocrystals are

responsible for irreversible trapping of the Li, which becomes electrochemically inactive. Fig. 4.7 presents the evolution of the capacity upon subsequent cycling for the materials considered so far.



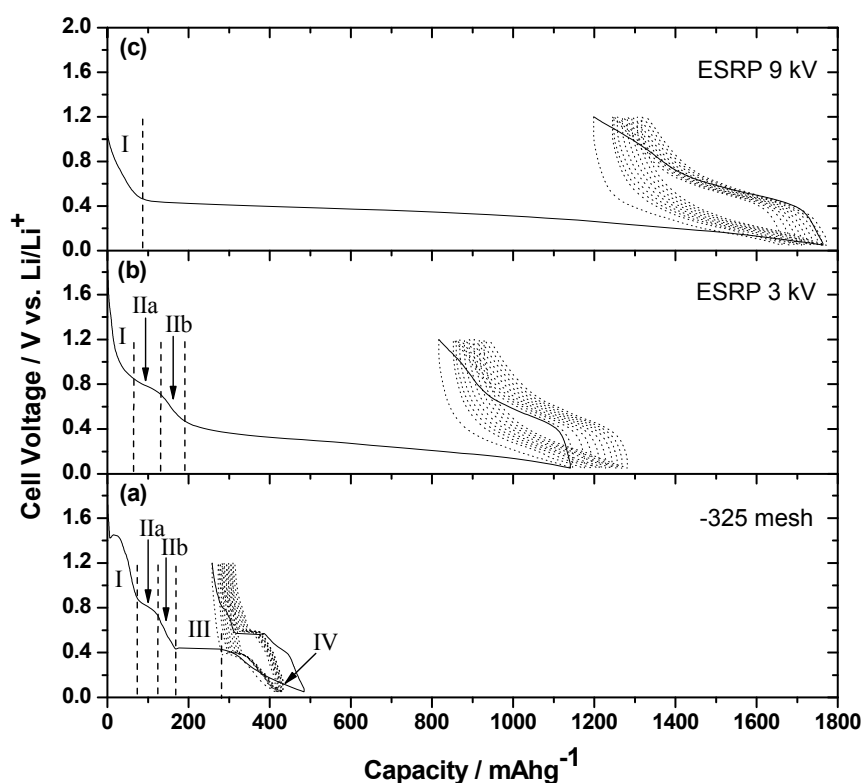
**Fig. 4.7.** Cycle performance of the materials tested between 0.0 and 2.0 V at 113 mA g<sup>-1</sup>.

From Fig. 4.7 it is seen that the cycling behaviour of the commercial powders is completely different from those of the synthesized materials. Despite the higher reversible capacity shown during the first cycle (i.e. 478 mA h g<sup>-1</sup>), a rapid capacity fading is observed after a few cycles, as is typically for micron-sized powders. The practical values are finally constant and are below 100 mA h g<sup>-1</sup>. On the other hand, both materials synthesized via ESRP presented a higher Li uptake during the second discharge, which exceeded the poor values of the first charge (i.e. ~250-280 mA h g<sup>-1</sup>). This behaviour, which is likely due to the presence of large surface areas, is observed for the first 5-6 cycles and it contributes to a substantial increase of the capacity up to ~450-465 mA h g<sup>-1</sup>. A series of irreversible processes can cause this initial difference between the discharge and charge capacities. For example: i) incomplete reaction of the residual SnO<sub>x</sub>; ii) extensive decomposition of the electrolyte and formation of the SEI layer; iii) structural rearrangement of the electrode due to initial uptake and removal of Li. One of the best ways to investigate such circumstances is to perform in situ AFM. Unluckily, it was not possible to perform a scan of the surface of the electrodes during cycling, but clearly this approach is important for future research.

Nevertheless, the observed features indicate that Sn-based nano-composite powders can enhance the mechanical properties of the electrodes, which were not immediately damaged by the volume changes of the first cycles. However, the capacities for both of them presented a moderate fading in the subsequent cycles.

Their evolution does not show a substantial difference, apart from the fact that after 50 cycles the materials synthesized at  $\sim 9$  kV presented a certain tendency towards stabilization of the capacity. This could be due to a slight difference in the average size of the crystallites that resulted from the process at  $\sim 3$  and  $\sim 9$  kV, as suggested by the XRD patterns. In both cases, the final capacity is significantly higher than that of the commercial powders.

Another electrochemical test was performed at a lower current density (i.e.  $23\text{mA g}^{-1}$ ) in order to distinguish between the various reactions occurring in the first cycle. The voltage window for discharge and charge was also reduced a little and ranged in this case from 0.05 to 1.20 V, in order to provide a better combination of adequate capacity and cycleability. It is stressed that at higher cycle numbers the current density was set as before (i.e.  $113\text{ mA g}^{-1}$ ). The voltage profiles of the materials during the first ten cycles are shown in Fig. 4.8.

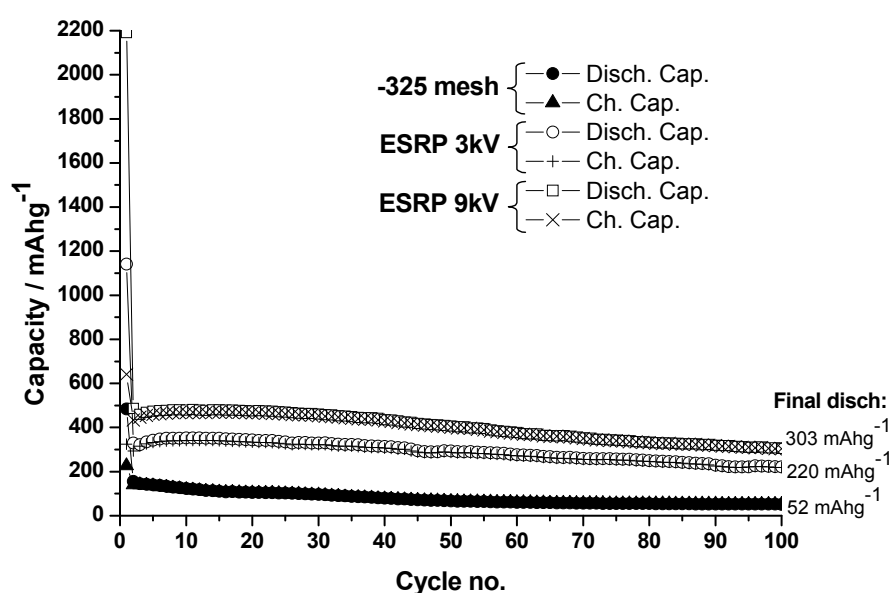


**Fig. 4.8.** Voltage profiles of the materials cycled between 0.05 and 1.20 V. Note that the first cycle (solid line) has been carried out at a reduced current density of  $23\text{ mA g}^{-1}$  for all the materials. The following nine cycles performed at  $113\text{ mA g}^{-1}$  (dotted lines) are also reported for further comparison. The regions are marked accordingly to Fig. 4.6.

From Fig. 4.8a it is noted that the use of a reduced current density during the first cycle enables a distinction between regions IIa and IIb, which are related to the SEI layer and the early stages of lithiation of the commercial powders. However, it should

be also remarked that this fact has a negative influence on the electrochemical behaviour. Indeed, the appearance of a hump at around 1.4 V (i.e. region I) causes an anomalous irreversible capacity, which is associated to the catalytic decomposition of the electrolyte by the tin surface [8]. Moreover, such reaction is known to be influenced by the cycling rate, matching well with the previous observation. Indeed, the use of a higher cycling rate yielded no trace for this catalytic reaction (Fig. 4.6a). As the SEI layer grows thicker, due to the formation of a passivating film on the surface of the electrode, the transport of the Li ions through the interface is hindered. This is a possible explanation for the poorer capacities observed at the end of the first discharge and charge. The increase in the cycling rate during the subsequent cycles does not improve the cycling behaviour anymore, and, after a further capacity fading, it yields only a minimal final capacity.

On the other hand, both materials synthesized via ESRP (Fig. 4.8b-c) present a huge increase of the discharge capacity, which exceed by far the theoretical value for Li-Sn alloy. Also in this case, no sharp plateaus are detected throughout their voltage profiles, indicating that the overall composition of the electrodes remains in a single phase region upon cycling, similarly as in a solid solution, where the potential depends on the state of charge. The observed reversibility for the cells is particularly poor during the first cycle (solid lines in Fig. 4.8), and only a small part of the initial capacity is retained upon charge. It should be noted, however, that the recovered capacity has a practical value, still higher than the one observed for commercial Sn. The increase of the cycling rate during the second cycle in these cases has also the effect of further lowering the capacity, as better visualized in Fig. 4.9.



**Fig. 4.9.** Cycle performance of the materials tested between 0.05 and 1.20 V at a current density of 113 mA<sub>g</sub><sup>-1</sup>. Note that only the first cycle was performed at 23 mA<sub>g</sub><sup>-1</sup>.



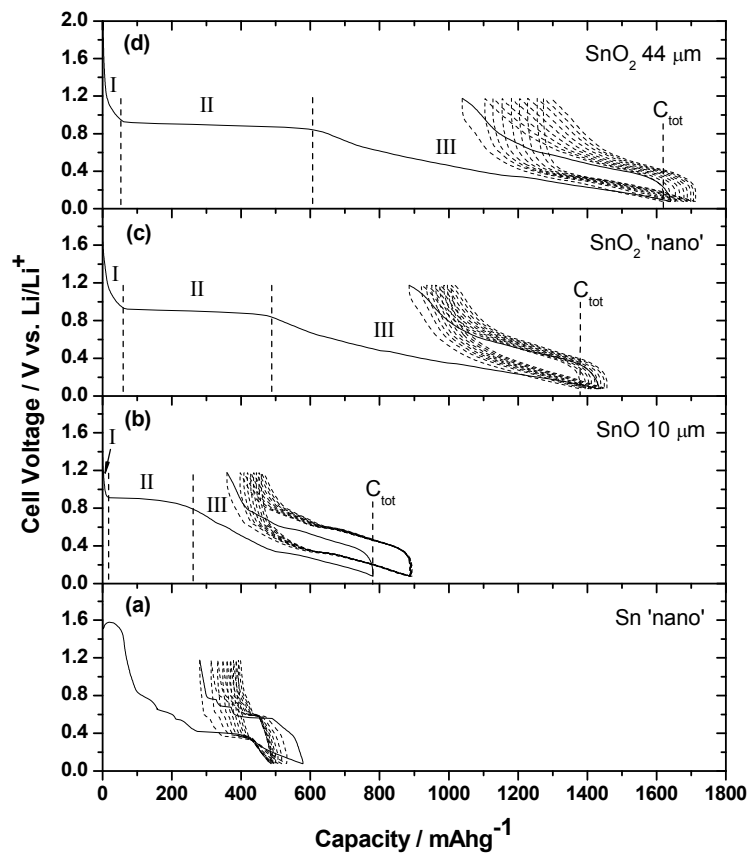
It is clearly noticed that the electrodes containing the nanocomposite Sn/SnO<sub>x</sub> powders can withstand prolonged cycling, retaining a certain capacity (i.e. ~220-300 mAhg<sup>-1</sup>). In particular, their behaviour is stable over the first 20-30 cycles. The moderate capacity fading observed for these materials is not as severe as in the case of commercial powders.

### 4.3.3 Electrochemical characterization of Sn, SnO and SnO<sub>2</sub>

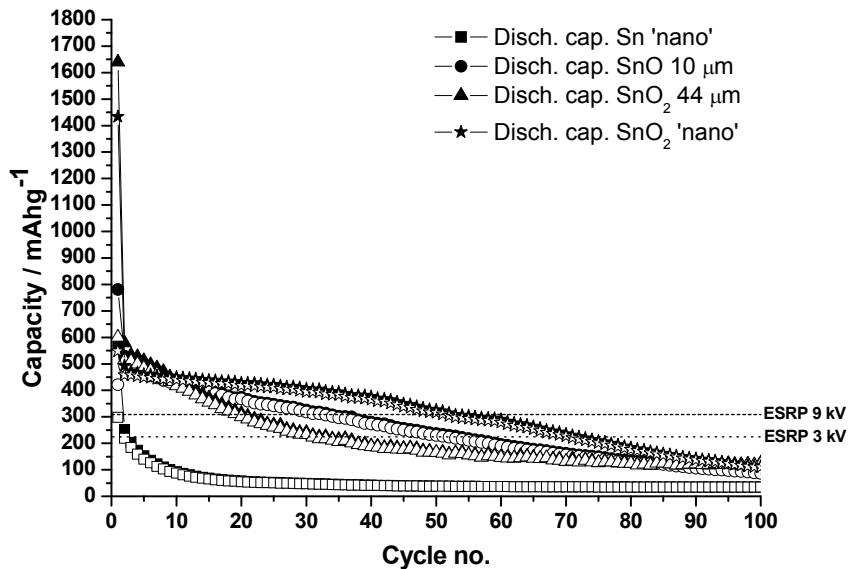
Overall, the various results indicated the presence of SnO<sub>x</sub> for the synthesized nanoparticles. Therefore, commercial ‘nano’ tin and tin oxide powders were tested electrochemically as well. An analogous galvanostatic procedure was used for the other commercial Sn-based powders (see Table 4.1). Their voltage profiles and corresponding cycle performances are shown in Fig. 4.10 and Fig. 4.11, respectively.

From Fig. 4.10 it is seen that the initial discharge capacity increased with the amount of oxygen present in the compounds, being the lowest value associated to the Sn ‘nano’ and the highest one to the micron-sized SnO<sub>2</sub>. The voltage profile of Sn ‘nano’ in Fig. 4.10a showed features similar to those discussed in Fig. 4.8a. In this respect, the ‘nano’ powders did not differ appreciably from the micron-sized ones. Besides, a definite plateau was clearly observed around 1.0 V for all the oxide powders (b), (c) and (d) in Fig. 4.10. This feature is related to the irreversible conversion reaction mentioned in eq. (4.1) where Li<sub>2</sub>O and Sn are initially formed. The flat plateau indicates that a real phase separation takes place and that two phases coexist. The plateaus (region II) related to micron and ‘nano’ SnO<sub>2</sub> powders exhibit a wider extension compared to that of the SnO powders, indicating that the storage of lithium is influenced under such conditions by the amount of oxygen available for the conversion reaction. Accordingly, the capacity recovery during the first charge was also affected by the composition. SnO and Sn ‘nano’ exhibited an initial coulombic efficiency (i.e. ≈54% and ≈51%) higher than that of SnO<sub>2</sub> and SnO<sub>2</sub> ‘nano’ (i.e. ≈37% and ≈38%). All the materials suffered from a more or less pronounced fading of the capacity in the following cycles performed at higher current density. This fact can be already noticed in the other nine cycles (dotted lines) reported in Fig. 4.10 and more clearly in Fig. 4.11, where all the charge-discharge capacities are compared.

From this last graph it is evident that the oxide powders cycled definitely better than the pure Sn ‘nano’. SnO<sub>2</sub> nanopowders showed the best capacity retention for at least 80 cycles. Despite their good initial performance, their capacity dropped significantly during the remaining part of the test, yielding final values comparable to the other materials. These final values, however, are lower than those of the nanostructured powders obtained by ESRP, which are indicated by the dotted lines.



**Fig. 4.10.** Voltage profiles for the other commercial Sn-based materials cycled between 0.05 and 1.20 V. Note that the first cycle (solid line) has been carried out at a reduced current density of 23 mA<sub>g</sub><sup>-1</sup> for all the materials. The following nine cycles performed at 113 mA<sub>g</sub><sup>-1</sup> (dotted lines) are also shown.



**Fig. 4.11.** Cycle performance of the other commercial Sn-based materials tested between 0.05 and 1.20 V at a current density of 113 mA<sub>g</sub><sup>-1</sup>. Note that only the first cycle was performed at 23 mA<sub>g</sub><sup>-1</sup>. The open symbols refer to charging of the cells, while the solid ones to discharge. The dotted line indicates the final values of the capacity for the nanostructured powders produced by ESRP.

## 4.4 Conclusions

Nanostructured powders have been produced by coupling electrospray of a Sn (II) chloride precursor solution to reductive precipitation by  $\text{NaBH}_4$ . Their typical morphology displays spherical-like agglomerates, whose structure consists of a multitude of monodispersed Sn nanocrystals of about 7-2 nm surrounded by an amorphous  $\text{SnO}_x$  phase.

Adequate amounts of materials were synthesized and collected for the preparation of coated electrodes in order to assemble coin cells. The electrochemical behaviour of the nanostructured powders as negative electrodes for Li-ion batteries was investigated by galvanostatic tests. Their voltage profiles and cycle performances were also compared to those of commercial tin and tin oxide (II, IV) powders having different mesh size. In particular, the related charge-discharge curves did not exhibit definite flat plateaus, as for the commercial materials, but rather a slight slope, indicating that upon reaction with lithium the materials behaved as though they were composed of a single phase over a wide range of composition. This fact prevented a rough estimation of the oxygen amount in the samples by means of a direct comparison with the characteristic plateau corresponding to the conversion reaction displayed by the commercial oxide powders under the same conditions.

Overall, the nanostructured powders by ESRP yielded enhanced discharge capacities. The irreversible capacity loss observed during their first cycle still represents a clear issue for efficient operation. This fact is related to the nature of the materials that result from reductive precipitation by  $\text{NaBH}_4$ , which usually exhibit large surface areas and therefore easier contamination. Conversely, both the synthesis process and the powder collection involved air exposure and consequently affected the purity of the processed materials.

Nonetheless, the nanostructured powders showed an adequate stability upon prolonged cycling, yielding a final capacity of about  $300 \text{ mAhg}^{-1}$ . This value is higher than those obtained for the commercial powders, which all suffered from capacity fading and limited coulombic efficiency during the first cycle.

Finally, the fabrication of the coated electrodes is an important step that should not be overlooked. The effective operation of this type of electrodes, where remarkable mechanical strains are present, involves a good dispersion of the active particles into the binder and, at the same time, a fair adhesion to the metal current collector. In most of the cases nanopowders manipulation and proper incorporation into composite electrodes are not trivial tasks. Not surprisingly, their good properties can be easily masked by an improper electrode assembly. Therefore, improving the cycling performances and the reversibility of such materials implies a suitable design and fabrication of the electrodes.

## 4.5 References

- [1] J. O. Besenhard, J. Yang, M. Winter, *Journal of Power Sources* **1997**, 68, 87.
- [2] M. Winter, J. O. Besenhard, M. E. Spahr, P. Novák, *Advanced Materials* **1998**, 10, 725.
- [3] M. Winter, J. O. Besenhard, *Electrochimica Acta* **1999**, 45, 31.
- [4] J. O. Besenhard, M. Hess, P. Komenda, *Solid State Ionics* **1990**, 40-41, 525.
- [5] R. A. Huggins, *Journal of Power Sources* **1999**, 81-82, 13.
- [6] Y. Idota, T. Kubota, A. Matsufuji, Y. Maekawa, T. Miyasaka, *Science* **1997**, 276, 1395.
- [7] J. Yang, M. Winter, J. O. Besenhard, *Solid State Ionics* **1996**, 90, 281.
- [8] L. Y. Beaulieu, S. D. Beattie, T. D. Hatchard, J. R. Dahn, *Journal of the Electrochemical Society* **2003**, 150.
- [9] J. Yang, M. Wachtler, M. Winter, J. O. Besenhard, *Electrochemical and Solid-State Letters* **1999**, 2, 161.
- [10] S. Naille, C. M. Ionica-Bousquet, F. Robert, F. Morato, P. E. Lippens, J. Olivier-Fourcade, *Journal of Power Sources* **2007**, 174, 1091.
- [11] O. Mao, J. R. Dahn, *Journal of the Electrochemical Society* **1999**, 146, 414.
- [12] M. Wachtler, M. Winter, J. O. Besenhard, *Journal of Power Sources* **2002**, 105, 151.
- [13] A. Trifonova, M. Wachtler, M. R. Wagner, H. Schroettner, C. Mitterbauer, F. Hofer, K. C. Moller, M. Winter, J. O. Besenhard, *Solid State Ionics* **2004**, 168, 51.
- [14] Y. Wang, J. Y. Lee, T. C. Deivaraj, *Journal of the Electrochemical Society* **2004**, 151.
- [15] A. A. van Zomeren, E. M. Kelder, J. C. M. Marijnissen, J. Schoonman, *Journal of Aerosol Science* **1994**, 25, 1229.
- [16] E. M. Kelder, O. C. J. Nijs, J. Schoonman, *Solid State Ionics* **1994**, 68, 5.
- [17] A. Jaworek, *Powder Technology* **2007**, 176, 18.
- [18] A. Jaworek, *Journal of Materials Science* **2007**, 42, 266.
- [19] A. Jaworek, A. Krupa, *Journal of Aerosol Science* **1999**, 30, 873.
- [20] M. Noh, Y. Kim, M. G. Kim, H. Lee, H. Kim, Y. Kwon, Y. Lee, J. Cho, *Chemistry of Materials* **2005**, 17, 3320.
- [21] I. A. Courtney, W. R. McKinnon, J. R. Dahn, *Journal of the Electrochemical Society* **1999**, 146, 59.
- [22] I. A. Courtney, J. R. Dahn, *Journal of the Electrochemical Society* **1997**, 144, 2045.
- [23] S. T. Chang, I. C. Leo, C. L. Liao, J. H. Yen, M. H. Hon, *Journal of Materials Chemistry* **2004**, 14, 1821.

- [24] P. Poizot, S. Laruelle, S. Grugeon, L. Dupont, J. M. Tarascon, *Nature* **2000**, 407, 496.
- [25] P. Poizot, S. Laruelle, S. Grugeon, J. M. Tarascon, *Journal of the Electrochemical Society* **2002**, 149.
- [26] P. Balaya, H. Li, L. Kienle, J. Maier, *Advanced Functional Materials* **2003**, 13, 621.



# Chapter 5

## One-step synthesis and assembly of coated nanocomposite layers

*The best way to make your dreams come true is to wake up.  
(Paul Valery)*

A direct approach for the fabrication of coated nanocomposite electrodes is presented in this chapter. The components of an electrode are here synthesized and/or assembled via a single-step process into a nanocomposite layer. Active nanoparticles can be directly synthesized, as well as dispersed within a polymeric binder, and deposited straight away as a composite layer onto a heated substrate via electrospray. In this way, an intimate contact between the binder and the active nanoparticles can be easily obtained in the coated layer. In-situ synthesis of nanoparticles by direct coupling pyrolysis reactions of precursor salts with electrospray (or electrospinning) of polymers offers a new way not only for the manufacture of coated nanocomposite layers for Li-ion battery electrodes, but also for other novel technological applications.

## 5.1 Introduction

The state of the art of several researches looks to nanostructured materials as the turning point for engineering devices with novel and different functionalities. In this respect, the unique physical and chemical properties of nanomaterials represent an essential resource for both the advancement of the existing technologies and the development of future applications. This fact holds true not only for technological fields where fast and precise information exchange are required (i.e. nanoelectronics, photonics or plasmonics), but also for all those applications involving conversion of chemical energy to electrical energy or chemical storage of electrical energy [1].

Energy storage and conversion via batteries and fuel cells, and more in general electrochemical devices, can clearly benefit from the use of nanostructured materials [2], which represent the basis for the emerging field of nano-ionics [1, 3-5]. In particular, nanostructures and nanocomposites are regarded as perfect candidates for advanced Li-ion battery electrodes [6-12]. However, it is also important to address correctly their advantages and disadvantages for such purposes, as well as the issues related to the control of their synthesis and properties. On the one hand, the reduced size of the nanostructures can really make the difference with conventional bulk materials in terms of:

- Enhanced charge transfer, leading to superior charge/discharge rates due to higher surface areas and larger contact between electrode and electrolyte [6].
- Reduced diffusion lengths,  $\ell$ , for charge carriers (i.e. electrons and  $\text{Li}^+$  ions), resulting in increased power delivery and enabling operation even with scarce electronic or ionic conductivities. (Note that the characteristic diffusion time,  $t_d$  scales as  $t_d \sim \ell^2 D$ , where  $D$  is the diffusion coefficient) [6, 13].
- Effective acceptance of strain upon uptake and removal of Li, promoting a stable cycling behaviour thereby making the system inherently safe [6, 14-16].
- Novel red-ox reactions that are not possible in the bulk [6, 17].
- New storage mechanisms for  $\text{Li}^+$  and  $\text{e}^-$  in neighbouring nano-phases, due to extended interfaces [18-20].

Moreover, nanoparticles exhibit an intrinsic, varied curvature that is responsible for capillary pressure effects. These are not only beneficial for enhancing the mechanical properties of novel nanocomposite electrodes, but they also account for relevant shifts in thermodynamic properties of the materials [13].

On the other hand, shortcomings of nanoparticles should be carefully taken into account for efficient fabrication of nanostructured electrodes. The first issue is obviously the control of the particles properties. Morphology, size, size distribution, agglomeration, composition and crystallinity play a key role in determining the



characteristics of suitable electrode materials. Besides, larger surface areas are also responsible for undesirable contamination and parasitic reactions. Their large surface-to-volume ratio implies also a lower tap density, which results in reduced volumetric energy densities, unless special compaction methods are adopted [6]. Furthermore, the hazards connected to the synthesis and the manipulation of nanoparticles cannot be neglected and safety issues, as well as health risks, need to be accurately assessed.

The matter concerning the practical use of these nanoparticles in a real electrode assembly is even more subtle. In most of the cases, the positive features of good active nanomaterials can be easily masked - if not completely smeared out - by improper selection or processing of the other inactive electrode components (i.e. binders, additives, current collectors). This occurs especially when the raw materials are processed in the powder form. The main problem arises from the difficulty in homogeneously dispersing the nanoparticles with the polymeric binder and carbon black during the preparation of a slurry. The resulting paste has to provide a fair adhesion to the current collector. It should also ensure a good electronic contact of the different parts in order to maintain the integrity of the whole electrode and to promote efficient electrochemical cycling. Negative electrodes based on metallic, alloyed or metal oxide particles are prone to suffer more from these inconveniences when compared to positive ones, since they experience large strains caused by volume changes during uptake and removal of Li. These circumstances can easily damage a poorly-assembled composite electrode, even though the nanoparticles could eventually withstand the cycling. In this respect, the mentioned effects interfere with a full characterization of the real benefits of nano-sized materials for Li-ion batteries. Unfortunately, this aspect is quite often overlooked.

Different strategies have been developed in order to tackle such issues and various solutions have been proposed so far. For example, the use of metal nanoparticles finely dispersed in a supporting carbon matrix [21] or nanoparticles embedded in carbon microspheres [22-24] as well as carbon-encapsulated hollow structures [25] constitute elegant concepts for advanced fabrication of negative electrodes. They result in a significant improvement of the mechanical stability of the materials during cycling, preventing particle agglomeration and enhancing the electronic conductivity of the entire electrode [21]. However, these methods generally require multi-step processes, which often involve the use of expensive precursors. Even in one-step synthesis approaches high temperatures (i.e. 700 °C) are usually required for the fabrication of such nanocomposites. Moreover, the materials still need to be thoroughly mixed in a slurry with the binder and successively coated on a current collector.

Alternative methods for fabricating advanced electrodes rely on various techniques that often enable the direct growth or deposition of the active materials on the current collectors, minimizing the number of the steps needed for the entire

manufacture process. For example, techniques as electrodeposition [26], template-synthesis [27, 28], physical vapour deposition [16], sputtering [29], vapour-solid-liquid (VLS) [30] or vapour-solid (VS) [31] growth have been widely used for these purposes and a series of interesting results have been achieved. In all the cases, the binder and the carbon black are not included in the fabricated electrode. In this scenario nano-architected electrodes (i.e. self-supported nanowires or nanotubes arrays, etc.) play a special role, since they represent ideal systems for novel 3D nanostructured electrodes. It is not surprising that the most promising results in terms of capacities and rate capabilities are normally obtained with this class of electrodes [32-34]. The open space between the structures contributes to enlarge the effective surface area and it allows easy infiltration of the electrolyte into the inner regions of the electrodes, decreasing the internal resistance and promoting the power delivery. Wires, rods and especially tubes provide favourable geometries to accommodate the strain involved during uptake and removal of Li, and each of them has directly its own contact with the substrate. In this way, each structure contributes directly to the overall electrochemical reaction and it is not required any other ancillary material for normal operation. However, the fabrication methods applied so far (i.e. template-assisted syntheses, VLS, VS, etc.) are quite cumbersome and even in the most favourable cases there are obvious limitations arising, for example, from pre-treatments needed for the substrates, the size of the template membranes, the use of expensive catalysts, the limited area coverage and the scarce amount of active material effectively grown.

The use of template-free methods for spontaneous, large-area growth of self-standing nanowires (i.e.  $\leq 0.5 \mu\text{m}$ ) arrays is probably at the moment one of the best ways for a relatively cheap, easy and quite efficient manufacture of advanced 3D nanostructured (negative) electrodes, involving only few process steps [35, 36]. Despite that, this interesting approach still suffers from limited mechanical stability in a battery assembly. The risk of breaking the wires during the fabrication of the whole device should also be taken into account. Damaging the wires causes a direct loss of capacity, since the electrical contact of the individual structures with the substrate is definitively lost.

Therefore, on the basis of the considerations above, it is also wise not to discard the role of the binder and eventual additives for practical purposes in commercially coated electrodes.

An increasing number of studies are actually devoted to the investigation of suitable binders and their influence on the cycle performance of negative electrodes [37-40]. Indeed, the active nanoparticles need an adequate “glue” that holds them together (with the conductive additive) and that reinforces the entire electrode during the electrochemical process. Particles must adhere to the current collector and not move far apart from each other in order to ensure percolation. Additionally, the

binder adhesion to the nanoparticles' surface should be optimal, promoting the transport of the charge carriers and preventing the particles from coalescence and growth. Hence the possibility of direct deposition of nanocomposite layers containing the active particles dispersed in a polymeric binder with eventual additives is obviously attractive. Besides, it is particularly convenient to generate in situ the nanoparticles within the binder, rather than dispersing them in a separate step. All these considerations lead to the idea that the process of synthesis of the active nanomaterials should be possibly not separated from their assembly in composite electrodes together with binders and eventual additives.

In this scenario, electrospray-based methods (i.e. ESD, ESP, electrospinning) offer a powerful tool in order to perform a one-step synthesis and assembly process for nanocomposite polymer/particles layers. In this respect, it is worthwhile to mention that these methods have been already applied to the field of Li-ion batteries for various purposes (see chapter 2).

On the one hand, ESP and ESD have been applied to the synthesis and deposition of thin film electrodes for Li-ion batteries *without* any polymeric binder. On the other hand, electrospinning has been used for the fabrication of composite polymeric nanofibers, which are either used directly to prepare membranes and separators, or carbonized in a separate step to yield carbon nanofibers loaded with active electrode materials. However, in all these cases the polymer has *not* been directly utilised for binding purposes in practical coated electrodes.

Herein, the active nanomaterials and the polymeric binder are handled together at the same time, finely inter-dispersed and directly assembled in one step in nanocomposite electrodes. Not surprisingly, the versatility of electrospraying enables devising various approaches and strategies in order to accomplish this goal. For this reason, the significance of the proposed method is multi-fold, since the applications are not limited to Li-ion battery electrodes but can be extended to several other purposes.

In the following sections a series of different materials processed with this direct approach will be presented. Although the study and the characterization of the obtained nanocomposite layers are still in an 'embryo' state, the initial results suggest that this method effectively represent a breakthrough for the manufacture of advanced coated electrodes and has the potential to be implemented on a larger scale.

## 5.2 Experimental

The experimental procedure is described in the following sub-sections, which are related to the various aspects of the synthesis and characterization.

### 5.2.1 Precursor solutions and suspensions

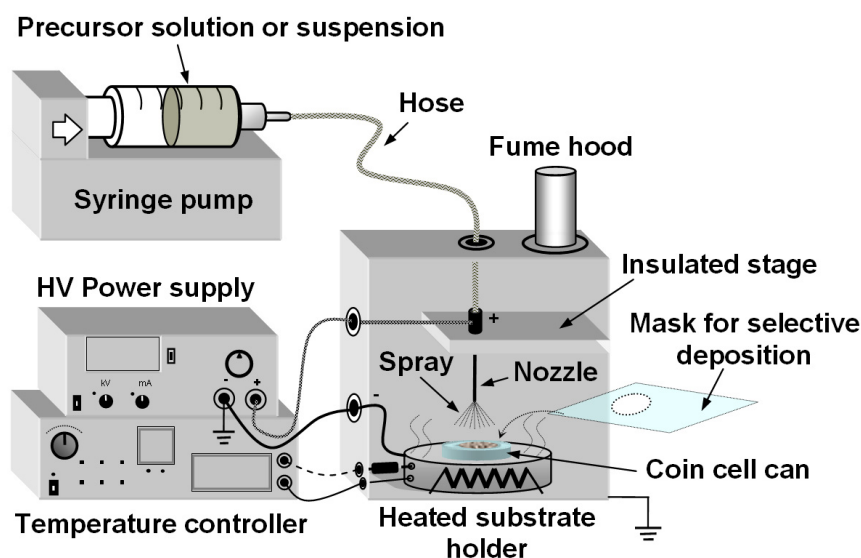
The precursor solutions containing the binder and the different metal precursor salts were prepared as follows. For a typical preparation  $\approx 0.1$  g of Polyvinylidene Fluoride powders (PVdF - Solef) were added to  $\approx 10$  ml of N-Methyl-2-pyrrolidone (NMP – Merk-Schuchardt) and sealed in a glass bottle. Constant stirring was applied in order to completely dissolve the PVdF in the NMP. Subsequently, an amount of approximately 0.5 g of the desired metal precursor salt (i.e.  $\text{SnCl}_2 \cdot 2\text{H}_2\text{O}$  – Riedel-de Haën;  $\text{Co}(\text{CH}_3\text{COO})_2 \cdot 4\text{H}_2\text{O}$  – Riedel-de Haën;  $\text{Fe}(\text{CH}_3\text{COO})_2$  – Alpha) was added to the NMP-PVdF solution. Vigorous stirring was then applied in order to achieve the complete dissolution of the precursor salts. Different colours were obtained, depending on the type of the ions present in solution. For instance, clear transparent solutions were obtained for  $\text{SnCl}_2 \cdot 2\text{H}_2\text{O}$ , while hues changing rapidly from greenish to dark-black were observed after initial stirring of the  $\text{Co}(\text{CH}_3\text{COO})_2 \cdot 4\text{H}_2\text{O}$  salt, and opaque dark-brown for  $\text{Fe}(\text{CH}_3\text{COO})_2$ . It should be pointed out that the use of acetate or chloride precursors, as well as the weight ratio of metal salt/PVdF, represents here a mere choice for the demonstration of the concept. The choice of the liquid precursors - both in terms of the materials selected, as well as their quantities and relative percentages - can be conveniently adjusted in order to comply with the requirements of specific applications. The same holds for other types of preparations, where, for instance, a concentrated suspension of active nanoparticles is employed as starting precursor.

A concentrated precursor suspension was obtained by dispersion of Si nanoparticles in a liquid NMP-PVdF mixture. In particular, the active Si nanoparticles (i.e. average size  $\approx 20$  nm) were previously synthesized via a gas-phase process (i.e. Laser Assisted Chemical Vapour Pyrolysis – LACVP) (further details can be retrieved in ref. [41]). In this case, approximately 0.14 g of Si nanopowders were dispersed in 10 ml of NMP containing  $\approx 0.7$  g of pre-dissolved PVdF. A homogeneous, stable suspension was obtained by sonication for one hour. The resulting precursor suspension exhibited a dark-brownish colour with intense red reflections due to the particular characteristics of the Si nanoparticles.

### 5.2.2 Aerosol generation and electrode coating

All the experiments were performed in air and the deposition of the nanocomposite layers was carried out inside a reaction chamber connected to a fume hood. A schematic drawing of the equipment used for the synthesis and assembly of the coated electrodes is shown in Fig. 5.1. The precursor solutions/suspensions were transferred to a glass syringe (Fortuna Optima) which was connected through a

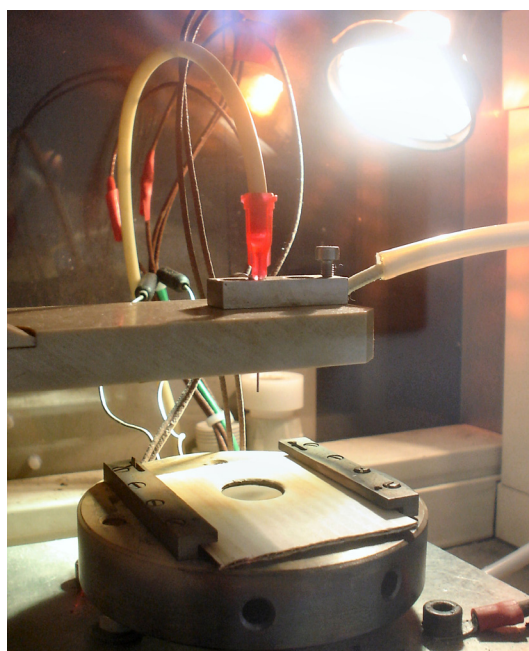
chemically-resistant hose (Watson-Marlow) to a stainless steel nozzle (EFD Ultra). The nozzle, on its turn, was connected to the positive pole of a high voltage power supply (HCN 14-12500). A syringe pump (Kd Scientific) enabled the feeding of the precursors to the nozzle at a controlled flow rate. Different nozzles with inner diameters ranging from 250 to 840  $\mu\text{m}$  were utilized in order to facilitate a continuous precursor flow and avoiding clogging, especially when feeding concentrated suspensions. The flow rate was tuned in the experiments in order to stabilize the electro spray process. Typical values were in a range of 0.20 – 0.40  $\text{mlh}^{-1}$ . The voltage applied for the atomization was generally adjusted from about 8.0 to 10.0 kV, in order to obtain a homogeneous layer deposition, depending on the characteristic properties of the precursor solution/suspension. The distance between the nozzle and the substrate was kept the same in all the experiments (i.e.  $\approx 20$  mm), and measured via a built-in digital calliper. The temperature of the substrate was maintained constant by a thermostat. The temperature was constantly monitored via thermocouples, in order to control the heating process by adjusting the power supplied to the hot plate, where the samples were mounted. The substrate temperature was set to  $\approx 280$   $^{\circ}\text{C}$  for the in-situ synthesis and assembly of the metal oxides, while it was fixed to  $\approx 200$   $^{\circ}\text{C}$  for the direct assembly of the Si nanoparticles.



**Fig. 5.1.** Schematic drawing of the electro spray equipment applied to the direct synthesis and assembly of coated nanocomposite electrodes.

In the various experiments a preliminary deposition was first performed on an aluminium foil stripe (PPI, thickness 45  $\mu\text{m}$ ) or on a stainless steel plate, in order to obtain suitable area coverage for easier characterization of the deposited materials. Analogous experimental conditions were then applied to the selective coating of the electrodes directly on the bottom part of coin cells. For this purpose, empty stainless

steel coin cell cans (i.e. CR2320 - Hohsen) were carefully weighted on a digital balance (Sartorius) with an accuracy of  $10^{-5}$  g, before being placed onto the heated substrate holder. Selective coating on a circular area concentric to the rim of the can was achieved by applying a cardboard mask with a punched hole of 14 mm diameter. The hole of the mask was centred to the middle of the coin cell can. The mask and can were held firmly to the hot plate by two lateral supports (Fig. 5.2). The use of cardboard is here twofold: it is a good insulator and it does not melt or burn when heated to high temperatures.



**Fig. 5.2.** Photo of the electro-spray in operation for the direct synthesis and assembly of coated nanocomposite layers. The electrified nozzle feeding the precursor solution and the heated substrate holder are clearly visible. The cardboard mask on the hot plate is applied in order to selectively deposit circular electrodes on a stainless steel coin cell can. This part is not visible in the image, since it is placed beneath the circular hole. The lamp facilitates the visualization of the current spraying mode.

After the coating process, the coin cell cans were weighted again on the balance and the amount of the deposited composite material was determined by mass difference. The typical weight of the composite layers was around 0.8 – 1.2 mg. The electrode fabrication via in-situ precursor pyrolysis was typically carried out in about twenty or thirty minutes, depending mainly on the flow rates, while for the concentrated Si suspension the deposition of an analogous amount of material took less time.

It is worthwhile to mention that the resulting electrodes do not need any further treatment and that they can be directly sealed in a full battery assembly by simply adding the remaining parts (i.e. electrolyte-soaked separator, lithium disk, spring, gasket and stainless steel lid).

### 5.2.3 Characterization and electrochemical tests

The produced materials were analyzed by different characterization techniques. X-ray diffraction (XRD) was performed on a Bruker (AXS D8 Advance) diffractometer equipped with a Cu-K $\alpha$  radiation source ( $\lambda = 1.5418 \text{ \AA}$ ); Scanning Electron Microscopy (SEM) was carried out on a Philips XL20 microscope. Besides, Transmission Electron Microscopy (TEM) analyses were performed by two microscopes operated at 300 kV, namely Philips CM30T and FEI Tecnai F20, both equipped with a LINK EDX probe (Oxford) for elemental analysis. Moreover, Atomic Force Microscopy (AFM) was carried out on a NT-MDT NTEGRA scanning probe microscope in semi-contact mode, using a Si cantilever and tip (NT-MDT, Silicon: NSG 03). The processed cans containing the deposited electrodes were assembled in complete cells in a He-filled glove-box (MBraun). The electrolyte consisted of 1 M LiPF $_6$  solution in EC:DMC (2:1 by wt. - Mitsubishi Chemicals) and metallic lithium disks were used as reference and counter electrodes for the electrochemical measurements. Galvanostatic tests were carried out by a Maccor cyler (S-4000) at constant gravimetric current densities (i.e. 113 mA $g^{-1}$  for SnO $_2$ , 358 mA $g^{-1}$  for CoO, 124 mA $g^{-1}$  for Fe $_2$ O $_3$ , and 100 mA $g^{-1}$  for Si). The cells were discharged and charged in different voltage ranges versus Li/Li $^+$ , depending on the electrode materials. Cyclic Voltammetry (CV) was also performed by an Autolab equipment (PGSTAT 12) with a scan rate of 0.1 mVs $^{-1}$  between 0.02 and 3.0 V for the transition metal oxides. Specimens for TEM 'post mortem' analysis of the electrode materials after electrochemical cycling were collected inside the glove-box, where the cycled coin cells were disassembled. The electrodes were washed thoroughly by EC for several times in order to remove completely the electrolyte salt. Subsequently, the electrodes were further soaked with NMP, in order to ease the removal of a bit of the coated electrode and its collection for the analysis.

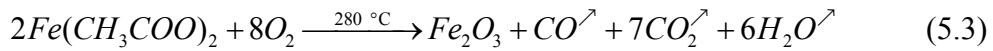
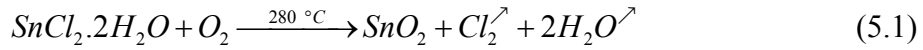
## 5.3 Results and discussion

Polyvinylidene Fluoride (PVdF) represents the polymer of choice for the direct assembly of nanocomposite electrodes, which do not contain any conductive additive here (i.e. carbon black). It is worthwhile to point out some characteristic properties of PVdF that account for its popularity as binder for Li-ion battery electrodes.

Indeed, it is a highly non-reactive, pure thermoplastic fluoropolymer suitable for applications where high purity and strength are required. PVdF fairly withstands heat, several solvents, acids, bases and in case of fire it has a low generation of smoke. It has also a rather low density (1.78 gcm $^{-3}$ ) and reduced production costs when compared to other fluoropolymers, due to its relatively easy melting process.

Moreover, it shows strong piezoelectricity when poled and it behaves as a ferroelectric polymer, exhibiting piezoelectric and pyroelectric properties. Interestingly, unlike most piezoelectric materials, PVdF contracts instead of expanding under the influence of an applied field. This property arises from its negative value for the piezoelectric coefficient (i.e.  $d_{33}$ ) and it is extremely valuable for batteries and sensors.

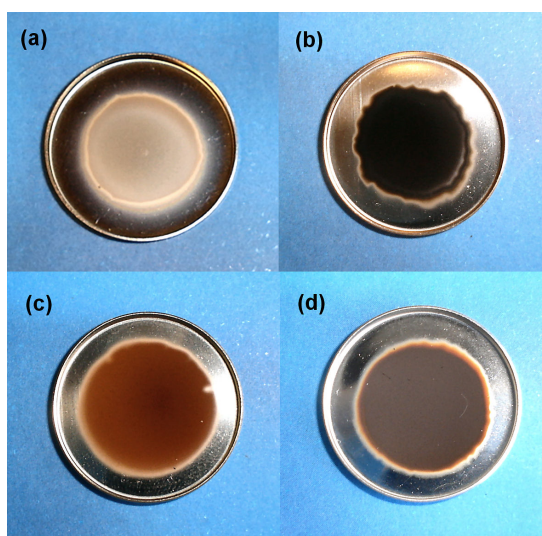
PVdF starts decomposing only at high temperatures ( $\geq 315$  °C in air) and its stability under inert atmosphere has been observed up to 350 °C [42]. This fact is crucial here for the pyrolysis of the electro-sprayed precursor solutions. In fact, the temperature of the substrate holder is set to 280 °C, which is high enough to allow the pyrolysis of the precursors, but still far from the threshold for the decomposition of PVdF. In this way the nanoparticles are synthesised and directly attached to the substrate. Some possible pyrolysis reactions at 280 °C in air for the precursor salts are the following:



On the basis of the initial weight ratio between the metal salts and the PVdF in the precursor solution (i.e. 5:1) it is possible to calculate via these equations the final weight ratio of the active oxide nanoparticles in the composite electrodes by assuming a homogeneous dispersion of the produced materials. Indeed, PVdF does not undergo decomposition and its weight is not influenced by the reactions. Hence, the weight ratio between the active particles and the PVdF can be evaluated by comparison of the molecular weights of the compounds. In particular, a rough ratio of about 76 % for  $\text{SnO}_2$ , of 60 % for  $\text{CoO}$  and of 69 % for  $\text{Fe}_2\text{O}_3$  can be estimated.

Fig. 5.3 shows the various materials directly coated as electrodes on coin cell cans. The photos in Fig. 5.3a-c represent some examples of in situ synthesis of oxide nanoparticles (i.e.  $\text{SnO}_2$ ,  $\text{CoO}$ ,  $\text{Fe}_2\text{O}_3$ ) via pyrolysis of precursor salts and their direct assembly in nanocomposite layers together with PVdF. On the other hand, the photo in Fig. 5.3d, presents a slightly different situation, in which the nanocomposite electrode results from the electro-spray deposition of a concentrated suspension containing Si nanoparticles and PVdF. Such a process can be eventually performed at lower temperatures, since in this case the particles are already formed and only solvent evaporation is required. From Fig. 5.3 it is seen that the overall morphology of the resulting composite electrodes is fairly homogeneous. Nonetheless, the deposition can be further improved by a fine tuning of the experimental parameters involved in the process.





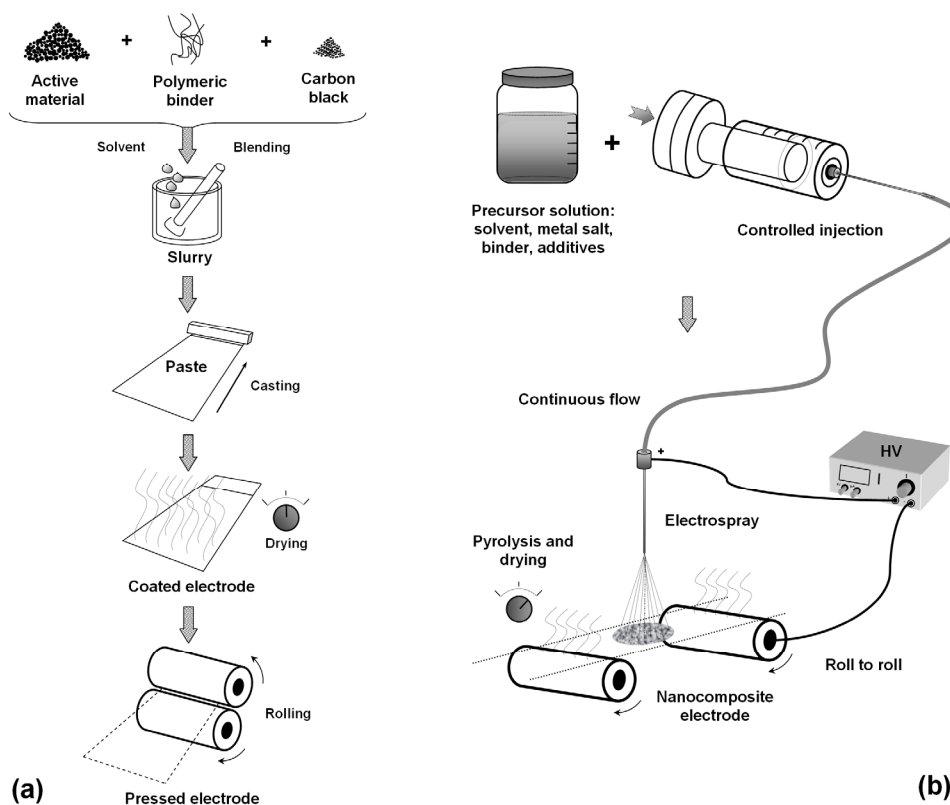
**Fig. 5.3.** Photos of different nanocomposite electrodes selectively deposited on stainless steel coin cell cans. (a)  $\text{SnO}_2/\text{PVdF}$  by direct pyrolysis of  $\text{SnCl}_2 \cdot 2\text{H}_2\text{O}$  at  $280^\circ\text{C}$ . (b)  $\text{CoO}/\text{PVdF}$  by direct pyrolysis of  $\text{Co}(\text{CH}_3\text{COO})_2 \cdot 4\text{H}_2\text{O}$  at  $280^\circ\text{C}$ . (c)  $\text{Fe}_2\text{O}_3/\text{PVdF}$  by direct pyrolysis of  $\text{Fe}(\text{CH}_3\text{COO})_2$  at  $280^\circ\text{C}$ . (d)  $\text{Si}/\text{PVdF}$  via deposition at  $200^\circ\text{C}$  from a concentrated suspension of Si nanoparticles by LACVP.

A precise control of the morphology of the deposited layers requires an insight of the underlying electro spray process. More specifically, it implies a comprehensive understanding of the mechanisms for droplet formation and evaporation followed by the generation of the composite polymer particles via the precursor pyrolysis. Therefore, the knowledge of the ‘scaling laws’ for the evaluation of the average size of the droplets emitted in the ‘cone-jet’ mode - on the basis of the intrinsic properties of the precursor solution/suspension and its flow rate - represents only the first step here. In fact, several other parameters, i.e. the temperature of the substrate, the distance between the nozzle and the substrate, the properties of the solvent, the polymer/solute concentration, the growth rate of the deposits, etc. are also decisive in determining the morphology of the grown films. In this respect, an interesting study on the formation of PVdF films by electro spray deposition [43] offers a general framework through which the control of the film morphology can be eventually improved.

In this work the physical properties of the precursor solutions/suspensions were not measured and the flow rates and voltages were simply adjusted in order to obtain a homogenous film deposition. Indeed, the main focus of this investigation is to demonstrate that the coating of nanocomposite electrodes can be performed in a faster, alternative way that offers several advantages over the standard procedures.

The drawings in Fig. 5.4 compare schematically a typical manufacturing process of laminated electrodes with the proposed concept of direct synthesis and assembly of Fig. 5.3. The main advantage of the electro spray is that the thickness of the coatings can be controlled with higher precision than by conventional casting and

the entire process can be performed in a one-step, continuous mode. Deposition times for electrode coating can be drastically reduced by means of multiple-nozzle systems, especially when low flow rates are required on single spraying points in order to generate homogeneously-sized droplets. In such a way, these nanocomposite materials that have been synthesized by a simple equipment, like the one shown in Figs. 5.1 and 5.2, could be produced on a larger scale via a roll-to-roll process.

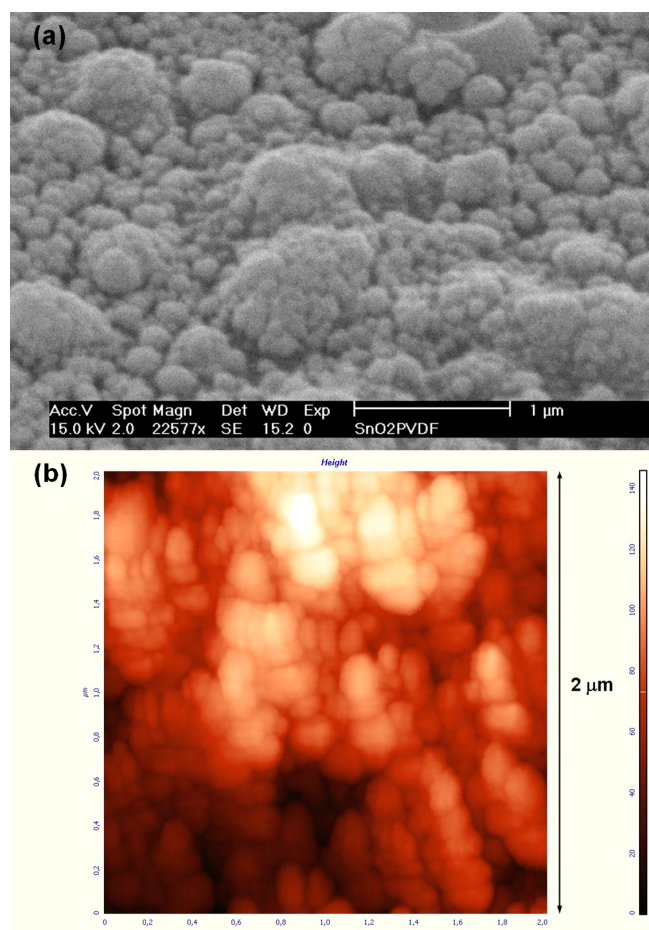


**Fig. 5.4.** Schematic drawing of a typical manufacturing process of coated electrodes (a). Raw materials are first mixed thoroughly with a solvent to prepare slurries. Casting of the pastes is achieved by the so-called ‘doctor-blade’ procedure. Subsequent coating of the current collector is attained by evaporation of the solvent and further consolidation of the composite layer. Rolling and pressing promotes the contact between active particles and carbon black. Scheme of the proposed one-step fabrication process (b). Electro spray provides a way for direct synthesis and deposition of the active materials together with the polymeric binder. Evaporation and pyrolysis serve as direct means for deposition and in-situ generation of the active nanoparticles.

### *I – SnO<sub>2</sub>/PVdF nanocomposite*

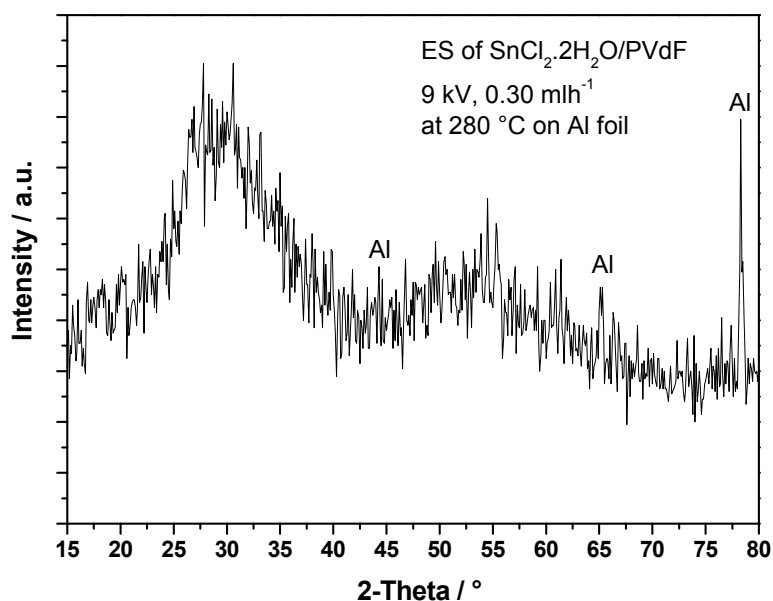
The typical morphology of the surface of the composite SnO<sub>2</sub>/PVdF electrodes obtained by electro spray and pyrolysis of the tin chloride precursor is shown in the different SEM and AFM micrographs of Fig. 5.5. The electrode surface exhibits the relics of the reacted droplets. A relatively dense morphology is observed for the spherical-like deposits, meaning that likely the evaporation of the solvent (i.e. NMP) occurred completely in air during the time of flight of the droplets.

Therefore, each charged droplet acted as a sort of ‘micro-reactor’ for the formation of the composite polymer-oxide materials. Both micrographs reveal the presence of sub-micrometric particles composed of SnO<sub>2</sub>/PVdF. Indeed, electro-spray pyrolysis of SnCl<sub>2</sub>·2H<sub>2</sub>O solutions at 250 °C in air yields amorphous SnO<sub>2</sub> [44]. The coated electrodes obtained at 280 °C displayed a faint white-yellowish hue, which is characteristic for SnO<sub>2</sub> materials, being in line with the expected reaction.



**Fig. 5.5.** SEM (a) and AFM (b) micrographs representing the typical morphology for the surface of the composite electrodes. The deposits result from direct atomization and reaction of a SnCl<sub>2</sub>/PVdF precursor solution at 280 °C. The relics of the droplets produced during the electro-spray are clearly visible in both images as conglomerated nanoparticles.

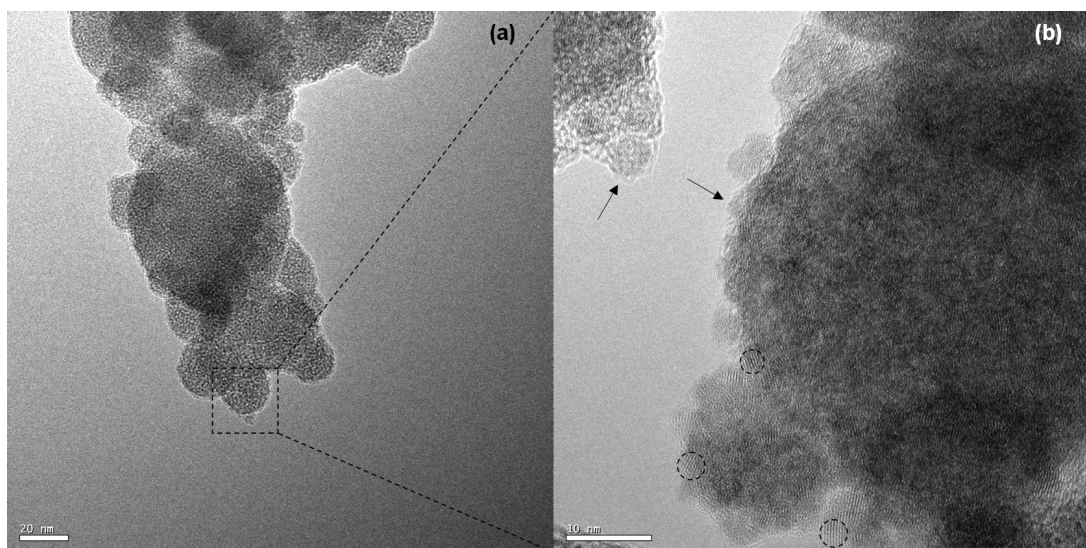
XRD was performed on a sample synthesized under identical conditions, but having a larger area coverage and a thicker layer of nanocomposite material deposited on an Al foil. The resulting diffraction pattern is represented in Fig. 5.6. The spectrum does not show any sharp diffraction peak of the lattice structure of SnO<sub>2</sub> and only characteristic diffractions related to the underlying Al foil can be discerned. However, broad diffractions are observed around 27 and 52 °, which are observed in the presence of nanocrystalline SnO<sub>2</sub> [45].



**Fig. 5.6.** XRD spectrum of the SnO<sub>2</sub>/PVdF composite layer by electro spray pyrolysis at 280 °C on Al.

From this analysis it can be concluded that the structure of the coated composite layer displays amorphous-like features, which are likely due to the relatively low temperature of the process and also to the presence of small nanoparticles, which cause intensive broadening of the characteristic diffraction peaks.

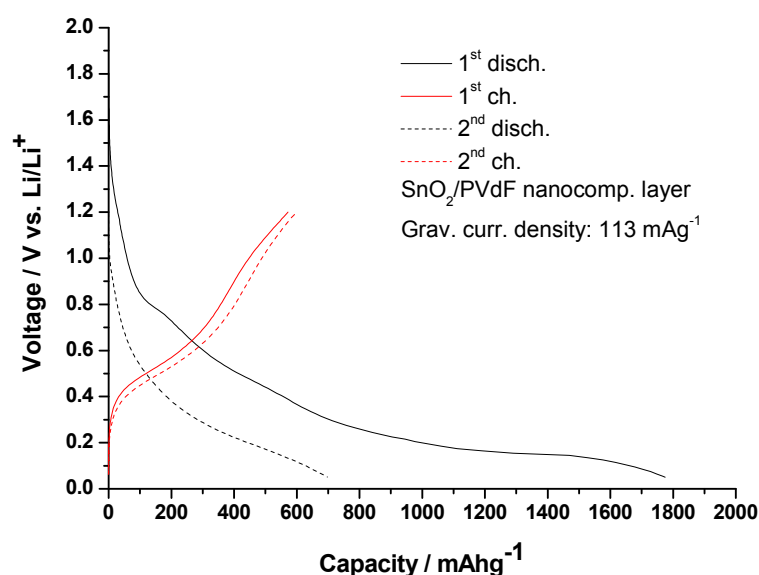
TEM analysis was then carried out in order to further characterize the structure and the texture of these synthesized materials. Fig. 5.7 shows TEM images of the as-produced nanocomposite material.



**Fig. 5.7.** TEM micrographs at different magnifications of the SnO<sub>2</sub>/PVdF nanocomposite obtained by electro spray pyrolysis at 280 °C. Note that the scale bar in image (a) corresponds to 20 nm, while in (b) is 10 nm. In image (b) the arrows indicate a detail of the amorphous PVdF layer in the composite, while the dotted circles highlight some nanocrystals of SnO<sub>2</sub>.

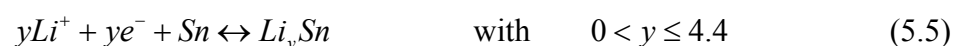
In Fig. 5.7a, the morphology previously observed in Fig. 5.5 becomes further disclosed. Conglomerated droplet relics, ranging approximately from 20 to 100 nm are clearly visible. These remnants are further sub-structured, as shown in Fig. 5.7b, where amorphous layers of PVdF and small nanocrystals of SnO<sub>2</sub> are observed throughout the sample. The analysis of the lattice fringes confirms that a characteristic form of SnO<sub>2</sub> (i.e. cassiterite) has been produced. Therefore, the structure of the electro sprayed deposits consists of an even dispersion of SnO<sub>2</sub> nanocrystals of about 2-5 nm and PVdF. It is important to note that the polymer here surrounds the particles, reinforcing the nanostructured material at a microscopic level, while promoting a mutual adhesion of the deposits and improving the overall contact with the substrate at a macroscopic scale.

The first results of the galvanostatic tests for such SnO<sub>2</sub>/PVdF nanocomposite as negative electrode in a Li battery assembly are presented in Fig. 5.8.



**Fig. 5.8.** Voltage profile of the nanocomposite SnO<sub>2</sub>/PVdF for the first two cycles of discharge-charge at 113 mA g<sup>-1</sup> between 0.0 and 1.2 V.

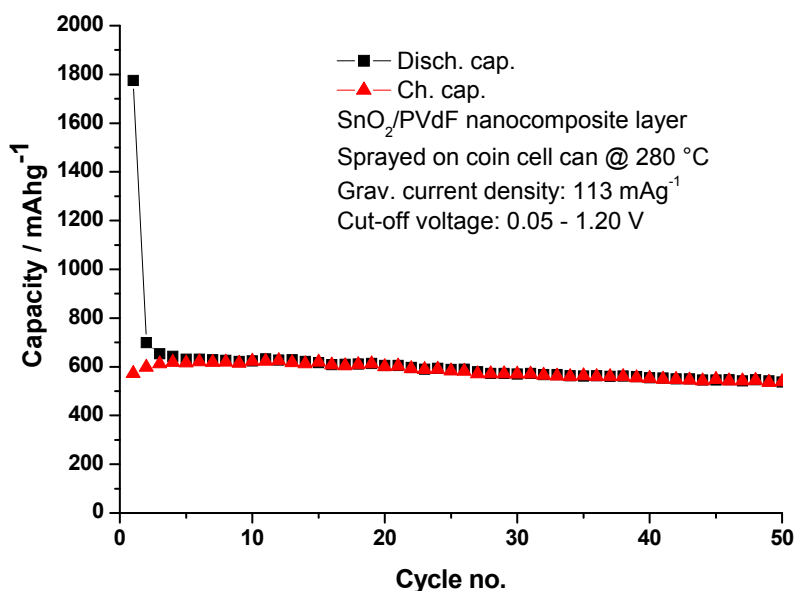
The first discharge capacity in Fig. 5.8 is almost 1800 mAhg<sup>-1</sup>, likely due to the surface area of the composite. Indeed, a remarkable amount of Li is irreversibly consumed in the formation of the SEI layer and in the conversion reaction of the oxide, according to the following general mechanism [46]:



After the first charge up to 1.2 V the recovered capacity is about one third of the initial value, which is in line with the poor reversibility exhibited by SnO<sub>2</sub>.

Surprisingly, no definite plateaus are displayed in the first discharge, and only a slight hump can be detected around 0.8 V. Overall, slopy curves are observed for charge and discharge. This behaviour then suggests that under these conditions the reaction in equation (5.4) takes places in a way where selective equilibrium is favoured to phase segregation. The capacity of both the second discharge and charge exceeded that of the first charge, indicating that a sort of activation of the nanoparticles takes place after the first cycle. Consequently, a small rise in capacity is seen for the first four charges in the following plot of the cycle performance (Fig. 5.9).

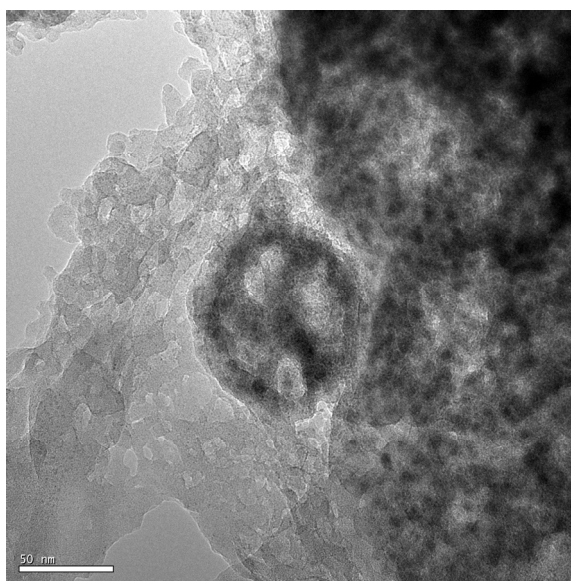
Despite the initial capacity loss, the nanocomposite performed quite well during the following cycles, showing a reversible capacity of  $580 \text{ mAhg}^{-1}$  after 50 cycles, as represented in Fig. 5.9.



**Fig. 5.9.** Cycle performance of the nanocomposite  $\text{SnO}_2/\text{PVdF}$  tested between 0.05 and 1.20 V at a gravimetric current density of  $113 \text{ mAhg}^{-1}$ . Note also the initial increase for the charge capacity.

It is worthwhile to remark that these electrodes were able to cycle without *any* conductive additive, in spite of the fact that  $\text{SnO}_2$  is a semiconductor and PVdF an excellent insulator. The moderate fading of the capacity after the first ten cycles can be also partly due to a limited electronic conductivity. However, the main issue of Sn-based materials is represented by their poor mechanical stability. The severe volume change (i.e. up to 256%) of the Sn host upon reaction with Li (eq. 5.5) usually damages the whole electrode already after a few cycles, especially when the materials are in their bulk form. The use of nanoparticles inhibits cracking and crumbling of the host material, nonetheless the whole composite is still subjected to a remarkable strain. Indeed, the mechanical properties of PVdF are seriously challenged by repeated extension and contraction of the whole electrode [38], as well as by local

loss of adhesion to the surface of the particles due their shape change upon charge and discharge. These circumstances progressively deteriorate the capacity retention for this class of electrodes. From Fig. 5.9 it can be inferred that the mechanical stability of the nanocomposite electrode is quite good and that the entire process of fabrication favoured the adhesion of PVdF, as well as the dispersion of the active nanomaterial. These facts were confirmed by the TEM ‘post mortem’ analysis of the cycled electrode as presented in Fig. 5.10, which shows an image of the nanocomposite materials after 50 cycles of discharge and charge.



**Fig. 5.10.** TEM micrograph for ‘post mortem’ analysis of the nanocomposite SnO<sub>2</sub>/PVdF electrode after 50 entire cycles of discharge-charge between 0.05 and 1.20 V. Note that the scale bar in the image corresponds to 50 nm.

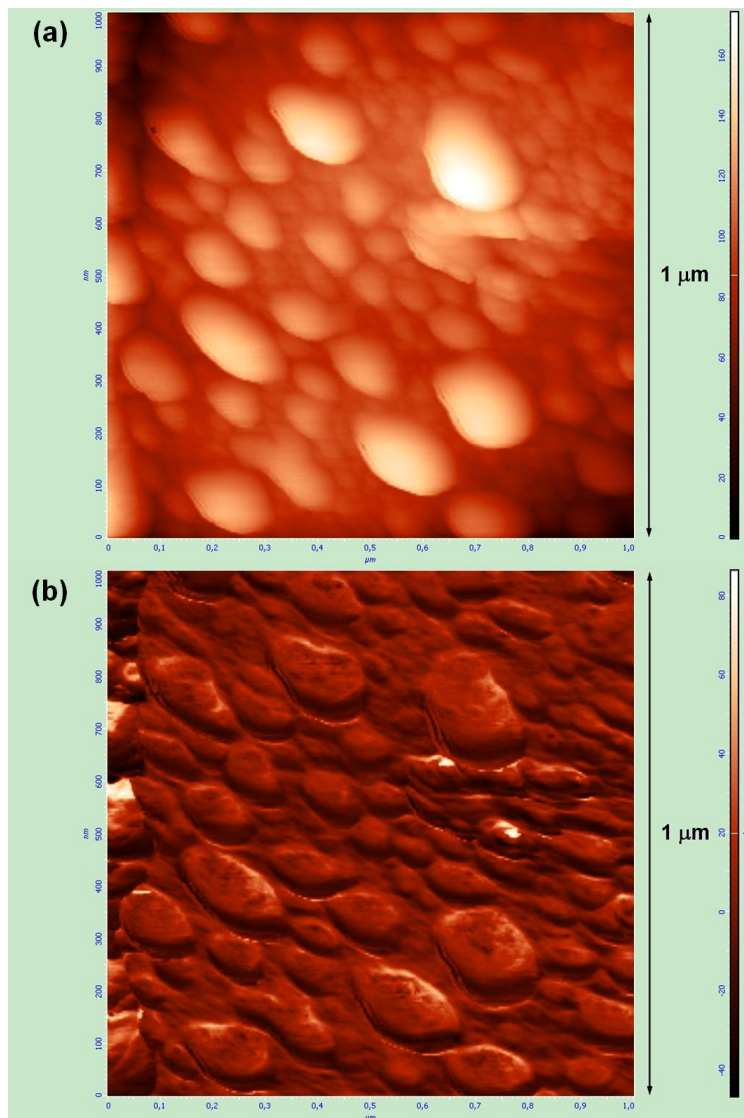
The micrograph displays the presence of nanoparticles, whose size is larger than that of the original nanocrystals. It is however stressed that their sizes are below 20 nm. Clearly, it is seen that the PVdF still surrounds the particles, so conserving the enveloping behaviour. Moreover, the individual reduced Sn nanoparticles did not grow into larger sintered clusters, which are prone to undergo cracking. From the image it is seen that the particles are not damaged by the cycling and that even though they grew in size they retained their structural integrity. Interestingly, also the remnant of a composite electro-sprayed droplet in the middle of Fig. 5.10 maintained its shape and its overall nanostructured features.

These initial results for the direct synthesis and assembly of nanocomposite SnO<sub>2</sub>/PVdF electrodes are promising. Despite the intrinsic hurdles related to the active material and the limited mechanical properties of the PVdF, this approach proved successful and it can be conveniently extended to the fabrication of similar Sn-based electrodes.

*II – CoO/PVdF nanocomposite*

A second example of a nanocomposite electrode synthesized by direct electro spray pyrolysis of  $\text{Co}(\text{CH}_3\text{COO})_2 \cdot 4\text{H}_2\text{O}/\text{PVdF}$  solution at  $280\text{ }^\circ\text{C}$  is now considered and discussed. This concerns the formation of CoO containing electrodes.

Fig. 5.11 represents the local surface morphology of the coated electrode, investigated by AFM. Two different images of the same scanned area are presented, showing the details of the surface topography (a) and the correspondent phase-shift detection (b), respectively.

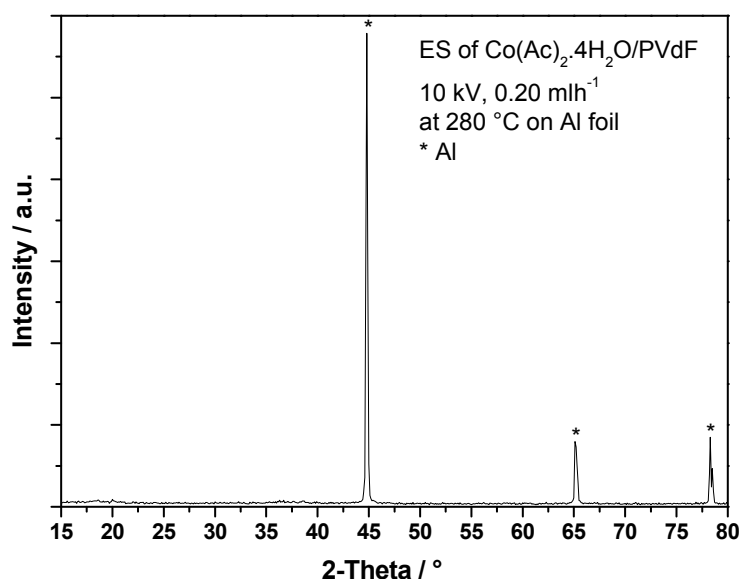


**Fig. 5.11.** AFM micrographs of the local surface morphology of the nanocomposite electrode obtained by direct electro spray pyrolysis of  $\text{Co}(\text{CH}_3\text{COO})_2 \cdot 4\text{H}_2\text{O}/\text{PVdF}$  precursor at  $280\text{ }^\circ\text{C}$ . Topographic image of the surface of the nanocomposite (a). Phase-shift detection image of the same surface (b). The area scanned in the micrographs is  $1\text{ }\mu\text{m} \times 1\text{ }\mu\text{m}$ . Note that the topographic image basically represents the variations in the amplitude of the oscillations of the cantilever, while the phase-shift detection image is related to the change in the phase of the same oscillations.



In both images the spherical-like sub-micrometric relics of the reacted droplets are clearly visible, similarly to those obtained for SnO<sub>2</sub>. In the phase-shift detection image (Fig. 5.11b) the details of the surface area are more discernible. The mapping of the phase-shift enables a deeper analysis of the surface, enhancing the image contrast due to higher sensitivity to the local mechanical properties of the material. In particular, small features which could not be observed in Fig. 5.11a are clearly seen in the remnants of the reacted droplets, displaying the composite nature of the deposited PVdF/CoO.

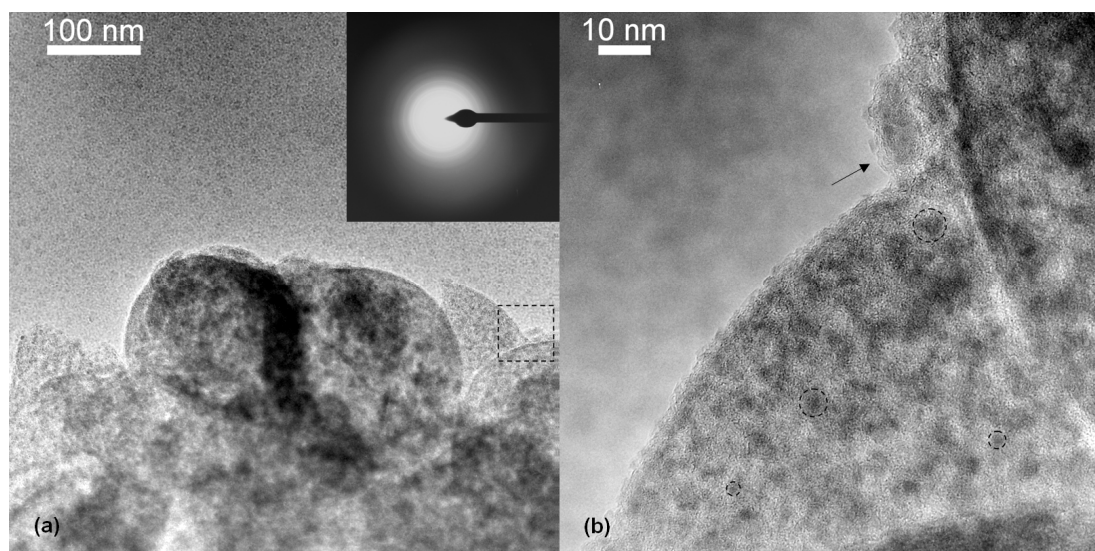
XRD was also performed on the same nanocomposite deposited on Al foil in order to investigate the crystallinity and the structure of the synthesized material. The correspondent diffraction pattern is represented in Fig. 5.12. The sharp diffractions belong to the Al foil, and no characteristic peaks related to the nanocomposite are detected. This fact indicates that the nature of the synthesized material is amorphous. Unfortunately, this result does not contribute to a direct identification of the phase for the cobalt oxide produced. The relatively low temperature of the synthesis process does not favour the formation of crystalline particles.



**Fig. 5.12.** XRD spectrum of the CoO/PVdF composite layer synthesized by electro spray pyrolysis at 280 °C on Al foil. The peaks marked by an asterisk refer to the Al lattice.

Nonetheless, it is known that spray pyrolysis of cobalt acetate solutions under air at low temperatures (i.e. 240-400 °C) results into the formation of a pure CoO phase [47-49], which transforms into Co<sub>3</sub>O<sub>4</sub> only at higher temperatures [49]. Sharp peaks are generally not observed for these CoO materials, but mainly broadened diffractions. In the present case, the small size of the nanoparticles in the PVdF and the strong peaks of the Al substrate have further hindered the detection of possible diffractions.

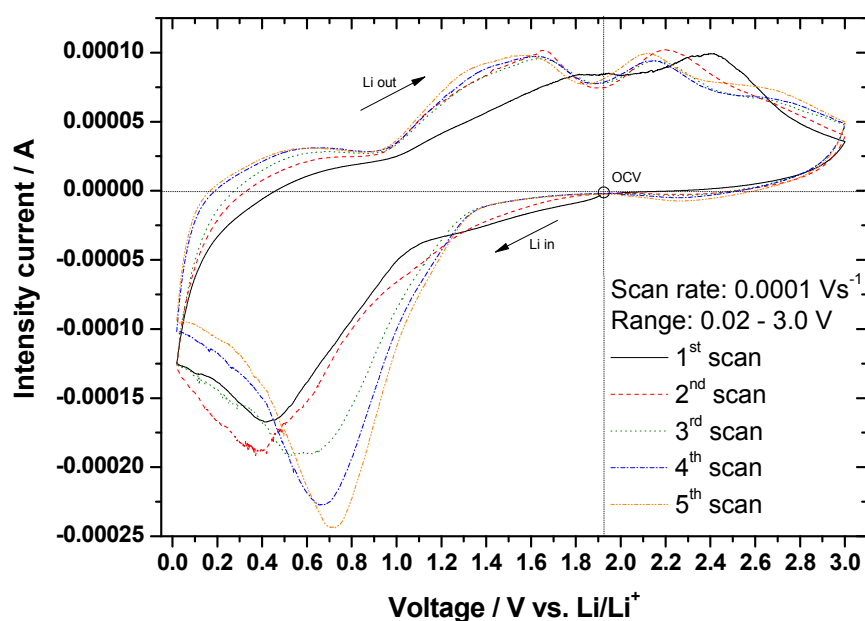
TEM was then carried out in order to shed light on the morphology and the structure of the nanocomposite. Fig. 5.13 displays sub-structures similar to those previously observed in Fig. 5.7 for SnO<sub>2</sub>/PVdF.



**Fig. 5.13.** TEM micrographs at different magnifications of the CoO/PVdF nanocomposite synthesized via electrospray pyrolysis at 280 °C. The inset in (a) is the SAED, while the dotted square encloses a part of the image that is presented in the other micrograph (b) at higher magnification. The arrow points to the amorphous PVdF layer in the composite, while the dotted circles highlight some nanoparticles of CoO.

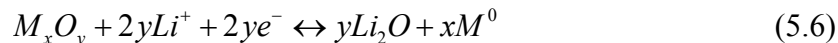
Spherical nanocomposite remnants with size in the range of 150-300 nm, are seen in Fig. 5.13a. The detail represented in Fig. 5.13b at higher magnification shows more clearly their inner structure. Also in this case the PVdF layer is clearly observed together with a multitude of darker spots, which are the synthesized CoO nanoparticles. The nanoparticles are homogeneously dispersed with the PVdF and their typical size roughly span from 1 to 10 nm. These nanoparticles do not exhibit evident lattice fringes, like those detected previously in Fig. 5.7b and appear amorphous. Selected area diffraction (SAED) was also carried out to analyze the crystallinity of the materials. The SAED inset of Fig. 5.13a exhibits a diffused pattern with some faint rings, but clearly no spotty diffractions are clearly visible. This fact supports the substantial amorphous character of the material, matching with the XRD measurements.

The electrochemical behaviour of the nanocomposite electrode was further investigated in a battery assembly by cyclic voltammetry (CV) in order to track down the characteristic reduction and oxidation processes of the material upon reaction with lithium. The CV plot in Fig. 5.14 shows the scans performed on the nanocomposite electrode at a rate of 0.1 mVs<sup>-1</sup> between 0.02 and 3.0 V vs. Li/Li<sup>+</sup>.



**Fig. 5.14.** CV plot for the CoO/PVdF nanocomposite synthesized by electro spray pyrolysis at 280 °C.

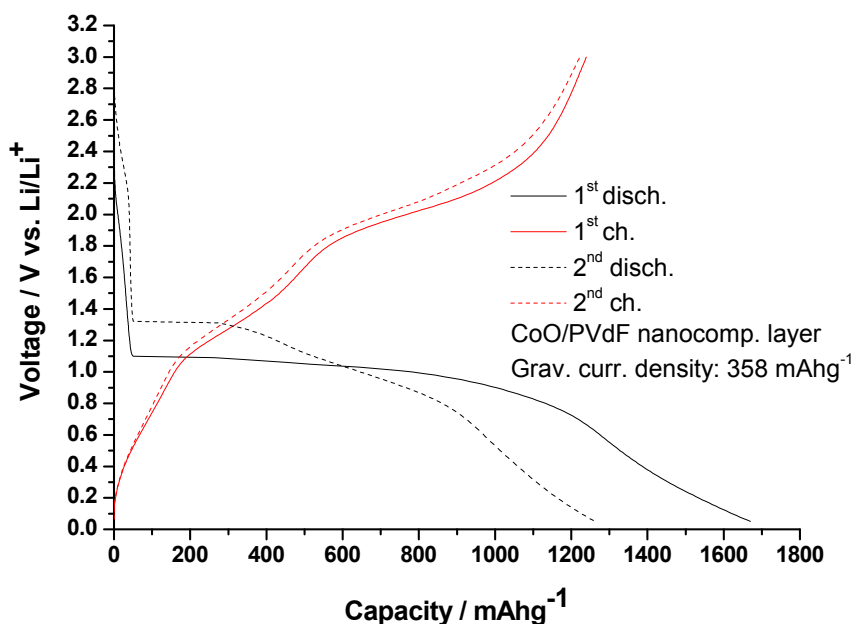
The shape of the profile confirms that the active nanoparticles are made of CoO. The general mechanism of reaction proposed for transition metal oxides (i.e.  $M_xO_y$ , where M is for instance Co, Fe or Cu) is the reversible conversion reaction [17]:



In the case of Co, the initial reaction of CoO with lithium involves the formation of  $Li_2O$  and the simultaneous reduction to metallic Co nanoparticles. This process involves a single step where  $Co^{2+}$  is fully reduced to  $Co^0$  and this feature is typically detected as a cathodic peak around 0.5 V vs.  $Li/Li^+$  [50-52]. Conversely, the reaction of  $Co_3O_4$  involves both  $Co^{3+}$  and  $Co^{2+}$  and the red-ox reaction for the phase transformation of  $Co^{m+}/Co$  is usually complex ( $m$  is between 2 and 3). The process of electron capture and loss in the initial conversion reaction is multi-step and it corresponds normally to two cathodic current peaks around 1.30 and 0.75 V and one anodic current peak around 2.10 V [53]. Nonetheless the crystallinity, the morphology and the particle size of the materials have remarkable influence on the resulting profiles and sometimes only one cathodic peak can be detected around 0.9 V and one anodic peak at 2.0 V for  $Co_3O_4$  [51]. In Fig. 5.14 the first cathodic scan shows only one definite peak around 0.45 V and two anodic peaks at about 1.90 and 2.40 V. The first peak at 0.45 V corresponds to the initial formation of the SEI layer and the generation of  $Li_2O$  together with metallic Co nanoparticles. The lithium consumed in the early formation of the SEI yields an irreversible capacity loss and only a small part of it can be eventually recovered in the following cycles. In the

anodic scan the two peaks are associated to the decomposition of the SEI layer and the recombination of Co and  $\text{Li}_2\text{O}$  to CoO and  $\text{Li}^+$ . The nanocomposite exhibited hysteresis between the lithiation and the de-lithiation processes. The second cycle scan differs from the first one. The main differences observed in the cathodic part are the slight change of slope and the moderate increase of the current peak. No substantial shift is recorded for the reduction peak at 0.45 V. On the other hand, the positions of the oxidation peaks in the same cycle are shifted to lower voltages, 1.60 and 2.2 V, respectively. These values are in agreement with the characteristic oxidation peaks found for CoO electrodes scanned under analogous conditions [50]. In the subsequent cycles the reduction peak shifts progressively to higher voltages and become broader, yielding at the same time larger currents. This interesting feature corresponds to an increase in capacity and indicates a faster kinetics for the reaction. Indeed, this effect can be caused by the activation of the nanoparticles, which should be further transformed into extremely small dots of  $\text{Co}^0$  surrounded by  $\text{Li}_2\text{O}$ , according to the mechanism of equation (5.6). At the same time, the extended interface between  $\text{Li}_2\text{O}$  and  $\text{Co}^0$  causes a significant extra-storage of  $\text{Li}^+$  and  $e^-$  in the respective nano-phases [18-20]. Additionally, the anodic peaks shift a bit towards lower voltages (i.e. 1.5 and 2.1 V) during the following cycles. Their height remains practically constant and a certain broadening is also noticed. A small oxidation shoulder is also detected after the second cycle near 2.7 V, but this feature is not completely clear and could indicate the formation of other species (i.e.  $\text{LiCoO}_2$ ).

The voltage profile of the nanocomposite CoO/PVdF electrode tested galvanostatically at  $358 \text{ mA g}^{-1}$  between 0.05 and 3.0 V is shown in Fig. 5.15.

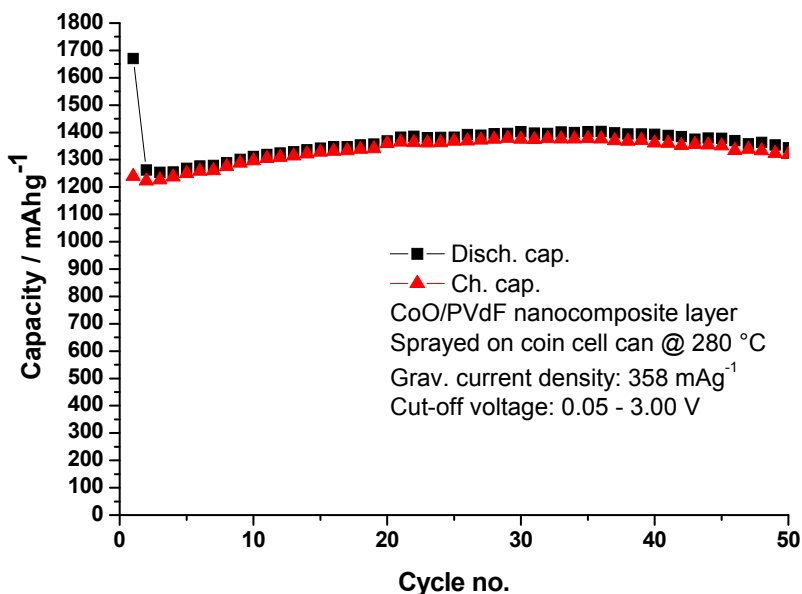


**Fig. 5.15.** Voltage profile of the nanocomposite CoO/PVdF for the first two cycles of discharge-charge at  $358 \text{ mA g}^{-1}$  between 0.05 and 3.0 V. Analogous curves were previously described in ref. [50].

The first discharge curve in Fig. 5.15 shows a long plateau around 1.1 V after the initial voltage drop. The plateau has a slight slope that extends roughly up to 0.6 V and then it is followed by a tail ending at 0.05 V. The initial plateau corresponds to the generation of the SEI layer around the nanoparticles and their simultaneous conversion to metallic Co and Li<sub>2</sub>O. It is worthwhile to note that this reaction accounts for a capacity larger than 1000 mAhg<sup>-1</sup>. Indeed, the theoretical capacity of CoO is 716 mAhg<sup>-1</sup>, and here the large contribution of the plateau is not surprising, considering the large surface area of the nanostructured CoO and the peculiar texture of the deposits (see Fig. 5.13). Additionally, the tail is responsible for a further enhancement of the final capacity which reaches 1670 mAhg<sup>-1</sup>. This part of the curve corresponds to extra storage of Li<sup>+</sup> and e<sup>-</sup> in the respective neighbouring Li<sub>2</sub>O and Co nano-phases [18-20]. Again, the reduced size of the original nanoparticles strengthens this phenomenon, since it enhances the interfacial area. However, the vast reactive surface area is also detrimental for the initial reversibility of the electrode. The consequent enhancement of the impurities due to the synthesis process on the surface of the nanoparticles represents a major hurdle for the initial charge recovery and leads to irreversible trapping of Li in the early stage of SEI formation. In fact, the first charge up to 3.0 V yields a capacity of about 1240 mAhg<sup>-1</sup>, which corresponds approximately to a coulombic efficiency of 74%. Some important features can be observed in the following charge. The steep part of the curve that starts at 0.05 V and bends at 1.1 V corresponds roughly to the extraction of the interfacial charge, while the following part of the curve up to 1.9 V is associated to the decomposition of the SEI layer [50]. For the voltage range of 1.9-3.0 V, the regeneration of CoO then takes place. The second discharge reveals also other interesting characteristics. A small shoulder around 2.2 V is detected in the initial part of the voltage drop between 2.7 and 2.0 V. This feature has been already observed and has been attributed to the intercalation of Li<sup>+</sup> into a small fraction of newly-formed LiCoO<sub>2</sub> [50]. Indeed, it has been demonstrated that a small amount of LiCoO<sub>2</sub> can be spontaneously formed in the presence of CoO, Li<sup>+</sup> and (CO<sub>3</sub>)<sup>2-</sup> [54, 55]. The extraction of Li<sup>+</sup> from LiCoO<sub>2</sub> usually occurs at voltages higher than 2.5 V and that may account for the small oxidation hump detected around 2.7 V in the CV plot after the first two cycles (see Fig. 5.14). Another prominent feature of the second discharge is the flat plateau rising at 1.3 V. This rise in potential is an intrinsic characteristic related to the initial conversion reaction of the CoO and its pulverization in the following cycles. In fact, after its initial decomposition into Co<sup>0</sup> and Li<sub>2</sub>O in the first discharge, only nanoparticles of 1-2 nm are present [17]. The regenerated CoO particles then should have a similar size. Therefore, a reduction of the host particle size occurs here as well during the first charge of the nanocomposite electrode. The result is that upon reaction with Li in the second discharge these CoO nanoparticles are pulverized and their surface energy is decreased due to interaction with the produced Li<sub>2</sub>O [24, 52].

The discharge curve at lower voltages displays a slant segment up to 0.6 V, which is then followed by a tail, as in the first discharge. The following charge curve does not differ from the first one, apart from some minor capacity loss. The subsequent cycles result also in activation for the materials. Indeed, the most interesting features of the electrode can be better appreciated in its performance.

Fig. 5.16 shows the cycle performance of the nanocomposite electrode and the evolution of charge and discharge capacities upon repeated cycling.



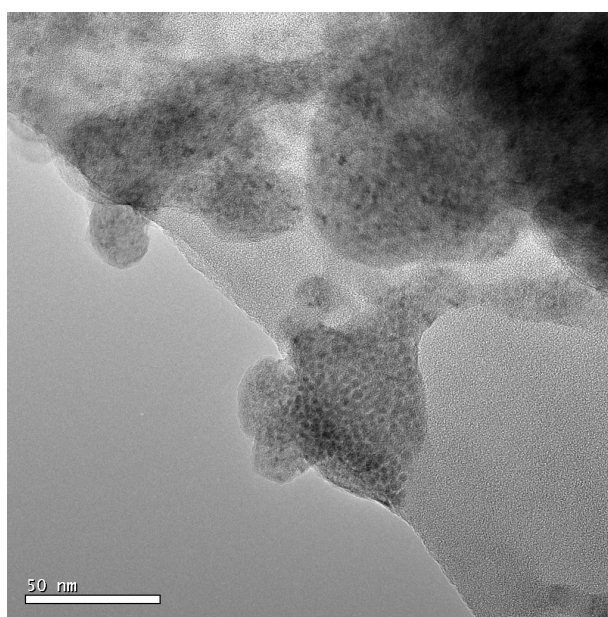
**Fig. 5.16.** Cycle performance of the nanocomposite CoO/PVdF tested between 0.05 and 3.0 V at a gravimetric current density of 358 mA $g^{-1}$ .

Despite the initial irreversible capacity loss in the first cycle, a steady increase of the capacity can be noticed after the 3<sup>rd</sup> cycle up to roughly cycle number 35. Previously this increase in capacity was explained as an ‘activation period’ [50], where for small current densities this enhancement was found up to cycle 22. From Fig. 5.16 it is seen that the correspondent discharge capacity at the 36<sup>th</sup> cycle reaches 1400 mA $hg^{-1}$ . However, this value is still lower than that of the first discharge (i.e. 1670 mA $hg^{-1}$ ). Therefore, it can be concluded that even though the activation period enabled the release of lithium from some irreversible Li<sub>2</sub>O generated during the first cycle, a certain amount of Li<sup>+</sup> is irreversibly lost in the initial reaction, due to the SEI formation and irreversible trapping by impurities. After the 36<sup>th</sup> cycle a slight decrease of the performances takes place. The final value of the discharge capacity after 50 cycles drops to 1350 mA $hg^{-1}$ , which is still more than three times and a half the theoretical value for the graphite. It is remarkable to note that such a result has been obtained without *any* conductive additive and in presence of PVdF. Indeed, the homogeneous formation of extremely small Co<sup>0</sup> dots favours a fast transport of the

electrons through the whole electrode, while the neighbouring  $\text{Li}_2\text{O}$  nano-phase enables both reversible storage and transport of  $\text{Li}^+$  in this particular system.

However, the mechanical strain that the electrode undergoes upon repeated cycling should not be overlooked. Uptake and removal of Li in CoO causes a theoretical volume change of about 52%, which needs to be taken into account and possibly accommodated by the PVdF. The situation of CoO is obviously much more favourable than that of Sn and Si, which both experience huge volume variations upon reaction with Li. The reduced change in volume contributes here to the good cycling performance. The particular structure and morphology of the nanocomposite electrode further improve the mechanical properties of the material, preventing the aggregation of the particles during cycling and enhancing the adhesion of the PVdF on their surface.

'Post mortem' TEM analysis of the cycled electrode confirmed also that the fabrication process was effective in enhancing the properties of the composite material. Fig. 5.17 shows a micrograph of the nanocomposite after 50 cycles.



**Fig. 5.17.** TEM micrograph for 'post mortem' analysis of the nanocomposite CoO/PVdF electrode after 50 entire cycles of discharge-charge between 0.05 and 3.0 V. Note that the scale bar in the image corresponds to 50 nm.

The nanoparticles are clearly separated from each other and their typical size is roughly 5 nm. The PVdF surrounds the particles and hinders their aggregation into large clusters. Moreover, the relics of the electrosprayed droplets, even though distorted, maintained their integrity. In this respect, it is important to observe that the creation of these spheroidal structures introduces an additional curved surface that is

responsible for an extra pressure directed inward, according to the general Young-Laplace equation:

$$\Delta P = \gamma \left( \frac{1}{R_x} + \frac{1}{R_y} \right) \quad (5.7)$$

where  $\Delta P$  is the difference between the inner and the outer pressure,  $\gamma$  is the surface tension and  $R_x$  and  $R_y$  are the two principal radii of curvature of the surface. In the ideal case of a sphere  $R_x = R_y$  and equation (5.7) transforms into:

$$\Delta P = \gamma \frac{2}{R} \quad (5.8)$$

This result is very general and describes, for example, the case of an ideal soap bubble, having only one interface. In the real case the actual value of the pressure is doubled, due to the presence of two interfaces. As far as the nanocomposite spheres are concerned, it is immediately seen that reducing their size implies increasing their internal pressure. This effect is simultaneously present here at two different levels: on the one hand, at the scale length of the individual nanoparticles capped by the polymer and, on the other hand, at the larger scale of the electrospayed remnants. In particular, this phenomenon helps holding the nanoparticles tight inside the reacted droplets and buffering their volume changes upon cycling. These features can be better appreciated later by comparing the micrographs of Figs. 5.20 and 5.24 in the following example of  $\text{Fe}_2\text{O}_3/\text{PVdF}$  nanocomposite.

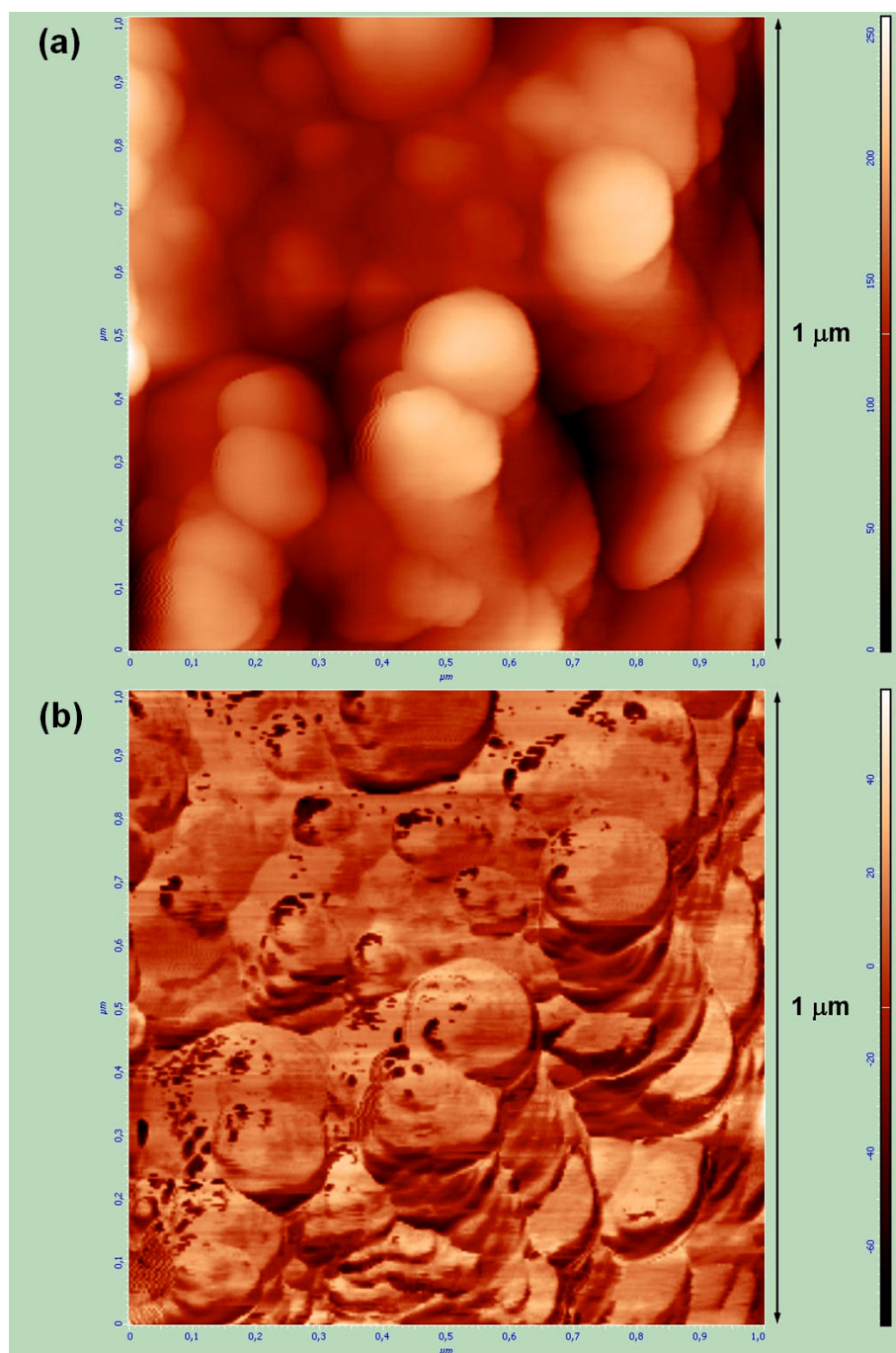
The first results obtained for the  $\text{CoO}/\text{PVdF}$  nanocomposite clearly show the impact of the approach chosen for the fabrication of this type of electrodes. Above all the possibility of tuning the size of the reacted droplets via electrospaying enables a superior control on the morphology of the entire electrode. Accordingly, the sub-micrometric structure of the nanocomposite can be optimized and the electrochemical performances can be even boosted by exploiting the phenomena occurring at the nanoscale (i.e. interfacial charge storage).

### *III – $\text{Fe}_2\text{O}_3/\text{PVdF}$ nanocomposite*

The third example of nanocomposite electrode that has been fabricated in an analogous manner concerns the electrospay pyrolysis of  $\text{Fe}(\text{CH}_3\text{COO})_2/\text{PVdF}$  solution at 280 °C.

Fig. 5.18 shows the local morphology of the surface of the electrode scanned by AFM. Two different images of the same area are presented, showing the details of the surface topography (a) and the correspondent phase-shift detection (b), respectively.

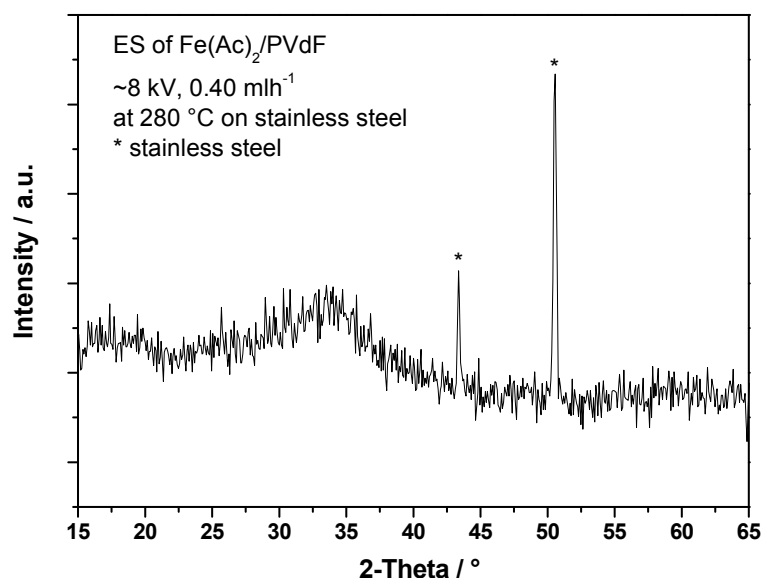




**Fig. 5.18.** AFM micrographs of the local morphology for the surface of the nanocomposite electrode by direct electrospay pyrolysis of  $\text{Fe}(\text{CH}_3\text{COO})_2/\text{PVdF}$  precursor at 280 °C. Topographic image of the surface of the nanocomposite (a). Phase-shift detection image of the same surface (b). The area scanned in the micrographs is 1  $\mu\text{m}$  x 1  $\mu\text{m}$ .

From the topographic image (Fig. 5.18a) it is seen that the deposits have a spherical-like shape and their size is clearly sub-micrometric. The remnants have a typical size of few hundred of nanometers. The composite nature of the material appears more evident in the image showing the contrast of the phase-shift detection (Fig. 5.18b).

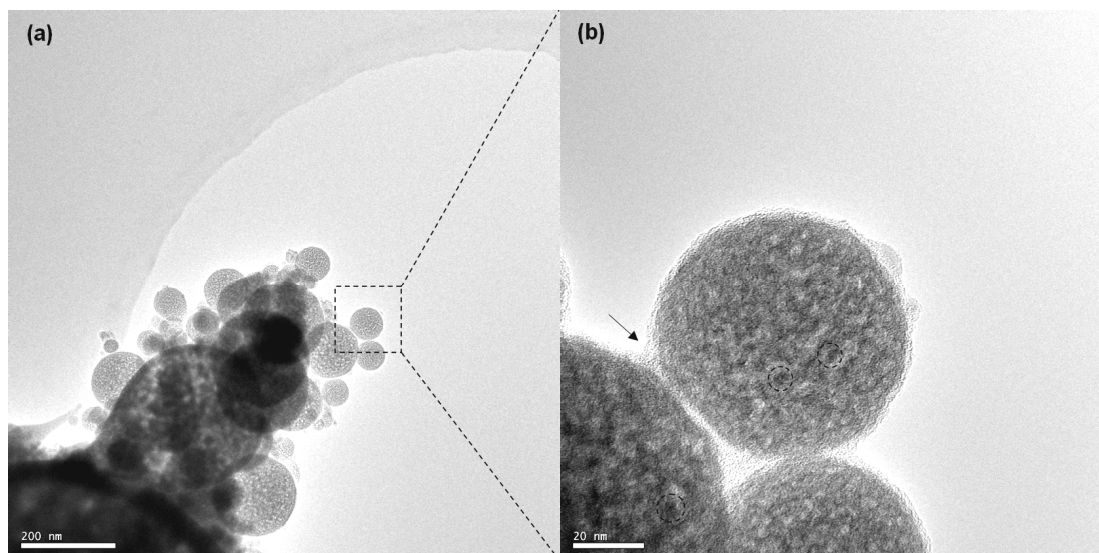
XRD (see Fig. 5.19) was carried out on the material directly deposited on a stainless steel support, in order to obtain a better signal for the nanocomposite layer compared to the deposition on Al foil.



**Fig. 5.19.** XRD spectrum of the Fe<sub>2</sub>O<sub>3</sub>/PVdF nanocomposite electrode synthesized by electrospray pyrolysis at 280 °C on a stainless steel support. The peaks marked by an asterisk refer to the characteristic diffractions of stainless steel.

The only peaks that are clearly visible in the plot are those related to the stainless steel substrate and the nanocomposite layer displays mainly amorphous characteristics. Nevertheless, the broad hump detected around 33° falls within the angular range where the strongest diffractions of Fe<sub>2</sub>O<sub>3</sub> occur. Indeed, characteristic diffractions by the planes (104) and (110) for α-Fe<sub>2</sub>O<sub>3</sub> are due at 33.15 and 35.61°, respectively (JCPDS no. 33-0664). Furthermore, γ-Fe<sub>2</sub>O<sub>3</sub> displays its strongest peak diffraction indexed (311) at 35.65° (JCPDS no. 39-1346). The reduced size of the nanoparticles dispersed within the PVdF and the relatively low temperature for the pyrolysis process are likely responsible for the observed diffraction pattern. However, the dark reddish-brown hue displayed by the fabricated electrodes (see Fig. 5.3c) clearly indicates that Fe<sub>2</sub>O<sub>3</sub> has been produced, since the other iron oxides with different stoichiometry have a distinctive black colour. In this respect, the thermal decomposition of Fe(CH<sub>3</sub>COO)<sub>2</sub> between 150 °C and 1000 °C in air is known to result in Fe<sub>2</sub>O<sub>3</sub>, which has been studied by Mössbauer Spectroscopy and X-ray diffraction, indicating that γ-Fe<sub>2</sub>O<sub>3</sub> and α-Fe<sub>2</sub>O<sub>3</sub> are the products of the thermal treatment for temperatures >250 °C [56]. Decomposition of Fe(CH<sub>3</sub>COO)<sub>2</sub>·2H<sub>2</sub>O in air at 400 °C has been also recently proposed for the production of superparamagnetic γ-Fe<sub>2</sub>O<sub>3</sub> nanoparticles for applications in medicine and biochemistry [57].

The structure of the nanocomposite  $\text{Fe}_2\text{O}_3/\text{PVdF}$  was investigated by TEM as well. In Fig. 5.20 two TEM images with different magnification are presented, showing the characteristic texture of the produced sample.

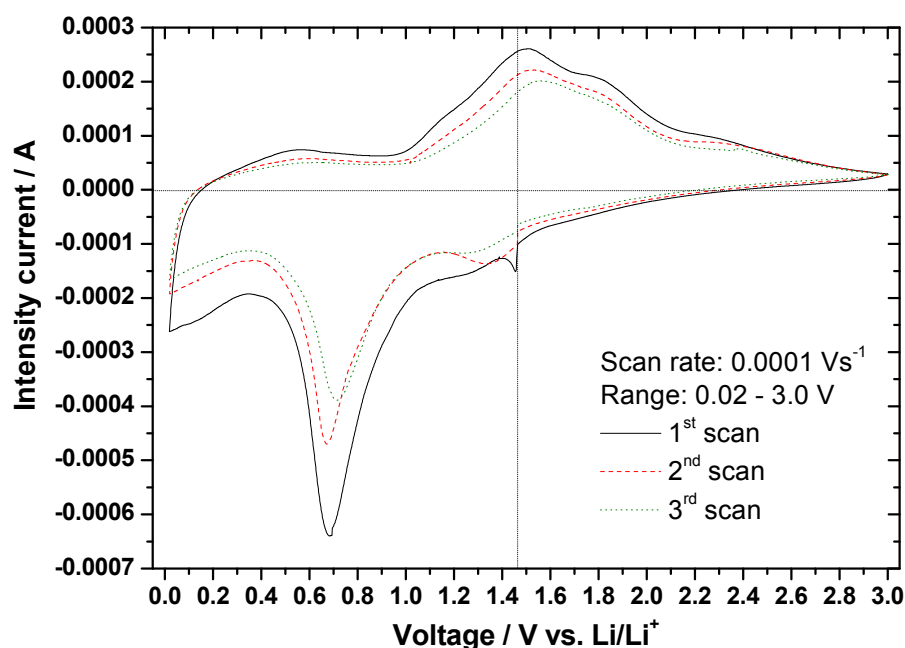


**Fig. 5.20.** TEM micrographs at different magnifications of the  $\text{Fe}_2\text{O}_3/\text{PVdF}$  nanocomposite obtained by electrospay pyrolysis at 280 °C. Note that the scale bar in image (a) corresponds to 200 nm, while in (b) is 20 nm. In image (b) the arrow points to the PVdF layer in the composite, while the dotted circles enclose some nanoparticles of  $\text{Fe}_2\text{O}_3$ .

Fig. 5.20a shows the overall morphology of the synthesized material, where the composite remnants have size similar to those previously obtained by AFM analysis. From this image it is also seen that the relics of the electrospayed droplets are indeed spherical and they are made up of a homogenous, mosaic-like structure in which the iron oxide and the PVdF are finely interdispersed. In the detail at higher magnification (Fig. 5.20b) the surface of these spheres is clearly seen as a layer of PVdF. The dark spots enclosed by the dotted circles in the same image correspond to the  $\text{Fe}_2\text{O}_3$  nanoparticles with size below 10 nm. Also in this case, no evident lattice fringes are observed, confirming the overall amorphous-like nature of the particles.

Cyclic voltammetry (CV) was carried out in order to investigate the reduction and oxidation processes of the material upon reaction with lithium. The CV plot in Fig. 5.21 represents the scans for the first three cycles on the nanocomposite electrode at a rate of  $0.1 \text{ mVs}^{-1}$  between 0.02 and 3.0 V vs.  $\text{Li/Li}^+$ . Comparing the different cycles it is seen that there is not so much difference between the first and the subsequent cycles, apart from the decrease in the overall area enclosed by the respective curves. In the first cycle a peak around 0.65 V appears in the cathodic process, which corresponds to the initial formation of the SEI layer and the conversion reaction of  $\text{Fe}_2\text{O}_3$  into  $\text{Fe}^0$  and  $\text{Li}_2\text{O}$  [58]. In the following anodic part a

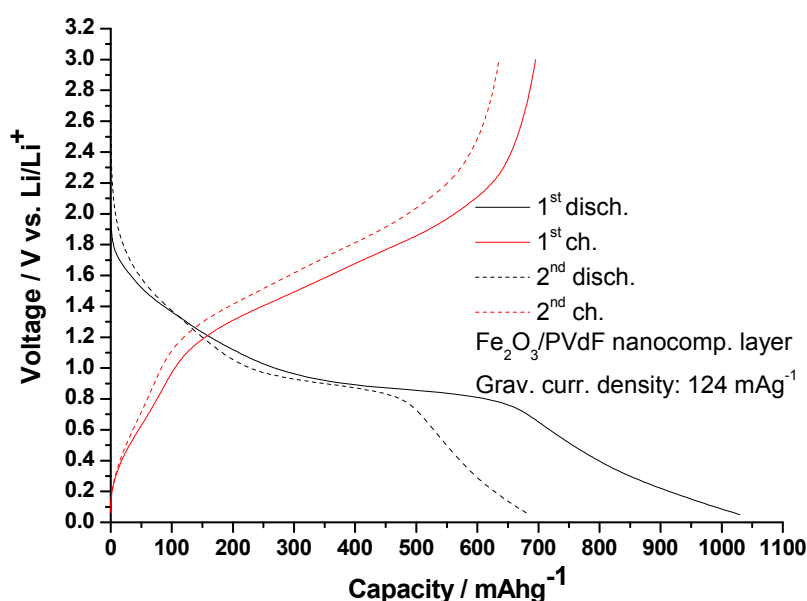
clear oxidation peak is observed at about 1.50 V, accompanied by a broad shoulder around 1.75 V.



**Fig. 5.21.** CV plot for the  $\text{Fe}_2\text{O}_3/\text{PVdF}$  nanocomposite electrode deposited via electrospray pyrolysis at  $280^\circ\text{C}$ .

These two features can be associated to the decomposition of the SEI layer and the reversible oxidation of  $\text{Fe}^0$  to  $\text{Fe}^{3+}$ . In the second cycle a few differences can be still noted. The reduction peak around 0.65 V maintains its position, yet its intensity has decreased and the appearance of a small reduction peak around 1.30 V can be observed. The origin of this feature is unclear, but could be related to the reaction of the electrolyte with the nanoparticles left after the first cycle of conversion and regeneration. The oxidation peak and shoulder around 1.5 and 1.75 V are also not shifted and they gradually merge. The third scan displays characteristics similar to those of the second one, except for a slight shift of the reduction peak towards higher voltages (i.e. 0.70 V) and the weakening of the peak at 1.30 V. Overall, the decrease of the intensities of the reduction/oxidation peaks upon cycling and of the whole area enclosed by the respective curves indicate that irreversible capacity loss takes place in these processes. Unlike the case of CoO nanoparticles, no visible activation of the nanocomposite is here recorded, meaning that the processes for  $\text{Fe}_2\text{O}_3$  are less reversible and probably the interactions with the SEI layer and the interfacial storage are not as effective as in the previous case.

Fig. 5.22 depicts the voltage profile of the  $\text{Fe}_2\text{O}_3/\text{PVdF}$  nanocomposite electrode upon galvanostatic test at  $124\text{ mA g}^{-1}$  between 0.05 and 3.0 V.

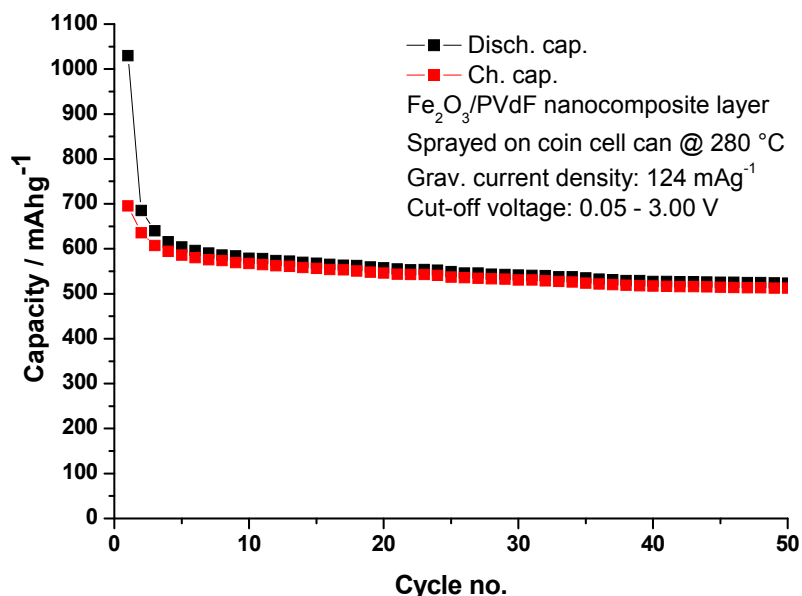


**Fig. 5.22.** Voltage profile of the nanocomposite  $\text{Fe}_2\text{O}_3/\text{PVdF}$  for the first two cycles of discharge-charge at  $124 \text{ mA g}^{-1}$  between 0.05 and 3.0 V.

The first discharge curve presents a long sloping part, followed by a plateau around 0.9 V, corresponding to the conversion reaction of the iron oxide. Then, a tail is also seen at lower voltages ending at 0.05 V. The final value for the discharge capacity is about  $1030 \text{ mAhg}^{-1}$ . The first charge up to 3.0 V reaches almost  $700 \text{ mAhg}^{-1}$ , corresponding to a coulombic efficiency of approximately 68%. A certain irreversibility of the electrode material is also visible in the following discharge and charge curves. They shift towards lower capacity values, displaying profiles very similar to those of the first cycle. Interestingly, no rise in the potential of the ‘conversion plateau’ is recorded during the second discharge, indicating that the process of reaction with lithium is in any case different from that of CoO. Indeed, the particles of  $\text{Fe}_2\text{O}_3$  are not directly decomposed upon reaction with lithium, while the initial formation of an intermediate  $\text{Li}_x\text{Fe}_2\text{O}_3$  compound has been reported [59].

The evolution of charge and discharge capacities upon repeated cycling can be better visualized in Fig. 5.23. The capacity fading is particularly evident in the first five cycles, which account for a slump to about  $600 \text{ mAhg}^{-1}$ . Despite that, after 50 cycles the final capacity is approximately  $515 \text{ mAhg}^{-1}$ . Therefore, it can be concluded that the  $\text{Fe}_2\text{O}_3/\text{PVdF}$  nanocomposite electrode mainly suffers from capacity loss in the first cycles and no activation of the nanoparticles is observed. The following cycles bring about only a moderate capacity fading. In this scenario it is also useful to consider the volume change of the host  $\text{Fe}_2\text{O}_3$  upon lithiation. The complete conversion reaction to form  $2\text{Fe}^0$  and  $3\text{Li}_2\text{O}$  according to equation (5.6) causes a theoretical volume change of about 93%, which needs to be accommodated by the PVdF. This value is not as severe as those related to most Li alloys, still it accounts

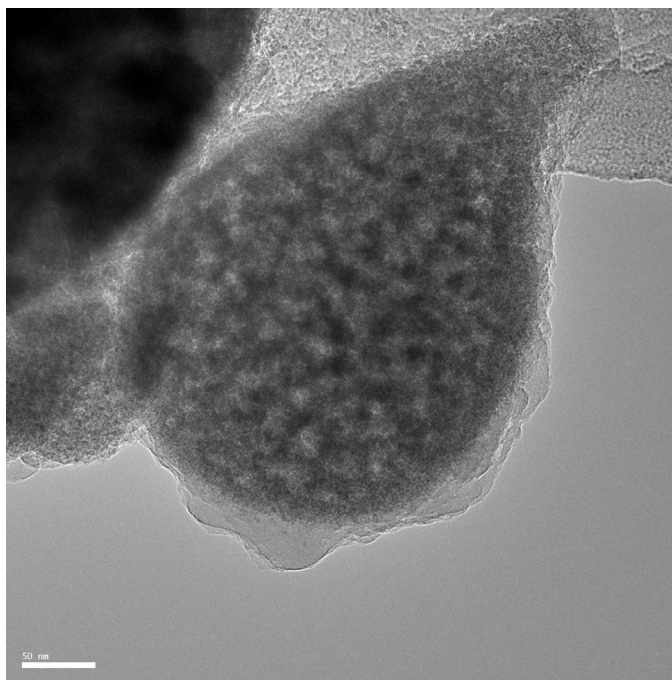
for mechanical strain in the electrode. Besides, the insulating properties of PVdF in the nanocomposite electrode further hamper efficient charge transport for  $\text{Fe}_2\text{O}_3$ , which is a poor electron conductor, especially when compared to other transition metal oxides like  $\text{RuO}_2$ .



**Fig. 5.23.** Cycle performance of the nanocomposite  $\text{Fe}_2\text{O}_3/\text{PVdF}$  tested between 0.05 and 3.0 V at a gravimetric current density of  $124 \text{ mA g}^{-1}$ .

In this respect, the effective transfer of electrons in  $\text{Fe}_2\text{O}_3$  nanomaterials has been addressed in previous studies, showing that it is of utmost importance for sustaining high current densities. In particular, the reduction in size of the active particles is in this case only a pre-requisite to increase the performances of the nanocomposite electrode. Still, it is not sufficient, since also the requirement of good electron transport should be met [60].

‘Post mortem’ TEM analysis was also performed on the cycled electrode in order to study the effects of the electrochemical process on its structure. Fig. 5.24 shows a micrograph of the nanocomposite after 50 cycles. The image reveals that the nanocomposite ‘bubbles’ are not destroyed by the cycling. The nanoparticles are still enclosed in the composite remnant, which maintained its spherical shape. It is interesting to see that the individual particles, despite a certain growth in size and agglomeration are not damaged. They are in close contact and this fact supports the idea that the main issue for  $\text{Fe}_2\text{O}_3$  nanoparticles is represented by the overall electrical conductivity of the composite electrode. From Fig. 5.24 it is seen that the remnant is surrounded by a visible surface layer formed upon cycling. This is probably due to the SEI formation and growth, which further hinders the electronic conduction.



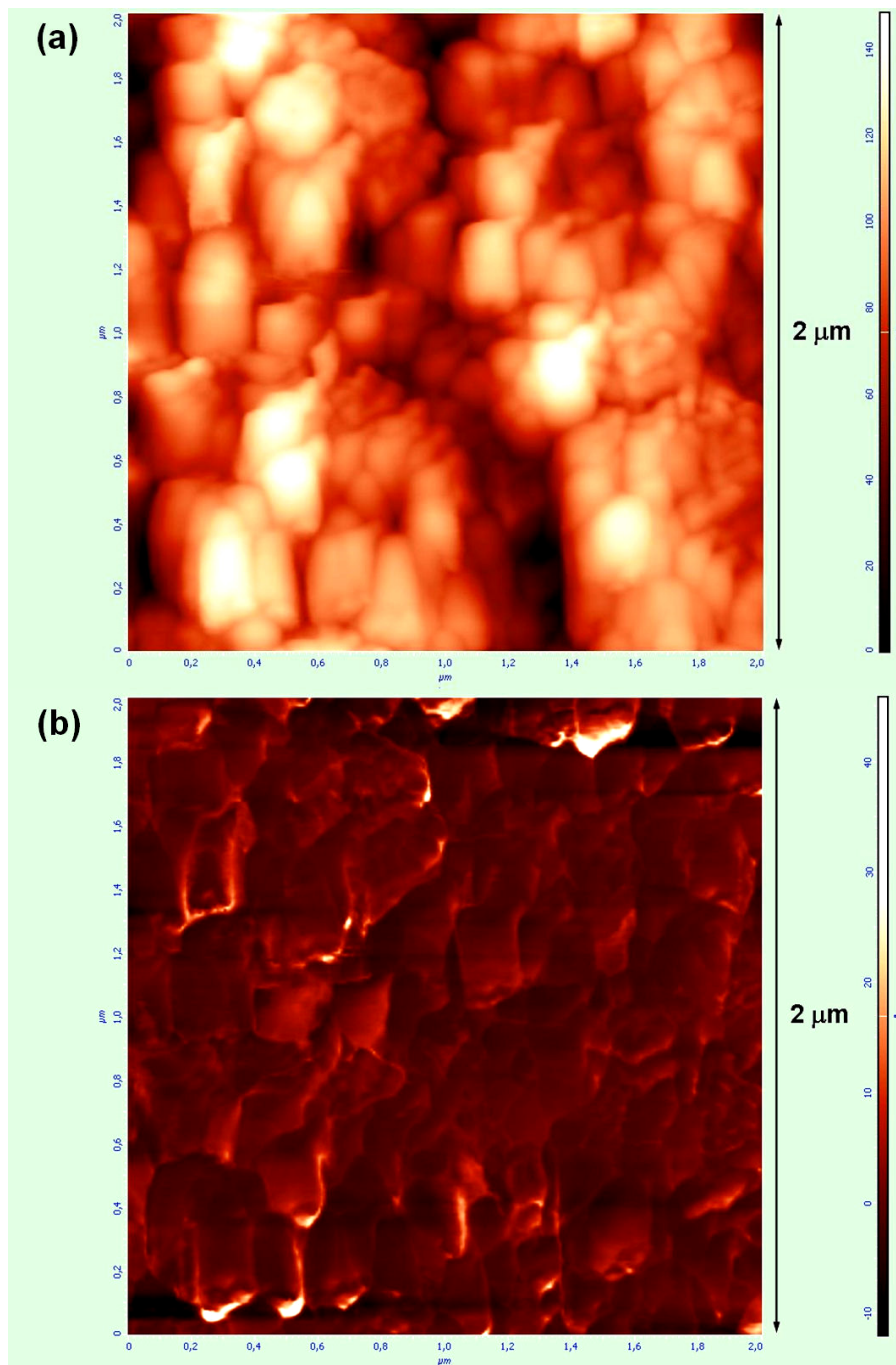
**Fig. 5.24.** TEM micrograph for ‘post mortem’ analysis of the nanocomposite  $\text{Fe}_2\text{O}_3/\text{PVdF}$  electrode after 50 cycles of discharge-charge between 0.05 and 3.0 V. Note that the scale bar in the image corresponds to 50 nm.

Therefore, it can be concluded that the  $\text{Fe}_2\text{O}_3/\text{PVdF}$  nanocomposite cycled relatively well, especially if one takes into account the intrinsic limitations arising from the electrical properties of the oxide and the absence of any conductive additive to promote the conduction between the composite structures. In particular, the possibility of having a carbon coating or filler around the remnants could lead to sensible improvement in the performances.

#### *IV – nano-Si/PVdF composite*

The last example of fabrication concerns the deposition of coated electrodes from a concentrated precursor suspension containing pre-formed Si nanoparticles added to dissolved PVdF. The electro spray deposition can be eventually performed at lower temperatures (i.e. 200 °C), since under these circumstances pyrolysis is not needed to form the active particles and the evaporation of the solvent (i.e. NMP) for the consolidation of the PVdF is directly promoted by the electro spray process.

Fig. 5.25 shows the local morphology of the surface of the composite electrode scanned by AFM. The images depict the same area, displaying the details of the surface topography (a) and the correspondent phase-shift detection (b), respectively. In Fig. 5.25a the electro sprayed deposits are easily seen. They exhibit sub-micrometric size and their shapes do not show the typical spherical structures as observed for the oxides.

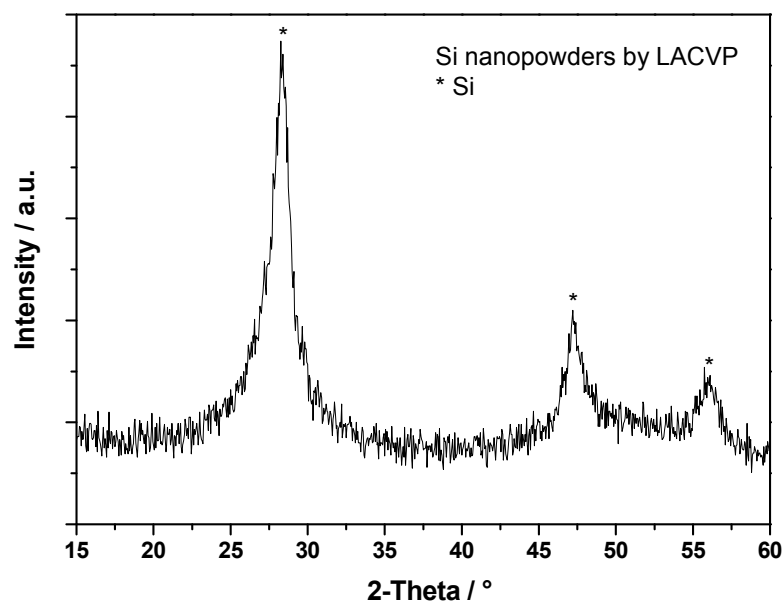


**Fig. 5.25.** AFM micrographs of the local morphology of the composite electrode by electrospray deposition of a concentrated suspension of nano-Si/PVdF at 200 °C. Topographic image of the surface of the composite electrode (a). Phase-shift detection image of the same surface (b). The area scanned in the micrographs is 2 μm x 2 μm.

The agglomeration of the nanoparticles in the composite deposits is further disclosed in Fig. 5.25b, where the phase contrast enables a clearer vision of the intimate structure of the remnants.



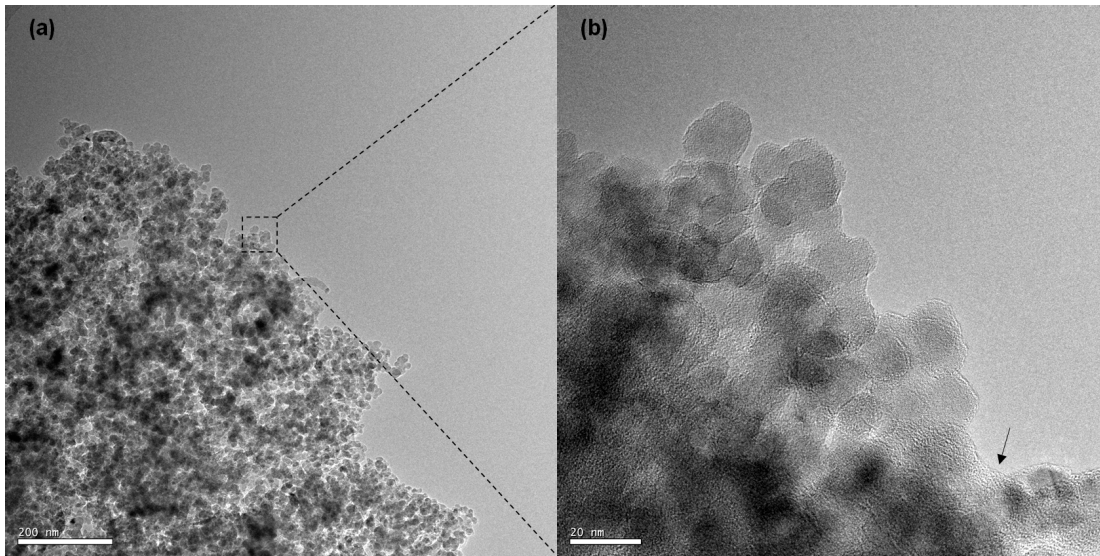
Fig. 5.26 presents the XRD pattern of the pristine Si nanoparticles synthesized by LACVP, as mentioned earlier.



**Fig. 5.26.** XRD spectrum of the pristine Si nanopowders synthesized by LACVP. The peaks marked by an asterisk refer to the characteristic diffractions of the Si lattice. Note the broadening of the peaks.

The diffraction pattern of Fig. 5.26 indicates that the Si nanoparticles generated by LACVP are crystalline. The three broad peaks observed around 28, 47 and 56 ° match respectively with the characteristic planes (111), (220) and (311) of the Si lattice, according to the crystallographic data (i.e. JCPDS no. 75-0590). No traces of crystalline Si oxides are detected in the spectrum, meaning that surface oxidation of the particles likely resulted in an amorphous oxide layer, which accounts for the stability of the nanoparticles in air.

The morphology and the structure of the nanoparticles in the deposited composite can be visualized in the TEM images of Fig. 5.27. From Fig. 5.27a it can be noted that the Si particles are agglomerated within the composite. A typical size of about 20-50 nm is observed for most of the particles, which overall exhibit a quite homogeneous size distribution. In this particular case it is somehow difficult to clearly distinguish the PVdF. Even in the detail at higher magnification (Fig. 5.27b) it is not completely clear if the PVdF surrounds the single particles or not (i.e. the amorphous layer pointed by the arrow is probably PVdF, however the individual particles are also surrounded by an amorphous layer, which is likely a surface oxide).

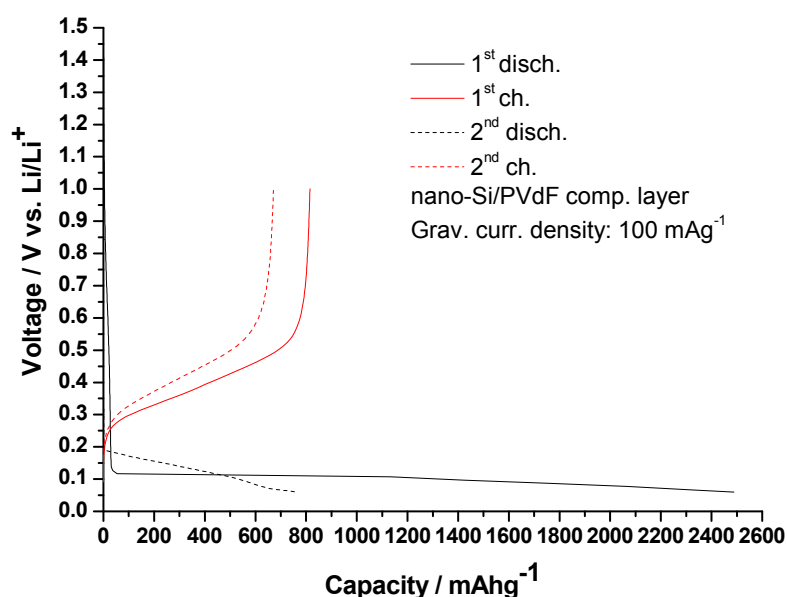


**Fig. 5.27.** TEM micrographs at different magnifications of the nano-Si/PVdF composite after electro spray deposition at 200 °C. Note that the scale bar in image (a) corresponds to 200 nm, while in (b) is 10 nm. In image (b) the arrow points to the amorphous surface layer of the particles.

In particular, it is important to bear in mind that the PVdF should preferably surround the particle agglomerates, rather than the single nanoparticles, since the processes of particle synthesis and electrode assembly are here separated. Indeed, the process of dispersion of the pre-formed nanoparticles by sonication in the dissolved PVdF solution to form the precursor suspension cannot be compared to the previous cases, where homogenous nanocomposite remnants directly resulted from the reacted droplets of the electro sprayed solution.

The voltage profile of the composite nano-Si/PVdF electrode tested galvanostatically at a gravimetric current density of about  $100 \text{ mA g}^{-1}$  between 0.06 and 1.0 V is presented in Fig. 5.28.

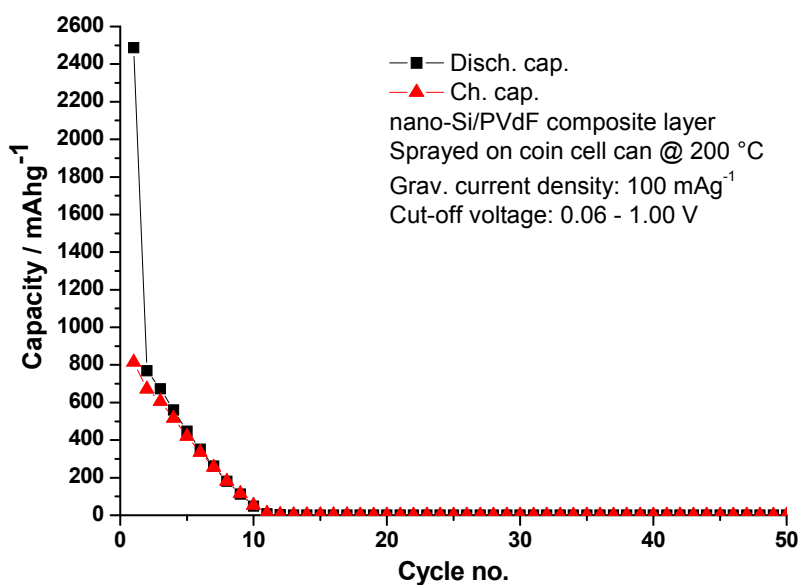
From the first discharge curve of Fig. 5.28 a sharp voltage drop is seen, followed by a long flat plateau starting around 0.1 V and ending at 0.06 V. This lower voltage threshold has been chosen in order to limit the capacity of the electrode to about  $2500 \text{ mAh g}^{-1}$  and to avoid the formation of the Li-rich alloy phase (i.e.  $\text{Li}_{22}\text{Si}_5$ ). This phase corresponds to a theoretical capacity of about  $4200 \text{ mAh g}^{-1}$ , still it is responsible for a huge volume change of the Si host lattice (i.e. theoretically 323%). Indeed, the alloying reaction of Li with Si causes a complete restructuring of the host lattice with the nucleation of intermediate intermetallic compounds and an increasing amount of mechanical stress in the composite electrode. In this respect, the nanoparticles can help buffering the local strain experienced by the material, yet the severe volume variation of the whole electrode cannot be simply accommodated by a binder like the PVdF, whose composite films with carbon black can generally be stretched to approximately 4 % before breaking [38].



**Fig. 5.28.** Voltage profile of the composite nano-Si/PVdF for the first two cycles of discharge-charge at  $100 \text{ mA g}^{-1}$  between 0.06 and 1.0 V.

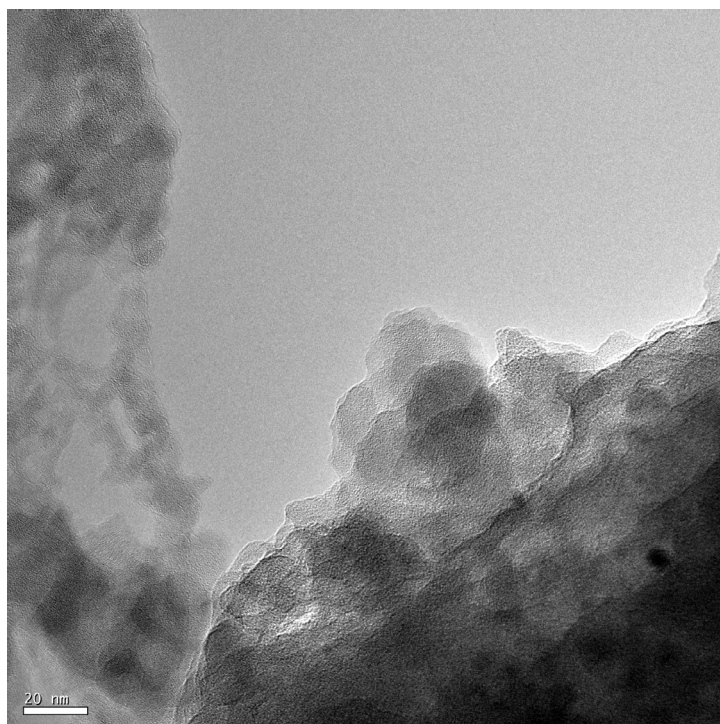
It is worthwhile to observe that the electrode is able to react with Li and start cycling without *any* conductive additive, despite the poor conductivity of the passivated Si particles and the insulating PVdF. However, the first charge up to 1.0 V displays a severe capacity fading to about  $810 \text{ mAhg}^{-1}$ , meaning that the charge recovery process is not efficient (i.e. 32%). It is difficult to assess which is the main cause for this severe capacity loss, but likely all the aforementioned issues are involved. The second discharge yields a capacity of approximately  $770 \text{ mAhg}^{-1}$ , followed by a second charge that drops to  $670 \text{ mAhg}^{-1}$ . Therefore, it is clear that the loss of capacity is still present after the first cycle, as it is also noted from the steeper slope of the second discharge-charge curves.

The evolution of charge and discharge capacities with increasing cycle number can be better visualized in Fig. 5.29, which shows the performance of the electrode. From this plot it is clearly seen that the nano-Si/PVdF electrode fails after 10 cycles. This fact is not surprising, since probably the PVdF does not completely surround the Si particles, but mainly their agglomerates, which are much easier to break. Moreover, the electronic transport at the interfaces is hampered by the scarce conductivity of the materials, while the adhesion and the strength of the PVdF are likely not sufficient to sustain repeated cycling. A possible way to improve the mechanical behaviour of PVdF in composite electrodes is to perform a thermal treatment up to  $350 \text{ }^\circ\text{C}$  [42]. Nonetheless, in this specific case it is of utmost importance to have the individual particles well dispersed within the binder, otherwise the positive effect of the heat treatment is ruled out by the fracture of the agglomerates and the loss of mutual contact for the individual particles.



**Fig. 5.29.** Cycle performance of the composite nano-Si/PVdF tested between 0.06 and 1.0 V at a gravimetric current density of 100 mA<sub>g</sub><sup>-1</sup>.

Finally, a ‘post mortem’ TEM analysis of the cycled electrode was performed in order to investigate the local structure of the composite after 50 cycles. Fig. 5.30 shows a micrograph of the material after the electrochemical process.



**Fig. 5.30.** TEM micrograph for ‘post mortem’ analysis of the nano-Si/PVdF composite electrode after 50 cycles of discharge-charge between 0.06 and 1.0 V. Note that the scale bar in the image corresponds to 20 nm.

In the image the PVdF and the embedded particles can be discerned. The individual particles do not seem damaged by the cycling, still the appearance of the sample suggests that materials with inhomogeneous size are left. Unlike the examples discussed previously, the composite does not exhibit distinctive features that can be directly related to the droplets produced by electrospaying.

Even though the preliminary electrochemical results are not encouraging for this type of nano-Si/PVdF composite this example is yet instructive. It highlights the importance not only of the choice of the different materials, but also of the way in which the single constituents are arranged in the whole electrode structure, as well as the crucial role of electrical contact and transport properties.

## 5.4 Conclusions and outlook

The results presented so far demonstrate that electrospay is a powerful technique that can be successfully applied to the fabrication of nanocomposite electrodes and that several types of materials can be manipulated at the same time in a direct, one-step process. The coated layers directly synthesized and assembled via this approach find a direct application in negative electrodes for Li-ion batteries. However, it is clear that this method offers much wider possibilities to directly produce nanocomposite layers for a multitude of different purposes. Tailoring the precursor droplet size, as well as the other experimental parameters influencing the transport and the chemical reactions of the precursors is of extreme importance for a successful fabrication of the layers. In particular, the results show that the local structure and morphology of the resulting nanocomposite droplet remnants influence the electrochemical behaviour of the electrodes. In this respect, the homogeneity in size for the active particles can be considered as a pre-requisite for a good electrochemical behaviour of the electrodes. Indeed, the intimate characteristics of the sub-micrometric structures constituting the electrode, as well as the even dispersion and adhesion of the binder on the nanoparticles' surface, play a key role in determining and enhancing the actual performances of the nanocomposites, especially when a suitable matching of the mechanical and electrical properties of the materials is involved.

As previously mentioned, the versatility of electrospaying makes it also possible to devise various approaches and strategies in order to fabricate nanocomposite layers and to implement their manufacture in full in-line, roll-to-roll processes. Commercial laminated electrodes with double-sided coatings by paste casting could be replaced by metal foils directly coated by simultaneous 'electrospaying-assisted printing' on both sides with obvious advantages. Different spraying configurations are clearly possible for this purpose and the use of bipolar coagulation is also an option.

As far as the precursor solution or suspension is concerned it is worthwhile to point out that only two types of preparation have been considered so far. Indeed, starting from the blank polymer solution three different approaches can be adopted for the creation of composite layers containing active nanoparticles. The first one is to dissolve the metal precursor and then to perform pyrolysis; the second one is to prepare a suspension by adding and dispersing pre-formed particles separately synthesized via gas-phase or solid-state syntheses; the third one is to generate in situ the nanoparticles within the metal precursor solution by red-ox reactions in the liquid phase accompanied by direct polymer capping, in order to form a very homogeneous ink for subsequent electrospray. This third approach has not been described here, though some preliminary experiments have been carried out. Therefore, it also represent an alternative route that is particularly attractive for having functional coatings directly by electrospray or even by ink-jet printing at relatively low temperatures.

## 5.5 References

- [1] J. Maier, *Nature Materials* **2005**, *4*, 805.
- [2] Y. G. Guo, J. S. Hu, L. J. Wan, *Advanced Materials* **2008**, *20*, 2878.
- [3] J. Maier, *Journal of Electroceramics* **2004**, *13*, 593.
- [4] J. Maier, *Solid State Ionics* **2004**, *175*, 7.
- [5] J. Maier, *Physical Chemistry Chemical Physics* **2009**, *11*, 3011.
- [6] A. S. Arico', P. Bruce, B. Scrosati, J. M. Tarascon, W. Van Schalkwijk, *Nature Materials* **2005**, *4*, 366.
- [7] M. Armand, J. M. Tarascon, *Nature* **2008**, *451*, 652.
- [8] P. Balaya, A. J. Bhattacharyya, J. Jamnik, Y. F. Zhukovskii, E. A. Kotomin, J. Maier, *Journal of Power Sources* **2006**, *159*, 171.
- [9] J. O. Besenhard, J. Yang, M. Winter, *Journal of Power Sources* **1997**, *68*, 87.
- [10] L. Beaulieu, D. Larcher, R. A. Dunlap, J. R. Dahn, *Journal of Alloys and Compounds* **2000**, *297*, 122.
- [11] J. M. Tarascon, M. Armand, *Nature* **2001**, *414*, 359.
- [12] S. Panero, B. Scrosati, M. Wachtler, F. Croce, *Journal of Power Sources* **2004**, *129*, 90.
- [13] J. Maier, *Journal of Power Sources* **2007**, *174*, 569.
- [14] M. Winter, J. O. Besenhard, *Electrochimica Acta* **1999**, *45*, 31.
- [15] J. Yang, M. Wachtler, M. Winter, J. O. Besenhard, *Electrochemical and Solid-State Letters* **1999**, *2*, 161.
- [16] J. Graetz, C. C. Ahn, R. Yazami, B. Fultz, *Electrochemical and Solid-State Letters* **2003**, *6*.
- [17] P. Poizot, S. Laruelle, S. Grugeon, L. Dupont, J. M. Tarascon, *Nature* **2000**, *407*, 496.

- [18] P. Balaya, H. Li, L. Kienle, J. Maier, *Advanced Functional Materials* **2003**, *13*, 621.
- [19] J. Jannik, J. Maier, *Physical Chemistry Chemical Physics* **2003**, *5*, 5215.
- [20] J. Maier, *Faraday Discussions* **2007**, *134*, 51.
- [21] G. Derrien, J. Hassoun, S. Panero, B. Scrosati, *Advanced Materials* **2007**, *19*, 2336.
- [22] R. Demir Cakan, M. M. Titirici, M. Antonietti, G. Cui, J. Maier, Y. S. Hu, *Chemical Communications* **2008**, 3759.
- [23] R. Demir-Cakan, Y. S. Hu, M. Antonietti, J. Maier, M. M. Titirici, *Chemistry of Materials* **2008**, *20*, 1227.
- [24] R. Yang, Z. Wang, J. Liu, L. Chen, *Electrochemical and Solid-State Letters* **2004**, *7*.
- [25] G. Cui, Y. S. Hu, L. Zhi, D. Wu, I. Lieberwirth, J. Maier, K. Mullen, *Small* **2007**, *3*, 2066.
- [26] S. T. Chang, I. C. Leo, C. L. Liao, J. H. Yen, M. H. Hon, *Journal of Materials Chemistry* **2004**, *14*, 1821.
- [27] N. Li, C. R. Martin, *Journal of the Electrochemical Society* **2001**, *148*.
- [28] N. Li, C. R. Martin, B. Scrosati, *Electrochemical and Solid-State Letters* **2000**, *3*, 316.
- [29] L. Y. Beaulieu, T. D. Hatchard, A. Bonakdarpour, M. D. Fleischauer, J. R. Dahn, *Journal of the Electrochemical Society* **2003**, *150*.
- [30] C. K. Chan, X. F. Zhang, Y. Cui, *Nano Letters* **2008**, *8*, 307.
- [31] C. K. Chan, R. Ruffo, S. S. Hong, R. A. Huggins, Y. Cui, *Journal of Power Sources* **2009**, *189*, 34.
- [32] L. Bazin, S. Mitra, P. L. Taberna, P. Poizot, M. Gressier, M. J. Menu, A. Barnabe', P. Simon, J. M. Tarascon, *Journal of Power Sources* **2009**, *188*, 578.
- [33] P. L. Taberna, S. Mitra, P. Poizot, P. Simon, J. M. Tarascon, *Nature Materials* **2006**, *5*, 567.
- [34] C. K. Chan, H. Peng, G. Liu, K. McIlwrath, X. F. Zhang, R. A. Huggins, Y. Cui, *Nature Nanotechnology* **2008**, *3*, 31.
- [35] Y. Li, B. Tan, Y. Wu, *Journal of the American Chemical Society* **2006**, *128*, 14258.
- [36] Y. Li, B. Tan, Y. Wu, *Nano Letters* **2008**, *8*, 265.
- [37] J. Li, R. B. Lewis, J. R. Dahn, *Electrochemical and Solid-State Letters* **2007**, *10*.
- [38] Z. Chen, L. Christensen, J. R. Dahn, *Journal of Applied Polymer Science* **2003**, *90*, 1891.
- [39] Z. Chen, L. Christensen, J. R. Dahn, *Electrochemistry Communications* **2003**, *5*, 919.
- [40] Z. Chen, L. Christensen, J. R. Dahn, *Journal of the Electrochemical Society* **2003**, *150*.
- [41] J. van Erven, Munao, D., Fu, Z., Trzeciak, T., Janssen, R., Kelder, E., Marijnissen, J.C.M., *KONA Powder and Particle Journal* **2009**, *27*, 157.
- [42] J. Li, L. Christensen, M. N. Obrovac, K. C. Hewitt, J. R. Dahn, *Journal of the Electrochemical Society* **2008**, *155*.
- [43] I. B. Rietveld, K. Kobayashi, H. Yamada, K. Matsushige, *Journal of Physical Chemistry B* **2006**, *110*, 23351.

- [44] J. Zhang, L. B. Chen, C. C. Li, T. H. Wang, *Applied Physics Letters* **2008**, *93*.
- [45] C. S. Yang, Q. Liu, S. M. Kauzlarich, B. Philips, *Chemistry of Materials* **2000**, *12*, 983.
- [46] I. A. Courtney, J. R. Dahn, *Journal of the Electrochemical Society* **1997**, *144*, 2045.
- [47] C. Chen, E. M. Kelder, J. Schoonman, *Journal of the Electrochemical Society* **1997**, *144*.
- [48] Y. Yu, C. H. Chen, J. L. Shui, S. Xie, *Angewandte Chemie - International Edition* **2005**, *44*, 7085.
- [49] Z. W. Zhao, K. Konstantinov, L. Yuan, H. K. Liu, S. X. Dou, *Journal of Nanoscience and Nanotechnology* **2004**, *4*, 861.
- [50] J. S. Do, C. H. Weng, *Journal of Power Sources* **2006**, *159*, 323.
- [51] G. X. Wang, Y. Chen, K. Konstantinov, M. Lindsay, H. K. Liu, S. X. Dou, *Journal of Power Sources* **2002**, *109*, 142.
- [52] F. Li, Q. Q. Zou, Y. Y. Xia, *Journal of Power Sources* **2008**, *177*, 546.
- [53] W. Y. Li, L. N. Xu, J. Chen, *Advanced Functional Materials* **2005**, *15*, 851.
- [54] P. Tomczyk, H. Sato, K. Yamada, T. Nishina, I. Uchida, *Journal of Electroanalytical Chemistry* **1995**, *391*, 133.
- [55] P. Tomczyk, M. Mosialek, J. Oblkowski, *Electrochimica Acta* **2001**, *47*, 945.
- [56] S. Music, M. Ristic, S. Popovic, *Journal of Radioanalytical and Nuclear Chemistry Articles* **1988**, *121*, 61.
- [57] K. Kluchova, R. Zboril, J. Tucek, M. Pecova, L. Zajoncova, I. Safarik, M. Mashlan, I. Markova, D. Jancik, M. Sebel, H. Bartonkova, V. Bellesi, P. Novak, D. Petridis, *Biomaterials* **2009**, *30*, 2855.
- [58] H. Liu, G. Wang, J. Park, J. Wang, C. Zhang, *Electrochimica Acta* **2009**, *54*, 1733.
- [59] D. Larcher, C. Masquelier, D. Bonnin, Y. Chabre, V. Masson, J. B. Leriche, J. M. Tarascon, *Journal of the Electrochemical Society* **2003**, *150*.
- [60] F. Jiao, J. Bao, P. G. Bruce, *Electrochemical and Solid-State Letters* **2007**, *10*.



# Chapter 6

## Synthesis of anisotropic gold nanoparticles by electrospaying into a reductive-surfactant solution

*It is easier to vary the course of a river  
than the character of a man.  
(Chinese Proverb)*

Gold nanoparticles are attractive for applications in catalysis, as well as for several other technological fields. This chapter presents another one-step approach by direct electrospaying into a reductive-surfactant solution for the fast and continuous preparation of quasi-spherical and anisotropic gold nanoparticles at room temperature. In this case, a precursor solution of  $\text{HAuCl}_4$  has been electrospayed into a reductive bath containing a capping agent. Dodecylaminomethanol (DDAM), a bi-functional molecule that acts both as reducing and subsequently as stabilizing agent, causes here the chemical reduction of  $\text{Au}^{3+}$  into  $\text{Au}^0$  from the electrospayed precursor droplets and the quick formation of a gold colloid. Gold represents here a possible example of material that can be produced.

## 6.1 Introduction

The intrinsic properties of metals at nano length-scales, dictated by the size, shape and crystalline structure of the resulting nanoparticles, are particularly attractive for various technological applications. The development of preparative methodologies for tailoring both particle shape and size has been intensified in the recent years, with a special attention to the preparation of noble metal nanoparticles (*viz.* Ag, Pt, Pd and Au) [1-6].

Liquid-phase synthesis is usually preferred over gas-phase approaches in the preparation of metallic anisotropic nanoparticles [7, 8]. Use of a size and shape-controlling molecule, named capping or stabilizing agent, is crucial for this type of synthesis. This molecule binds on specific facets of the nanocrystal formed in solution. It promotes the growth at the 'free' crystal facets, which determines the final shape of the grown particle [9-12].

The standard protocol for the preparation of anisotropic nanoparticles in aqueous phase is referred to as 'seed-mediated growth' [6, 13-15]. It is a multi-step method that requires the participation of different chemicals (precursor, several reducing agents, capping agent). The so-called 'polyol process' is relevant when organic solvents are used [5-8]. However, this method requires high temperatures and long time reactions. The concurrent control of shape, size and crystal structure in the same liquid-phase preparation still represents a real challenge for this type of synthesis. For instance, anisotropic multiple twinned nanoparticles are attractive candidates for catalytic applications because of the favourable adsorption of small molecules, such as oxygen and hydrogen, on their twin boundaries [4, 16, 17]. However, the standard synthesis methods yield usually particles whose characteristics limit or exclude their catalytic applications (i.e. relatively large sizes) [1, 18, 19].

Conversely, the preparation of metallic nanoparticles can be also carried out via gas phase, relying on the generation of a metallic aerosol. The aerosol can be obtained, for example, by electrospraying of a metallic colloidal solution [20-23], by spark discharge generation between two metallic electrodes [24-27] or by evaporation/condensation of a metallic mesh coupled with an excimer lamp [28, 29]. In the last two cases, small, spherical primary particles (< 5 nm) are formed from the mesh or electrode, which agglomerate in an uncontrolled way to form clusters of 50-200 nm [27-29].

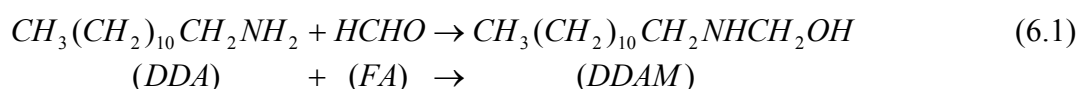
Electrospraying generates highly charged, self-dispersing droplets, limiting the agglomeration of the resulting particles. Besides, it is also the least energy-consuming method, when compared to those mentioned before. This technique has been used for the spraying of metallic nanoparticles from colloidal solutions on a substrate [30] or, in absence of the substrate, for the production of fine powders of small sizes (< 10  $\mu\text{m}$ ) [23]. The solid particles are obtained once the solvent

evaporates from the fine droplets generated by the electro-spraying of the colloidal solution. The size of the particles can be tuned before electro-spraying by modification of the metal concentration in the colloid.

A novel method for the preparation of anisotropic gold nanoparticles that combines the advantages of the liquid and gas-phase approaches is presented here. Shape and size can be controlled by the presence of a capping agent in the liquid phase, while small particle sizes, suitable for catalysis applications, can be achieved by the formation of a precursor aerosol. This new technique relies on electro-spraying of a metallic precursor solution into liquid solutions containing reductive surfactants. It is a one-step preparation method with reaction times of few minutes that is carried out at room temperature. Continuous production on a larger scale via this process can be achieved by multiplexed nozzle systems. Furthermore, an attractive feature is that apart from the metallic precursor only one additional chemical compound is required here, namely dodecylaminomethanol (DDAM), a molecule that acts both as the reducing and as the capping agent. Anisotropic gold nanoparticles are synthesized and stabilized in the liquid phase by reduction of  $\text{Au}^{3+}$ , contained in the electro-sprayed droplets of  $\text{HAuCl}_4$  solutions, into  $\text{Au}^0$  by a reductive solution of DDAM. The effects of the principal operating conditions (i.e. flow rate, initial precursor concentration and applied voltage) on the particle shape and size are discussed.

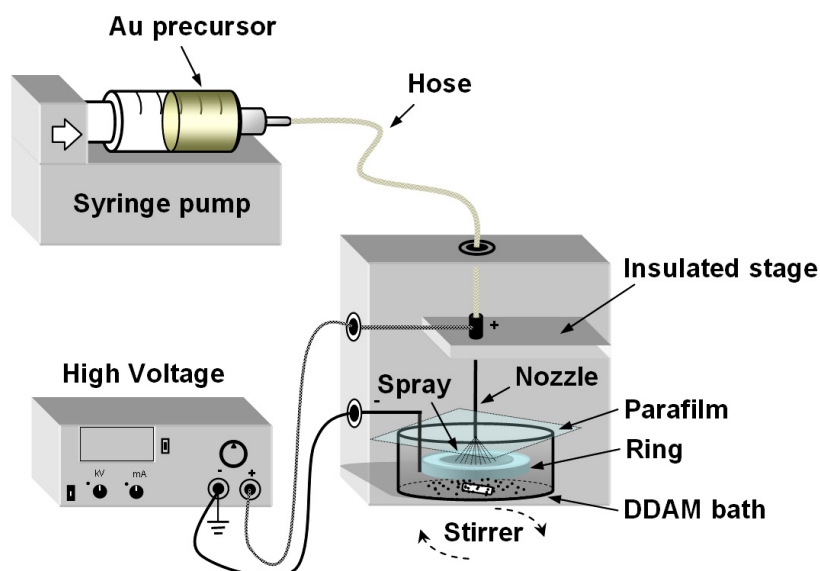
## 6.2 Experimental

Precursor solutions for the spraying, with concentrations of gold covering two orders of magnitude (0.25-24.5 mM), were prepared by dissolving  $\text{HAuCl}_4 \cdot 3\text{H}_2\text{O}$  (>99.9%, Aldrich) in isopropanol (>99%, J.T. Baker). Water is not recommended as the solvent because its electrical conductivity and surface tension are too high and hinder stable electro-spraying (ES). The reductive-surfactant solution of DDAM in cyclohexane (>99%, J.T. Baker) was prepared by reaction of dodecylamine (DDA) (> 99.5%, Fluka) and formaldehyde (FA) (ACS reagent, Sigma-Aldrich) at room temperature [31]. For a typical preparation, 4 mmol of DDA is dissolved in 25 ml cyclohexane, then 0.16 mol of aqueous FA (37 wt.% in water) is added. After vigorous stirring for at least 10 min, (the time needed for complete DDA conversion as proven by GC-MS and  $^{13}\text{C}$  NMR [31]) the cyclohexane phase, now containing DDAM, is separated from the aqueous phase with the residual FA:



According to the reaction stoichiometry, a solution of 0.16 M of DDAM in cyclohexane is obtained [31].

In each experiment, a 10 ml glass syringe (Fortuna Optima) was filled with 5 ml of the Au precursor solution. The syringe was placed in a syringe pump (Kd Scientific model 100 series), which was used to inject the precursor solution with a constant flow rate through an electrified nozzle with a flat rim and straight cut-off (stainless steel, 0.25 mm i.d., EFD Ultra). Typically, flow rates of 0.5 and 2 mlh<sup>-1</sup> were selected. The voltage between the nozzle and the counter-electrode was set around 4.5 or 9.5 kV in order to generate the precursor aerosol. A counter-electrode ring (soldering alloy-Sn:Pb 60:40) is placed each time in a beaker containing 21 ml of 0.16 M DDAM solution. A simplified scheme of the experimental set-up for electro spraying is shown in Fig. 6.1 and the operating conditions of the experiments carried out are shown in Table 6.2.



**Fig. 6.1.** Schematic drawing of the experimental setup employed for electro spraying in a reductive-surfactant solution.

The experiments are labeled according to the following notation as R-precursor concentration-flow rate-voltage value. The experimentation time varied from 3 to 50 min, depending on the flow rate and the precursor concentration employed, in order to obtain the same final gold concentration in the colloid (i.e. approximately 0.10 mM).

Before starting the reaction, the tubing (chemically resistant rubber hose, Watson Marlow) connecting the syringe with the nozzle was completely filled with the precursor solution. Then a selected voltage was applied between the nozzle and the counter-electrode and stirring of the reductive solution was started. After these steps, the syringe pump was switched on and onset of ES immediately occurred, with

the emission of charged droplets attracted towards the reductive-surfactant solution. The shape of the droplets was influenced by the form of the meniscus and the mode of spraying for a fixed flow rate. In our experiments the spherical shape of the pendant liquid droplet was progressively deformed to a conical shape for low voltages ( $\leq 5$  kV). A thin jet was ejected from the tip of this conical meniscus. For this reason, this mode is known as ‘cone-jet’. For higher voltages ( $\geq 9$  kV), at a fixed flow rate, more jets are introduced, distributing the initial flow among different cone-jets. This mode is also known as ‘multi-jet’ [32].

Finally, the crystal structure and the size of the produced particles were further investigated by a Philips CM30T transmission electron microscope (TEM) operated at 300 kV. The total gold content in the precursor and colloidal solutions was determined by a graphite furnace atomic absorption spectroscopy (AAS) (PerkinElmer 4100ZL).

## 6.3 Results and discussion

In the following subsection some basic elements of the electro spraying technique are given in order to aid the discussion in relation to the experimental conditions applied.

### 6.3.1 Scaling laws for electro spraying

The size of the droplets in the electro spray is governed by a combination of parameters. Hartman et al. [33, 34] proposed the following expressions for the calculation of the droplet size in the ‘cone-jet’ mode:

$$d_{d,v} = c \left( \frac{\rho \varepsilon_0 Q^4}{I^2} \right)^{\frac{1}{6}} \quad (6.2)$$

for the *varicose break-up*, where nearly-monodispersed droplets are formed, due to minimal perturbation by the lateral electrical forces on the emitted jet, and:

$$d_{d,w} = \left( 0.8 \frac{288 \varepsilon_0 \gamma Q^2}{I^2} \right)^{\frac{1}{3}} \quad (6.3)$$

for the break-up by *whipping motions*, where the droplets generally lose their monodispersity due to enhanced lateral electrical forces that cause the emitted jet to

whip and break irregularly. In these equations,  $\rho$  is the density of the liquid,  $c$  is a numerical constant close to 2,  $\varepsilon_0$  is the permittivity of free space,  $\gamma$  is the surface tension and  $I$  represents the current flowing through the liquid cone, which is approximately given by:

$$I \approx 2(\gamma\kappa Q)^{1/2} \quad (6.4)$$

where  $Q$  is the flow rate of the liquid and  $\kappa$  is the electrical conductivity of the liquid. The flow rate  $Q$  is the factor dominating the droplet size, but also  $\gamma$  and  $\kappa$  are of importance since they are contained in  $I$ . The voltage does not appear in these equations since electrospraying is a field-driven process. These considerations apply only to the ‘cone-jet’ mode. Indeed, a complete description in terms of ‘scaling laws’ (i.e. equations 6.2-6.4) for ‘multi-jet’ mode, does not exist at the moment.

Considering the electrospraying of pure isopropanol (IPA), whose electrical conductivity,  $\kappa=5.8 \cdot 10^{-6} \text{ S} \cdot \text{m}^{-1}$ , is lower than the value expected for the gold precursor solutions, the maximum droplet size that can be obtained at the typical flow rates used, 0.5 and 2  $\text{mlh}^{-1}$ , has been calculated according to equations 6.2 and 6.3 (Table 6.1).

The physical properties of IPA at 25 °C used for the calculation are:  $\rho=790 \text{ kg} \cdot \text{m}^{-3}$ ,  $\gamma=22 \cdot 10^{-3} \text{ N} \cdot \text{m}^{-1}$  and  $\mu = 1.96 \cdot 10^{-3} \text{ Pa} \cdot \text{s}$ .

**Table 6.1.** Current and droplet size expected for pure IPA.

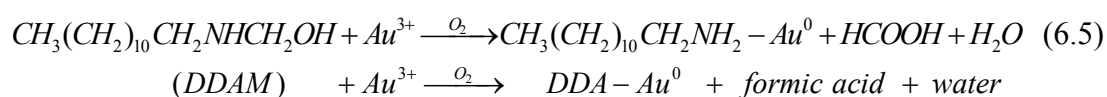
$Q$ ( $\text{mlh}^{-1}$ )	$I$ (nA)	$d_{d,v}$ ( $\mu\text{m}$ )	$d_{d,w}$ ( $\mu\text{m}$ )
0.5	8.4	11.5	23.0
2	16.8	23.1	36.5

For pure IPA, the jet break-up mechanism is likely to occur via varicose instabilities, since it results  $d_{d,v} < d_{d,w}$  for both flow rates used. Accordingly, in the ‘cone-jet’ mode, droplet sizes smaller than 23  $\mu\text{m}$  and a reasonable monodispersity for the aerosol produced are expected.

In ‘multi-jet’ mode, the droplet emission frequency is much higher than in the ‘cone-jet’ mode, together with the electrical forces involved and consequently the current flowing between the cone and the counter-electrode. The thin jets break-up into a fine, highly-charged aerosol mist mainly by *whipping* motions [35]. In this scenario, also the occurrence of electrical discharges in the surrounding atmosphere should be considered, which can completely destabilize the droplet production process and easily lead to a loss of monodispersity. Therefore, the ‘multi-jet’ mode can also result in a non-uniform droplet production, where irregular liquid fragments are sometimes emitted. Hence, larger particle sizes can be expected under such particular circumstances.

### 6.3.2 Formation of the colloids

The  $Au^{3+}$  anions are directly driven into the stirred DDAM solution during the electro spraying of the precursor droplets. The DDAM causes the reduction of  $Au^{3+}$  to  $Au^0$ , as well as the release of the ad-species DDA that acts as a surfactant. More specifically, the reductive functional group in DDAM,  $-NHCH_2OH$ , is oxidized to  $-NHCOOH$  by  $Au^{3+}$ , which is reduced to  $Au^0$ . The  $-NHCOOH$  group is not stable and decomposes into  $-NH_2$  and formic acid. Consequently, DDA is released and this is readily adsorbed and assembled on the surface of the nanoparticles. The whole process is then responsible for the formation of the stabilized colloids, governed by a colour change of the solution to a characteristic pink hue:



The protection of the nanoparticles in the colloidal solution by DDA was demonstrated by FT-IR analysis [31].

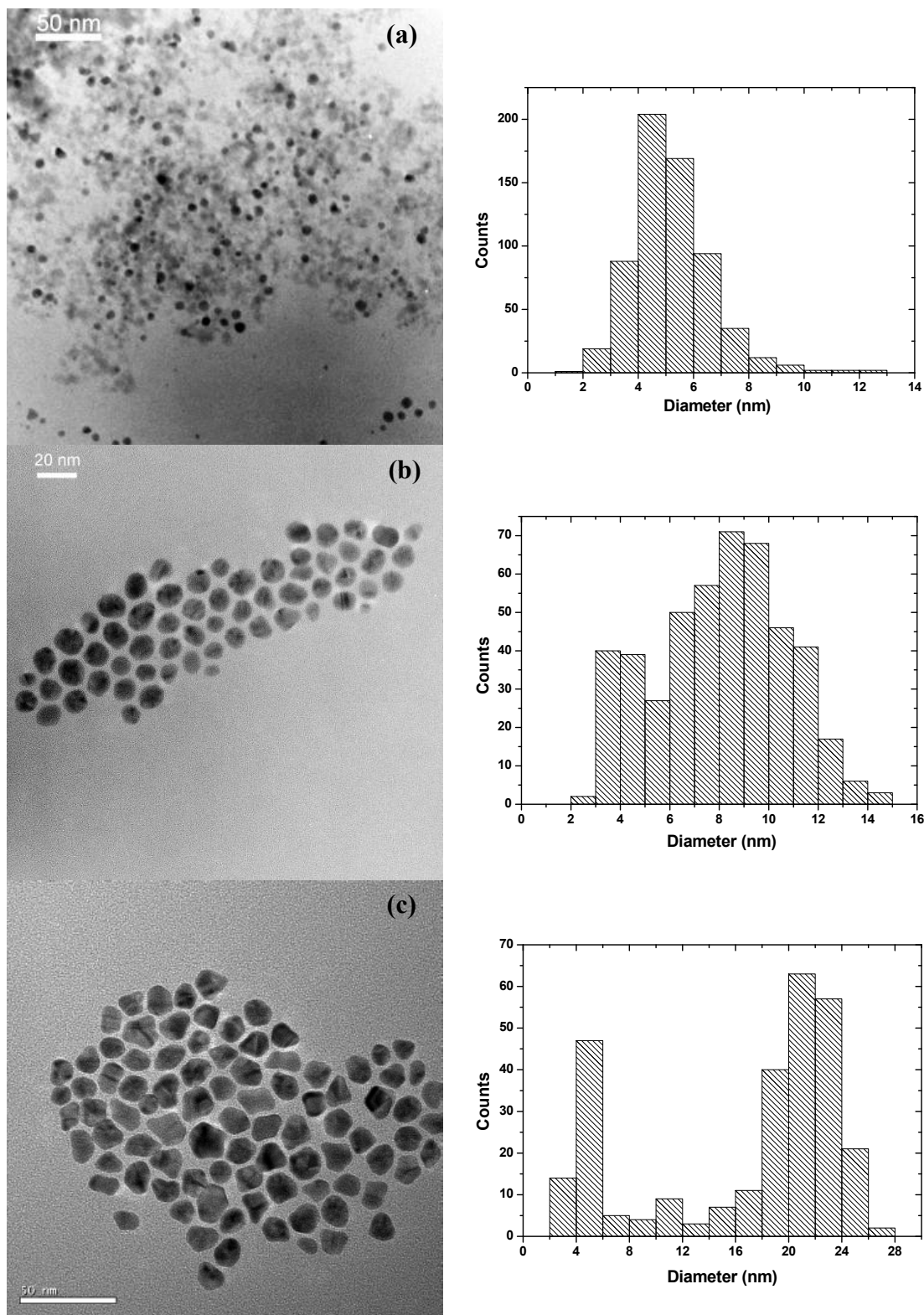
It is worth noting that all the resulting colloidal solutions had a pink colour (see Fig. 6.2), in contrast to the characteristic red colour displayed by spherical gold nanoparticles. The plasmon resonance, measured with a UV-Vis spectrophotometer (UNICAM UV 500), is detected at a wavelength of 524 nm, which is the typical range for small gold nanoparticles (< 30 nm) [36, 37].



**Fig. 6.2.** Photo showing the typical colour obtained for the Au colloidal solutions by electro spraying into a reductive-surfactant solution (i.e. DDAM dissolved into cyclohexane).

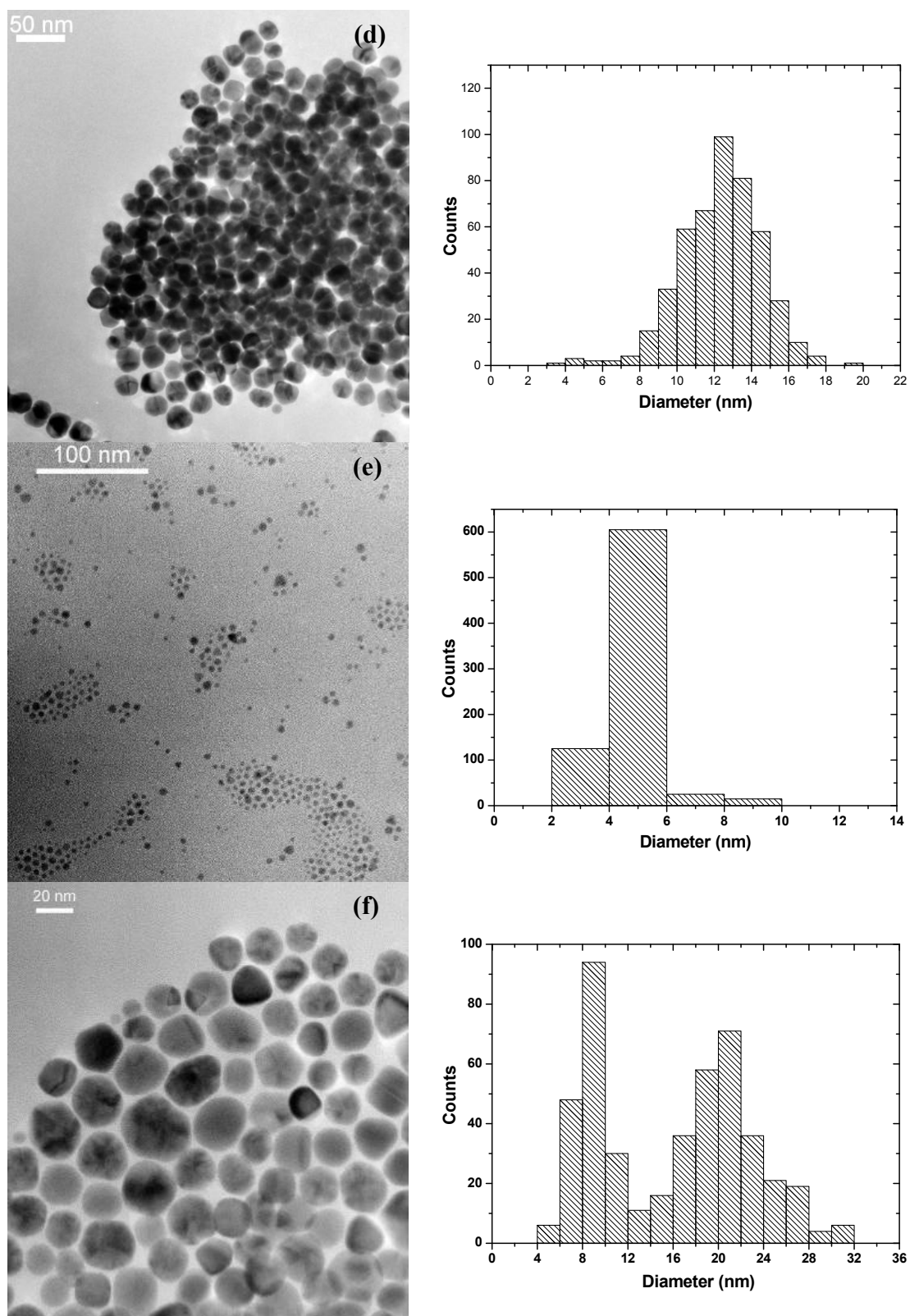
The average particle sizes measured by TEM on the same day of the synthesis are reported in Table 6.2. For those particles with a quasi-spherical shape, the size represents the diameter, while for the specific faceted shape it refers to the diagonal.

The particle morphology and their relative size distribution are shown in Fig. 6.3.

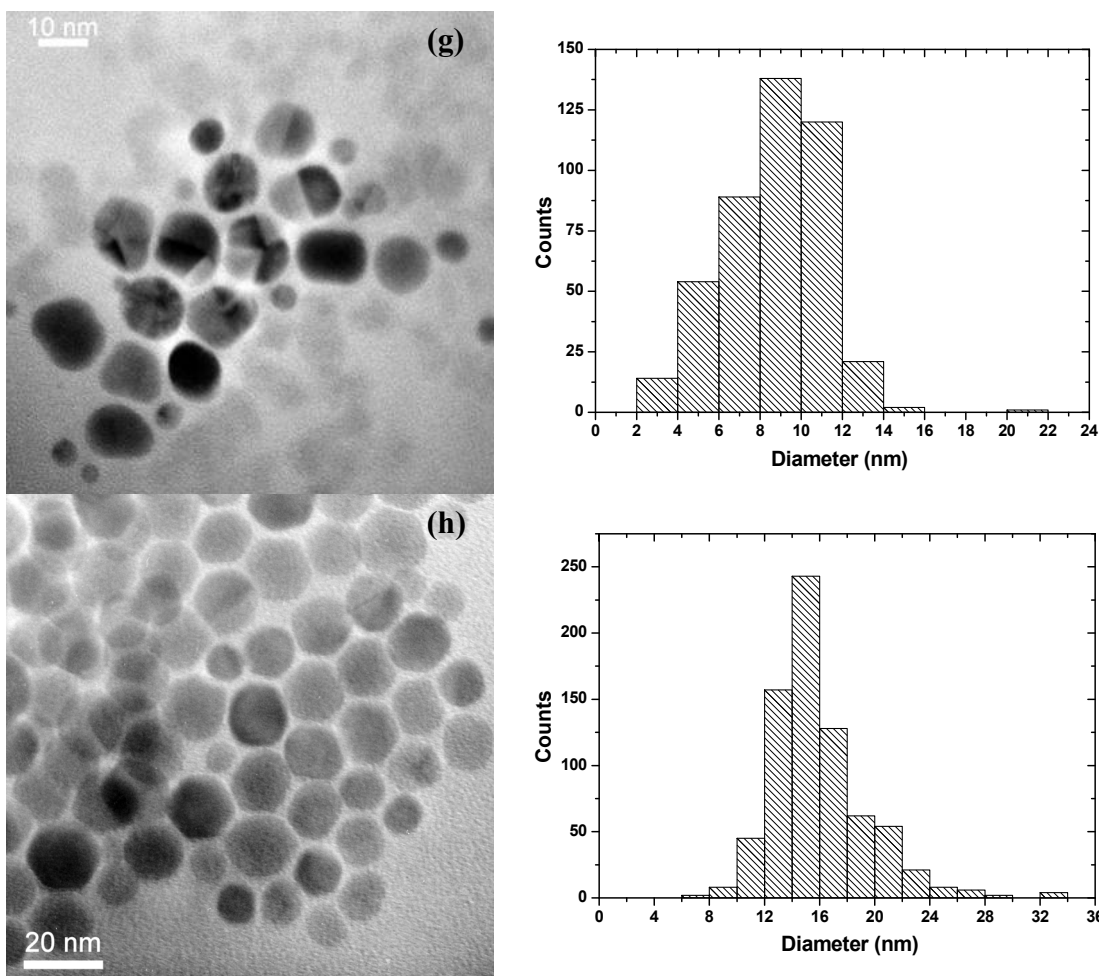


**Fig. 6.3.** TEM micrographs and particle size distributions of the samples related to experiments: a) R-4-0.5.9, b) R-2.2-2-9.5, c) R-4-2-9.5 of Table 6.2.





**Fig. 6.3 (Continuation).** TEM micrographs and particle size distributions of the samples related to experiments: d) R-24-2-9.5a, e) R-24-2-9.5b, f) R-24-2-9.5c of Table 6.2. Sample R-24-2-9.5c was measured 2 weeks after preparation.



**Fig. 6.3 (Continuation).** TEM micrographs and particle size distributions of the samples related to experiments: g) R-4-2-4.5, h) R-27.7-2-0 of Table 6.2.

The size distribution is quite broad (see Table 6.2, Fig. 6.3). This heterogeneity in size is expected when a burst-nucleation within an extremely short period of time, followed by a slow growth, does not occur [38]. In the system under investigation, nucleation proceeds simultaneously to the particle formation due to the continuous electro spraying of  $\text{Au}^{3+}$  species into the stirred reductive solution. Then a ‘seed-mediated’ growth is likely to take place. The particle size distribution in this case can be narrowed by a subsequent ripening of the nanoparticles [39] and, when there is a clear bimodal distribution, as in the experiment R-24-2-9.5a, centrifugation can be a tool to separate both sizes (R-24-2-9.5b).

The experimental parameter settings, *i.e.* flow rate, gold concentration in the precursor solution and applied voltage for the atomization of the precursor, determine the particle size. More specifically, this feature depends on the droplet size, the concentration of  $\text{Au}^{3+}$  per droplet and the emission frequency of the generated droplets.

**Table 6.2.** Gold nanoparticles prepared by electrospraying under different experimental conditions.

Sample	$C_{prec.}$ (mM)	$Q_{prec.}$ (mlh <sup>-1</sup> )	$t_{exp.}$ (min)	$F_{prec.}$ (mgh <sup>-1</sup> )	$V$ (kV)	Mode	$d_p$ (nm)	Shape
R-4-0.5-9	4	0.5	48	1.0	9.0	M-J	5.3±1.4	Q-Sph.
R-2.2-2-9.5	2.2	2	12	0.8	9.5	M-J	8.0±2.6	Q-Sph.
R-4-2-9.5	4	2	12	1.6	9.5	M-J	12.4±2.8	Bran.
R-24-2-9.5a	24	2	3	9.5	9.5	M-J	5 and 20	
R-24-2-9.5b <sup>+</sup>							5±1	Sph.
R-24-2-9.5c <sup>§</sup>							9 and 21	Ico. and Deca.
R-4-2-4.5	4	2	12	1.6	4.5	C-J	8.8±2.4	Deca.
R-27.7-2-0	27.7	2	3	10.8	0	Drip.	15.9±3.5	Hex.

**Key:** M-J→Multi-jet; C-J→Cone-jet; Drip.→Dripping; Q-Sph.→Quasi-Spherical; Sph.→Spherical; Bran.→Branched; Ico.→Icosahedral; Deca.→Decahedral; Hex→Hexagonal.

The final gold concentration in the resulting colloids is always around 0.10 mM.

<sup>+</sup> Sample R-24-2-9.5a measured after centrifugation to remove the bigger particles.

<sup>§</sup> Sample R-24-2-9.5a measured two weeks after preparation.

### *I – Influence of the flow rate*

A lower flow rate favours smaller particle sizes (*cf.* experiments R-4-0.5-9 and R-4-2-9.5 in Table 6.2) at the same precursor concentration and similar applied voltage in the ‘multi-jet’ mode.

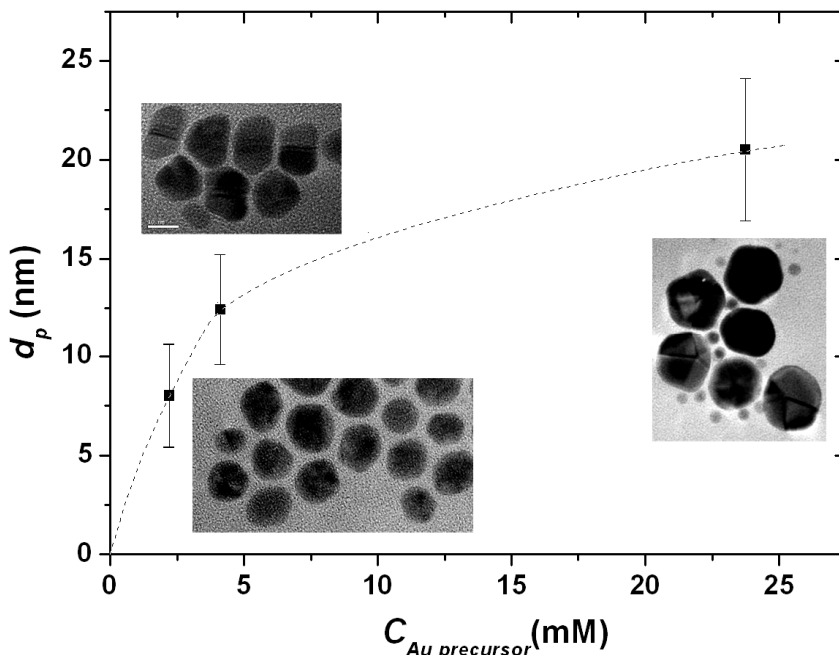
The lower the flow rate, the smaller the droplet size in the generated aerosol (see Equations 6.4 and 6.5 for the ‘cone-jet’ mode) and the lower the feed rate of the gold species into the reductive-surfactant solution. Simultaneously, the concentration of gold in the droplet is expected to increase, because for smaller droplets the solvent evaporates faster. The first aspect (droplet size) seems to have a stronger influence on the particle size. The resulting particle sizes: 5.3±1.4 nm at 0.5 mlh<sup>-1</sup> (R-4-0.5-9) and 12.4±2.8 nm at 2.0 mlh<sup>-1</sup> (R-4-2-9.5) indicate that more than one nanoparticle is produced from one single droplet of a few μm.

### *II – Influence of the gold concentration in the precursor solution*

A higher initial concentration of Au<sup>3+</sup> in the precursor solution, at a given flow rate and applied voltage in the ‘multi-jet’ mode, favours larger particle sizes (R-2.2-2-9.5, R-4-2-9.5 and R-24-2-9.5 in Table 6.2), except for the last case, where the formation of particles with an average size of 5 nm occurs. On the one hand, a higher concentration of Au<sup>3+</sup> implies a higher electrical conductivity of the solution ( $\kappa$ ) and consequently the formation of smaller droplets as suggested by equations 6.2-6.4. On the other hand, also a competition between the nucleation-growth process of the gold particles due to the continuous supply of species (*i.e.* the more concentrated the

emitted droplets, the bigger the amount of precursor readily available for particle formation and growth) and the moderate decrease of the average droplet size by increasing the whole solution conductivity can be expected.

The evolution of the particle size with the gold precursor concentration at the fixed flow rate of  $2.0 \text{ mlh}^{-1}$  and applied voltage of  $9.5 \text{ kV}$  is presented in Fig. 6.4.



**Fig. 6.4.** Dependence of the particle size on the sprayed gold precursor solution. Flow rate:  $2 \text{ mlh}^{-1}$  and applied voltage:  $9.5 \text{ kV}$ . The insets show TEM images of the samples synthesized under the corresponding conditions (experiments R-2.2-2-9.5, R-4-2-9.5 and R-24-2-9.5a)

From Fig. 6.4 it is noted that the influence of the gold concentration is more pronounced at values below  $5 \text{ mM}$  in the precursor solution. Additionally, the particle size can be reduced, for a given concentration, by further decreasing the droplet size, i.e. by using lower flow rates.

### III – Influence of the applied voltage

Increasing the voltage causes the introduction of multi-jet operation; however, this can also enhance the presence of some liquid fragments for the electro sprayed precursor, which result from irregular break-up of the thin jets under conditions of electrical discharge. This is a possible explanation for the outcome of experiment R-4-2-9.5 which was performed at  $9.5 \text{ kV}$ . Indeed, larger particle sizes are obtained than in experiment R-4-2-4.5 carried out at  $4.5 \text{ kV}$  (i.e.  $12.4 \text{ vs. } 8.8 \text{ nm}$ , respectively, both at the same flow rate, precursor concentration and reaction time – see Table 6.2).

Furthermore, a reference experiment was carried out without applying any voltage, by dripping the gold precursor solution into the reductive-surfactant solution. The

experiment labeled R-27.7-2-0 in Table 6.2 and the related TEM image reported in Fig. 6.3.g, show that the particle size is hardly affected, at least when compared with R-24-2-9.5. The main difference comes from the particle morphology, exhibiting single-crystal instead of polycrystalline shapes. Indeed, also that the kinetics of the nanoparticle synthesis was directly affected by the use of the voltage. Without any voltage, the reaction kinetics was considerably slow, and it took several minutes before the reductive solution started to change gradually in colour and reached the final hue after complete dripping of the precursor. On the other hand, experiments with ES, showed a steady change of colour of the reductive solution, which normally had reached its final hue at the end of the experiment.

Taking into account the influence of the experimental parameters, it can be concluded that the charged droplets created by the ES are mainly responsible for the observed nanoparticle polycrystallinity and that the size of the produced particles is governed by the droplet size, gold concentration and stability of the ES process.

Interestingly, only polyhedral particles were synthesized according to the TEM micrographs (Fig. 6.3). Depending on the operating conditions, they are geometrical projections of irregular shapes (R-4-0.5-0, R-2.2-2-9.5 and R-4-2-9.5; Figs. 6.3a, b and c, respectively) or faceted particles, like decahedrons, dodecahedrons and icosahedrons (R-24-2-9.5a and R-4-2-4.5; Figs. 6.3d and e, respectively), which, however, are difficult to distinguish clearly. The formation of mixtures of nanoparticles with different morphologies usually occurs when there is a heterogeneous reaction environment for each particle [39].

The lowest flow rate ( $0.5 \text{ mlh}^{-1}$ , R-4-0.5-9) results in small, uniform nanoparticles ( $5.3 \pm 1.4 \text{ nm}$ ) with quasi-spherical shapes (Fig. 6.3a) having a 4.5 nm edge. An increase in flow rate, maintaining the same precursor concentration (R-4-2-9.5), results in a change of the morphology of the particles, and their size. Branched nanoparticles are then produced (Fig. 6.3b). The formation of these anisotropic nanoparticles is caused by a preferential addition of gold atoms at the high-energy edge sites [18, 19]. The metallic gold atoms are preferentially added to the energetically most favorable sites. At a high precursor concentration (R-24-2-9.5a), well-defined polycrystalline nanoparticles, mainly icosahedrons and some decahedrons having 10 and 12 nm edges, respectively, are obtained (Fig. 6.3c). Their average size is  $20.5 \pm 3.6 \text{ nm}$ . It is worth mentioning that also short rods of 20 nm length were observed. The presence of the rods suggests that the decahedrons are polycrystalline with multiple-twinned structures, as reported earlier in the literature [9-12]. The small, spherical, single-crystal nanoparticles of 5 nm, likely the most recently formed, were not considered, though their concentration in the colloid was high enough to show a bimodal distribution. These small particles could be separated off by centrifugation (R-24-2-9.5b, Fig. 6.3d). This bimodal distribution is attributed to the different ageing time of the particles in the solution as a consequence of the

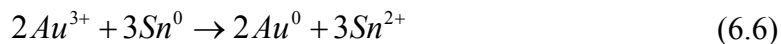
semi-batch operation and/or to the possibility that not all the droplets were uniformly charged at this high gold precursor concentration, resulting in a fraction of single-crystal nanoparticles.

The evolution of the nanoparticle shape with the precursor concentration is also represented in Fig. 6.4. The concentration of gold in the emitted droplet is important for the particle shape. The more concentrated the emitted droplets, the larger the amount of precursor readily available for particle formation and growth. Accordingly, more regular nanoparticles are obtained.

### 6.3.3 Stability of the colloids

The ‘as-prepared’ colloidal solutions can contain up to 25% less gold than expected according to the mass feed flow rate and the reaction time. For instance, for experiment R-4-2-9.5, the measured concentration of total gold by AAS is 0.06 mM, whereas the expected one is 0.08 mM. Deposition of gold on the counter-electrode can occur by some interaction between the gold and the metals of the electrode (soldering Sn alloy), as indicated by the slight darkening of the counter-electrode after reaction.

Considering the standard reduction potentials of the metals, gold has a higher potential ( $E^\circ = 1.498 \text{ V}$ ) than tin ( $E^\circ = -0.1375 \text{ V}$ ), therefore, gold can be spontaneously reduced by the tin electrode by electroless deposition:



This phenomenon can be avoided by using an inert or coated electrode. Also the partial reduction of gold can eventually occur at the surface of the electrode:



$Au^+$  in solution undergoes disproportion according to the following reaction:



because  $E^\circ (Au^+/Au^0) > E^\circ (Au^{3+}/Au^0)$ . However,  $Au^+$  exists only as a stable form in solution as a complex ion *i.e.*  $[AuCl_2]^-$  [40]. However, solutions containing  $[AuCl_2]^-$  are colourless and therefore this process is less expected.

Two weeks after preparation, some particles in solution precipitated at the bottom of the beaker and the total amount of gold in the solution was reduced by 80% though the particle size had not changed (R-24-2-9.5c, Fig. 6.3e), which reveals the instability of the colloidal solutions over this period. This instability may be due to a change in the ionic strength of the colloidal solution caused by the presence of IPA.

Indeed, gold nanoparticles prepared by the same precursor ( $\text{HAuCl}_4 \cdot 3\text{H}_2\text{O}$ ) and reductive solution (DDAM in cyclohexane) following the same methodology described by Chen and Wang [31], which is based on a novel phase-transfer preparation method, are stable for months. This instability can be avoided by washing the excess of reducing agent (DDAM) of the 'as-prepared' colloid with ethanol and by subsequent re-dispersion of the nanoparticles in a non-polar solvent.

The method of electro spraying into a reductive solution allows a fast one-step synthesis of anisotropic gold nanoparticles at room temperature with an appropriate size for catalytic applications (5-12 nm edge). The experimentation time varies from 3 to 50 min with a final gold colloid concentration that is around 0.10 mM. The use of higher Au concentrations can lead to larger particle sizes due to their easier growth when more precursor is directly available in the electro sprayed droplets, unless lower flow rates (i.e. smaller droplets) are used to compensate for the increase. Ultimately, the droplet size and gold concentration determine the resulting particle size.

The continuous production of the polycrystalline anisotropic gold nanoparticles with controlled size on a larger scale by electro spraying can be envisioned by out-scaling via multiplexed nozzle systems. The current operation is carried out semibatch-wise, resulting in increasing concentrations of particles in the reductive solution and a broad age distribution. If particle growth occurs by agglomeration or Ostwald ripening one may consider even electro spraying into a flowing film solution, resulting in a real continuous operation with more uniform age distribution.

The use of other bifunctional components, acting both as reducing and as capping agent is obvious [41]. Here DDAM was used to avoid contamination of the gold catalytic performance by too strongly binding capping agents based on sulphur or phosphorous. Although the technique has been demonstrated for the production of gold nanoparticles for catalytic application, in principle it can be developed for the production of any type of metallic nanoparticles with applications in other fields, e.g. batteries, hydrogen storage and optoelectronics.

## 6.4 Conclusions

A versatile method for the fast preparation in one-step of anisotropic gold nanoparticles in organic solvents at room temperature is reported, which offers an outlook for larger scale and continuous production of metallic nanoparticles in general. It is based on electro spraying into a reductive solution, using a bifunctional component, acting both as a reducing and as capping agent. In this study, anisotropic gold nanoparticles with appropriate sizes for catalysis applications (5-12 nm edge length) have been successfully produced. The droplet size of the precursor solution in

the spray, can be tuned by selecting the flow rate, precursor concentration and applied voltage, which are the major parameters determining the particle size. Quasi-spherical nanoparticles of 4.5 nm edge can be obtained in 50 min, while decahedrons of 10-12 nm edge are obtained in 3 min. This shorter preparation time results in a larger particle size, in a wider size distribution and a larger heterogeneity in shapes. The high flexibility of this method combined with the ease of operation and the reduced costs of the equipment makes this process a good candidate for quantitative production of nanoparticles in general, *i.e.* scale up by multiplexed nozzle systems.

## 6.5 References

- [1] B. Wiley, Y. Sun, B. Mayers, Y. Xia, *Chemistry - A European Journal* **2005**, *11*, 454.
- [2] J. Xu, S. Li, J. Weng, X. Wang, Z. Zhou, K. Yang, M. Liu, X. Chen, Q. Cui, M. Cao, Q. Zhang, *Advanced Functional Materials* **2008**, *18*, 277.
- [3] D. Seo, C. I. Yoo, I. S. Chung, S. M. Park, S. Ryu, H. Song, *Journal of Physical Chemistry C* **2008**, *112*, 2469.
- [4] Y. Xiong, Y. Xia, *Advanced Materials* **2007**, *19*, 3385.
- [5] Q. Zhang, J. Xie, J. Yang, J. Y. Lee, *ACS Nano* **2009**, *3*, 139.
- [6] B. Lim, M. Jiang, J. Tao, P. H. C. Camargo, Y. Zhu, Y. Xia, *Advanced Functional Materials* **2009**, *19*, 189.
- [7] A. R. Tao, S. Habas, P. Yang, *Small* **2008**, *4*, 310.
- [8] M. Grzelczak, J. Perez-Juste, P. Mulvaney, L. M. Liz-Marzan, *Chemical Society Reviews* **2008**, *37*, 1783.
- [9] Y. Sun, B. Mayers, T. Herricks, Y. Xia, *Nano Letters* **2003**, *3*, 955.
- [10] C. J. Murphy, *Science* **2002**, *298*, 2139.
- [11] K. M. Bratlie, H. Lee, K. Komvopoulos, P. Yang, G. A. Somorjai, *Nano Letters* **2007**, *7*, 3097.
- [12] G. H. Zhang, W. L. Guo, X. K. Wang, *Materials Research Innovations* **2007**, *11*, 201.
- [13] B. D. Busbee, S. O. Obare, C. J. Murphy, *Advanced Materials* **2003**, *15*, 414.
- [14] T. K. Sau, C. J. Murphy, *Journal of the American Chemical Society* **2004**, *126*, 8648.
- [15] C. J. Murphy, T. K. Sau, A. M. Gole, C. J. Orendorff, J. Gao, L. Gou, S. E. Hunyadi, T. Li, *Journal of Physical Chemistry B* **2005**, *109*, 13857.
- [16] Y. Xiong, J. M. McLellan, Y. Yin, Y. Xia, *Angewandte Chemie - International Edition* **2007**, *46*, 790.
- [17] F. Calvo, A. Carre, *Nanotechnology* **2006**, *17*, 1292.
- [18] G. Berhault, M. Bausach, L. Bisson, L. Becerra, C. Thomazeau, D. Uzio, *Journal of Physical Chemistry C* **2007**, *111*, 5915.
- [19] B. Wiley, T. Herricks, Y. Sun, Y. Xia, *Nano Letters* **2004**, *4*, 1733.
- [20] I. W. Lenggoro, B. Xia, K. Okuyama, J. F. De la Mora, *Langmuir* **2002**, *18*, 4584.



- 
- [21] F. Schulz, S. Franzka, G. Schmid, *Advanced Functional Materials* **2002**, *12*, 532.
- [22] J. Suh, B. Han, K. Okuyama, M. Choi, *Journal of Colloid and Interface Science* **2005**, *287*, 135.
- [23] A. Jaworek, *Powder Technology* **2007**, *176*, 18.
- [24] J. H. Byeon, J. H. Park, J. Hwang, *Journal of Aerosol Science* **2008**, *39*, 888.
- [25] N. S. Tabrizi, M. Ullmann, V. A. Vons, U. Lafont, A. Schmidt-Ott, *Journal of Nanoparticle Research* **2009**, *11*, 315.
- [26] N. S. Tabrizi, Q. Xu, N. M. Van Der Pers, U. Lafont, A. Schmidt-Ott, *Journal of Nanoparticle Research* **2009**, *11*, 1209.
- [27] M. Seipenbusch, A. P. Weber, A. Schiel, G. Kasper, *Journal of Aerosol Science* **2003**, *34*, 1699.
- [28] K. Deppert, T. Krinke, M. H. Magnusson, J. O. Malm, L. Samuelson, *Journal of Aerosol Science* **1998**, *29*.
- [29] K. Nakaso, M. Shimada, K. Okuyama, K. Deppert, *Journal of Aerosol Science* **2002**, *33*, 1061.
- [30] P. H. M. Bottger, Z. Bi, D. Adolph, K. A. Dick, L. S. Karlsson, M. N. A. Karlsson, B. A. Wacaser, K. Deppert, *Nanotechnology* **2007**, *18*.
- [31] Y. Chen, X. Wang, *Materials Letters* **2008**, *62*, 2215.
- [32] M. Cloupeau, B. Prunet-Foch, *Journal of Aerosol Science* **1994**, *25*, 1021.
- [33] R. P. A. Hartman, D. J. Brunner, D. M. A. Camelot, J. C. M. Marijnissen, B. Scarlett, *Journal of Aerosol Science* **1999**, *30*, 823.
- [34] R. P. A. Hartman, D. J. Brunner, D. M. A. Camelot, J. C. M. Marijnissen, B. Scarlett, *Journal of Aerosol Science* **2000**, *31*, 65.
- [35] A. Jaworek, A. Krupa, *Journal of Aerosol Science* **1999**, *30*, 873.
- [36] T. Sakura, Y. Nagasaki, *Colloid and Polymer Science* **2007**, *285*, 1407.
- [37] Y. Yang, S. Matsubara, M. Nogami, J. Shi, *Materials Science and Engineering B: Solid-State Materials for Advanced Technology* **2007**, *140*, 172.
- [38] J. Park, J. Joo, G. K. Soon, Y. Jang, T. Hyeon, *Angewandte Chemie - International Edition* **2007**, *46*, 4630.
- [39] Q. Zhang, J. Xie, J. Y. Lee, J. Zhang, C. Boothroyd, *Small* **2008**, *4*, 1067.
- [40] P. Silvestroni, *Fondamenti di Chimica, Ed. Masson Milan* **1997**.
- [41] P. T. Witte, *WO2009-096783A1* **2009**.



# Summary

*“...You pick the place and I’ll choose the time...  
...and I’ll climb the hill in my own way...  
...just wait a while for the right day...”  
(Pink Floyd – Fearless)*

## Conclusions and outlooks

Nanostructured materials play a crucial role in the development of novel devices as well as in the improvement of current technological applications. Energy storage via Li-ion batteries represents one of the fields where major breakthroughs are expected by the use of nanostructures. In such a way the limitations posed by conventional materials found in commercial applications may be overcome.

In this thesis the synthesis of nanostructured functional materials for Li-ion battery negative electrodes has been approached via an aerosol route based on electrospraying. Two different electrospray-assisted methods have been investigated for the synthesis and the assembly of various types of nanoparticles and nanocomposites. One method implements the generation of nanoparticles via a novel route bridging charged aerosols with red-ox reactions in liquids. The second method is devised in a way that complete synthesis and assembly of nanocomposite coated electrodes can be carried out via a one-step process based on pyrolysis and/or deposition of precursor solutions and suspensions containing both active and inactive components. The ultimate applications of these methods are not restricted to Li-ion batteries, since both the techniques developed and the materials involved are attractive for other purposes (i.e. catalysis, fuel cells, solar cells, etc.).

The challenges related to the use of alternative materials to enhance the performances of advanced Li-ion battery electrodes are discussed in chapter one,

where a particular attention is devoted to negative electrodes and their electrochemical reaction mechanisms. Nanostructured materials are presented as attractive candidates to address the shortcomings of the most promising materials for advanced negative electrodes, namely Li-alloys and transition metal oxides. The issues related to their volume changes upon reaction with lithium and the possible roles of nanostructured materials are also addressed in this context.

The fundamentals of electro spraying are described together with its operational spraying modes in chapter two. In particular, the description of the so-called “cone-jet mode” is emphasized, due to its relevance for the production of nanoparticles with tunable features. Advantages and disadvantages of electro spraying are taken into account along with strategies to solve its main issue (i.e. limited production rate). Besides, electro spray-based techniques, e.g. electrostatic spray pyrolysis/deposition and electro spinning are presented as versatile and cost-effective methods for the synthesis of nanostructured materials. In particular, some relevant examples of applications directly related to Li-ion batteries are given.

A novel route for the synthesis of nanostructured powders in liquid phases is described in chapter three, where electro spraying of metal chlorides precursor solutions has been coupled to reductive precipitation in order to generate metallic and metallic-like particles. Tin-based materials are chosen for the synthesis due to their potential applications to negative electrodes in Li-ion batteries. Electro spraying in the cone-jet and multi-jet mode is combined with reductive precipitation by  $\text{NaBH}_4$  to generate small metallic and metallic-like nanoparticles with different compositions. Applying electro spraying to the feeding precursors has proved effective in decreasing the size of the primary particles, which then suffered from enhanced reactivity towards oxygen and moisture. Although these experiments have been carried out in air and the amount of the collected powders have been rather limited, the results suggest that the technique has a potential for a larger production of various nano materials with different features and textures. Therefore, inert gas atmospheres and suitable solvents are needed in all the cases where the generated nanoparticles react quickly with oxygen and/or moisture. This type of synthesis can be conveniently extended to various types of materials by use of dedicated precursors, reductive agents and eventually stabilizers. The production rate issue could be addressed, provided that the flow rates can be further enhanced by employing multiplexed-nozzle systems for parallel atomization of the precursors. Additionally, the reductive bath could be implemented with the presence of a constant flow and a further in-line separation unit for the precipitated particles, in order to enable a continuous production process.

Sn-based nanopowders produced via this route are then studied in the context of negative electrodes in chapter four. Nanostructured powders are obtained by electro spraying a Sn (II) chloride solution into a reductive bath with  $\text{NaBH}_4$ . Their

typical morphology shows spherical-like agglomerates, whose structure consists of small Sn nanocrystals surrounded by an amorphous SnO<sub>x</sub> phase. Adequate amounts of materials have been obtained in order to prepare coated electrodes for electrochemical measurements on coin cells. The electrochemical behaviour of the nanostructured powders has been investigated by galvanostatic tests. Their voltage profiles and cycle performances are compared to those of commercial tin and tin oxide (II, IV) powders having different mesh size. In particular, the related charge-discharge curves do not exhibit distinct flat plateaus, unlike those of commercial materials. Overall, the nanostructured powders yield enhanced discharge capacities. Unfortunately, the irreversible capacity loss in their first cycle represents a clear issue for effective operation. This fact is likely related to the nature of the materials resulting from reduction by NaBH<sub>4</sub>, which generally exhibit large surface areas and therefore easier contamination. In this respect, it should be also stressed that both the synthesis process and the powder collection involved air exposure and these circumstances affected the purity of the processed materials. Nonetheless, the nanostructured powders displayed adequate stability upon cycling, yielding a final capacity of about 300 mAhg<sup>-1</sup> after 100 cycles. This value is higher than those obtained for the commercial powders, which all showed capacity fading and limited coulombic efficiency during the first cycle. Improvements of the entire synthesis and collection processes are clearly possible and these conditions should positively reflect on the performances of the resulting materials. Still, this requisite alone could be not sufficient, because the step concerning the fabrication of the coated electrodes should not be overlooked. Effective operation of this type of electrodes, where remarkable mechanical strains are present, requires a good dispersion of the active particles into the binder and a strong adhesion to the current collector. In most of the cases manipulation and incorporation of nanopowders into composite electrodes with inactive components are not trivial tasks. Not surprisingly, good properties of active nanopowders can be easily masked by improper electrode assembly. Therefore, improving the cycling performances and the reversibility of such materials requires also a suitable design and assembly of the composites.

A direct approach for the fabrication of coated nanocomposite electrodes is presented in chapter five. The components of an electrode are synthesized and assembled at relatively low temperatures onto a heated substrate via a single-step electrospray-assisted process in order to deposit nanocomposite layers. Active nanoparticles have been directly synthesized and dispersed within a polymeric binder (i.e. PVdF), while being deposited at once as composite electrodes on selected areas. In this way, an intimate contact between the binder and the active nanoparticles is obtained in the coatings. Different materials have been investigated in order to form PVdF/oxide nanocomposites based on Sn, Co and Fe from the pyrolysis of their respective electrosprayed precursors in air. The results show that the morphology, the

texture and the structure of these deposits are reminiscent of the whole process. Spherical remnants of the electro sprayed droplets are found for all the PVdF/oxide nanocomposites produced. Monodispersed oxide nanoparticles of few nanometers are observed inside the spherical deposits. The nanoparticles are evenly dispersed within the remnants and they are in close contact with the surrounding PVdF. Therefore, electro spraying of polymer/metal precursor solutions subjected to pyrolysis at low temperatures enables the direct formation and assembly of promising electrode layers. It should be stressed that this technique offers a powerful tool to produce controlled ensembles of relics from the precursor droplets, whose initial size can be tuned by adjusting the experimental conditions. In this way, it would be possible not only to tailor the initial size of the reactive droplets, but also to have a nearly-monodispersed ensemble of remnants, which directly contribute to the overall properties of the deposited layers. Moreover, the pyrolysis and drying processes can be controlled by adjusting the temperature applied to the substrate and its relative distance from the nozzle, in order to influence the shape and the texture of the ultimate deposits. The preliminary results suggest that in principle it is possible to adjust not only the overall morphology of the deposited layers, but also their intimate structure and texture, as well as the contact between the parts. Although these nanocomposites can be used for various applications, the coated layers have been investigated as negative electrodes for Li-ion batteries by galvanostatic charge and discharge tests. The analysis of the samples shows that a proper tuning of the process via the experimental parameters can strongly improve the electrochemical performances of the electrodes. In this way cobalt oxide retains a remarkable capacity of about  $1300 \text{ mAhg}^{-1}$  after repeated charge and discharge. In this respect, the homogeneity in size of the active nanoparticles can be considered a pre-requisite for good electrochemical behaviour of the electrodes. Indeed, the characteristics of the sub-micrometric structures constituting the electrode, as well as the even dispersion and adhesion of the binder on the nanoparticles' surface, play a crucial role in determining and enhancing its performances. Consequently, a suitable match of the mechanical and electrical properties of the different materials is required for an effective and durable operation. The versatility of electro spraying makes it also possible to devise various approaches and strategies to fabricate nanocomposite coatings and to implement their manufacture in direct in-line, roll-to-roll processes. In this respect, commercial laminated electrodes with double-sided coatings by paste casting could be replaced by metal foils directly coated by simultaneous electro spraying on both sides with obvious advantages. It is worth noticing that the preparation of the precursors for electro spraying can be implemented in different ways. Accordingly, starting from a blank polymer solution three different approaches could be adopted for the creation of nanocomposite layers. The first one consists in the dissolution of metal salts and a subsequent pyrolysis of their final solution. The second one involves the preparation

of a homogeneous suspension by dispersion of pre-formed particles separately synthesized via gas-phase or solid-state routes. The third one relies on in-situ formation of the nanoparticles in the metal precursor solution by red-ox reactions and simultaneous polymer capping, in order to form a homogeneous 'ink' for subsequent deposition. This approach has not been reported, though some preliminary experiments have been also performed. Interestingly, this type of preparation could provide an attractive route to functional coatings directly by electro spraying at relatively low temperatures.

A slight variant of electro spraying coupled to chemical reactions in reductive baths is presented in chapter six. In particular, a one-step approach by direct electro spraying into a reductive-surfactant solution has been carried out for the fast and continuous preparation of quasi-spherical and anisotropic gold nanoparticles at room temperature. In this case, a precursor solution of  $\text{HAuCl}_4$  has been electro sprayed into a reductive bath with organic solvents where also a capping agent is present. Dodecylaminomethanol (DDAM), a bi-functional molecule that acts both as reducing and subsequently as stabilizing agent, causes the chemical reduction of  $\text{Au}^{3+}$  into  $\text{Au}^0$  from the electro sprayed precursor droplets and the quick formation of gold colloids. Gold nanoparticles are attractive for catalysis purposes and in this context they represent merely a possible example of nanostructures that can be directly produced and stabilized. Anisotropic gold nanoparticles with appropriate sizes for catalysis applications (5-12 nm edge length) have been successfully produced together with quasi-spherical nanoparticles of 4.5 nm edge. Even though an accurate control on the size distributions of the produced particles is still missing, the high flexibility of this method and its cost-effective features make this process a good candidate for production of stabilized nanoparticles, whose production can be scaled up by use of multiplexed-nozzle systems.

To conclude, significant breakthroughs can be envisaged for the fabrication of nanostructured functional materials via electro spray-based approaches. In particular, the challenges related to the synthesis and the assembly of nanocomposite materials for Li-ion batteries and fuel cells (i.e. electrodes, membranes and electrolytes) may be solved. The combination of theoretical studies and process engineering may eliminate shortcomings of existing processes and enable the development of the next generation of electrochemical devices and catalysis systems with much enhanced performances.





# Samenvatting

*Een stap is al een richting.*

*Doe maar gewoon, dan doe jij al gek genoeg.  
(Nederlandse wijsheid)*

## Conclusies en vooruitzichten

Nanogestructureerde materialen spelen een cruciale rol in de ontwikkeling van nieuwe apparaten en in de verbetering van de huidige technologische toepassingen. Energie-opslag via Li-ionbatterijen is een van de gebieden waar grote doorbraken worden verwacht door het gebruik van nanogestructureerde materialen. Op die manier kunnen beperkingen van conventionele materialen in commerciële systemen worden overwonnen.

In dit proefschrift worden functionele nanogestructureerde materialen voor negatieve elektroden voor Li-ion batterijen gesynthetiseerd via een aerosol route. Twee verschillende methoden, gebaseerd op elektrospinnen, zijn onderzocht voor de synthese en de assemblage van verschillende soorten nanodeeltjes en nanocomposieten. De eerste methode betreft de productie van nanodeeltjes via een nieuwe route waar geladen aerosols opgevangen worden in een vloeistof waar via red-ox reacties het gewenste materiaal wordt gemaakt. De tweede methode beslaat eenmethode die de synthese van de actieve componenten combineert met assemblage tot een nanocomposiet elektrode op een substraat. Dit proces gebeurt dus in een enkele-stap en werkt op basis van pyrolyse en/of depositie van precursor oplossingen en suspensies met actieve en inactieve componenten. De uiteindelijke toepassingen van deze methoden zijn niet beperkt tot Li-ionbatterijen, aangezien de ontwikkelde

techniek uitermate generiek is waardoor er vele andere toepassingen mee bediend kunnen worden, hierbij dient men te danken aan dunne lagen voor katalyse, brandstofcellen, zonnecellen, enz..

De uitdagingen in verband met het gebruik van alternatieve materialen om de prestaties van geavanceerde Li-ionbatterij-elektroden te verbeteren worden besproken in hoofdstuk een, waar bijzondere aandacht wordt besteed aan de negatieve elektroden en hun elektrochemische reactiemechanismen. Nanogestructureerde materialen worden gepresenteerd als aantrekkelijke kandidaten om de problemen van de meeste geavanceerde negatieve elektroden, namelijk Li-legeringen en overgangsmetaaloxiden, op te lossen. De elektrodedegradatie door volumevariaties als gevolg van reactie met lithium en de daarbij komende implicaties van de nanogestructureerde materialen worden eveneens besproken.

De basistheorie van elektrospinnen, samen met zijn operationele modi, wordt in hoofdstuk twee beschreven. In het bijzonder wordt de beschrijving van de zogenoemde “cone-jet” benadrukt, mede in het belang voor het sturen van de uiteindelijke eigenschappen van de geproduceerde nanodeeltjes. Voor- en nadelen van elektrospinnen worden in beschouwing genomen om uiteindelijk te kunnen besluiten hoe het hoofd te bieden aan de hamvraag: “hoe kan de productiesnelheid verhoogd worden”. Daartoe worden technieken gebaseerd op elektrospinnen (bijv. elektrospinnen middels pyrolyse en/of depositie alsmede elektrospinning) gepresenteerd als eenvoudige en goedkope methoden voor de synthese van nanogestructureerde materialen. Daarnaast worden sommige belangrijke voorbeelden van toepassingen met betrekking tot Li-ionbatterijen gegeven.

Een nieuwe route voor de synthese van nanogestructureerde poeders in de vloeibare fase wordt beschreven in hoofdstuk drie, waar elektrospinnen van metaalchloriden oplossingen is gekoppeld aan reductieve precipitatie om metaal en metaalachtige deeltjes te vormen. Materialen gebaseerd op tin zijn hiervoor geselecteerd vanwege hun potentiële toepassingen voor negatieve elektroden voor Li-ion batterijen. Elektrospinnen in de cone-jet en multi-jet mode wordt gecombineerd met reductieve precipitatie middels het reductiemiddel  $\text{NaBH}_4$  om zo in een vloeibaar medium, kleine metaal en metaalachtige nanodeeltjes met verschillende samenstellingen te synthetiseren. Tevens is het mogelijk om de grootte van de deeltjes te sturen. Echter kleinere deeltjes vertonen een hogere reactiviteit tegenover zuurstof en vocht. Hier zijn de experimenten in lucht uitgevoerd, maar onder een inert gas met een geschikt oplosmiddel is eveneens mogelijk. Dit soort syntheses kan gemakkelijk worden uitgebreid tot verschillende soorten materialen door het gebruik van geschikte precursors, reductiemiddelen en uiteindelijk stabilisatoren. Om de productie te verhogen kan gebruik gemaakt worden multi-nozzlesystemen waar dan parallelle atomisering van de precursors plaatsvindt. Om een continu proces te

verkrijgen zou het reductiebad moeten worden uitgerust met een in-line scheidingsunit om de geprecipiteerde deeltjes te verwijderen.

In hoofdstuk vier worden de op tin-gebaseerde nanopoeiders, geproduceerd via deze route, vervolgens onderzocht ten behoeve van negatieve elektroden. Nanogestructureerde poeders worden geproduceerd door elektrosprayen van Sn(II)chlorideoplossingen in een reductiebad met NaBH<sub>4</sub> als reductiemiddel. De morfologie van de gevormde deeltjes vertoont bolvormige agglomeraten waarvan de structuur bestaat uit nanokristallen van tin omgeven door een amorfe SnO<sub>x</sub> fase. Afdoende hoeveelheden materiaal wordt verkregen voor de verdere verwerking zoals het maken van coatings van elektroden voor elektrochemische metingen in knooppellen. Het elektrochemische gedrag van de nanogestructureerde poeders wordt onderzocht met behulp van galvanostatische testen. De spanningsprofielen en prestaties worden vergeleken met die van commercieel tin en tin(II,IV)oxide poeders met verschillende korrelgrootte. Opmerkelijk is dat hun laad- en ontladcurve geen duidelijke vlakke plateaus vertonen zoals gebruikelijk is bij de commerciële materialen. In het algemeen vertonen de nanogestructureerde poeders verbeterde capaciteiten voor ontladen, maar helaas is de irreversibele capaciteit na de eerste cyclus dusdanig groot, dat dat toepassing evenwel vooralsnog in de weg staat. De hoge irreversibele capaciteit is waarschijnlijk toe te schrijven aan de reactie met NaBH<sub>4</sub> die kleine deeltjes oplevert met een groot oppervlak waardoor er bij blootstelling aan lucht een relatief groot gedeelte oxide ontstaat, wat verantwoordelijk is voor die irreversibele capaciteit. Echter, de nanogestructureerde poeders vertonen vervolgens een relatief hoge reversibele laad- en ontladcapaciteit van ongeveer 300 mAhg<sup>-1</sup> na 100 cycli. Deze waarde is significant hoger dan die verkregen voor commerciële poeders. Verbeteringen van het gehele proces van synthese en collectie zijn mogelijk, toch zou dit niet het enige vereiste zijn voor verbetering van het totale elektrodesysteem. De assemblage of wel het coaten beslaat ook een belangrijk deel en mag in die zin zeker niet worden verwaarloosd. Om een doeltreffende werking van dit type van elektroden te verkrijgen, waar mechanische spanningen een belangrijke rol spelen, wordt een goede dispersie van de actieve deeltjes in het polymeer vereist waarbij een sterke hechting aan het metalen substraat eveneens een must is. In de meeste gevallen zijn manipulatie en verwerking van nanopoeiders in composietelektroden met inactieve componenten niet triviaal. Logischerwijs kunnen zo goede eigenschappen van actieve nanopoeiders gemakkelijk worden verbruist door onjuiste fabricage van de elektrode. Daarom is verbetering van de elektrochemische prestaties en de reversibiliteit van deze materialen eveneens afhankelijk van gedegen ontwerp en assemblage.

Een wijze voor de fabricage van composietelektroden wordt gepresenteerd in hoofdstuk vijf. De componenten van een elektrode worden gesynthetiseerd en geassembleerd bij relatief lage temperaturen op een verhit substraat middels een een-

staps proces van elektrospayen. Actieve nanodeeltjes worden gesynthetiseerd en gedispergeerd in een polymeer bindmiddel (bijv. PVDF) gedurende depositie op geselecteerde oppervlakken. Op deze manier wordt een nauw contact tussen het bindmiddel en de actieve nanodeeltjes verkregen in de coatings. Verschillende oxidische materialen van Sn, Co en Fe zijn onderzocht in PVDF/oxide nanocomposieten. De resultaten tonen aan dat de textuur van deze lagen wordt beïnvloed door het hele proces, maar heeft hier veelal geleid tot bolvormige nanostructuren, waarbij homogeen verdeelde oxides van enkele nanometers aanwezig zijn in de “balonnen” van de polymere binder. Er blijkt derhalve, dat met behulp van elektrospayen van polymeer/metaalzoutoplossingen welke onderworpen worden aan pyrolyse en reductie/oxidatie bij relatief lage temperaturen, geavanceerde elektrodelagen gedeponeerd kunnen worden. Hierbij zij tevens benadrukt dat de techniek een krachtig hulpmiddel is om nanodeeltjes te produceren met een gewenste textuur, door sturing middels de procesparameters. Dit beperkt zich overigens niet alleen tot de nanodeeltjes maar geldt ook voor de andere componenten in de composiet, opdat er een optimale werking verkregen wordt met betrekking tot de toepassing. De procesparameters die hierbij een rol spelen zijn substraattemperatuur, de afstand van de sproeinaald tot het substraat, samenstelling van de vloeistof en stroomsnelheid. De eerste resultaten tonen tevens aan dat er een goed contact ontstaat tussen het polymeer en de gevormde metaaloxiden. Ondanks dat de lagen voor allerlei toepassingen gebruikt kunnen worden, zijn de gevormde lagen slechts getest op lithiumopslag ten behoeve van negatieve elektroden voor Li-ionbatterijen. Deze testen omvatten met name galvanostatische laad- en onlaadtesten. Er blijkt dat door een juiste sturing van het proces middels de procesparameters de elektrochemische prestaties van de elektroden sterk verbeterd kan worden. Zo heeft een kobaltoxide-elektrode een capaciteit van 1300 mAh/g na langdurig laden en ontladen. In dit opzicht kan de homogeniteit als maat van de actieve nanodeeltjes worden beschouwd ofwel een voorwaarde voor goed elektrochemische gedrag van de elektrodes. Hierbij spelen de kenmerken van de sub-micrometrische structuren van de elektroden, evenals de gelijkmatige verspreiding en hechting van het bindmiddel aan het oppervlak van de nanodeeltjes, een cruciale rol in de verbetering van hun prestaties. Bijgevolg is een geschikte koppeling van de mechanische en elektrische eigenschappen van de verschillende materialen nodig voor een doeltreffende en duurzame werking. De veelzijdigheid van electrospayen maakt het ook mogelijk om verschillende benaderingen en strategieën te ontwikkelen om nanocomposietcoatings te fabriceren en om hun productie in directe in-line, roll-to-roll processen te implementeren. In dit verband kunnen commerciële gelamineerde elektroden met dubbelzijdige coatings door extruderen worden vervangen door coatings op een metalen folie door rechtstreeks te electrospayen aan beide zijden van de folie. Het concept van elektrospayen kan op meerdere wijzen ingezet worden, drie methodes

zijn hier toegepast. Allereerst via een oplossing van metaalzouten en een daaropvolgende pyrolyse. Een tweede methode behelst het sprayen van een homogene suspensie van deeltjes in een oplossing met een polymeer, waarbij composietlagen worden gevormd. Een derde methode is gebaseerd op in-situ vorming van de nanodeeltjes vanuit een metaal precursor-oplossing door red-ox reacties en gelijktijdige polymeerafzetting. Dit laatste kan gezien worden als het sprayen van een actieve inkt. Deze methode is niet direct gerapporteerd, maar de eerste en voorlopige experimenten zijn reeds uitgevoerd. Interessant is dat dit soort van methodes een aantrekkelijke route van rechtstreekse depositie van functionele coatings middels electrospoeien kan bewerkstelligen, zelfs bij relatief lage temperaturen.

Een variant van electrospayen gekoppeld aan chemische reacties bij reductief oplossen, wordt gepresenteerd in hoofdstuk zes. In het bijzonder wordt een een-staps benadering door middel van rechtstreeks electrospayen in een reductief-opervlakteactieve oplossing, uitgevoerd voor een snelle en continue productie van quasi-sferische en anisotrope gouden nanodeeltjes bij kamertemperatuur. In dit geval wordt een  $\text{HAuCl}_4$  oplossing gesprayd in een reductief bad met organische oplosmiddelen, waar ook een “capping” agent aanwezig is. Dodecylaminomethanol (DDAM), een bi-functioneel molecuul dat fungeert als zowel reductiemiddel als wel als stabilisator, veroorzaakt de chemische reductie van  $\text{Au}^{3+}$  naar  $\text{Au}^0$  van de opgevangen druppels, waarbij een snelle vorming van goudcolloïden wordt bewerkstelligd. Gouden nanodeeltjes zijn aantrekkelijk voor katalysedoeleinden en in dit verband vertegenwoordigen ze slechts een mogelijk voorbeeld van nanostructuren die direct kunnen worden geproduceerd en gestabiliseerd. Anisotropische gouden nanodeeltjes met de juiste groottes voor katalysetoepassingen (5-12 nm in lengte) zijn met succes geproduceerd samen met quasi-sferische nanodeeltjes van 4.5 nm diameter. Hoewel een nauwkeurige controle over de distributies van de groottes van de geproduceerde deeltjes nog steeds ontbreekt, maken de hoge flexibiliteit van deze methode en de kosten-effectieve productie, dit proces een goede kandidaat voor de productie van gestabiliseerde nanodeeltjes, waarvan de productie kan worden opgeschaald voor het gebruik van multi-nozzlesystemen.

Tot slot kunnen belangrijke doorbraken worden verwacht voor de fabricage van nanogestructureerde functionele materialen via electro-spray-gebaseerde benaderingen. In het bijzonder kunnen de uitdagingen in verband met de synthese en de assemblage van nanocomposietmaterialen voor Li-ion batterijen en brandstofcellen (dwz elektroden, membranen en elektrolyten) worden verbeterd. De combinatie van theoretische studies en procestecnologie kan ingezet worden om de eventuele tekortkomingen verder te elimineren, zodat de bestaande processen een verdergaande ontwikkeling mogelijk maken voor de volgende generatie van elektrochemische apparaten en katalyse systemen met verbeterde prestaties.



# Appendix A

## Electrochemical aspects

*“...we could share what we hide...after all...”  
(Apparat - Komponent)*

This appendix provides a short description of a few basic concepts related to electrochemical systems, with a particular focus on (rechargeable) batteries. Some general -but also peculiar- aspects are briefly analyzed and discussed.

## A.1 Nernst equation and thermodynamics of a cell

The thermodynamic voltage of a cell,  $V_{th}$ , is defined as the difference between the thermodynamic reduction potentials,  $E_{th}$ , of the two electrodes:

$$V_{th} = E_{th}(Cathode) - E_{th}(Anode) \quad (A.1)$$

where ‘‘cathode’’ is by definition the site where reduction takes place and ‘‘anode’’ the one where oxidation occurs. The Gibbs free energy associated to the electrochemical process is then:

$$\Delta G = -nFV_{th} \quad (A.2)$$

where  $n$  is the number of electrons transferred and  $F$  is Faraday’s constant (see later equation A.21). Moreover, the Gibbs free energy for a reaction is expressed as:

$$\Delta G = \Delta G^\circ + RT \ln \left( \frac{\prod a_{prod}}{\prod a_{react}} \right) \quad (A.3)$$

where  $a_{prod}$  and  $a_{react}$  are the activities of the products and the reactants, respectively,  $\Delta G^\circ$  is the standard free energy,  $R$  the ideal gas constant and  $T$  the temperature. Considering the general electrochemical reaction in a cell where two species can be reversibly oxidized and reduced:



the application of (A.2) and (A.3) enables the derivation of the Nernst equation:

$$V_{th} = V^\circ - \frac{RT}{nF} \ln \left( \frac{a_{Red_1} a_{Ox_2}}{a_{Ox_1} a_{Red_2}} \right) \quad (A.5)$$

where  $V^\circ$  is the standard cell voltage (i.e. the thermodynamic voltage of the cell under standard conditions) and  $V^\circ$  is the difference of the standard electrode potentials. It is important to observe that Nernst equation applies to the thermodynamic potentials  $E_{th}$  of each electrode. In particular,  $E_{th}$  is defined as the potential of the considered electrode (as a cathode) versus the Standard Hydrogen Electrode (SHE). The standard potential of such electrode is referred to as standard electrode potential  $E^\circ$ :

$$E_{th} = E^\circ - \frac{RT}{nF} \ln \left( \frac{a_{Red}}{a_{Ox}} \right) \quad (A.6)$$



The direction of the reaction can be evaluated by thermodynamics at constant temperature and pressure:

- a.  $\Delta G < 0 \Rightarrow V_{th} > 0 \Rightarrow$  Spontaneous reaction
- b.  $\Delta G = 0 \Rightarrow V_{th} = 0 \Rightarrow$  Equilibrium
- c.  $\Delta G > 0 \Rightarrow V_{th} < 0 \Rightarrow$  Forced reaction

From (A.1) it is seen that if  $E_{th}(Cathode) > E_{th}(Anode)$  the reaction is spontaneous and the cell behaves as a galvanic cell; vice versa the reaction needs an external driving force (i.e. a power supply) to proceed and the system acts as an electrolytic cell. The thermodynamic voltage is also referred to as open circuit voltage (OCV), because it is measured under conditions in which no current flows through the cell. When a current flows, the measured voltage is no longer determined by the thermodynamics, but other non-thermodynamical processes intervene. These processes are directly related to various mechanisms that take place in the cell, namely: *mass transfer* in proximity of the electrodes, *charge transfer* at the electrode interface and *internal resistance* opposed to the movement of the charge carriers.

## A.2 Effects of the current flow on a cell

The flow of an electrical current,  $i$ , in a cell causes that the electrode potentials under such conditions,  $E_i$ , are no longer equal to  $E_{th}$ , so that an *overpotential*,  $\eta$ , is present according to:

$$\eta = E_i - E_{th} \quad (A.7)$$

The overpotential is then constituted by two terms according to:

$$\eta = \eta_{CT} + \eta_{MT} \quad (A.8)$$

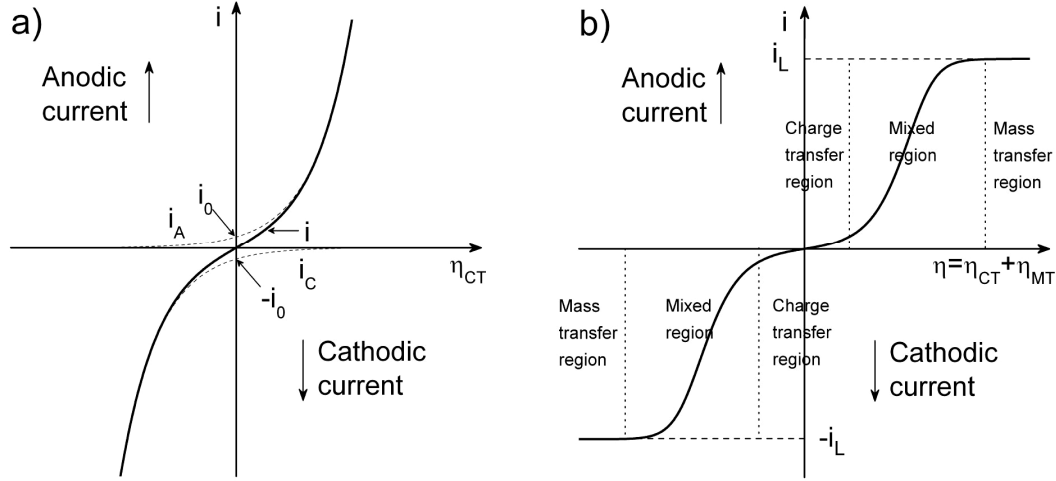
where  $\eta_{CT}$  is the charge transfer overpotential and  $\eta_{MT}$  the mass transfer overpotential.

### *I – Charge transfer*

The charge transfer overpotential  $\eta_{CT}$  is defined by the Butler-Volmer equation:

$$i = i_0 \left[ \exp\left(\frac{\alpha_s n F \eta_{CT}}{RT}\right) - \exp\left(-\frac{(1 - \alpha_s) n F \eta_{CT}}{RT}\right) \right] \quad (A.9)$$

where  $i$  is the current flowing through the cell,  $i_0$  is the exchange current,  $\alpha_s$  is the symmetry factor. A schematic representation of this equation is shown in Fig. A.1a.



**Fig. A.1.** Schematic drawing of the current  $i$  versus the charge transfer overpotential (i.e. Butler-Volmer equation) (a) and as a function of the total overpotential  $\eta = \eta_{CT} + \eta_{MT}$  [1].

It is further observed that the total current is a combination of two terms, namely the cathodic current  $i_C$  (corresponding to the reduction direction of the electrode reaction) and the anodic current  $i_A$  (corresponding to the oxidation direction of the electrode reaction) according to the following formulae:

$$i_A = i_0 \exp\left(\frac{\alpha_s n F \eta_{CT}}{RT}\right) \quad (\text{A.10})$$

$$i_C = -i_0 \exp\left(-\frac{(1-\alpha_s) n F \eta_{CT}}{RT}\right) \quad (\text{A.11})$$

In particular, considering the last three equations it can be noted that if  $\eta_{CT} \gg 0$  then it is  $i \approx i_A$ . Conversely if  $\eta_{CT} \ll 0$  then results  $i \approx i_C$ . Moreover, if  $\eta_{CT} \rightarrow 0$  equation (A.9) can be approximated to:

$$\eta_{CT} \approx \left(\frac{RT}{nF}\right) \frac{i}{i_0} \quad (\text{A.12})$$

which is linear in  $i$ . Consequently, a charge transfer resistance can be defined as:

$$R_{CT} = \frac{\eta_{CT}}{i} = \frac{RT}{i_0 n F} \quad (\text{A.13})$$

in order to obtain an equivalent of the Ohm's second law (i.e.  $\eta_{CT} = R_{CT} \cdot i$ ).

### II – Mass transfer

The mass transfer overpotential,  $\eta_{MT}$  is defined as follows:

$$\eta_{MT} = -\frac{RT}{nF} \ln\left(1 - \frac{i}{i_L}\right) \quad (\text{A.14})$$

where  $i_L$  is the maximum (i.e. limit) current determined by the reaction kinetics due to the mass transfer. This expression can be approximated to:

$$\eta_{MT} \approx \left(\frac{RT}{nF}\right) \frac{i}{i_L} = i \left(\frac{RT}{i_L nF}\right) = iR_{MT} \quad (\text{A.15})$$

where  $R_{MT}$  can be defined as a mass transfer resistance, so as to have an analogous of the Ohm's second law. From Fig. A.1b, it is also seen that the maximum current  $i_L$  is reached for high overpotentials  $\eta$ .

In a full cell overpotentials are developed at both electrodes. Therefore, at the positive side  $\eta_+$  is present, as well as  $\eta_-$  at the negative side. The voltage of the cell,  $V_i$ , when a current  $i$  flows through it is then given by:

$$V_i = V_{th} + \eta_+ + \eta_- \quad (\text{A.16})$$

In Fig. A.2 the variation of the cell voltage upon current flow is schematically shown. In particular it can be seen that during the discharge process is  $V_d = V_i < V_{th}$ , while during charge is  $V_{ch} = V_i > V_{th}$ .

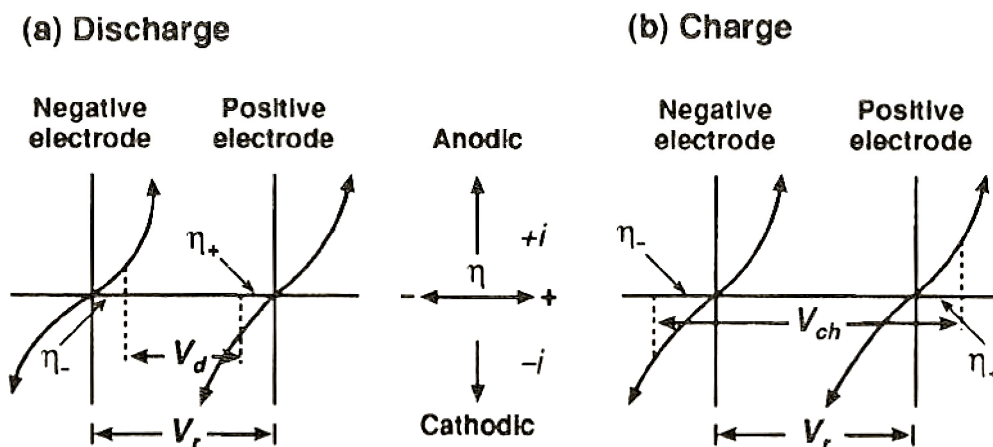


Fig. A.2. Variation of the cell voltage due to current flow during discharge and charge [2].

### III – Internal resistance of the cell

The last contribution that has to be taken into account is the internal resistance of the cell,  $R_{int}$ . In this way during the discharge the actual voltage of the cell is:

$$V_d = V_i = V_{th} - |\eta_+| - |\eta_-| - iR_{int} \quad (\text{A.17})$$

which can be conveniently approximated to:

$$V_d = V_i = V_{th} - iR_{CT} - iR_{MT} - iR_{int} = V_{th} - iR' \quad (\text{A.18})$$

where  $R'$  has the following expression:

$$R' = R_{CT} + R_{MT} + R_{int} \quad (\text{A.19})$$

Analogous considerations hold for the charge process as well.

## A.3 Theoretical capacity of electrode materials

The capacity,  $Q_{tot}$ , defines the total amount of electrical charge that a cell or an electrode material is able to store. The *specific capacity*,  $C_{sp}$ , of a material is then defined as the capacity per unit of mass according to the general formula:

$$C_{sp} = \frac{Q_{tot}}{m} = \frac{1}{m} \cdot \int_0^t i(\tau) d\tau \quad (\text{A.20})$$

where  $i(\tau)$  is the electrical current flowing through the cell,  $m$  is the material mass and  $t$  the time. Despite this simple definition, the calculation of  $C_{sp}$  is not trivial and it can often lead to misconceptions. Therefore, a *theoretical capacity*,  $C_{th}$ , can be rigorously defined on the basis of Faraday's laws. In such a way, the theoretical electrical charge that is stored in an active material in an electrochemical reaction can be evaluated by summarizing the two laws of Faraday:

1. The mass of a substance altered at an electrode is directly proportional to the quantity of electricity transferred at that electrode. Quantity of electricity refers to the quantity of electrical charge, typically measured in coulomb (C). The Faraday's constant is defined as the amount charge carried by one mol of electrons, according to:

$$F = N_A \cdot e \approx 96485 \text{ C} \cdot \text{mol}^{-1} \quad (\text{A.21})$$

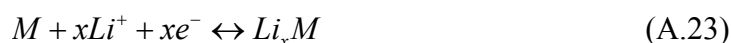
where  $N_A$  is the Avogadro's number and  $e$  represents the electron charge.

2. For a given quantity of electricity (electric charge), the mass of an elemental material altered at an electrode is directly proportional to the element's equivalent weight. The equivalent weight of a substance is its molar mass divided by an integer that depends on the reaction undergone by the material.

The mathematical expression for their combination is the following:

$$m = \frac{Q_{tot} M_m}{nF} \quad (\text{A.22})$$

where  $m$  is the mass of the substance at the electrode,  $M_m$  is the molar mass of the same substance, and the other quantities have been already defined. In particular, when the current passed through the cell is constant, then it is  $Q_{tot} = i \cdot t$ . Under such condition, if one considers the general reaction of an active material  $M$  with lithium:



then the theoretical capacity per unit of mass can be then calculated by combination of equations A.20 and A.22:

$$C_{th} = \frac{x \cdot F}{M_m} \quad (\text{A.24})$$

where  $n = x$ . In this way  $C_{th}$  is expressed in units of  $\text{Cg}^{-1}$ . Capacities are often reported in units of  $\text{mAhg}^{-1}$ , which are immediately obtained by:

$$C'_{th} = \frac{x \cdot F}{M_m \cdot 3.6} \quad (\text{A.25})$$

In practical applications the capacity of a battery is defined as the total amount of electrical charge that is provided by (or supplied to) the battery when its voltage spans a certain range limited by pre-fixed cut-off values. In most of the cases the capacity of a battery differs significantly from its theoretical value. Furthermore, it strongly depends on the current applied during discharge and charge. The practical specific capacity of an electrode material can be also calculated from the practical capacity divided by the mass of the electrode.

### A.3.1 Errors on the practical capacity of the tested electrodes

In the previous chapters only the experimental values of the practical capacity have been reported. However, it should be noted that these values are unavoidably affected by errors and their propagation. Indeed, if the final values have to be thoroughly calculated their respective uncertainties should be evaluated. In particular, the galvanostatic tests performed by the battery cycler require applying a constant current to a defined mass of the electrode. In this way the applied gravimetric current density ( $\text{mA g}^{-1}$ ) is fixed and the obtained capacity is calibrated on the basis of the theoretical capacity (i.e. equation A.25) of the material of interest. Therefore one should consider the practical capacity:

$$C_{pr} = \frac{Q_{pr}}{m_t} = \frac{1}{m_t} \cdot I \cdot t \quad (\text{A.26})$$

where  $I$  is the constant current flowing through the cell, controlled by the cycler,  $t$  is the time of the process and  $m_t$  is the total mass of the electrode. Therefore, a first, rough calculation of the error for  $C_{pr}$  is the following:

$$\Delta C_{pr} = \left( \frac{t}{m_t} \right) \Delta I + \left( \frac{I}{m_t} \right) \Delta t + \left( \frac{I \cdot t}{m_t^2} \right) \Delta m_t \quad (\text{A.27})$$

It should be observed that the uncertainties  $\Delta I$  and  $\Delta t$  are negligible and that the biggest source of error is related to the total mass of the electrode. Therefore it is reasonable to assume:

$$\Delta C_{pr} \approx \left( \frac{I \cdot t}{m_t^2} \right) \Delta m_t \quad (\text{A.28})$$

In particular, the final value of the actual capacity is calibrated on the basis of equation A.25, where all the quantities of the material of interest are exactly known and the uncertainty arises mainly from the propagation of the error for the mass of the active material and those of the binder and the carbon black, influencing the relative weight ratios of the components. In particular, two particular cases are considered.

#### *I – Coated electrodes on copper foil obtained by paste casting*

The composite electrodes are made up of the active material, the binder and carbon black, which are thoroughly mixed in a fixed weight ratio in a slurry and then coated to a copper disk. The mass of the whole composite electrode,  $m_t$  is determined by subtraction:

$$m_t = m_{coat} - m_{coll} \quad (\text{A.29})$$

where  $m_{coat}$  is the mass of the entire coated electrode on the metallic support, and  $m_{coll}$  is the mass of the blank current collector. Therefore the absolute error on  $m_t$  is:

$$\Delta m_t = \Delta m_{coat} + \Delta m_{coll} \quad (\text{A.30})$$

where the propagation of the errors for the masses of the components yields:

$$\Delta m_{coat} = (\Delta m_{am} + \Delta m_{bind} + \Delta m_{CB}) \quad (\text{A.31})$$

All the uncertainties on the masses are connected to the sensitivity of the balance, which is  $\pm 10^{-5}$  g. The typical mass of the composite electrodes obtained in this way is normally about 1-2 mg.

#### *II – Coated electrodes via direct electrospray on coin cell cans*

The composite electrodes in this case are made up only of the active material and the binder, which are directly synthesized and assembled on coin cell cans. Considerations similar to the previous case can be made. However, it should be kept in mind that the uncertainties on the weight of the dissolved precursors and polymer binder propagate on further chemical reactions, which determine the final products and the active/inactive component masses and their respective proportions.

## **A.4 Electro spraying: an ‘atypical’ electrolytic cell?**

Electrospraying (ES) or Electrohydrodynamic Atomization (EHDA) is a physical phenomenon that refers to the atomization of liquids when subjected to intense electric fields. The formation of the so-called Taylor cone and the thin charged jet emitted from its apex have been explained by means of two different mechanisms of charge transfer: *charge conduction* and *charge convection*.

Inside the liquid, the charge is transported by conduction and the liquid cone has been regarded as an almost perfect conductor with low electric field strengths on its inner part. However, the electric field, the surface charge and the axial liquid velocity increase from the base of the cone toward its tip during the EHDA process. These effects are related to charge convection, through which free charges present on the surface of the liquid are accelerated by the tangential component of the electric field towards the cone apex. It is important to observe that the free charge in a liquid is mainly constituted by ions that are created during the atomization process. Ions in

the liquid play a key role in EHDA, since without surface free charges the continuous production of charged jets and droplets of the same polarity would not be possible.

The buildup of charges in the jet and the emitted droplets has been described by some authors as an electrophoretic mechanism [3-5]. Electrophoretic charging in a solution occurs when a partial separation of the positive ions from the negative ions takes place, due to the presence of an applied electric field. In this way, an excess of charge with a certain sign is developed on the surface of the liquid at the tip of the electrified nozzle.

It is important to observe that the buildup and loss of an excess of one ion polarity in the charged jet and droplets imply a current flowing through the entire circuit. A small continuous current is indeed measured during EHDA (i.e. generally 0.1-1  $\mu\text{A}$ ), meaning that *electrons* flow through the metallic wires connecting the electrodes (i.e. the nozzle and the counter-electrode) with the high voltage power supply. The crucial point is that *if* the assumption of an electrophoretic mechanism holds, then the requirements for charge balance in such system, which yields a quasi-continuous steady-state current at the counter electrode with the same polarity of the electrified capillary, involve an electrochemical conversion of ions to electrons [6].

Following this line of reasoning, in the absence of a charge-balancing process, the buildup of charge in the nozzle would create a field in solution opposing the external applied field, thus contrasting the driving force for ion migration (i.e. electrophoretic charge separation), which on its turn would cause the extinction of charged droplet emission. This fact implies that an ES setup can be eventually regarded as a “special type” of electrolytic cell and that electrochemistry is somehow inherent to the EHDA process. This aspect of ES has been neglected until 1991, when it was first proposed that the mechanism responsible for charge balance in the electrified nozzle is electrochemical in nature [6], even though quite some doubt remains. According to this different perspective ES could be described as a controlled-current electrolytic cell (CCEC) and its peculiarity would arise from the fact that a portion of charge transport between the electrodes occurs via the gas phase, rather than the liquid phase (i.e. a liquid electrolyte) as in a conventional electrolytic cell.

## A.5 References

- [1] L. Simonin, *Synthesis and characterisation of tin and antimony nano-compounds for lithium battery applications*, PhD Thesis **2009**.
- [2] R. W. D. A. J. Rand, R. M. Dell, *Batteries for electric vehicles*, Wiley Research Studies Press **1998**.



- [3] I. Hayati, A. Bailey, T. F. Tadros, *Journal of Colloid and Interface Science* **1987**, *117*, 222.
- [4] M. G. Ikonou, A. T. Blades, P. Kebarle, *Analytical Chemistry* **1990**, *62*, 957.
- [5] D. P. H. Smith, *IEEE Trans. Ind. Appl.* **1986**, *1A-22*, 527.
- [6] A. T. Blades, M. G. Ikonou, P. Kebarle, *Analytical Chemistry* **1991**, *63*, 2109.



# Appendix B

## Particle formation in liquid media

*“...I was looking back to see  
if you’re looking back at me  
to see me looking back at you...”  
(Massive Attack - Safe from harm)*

This appendix discusses the basic concepts behind the formation of solid particles in liquid media. The fundamentals of homogeneous nucleation and growth of nanoparticles in liquid solutions are described, as well as the evaporation of precursor liquid droplets in a gas atmosphere. Droplet drying and precipitation of particles at the interface gas-liquid are also illustrated.

## B.1 Nanoparticles via homogeneous nucleation

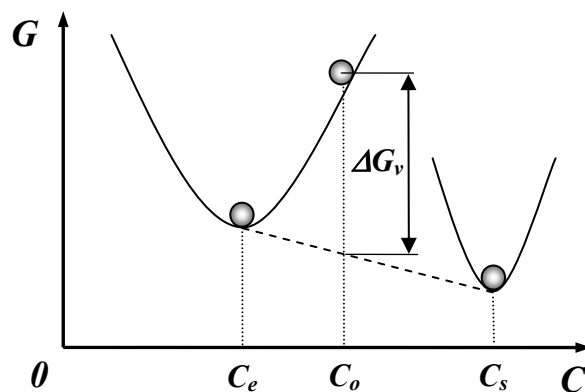
The formation of nanoparticles via homogeneous nucleation requires the creation of a *supersaturation* of growth species. For example, a reduction in temperature of an equilibrium mixture, such as a saturated solution can lead to supersaturation. Another method is to generate supersaturation through chemical reactions, by converting in situ highly soluble chemicals into less soluble ones. Nanoparticles can be synthesized through homogeneous nucleation in liquid, gas and solid media, being the fundamentals of nucleation and subsequent growth essentially the same [1].

The basic ideas are here presented as a general background for the generation of metallic nanoparticles by reductive precipitation of liquid precursors. The driving force for the formation of the nuclei, as well as their subsequent growth are here discussed in an ideal thermodynamic context, which is clearly far from the real experimental conditions. Nevertheless, they provide a first approach to the key points of the phenomenon.

## B.2 Basic aspects of homogeneous nucleation

A solution with a solute exceeding the solubility or “supersaturation” has a high Gibbs free energy. In this case the overall energy of the system could be reduced by segregating the solute from the solution.

Fig. B.1 shows the reduction of the overall Gibbs free energy,  $G$ , of a supersaturated solution by forming a solid phase while maintaining an equilibrium concentration in the solution.



**Fig. B.1.** Schematic plot of the reduction of the overall Gibbs free energy for a supersaturated solution. Note the formation of a solid phase, while an equilibrium concentration in the solution is maintained.  $C$  is the concentration of the solute,  $C_0$  the initial concentration,  $C_e$  the equilibrium concentration and  $C_s$  the concentration at which the solid phase is formed.

The decrease of Gibbs free energy represents the driving force for both processes of nucleation and growth. The change in Gibbs free energy per unit volume of the solid phase,  $\Delta G_v$ , is dependent on the concentration of the solute according to the following expression:

$$\Delta G_v = -\frac{k_B T}{\Omega} \ln(C/C_0) = -\frac{k_B T}{\Omega} \ln(1 + \Sigma) \quad (\text{B.1})$$

where  $C$  is the concentration of the of the solute,  $C_0$  is the initial concentration,  $k_B$  is the Boltzmann constant,  $T$  the temperature,  $\Omega$  the atomic volume and  $\Sigma$  is the supersaturation defined as  $(C-C_0)/C_0$ . In absence of supersaturation (i.e.  $\Sigma=0$ ),  $\Delta G_v$  is zero and no nucleation occurs. When  $C > C_0$ ,  $\Delta G_v$  is negative and nucleation occurs spontaneously.

Assuming a spherical nucleus of radius  $r$ , the change in the chemical potential,  $\Delta\mu_v$ , associated to the volume energy is:

$$\Delta\mu_v = \frac{4}{3} \pi r^3 \Delta G_v \quad (\text{B.2})$$

However, the decrease in energy associated to the nucleation of the solid phase is counter-balanced by the introduction of an extra surface energy related to the newly formed phase. Consequently, the increase in surface energy of the system is expressed as:

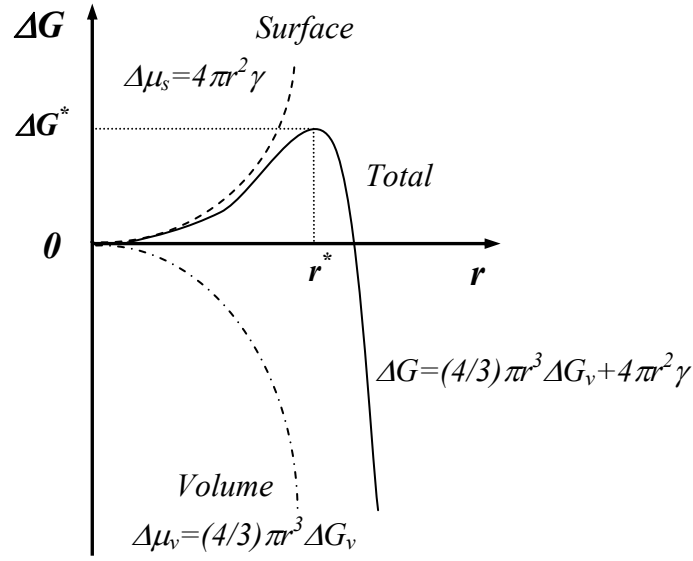
$$\Delta\mu_s = 4\pi r^2 \gamma \quad (\text{B.3})$$

where  $\gamma$  is the surface energy per unit area. The total change of chemical potential for the formation of the nucleus,  $\Delta G$ , is given by:

$$\Delta G = \Delta\mu_v + \Delta\mu_s = \frac{4}{3} \pi r^3 \Delta G_v + 4\pi r^2 \gamma \quad (\text{B.4})$$

Fig. B.2 represents the total change of the chemical potential  $\Delta G$ , the volume free energy  $\Delta\mu_v$  and the surface free energy  $\Delta\mu_s$  terms, as a function of the nucleus' radius.

It can be noticed that the created nucleus is stable only when its radius exceeds a critical size,  $r^*$ , (i.e. critical radius). Therefore, a nucleus with  $r < r^*$  spontaneously dissolves into the solution in order to reduce the overall free energy. Conversely, a nucleus with  $r > r^*$  is stable and undergoes subsequent growth. When the radius of the nucleus equals the critical radius (i.e.  $r=r^*$ ),  $(d\Delta G/dr)_{r^*}$  equals zero and  $r^*$  and the critical chemical potential  $\Delta G^*$  are respectively defined by the following relations:



**Fig. B.2.** Schematic plot for the change of volume free energy,  $\Delta\mu_v$ , surface free energy,  $\Delta\mu_s$ , and total free energy,  $\Delta G$ , as a function of the radius of the nucleus.

$$r^* = -\frac{2\gamma}{\Delta G_v} \quad (\text{B.5})$$

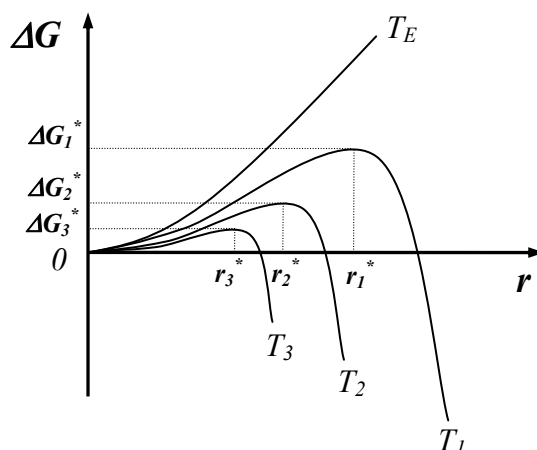
$$\Delta G^* = \frac{16\pi\gamma}{(3\Delta G_v)^2} \quad (\text{B.6})$$

$\Delta G^*$  represents the energy barrier that must be overcome in order to have nucleation and  $r^*$  represents the minimal size for a stable spherical nucleus.

It is worth noticing that all the above equations are referred to a supersaturated solution, nevertheless they can be generalized for a supersaturated vapour and a supercooled gas or liquid. In the synthesis via homogeneous nucleation from supersaturated solution or vapour, the critical radius represents the limit for the smallest nanoparticles that can be produced.

From equations (B.5) and (B.6) it is seen that in order to reduce the critical radius and the activation energy for nucleation it is necessary to increase the change in the Gibbs free energy,  $\Delta G_v$ , and to reduce the surface energy of the new phase,  $\gamma$ . According to equation (B.1),  $\Delta G_v$  can be significantly increased by enhancing  $\Sigma$  for a given system.

The temperature plays also an important role in the entire process. Fig. B.3 shows a comparison for  $r^*$  and  $\Delta G^*$  of three spherical nuclei with different values of supersaturation. The temperature can influence surface energy as well; changes of its value for a solid nucleus are especially observed near the so-called “roughening temperature”.



**Fig. B.3.** Schematic illustrating the effect of the temperature on the critical radius and the critical chemical potential of three spherical nuclei. Note that the supersaturation increases with decreasing temperature and that the surface energy is also temperature-dependent. In the plot is  $T_E > T_1 > T_2 > T_3$ , being  $T_E$  the equilibrium temperature.

The rate of nucleation per unit volume and per unit time,  $R_N$ , is proportional to: (i) the probability,  $P_{th}$ , for a thermodynamic fluctuation of the critical chemical potential  $\Delta G^*$ , expressed by the following Boltzmann factor:

$$P_{th} = \exp\left(-\frac{\Delta G^*}{k_B T}\right) \quad (\text{B.7})$$

to (ii) the number of growth species per unit volume,  $n_{sp}$ , which can be used as nucleation centers (in homogeneous nucleation it equals the initial concentration  $C_0$ ) and to (iii) the successful jump frequency of the growth species,  $\Gamma$ , from a site to another, given by:

$$\Gamma = \frac{k_B T}{3\pi d_{gs}^3 \mu} \quad (\text{B.8})$$

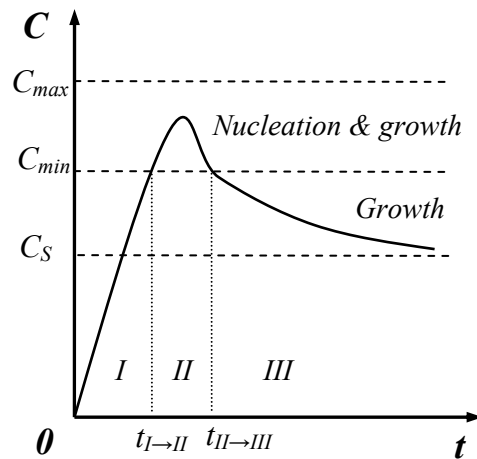
where  $d_{gs}$  is the diameter of the growth species and  $\mu$  is the viscosity of the solution. Therefore, the rate of nucleation can be finally expressed by:

$$R_N = n_{sp} P_{th} \Gamma = \frac{C_0 k_B T}{3\pi d_{gs}^3 \mu} \exp\left(-\frac{\Delta G^*}{k_B T}\right) \quad (\text{B.9})$$

It can be seen that high initial concentration, or supersaturation (i.e. a large number of nucleation sites), low viscosity and low critical energy barrier result in a large number

of nuclei. In particular, for a given concentration of solute, the larger the number of the formed nuclei, the smaller their average size.

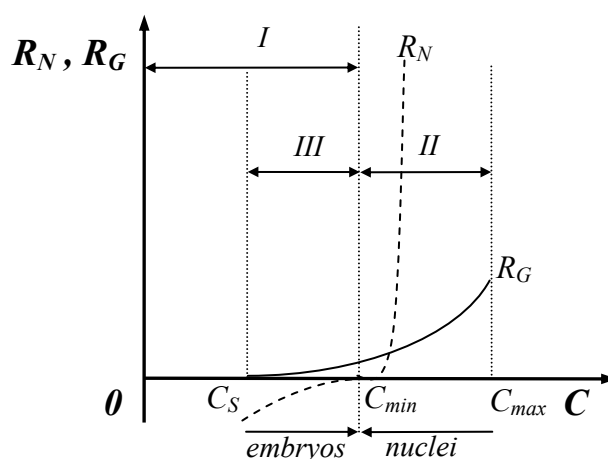
Fig. B.4 shows a schematic plot for the processes of nucleation and subsequent growth. When the concentration of the solute increases as a function of time (i.e. region I), no nucleation can occur even above the equilibrium solubility. Nucleation can take place only when the supersaturation reaches a value above the solubility, which corresponds to the energy barrier defined by equation (B.6) for nuclei formation (i.e. region II). After the initial nucleation, the supersaturation of the growth species decreases and the change in Gibbs free energy reduces. As soon as the concentration decreases below this specific value, which corresponds to the critical energy, nuclei can no longer be formed. Conversely, the growth of the generated nuclei proceeds until the concentration of growth species reaches the equilibrium concentration or solubility (i.e. region III).



**Fig. B.4.** Schematic plot for the processes of nucleation and successive growth. Note that even above the equilibrium solubility (i.e.  $C=C_{min}$ ) nucleation cannot take place until the energy barrier is fully overcome.

Fig. B.5 presents a similar plot which schematizes the relations between nucleation, growth rates and concentration of growth species in a slightly different way. It can be seen that initially no nucleation occurs, although the concentration of growth species increases above the equilibrium concentration. However, after reaching supersaturation and thus overcoming the critical energy barrier, nucleation rate increases very rapidly, as the concentration rises further. It is important to note that, although the growth cannot proceed when no nuclei are present, the growth rate is above zero for a concentration higher than its equilibrium solubility. Once the nuclei are formed, growth occurs simultaneously. It should be also remarked that above the minimum concentration nucleation and growth are inseparable processes, which, however, run at different speeds.





**Fig. B.5.** Schematic showing the nucleation and growth rates versus the concentration of the growth species. The nucleation rate  $R_N$  is represented by the dashed line, while the growth rate  $R_G$  corresponds to the solid line.

From these considerations it is expected that the synthesis of nanoparticles with uniform size distribution can be best achieved if all the nuclei are generated at the same time. In this case, all the nuclei are likely to have similar size, since they are formed under identical conditions. Moreover, all the nuclei can undergo the same subsequent growth, forming monodispersed particles. Therefore, it is clear that it is highly desirable to have nucleation running only in a very short period of time. In practice, the concentration of the growth species is abruptly raised to a very high supersaturation and then quickly quenched below the minimum concentration, in order to achieve sharp nucleation. Below this ‘threshold’ concentration no new nuclei are formed, whereas the existing ones continue to grow until the concentration of the growth species reduces to that of equilibrium. The size distribution of the particles can be further altered in the successive growth process. In particular, the size distribution of initial nuclei may be narrowed or widened depending on the kinetics of the growth process (i.e. other mechanisms ripening, coalescence etc. can also take place). Uniformly-sized nanoparticles can be obtained, provided that controlled growth conditions can be fulfilled.

### B.3 Growth of nuclei

The size distribution of nanoparticles is dependent on the subsequent growth process that the generated nuclei undergo. This process involves several steps, such as: (i) generation of growth species, (ii) diffusion of the growth species to the growth surface, (iii) adsorption on the growth surface, (iv) surface growth via irreversible incorporation of the growth species onto the growth surface. Furthermore, these steps

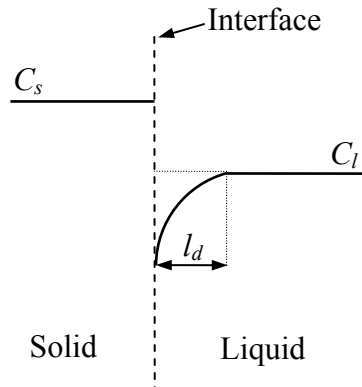
can be grouped into two processes. Supplying the growth species to the growth surface is termed as “diffusion”. It includes generation, diffusion and adsorption of the growth species onto the growth surface. On the other hand, incorporation of the growth species absorbed onto the growth surface, is referred as to “growth”. A *diffusion-limited* process generally yields a different size distribution for the particles when compared to a *growth-limited* one.

### B.3.1 Growth controlled by diffusion

In all the cases where the concentration of the growth species reduces below the minimum concentration for generation of new nuclei, nucleation stops. However, the growth of the existing nuclei proceeds. If the process is controlled by the diffusion of the growth species from the “bulk” solution to the particle surface, then the growth rate can be expressed as:

$$\frac{dr}{dt} = D(C_l - C_s) \frac{V_m}{r} \quad (\text{B.10})$$

where  $r$  is the radius of the spherical nucleus,  $D$  is the diffusion coefficient of the growth species,  $C_l$  is the bulk concentration,  $C_s$  is the concentration on the surface of the solid particles, and  $V_m$  is the molar volume of the nuclei. This situation is schematically represented in Fig. B.6.



**Fig. B.6.** Schematic representation of the concentration profile at the interface of a growing solid phase in contact with a liquid phase. Note the formation of a depletion boundary layer in the liquid region in proximity of the solid-liquid interface.

The solution of the differential equation (B.10) can be written by considering the change of bulk concentration negligible and an initial size of the nucleus  $r_0$ , so that:

$$r^2 = 2D(C_l - C_s)V_m t + r_0^2 \quad (\text{B.11})$$

and rewritten by taking  $k_D = 2D(C_l - C_s)V_m$  is simply:

$$r^2 = k_D t + r_0^2 \quad (\text{B.12})$$

Therefore, the radius of a particle during a diffusion-controlled process grows with a square-root dependence from the growth time. In particular, for two particles which have an initial radius difference  $\delta r_0$ , the radius difference at subsequent time,  $\delta r$ , decreases with increasing time according to:

$$\delta r = \frac{r_0 \delta r_0}{r} \quad (\text{B.13})$$

and expressing  $r$  through eq. (B.12) is:

$$\delta r = \frac{r_0 \delta r_0}{\sqrt{k_D t + r_0^2}} \quad (\text{B.14})$$

Therefore, the radius difference decreases with increasing radius of nucleus and for prolonged growth time. From this, it can be concluded that a diffusion-controlled process facilitates the formation of uniformly-sized particles.

### B.3.2 Growth controlled by surface processes

The growth rate of nanoparticles is controlled by surface processes when the diffusion of growth species from the bulk to the growth surface is sufficiently rapid. In this case the concentration on the surface equals the one in the bulk (i.e. no depletion layer in Fig. B.6). Two different mechanisms for the surface processes are possible: mononuclear growth and poly-nuclear growth. In the first case the growth proceeds layer by layer. The growth species are incorporated into one layer, and the formation of the subsequent layer starts only after the complete growth of the previous one. In this case there is time enough for the growth species to diffuse on the surface, and the growth rate is proportional to the surface area according to:

$$\frac{dr}{dt} = k_m r^2 \quad (\text{B.15})$$

where  $k_m$  is a constant dependent on the concentration of the growth species.

The solution of the previous equation is the following:

$$\frac{1}{r} = \frac{1}{r_0} - k_m t \quad (\text{B.16})$$

It can be seen that the radius difference increases with an increasing radius of the nucleus.

$$\delta r = r^2 \frac{\delta r_0}{r_0^2} \quad (\text{B.17})$$

Substituting equation (B.16) in (B.17) results in:

$$\delta r = \frac{\delta r_0}{(1 - k_m r_0 t)^2} \quad (\text{B.18})$$

where  $k_m r_0 t < 1$ . This boundary condition is derived from equation (B.16) and it takes into account that in all the real cases the radius is finite (i.e.  $r < \infty$ ). Equation (B.18) indicates that the radius difference increases with increasing growth time, and clearly this occurrence does not promote the formation of monodispersed particles.

In the case of poly-nuclear growth, the surface process is so fast that the growth of the second layer proceeds before the completion of the first one. The growth rate of the nuclei is independent from both size and time, according to:

$$\frac{dr}{dt} = k_p \quad (\text{B.19})$$

where  $k_p$  is a constant that depends only on the temperature. Hence, the particles grow linearly with time:

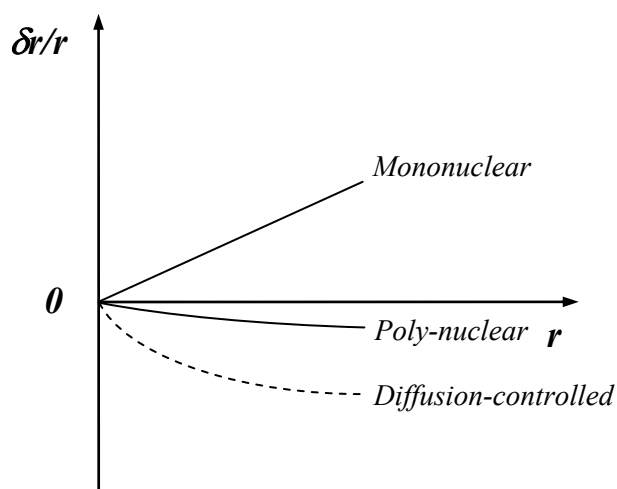
$$r = k_p t + r_0 \quad (\text{B.20})$$

In this case, the radius difference remains constant regardless of the growth time and the absolute particle size:

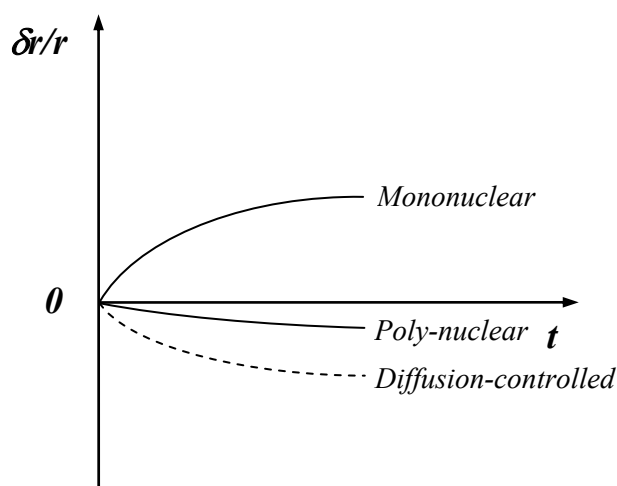
$$\delta r = \delta r_0 \quad (\text{B.21})$$

However, it should be noted that although the absolute radius difference does not change, the relative radius difference is inversely proportional to the particle radius and the growth time. Therefore, as the particles grow in size, their relative radius difference becomes smaller, promoting the synthesis of uniformly-sized particles.

Figs. B.7 and B.8 schematically represent the relative radius difference as function of particle size and growth time for all the above-mentioned mechanisms of growth.



**Fig. B.7.** Schematic representing the evolution of the relative radius difference as function of the particle size for all the mechanisms of growth discussed above.



**Fig. B.8.** Schematic representing the evolution of the relative radius difference as function of the growth time for all the mechanisms of growth discussed above.

It is clear from these considerations that the synthesis of monodispersed particles by homogeneous nucleation requires preferably a diffusion-controlled growth mechanism. It has been suggested that generally the growth of nanoparticles involves all the three mechanisms discussed so far. In particular, when the nuclei are small, monolayer growth could dominate, poly-nuclear growth could become predominant as the nuclei become bigger, and finally diffusion may regulate the growth of relatively large particles. However, it is worth noting that this would be only the case when no other procedures are applied in order to prevent certain growth mechanisms.

Different growth mechanisms can become predominant when suitable conditions are established. For example, the growth of nuclei can be most likely dominated by a diffusion-controlled process when the supply of growth species is very slow, due to a slow chemical reaction.

There are several ways which can promote a diffusion-limited growth. For example, keeping an extremely low concentration of growth species results in very large diffusion paths, and consequently diffusion could become the limiting step. Another possibility is to increase the viscosity of the solution or introducing a diffusion barrier such as a monolayer on the surface of the growing particles.

A controlled supply of growth species is also another method to influence the growth process. In particular, when growth species are generated through chemical reactions, the rate of reaction can be eventually manipulated via the control of the concentration of by-product, reactant and catalyst.

## **B.4 Particle formation via aerosol drying**

The formation of (nano)particles can be also achieved via a kinetic approach, where usually either the amount of precursors available for the growth is being limited, or the process is confined in a limited space such as in aerosol techniques.

The drying process of a droplet containing a solute has been described in way where five different stages can be identified [2]:

1. Initial heating and evaporation. The temperature of the droplet varies from an initial value to that of equilibrium.
2. Quasi-equilibrium evaporation. It basically corresponds to the drying of a pure liquid droplet.
3. Crust formation and growth. The concentration of the solid on the surface exceeds a critical value and formation of a crust occurs. In this stage the temperature of the droplet rises due to an increased resistance to heat and mass transfer.
4. Boiling. The boiling point is reached when the temperature of the surrounding gas is higher than the boiling threshold of the liquid. A large amount of vapour is released, causing the droplet pressure to increase. Depending on the characteristics of the crust, the particle can inflate, or crack, or it can explode and disintegrate. By the end of this step no liquid is left in the particle.
5. Porous drying. The liquid bound to the surface of the particle is evaporated from the quasi-dry porous remnant. The temperature of the droplet increases slowly in this stage.

### B.4.1 Evaporation of a pure liquid droplet

For droplets with size much larger than the gas mean free path (i.e.  $d_d \gg \ell_g$ ), the rate of evaporation is controlled by the rate at which vapour can diffuse away from the droplet. The rate is given by the following equation:

$$\frac{d(d_d)}{dt} = \frac{4D_v M_m}{R\rho_d d_d} \left( \frac{p_\infty}{T_\infty} - \frac{p_d}{T_d} \right) \phi \quad (\text{B.22})$$

where  $d_d$  is the droplet diameter,  $D_v$  the diffusion coefficient of vapor in air,  $M_m$  the molecular mass of the liquid,  $R$  the gas constant,  $\rho_d$  the density of the liquid,  $p_\infty$  and  $T_\infty$  are the ambient partial pressure and temperature of the vapor,  $p_d$  and  $T_d$  the partial pressure and temperature at the surface of the droplet, respectively and  $\phi$  is the Fuchs correction factor, which accounts for the kinetic processes at the surface of the droplet and is needed for droplets smaller than one micron [3]. Moreover, if there is a velocity difference between the droplet and the surrounding gas especially if the size of the droplets is of few microns other corrections may be necessary. When all the above corrections are negligible equation B.22 can be integrated in order to get the time required for a droplet of a given size  $d_1$  to evaporate completely:

$$\int_{d_1}^0 d_d d(d_d) = \int_0^{t_{ev}} \frac{4D_v M_m}{R\rho_d} \left( \frac{p_\infty}{T_\infty} - \frac{p_d}{T_d} \right) dt$$

$$d_1^2 = \frac{8D_v M_m t_{ev}}{R\rho_d} \left( \frac{p_\infty}{T_\infty} - \frac{p_d}{T_d} \right) \quad (\text{B.23})$$

$$t_{ev} = \frac{R\rho_d d_d^2}{8D_v M_m \left( \frac{p_\infty}{T_\infty} - \frac{p_d}{T_d} \right)} \quad \text{for } d_d > 1.0 \mu\text{m}$$

This equation is quite accurate for calculating the evaporation times of large droplets, (i.e.  $10 \leq d_d \leq 50 \mu\text{m}$ ), since such droplets are often larger than one micron during most of their drying time. For droplets smaller than  $0.1 \mu\text{m}$ , the partial pressure of the vapor at the droplet surface needs to be further corrected [3].

### B.4.2 Evaporation of droplets containing dissolved solids

The ideal case of a precursor droplet containing some dissolved solid or salt is first discussed, assuming complete drying and formation of compact spherical structures.

Therefore, under these hypotheses, the diameter of the resulting particle,  $d_p$ , can be calculated as:

$$d_p = \sqrt[3]{f \frac{\rho_d}{\rho_p} d_d^3} \quad (\text{B.24})$$

where  $f$  is the mass fraction of the material of interest in solution,  $\rho_d$  is the density of the solution,  $\rho_p$  the density of the particle made up of the solid material and  $d_d$  is the (initial) size of the droplet [4]. However, in real cases the process is much more complex. In the initial stage of drying the evaporation from a droplet containing a solute can be described by equation B.22, with the only exception that the vapor pressure of the liquid decreases due to the presence of the solute. The vapor pressure at the surface of the droplet, under the assumption of ideality for the gas phase is given by:

$$p_d^* = a_s x_s p_{sat} \quad (\text{B.25})$$

where  $p_d^*$  is the corrected vapor pressure at the surface,  $a_s$  is the activity coefficient of the solvent at the droplet surface,  $x_s$  the solute mole fraction at the surface of the droplet and  $p_{sat}$  is the saturation vapor pressure. The determination of the activity coefficient is not a trivial task and some possible approaches have been discussed [5]. The main point is that when the concentration of the solute at the droplet surface reaches supersaturation, precipitation of the solute can occur, leading to the formation of a solid crust.

### B.4.3 Onset of precipitation and crust formation

The solute concentration at the surface of the droplet needs to be evaluated in order to determine the time when precipitation begins. The solute concentration is often not uniform, because the solvent evaporates at the surface of the droplet at a higher rate than that of the solute diffusion into the same droplet. The solute concentration can be described by the following equation:

$$\frac{dC}{dt} = \frac{1}{r^2} \frac{d}{dr} \left( D_s r^2 \frac{dC}{dt} \right) \quad (\text{B.26})$$

where  $C$  is the solute concentration,  $r$  is the distance in spherical coordinates and  $D_s$  is the diffusion coefficient of the solute in the liquid. The following boundary conditions are also required:

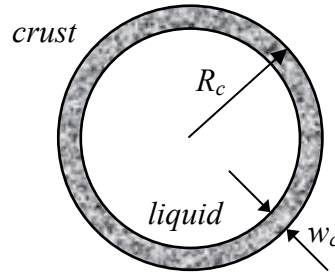


$$\begin{aligned}
C &= C_0 & \text{at } t &= 0 \\
\frac{dC}{dr} &= 0 & \text{at } r &= 0 \\
D_s \frac{dC}{dr} &= \frac{1}{4\pi r^2} \frac{dm_d}{dt} & \text{at } r &= a
\end{aligned} \tag{B.27}$$

where  $C_0$  is the initial solute concentration and  $m_d$  is the mass of the droplet. It is important to observe that the droplet radius,  $a$ , is not constant but changes during the evaporation of the solvent. Equation B.26 is valid until the solute surface concentration reaches the critical value and the solute starts precipitating. At this point the onset for the formation of a solid crust occurs, accompanied by a significant increase of the resistance to heat and mass transfer, causing a sharp increase of the droplet temperature. The growth of the crust results in an increase of its thickness,  $w_c$ , which can be calculated by a solid mass balance:

$$m_{dm} = \frac{4}{3} \pi C (R_c - w_c)^3 + m_d - \frac{4}{3} \pi \rho (R_c - w_c)^3 \tag{B.28}$$

where  $m_{dm}$  is the mass of the dry matter, and  $\rho$  is the density of the liquid phase and  $R_c$  is the radial coordinate of the surface of the crust (see Fig. B.9).



**Fig. B.9.** Schematic drawing of the crust formation from an evaporating liquid droplet.

The solution of equation B.28 for  $w_c$  yields:

$$w_c = R_c \left[ 1 - \left( \frac{m_d - m_{dm}}{m_c - m_{dm}} \right)^{1/3} \right] \tag{B.29}$$

where  $m_c$  is the mass of the droplet for the critical solute concentration threshold. The resistance to evaporation increases remarkably during the crust growth, while the amount of heat transferred to the droplet is approximately the same, resulting in an enhanced temperature. When the temperature of the surrounding air is above the boiling point of the solution, the droplet starts boiling and the drying process occurs.

### B.4.4 Drying and formation of solid particles

Boiling of the liquid results in a significant amount of vapor developed under the crust. The vapor cannot diffuse out at the same rate at which is produced. This fact causes a rise in the inner pressure, and, due to the difference between internal and external pressures, the diffusion of the vapor through the crust slightly increases. Moreover, depending on the characteristics of the crust (i.e. permeability, strength, elasticity) the droplet can inflate or even disintegrate. The crust can also crack, causing vapor release and a consequent pressure drop accompanied by an eventual 'healing' of the cracks. Then the pressure builds up again and an oscillatory behavior occurs for the crack formation and the droplet temperature. At this stage the particle morphology is determined. A schematic diagram is presented in Fig. B.10, where the different particle morphologies are related to the drying process and the crust properties [6].

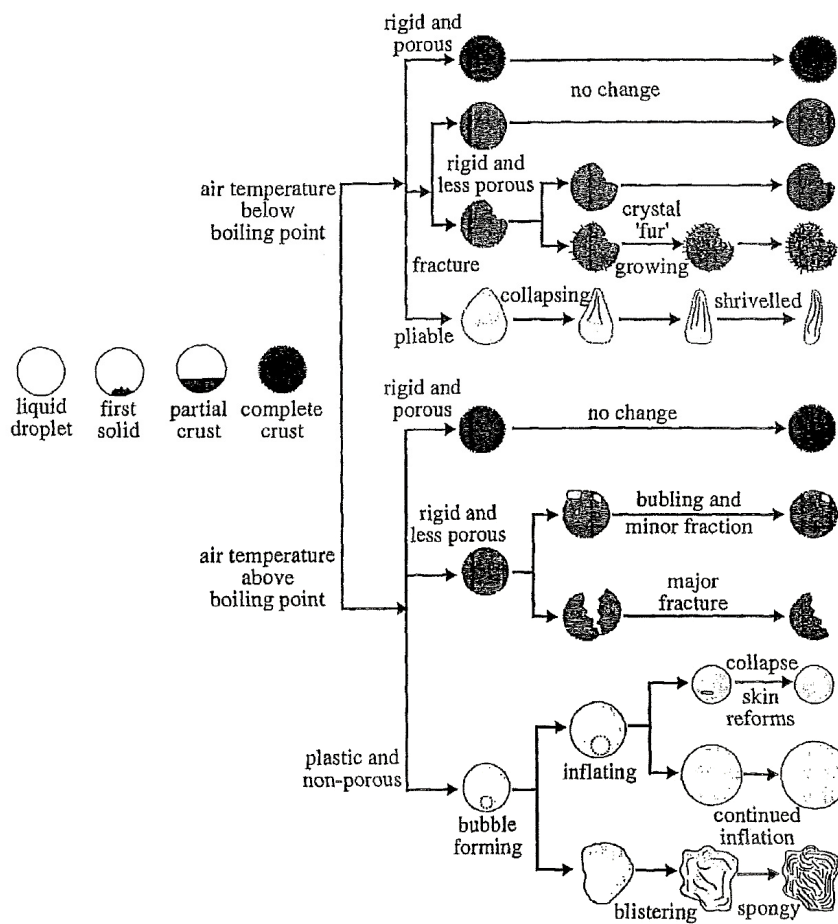


Fig. B.10. Schematic diagram of the morphology of the dried particles [6].

Finally, the drying process forces the evaporation of the remaining liquid in the particle pores and micropores. At this stage the temperature of the particle slowly reaches that of the surrounding gas.

On the basis of this description, it is reasonable to assume that the formation of the nanocomposite polymer/metal oxide relics discussed in chapter five is likely to follow a path where the air in proximity of the heated substrate is above the boiling point of the solvent used. Besides, the electrosprayed droplets are further subject to forced evaporation of the solvent, due to the presence of the applied electric field. The morphology observed for the relics suggests the formation of rigid and possibly porous structures. At the moment it is unclear which the role of the polymer is, since its physical and chemical properties could directly affect both the reaction and drying processes in a way that a change in the evolution of the particle morphology could occur at different stages of the process. Nevertheless, the properties of PVdF, which is highly non-reactive and withstands heat, as well as chemical attack by other substances, leave space for assumptions that its presence should not interfere with the formation of the other solid oxide nanostructures in the reacted droplets. Its presence could act mainly as glue in the formation of the composite spherical remnants which appear to not suffer from major fractures and eventually traces of minor bubbling could be present in the final materials.

## B.5 References

- [1] G. Cao, *Nanostructures & Nanomaterials - Synthesis, properties & applications*, Imperial College Press **2004**.
- [2] S. Nestic, J. Vodnik, *Chemical Engineering Science* **1991**, 46, 527.
- [3] W. C. Hinds, *Aerosol Technology. Properties, Behaviour, and Measurement of Airborne Particles*, Wiley-Interscience publication, John Wiley & Sons Inc. **1999**.
- [4] J. Van Erven, R. Moerman, J. C. M. Marijnissen, *Aerosol Science and Technology* **2005**, 39, 941.
- [5] P. H. W. Vercoulen, *Electrostatic Processing of Particles - A tool in particle technology*, PhD Thesis **1995**.
- [6] D. H. Charlesworth, Marshall, W. R., *A.I.Ch.E. J.* **1960**, 6, 9.



# Appendix C

## Volume change and effects on energy density

*“...una rondella non fa primavera...”  
(Elio e le Storie Tese – Carro)*

This appendix briefly describes the volume change of the lattice hosts, due to uptake and removal of lithium during the electrochemical process. The basic formulas are given together with a more detailed analysis of the variation of the energy density with respect to the amount of lithium stored in Li-alloys during the alloying process. This last part has been included in order to assess which type of dependence can be expected for the energy density upon increasing content of Li in the reacted alloys and its further implications.

## C.1 Molar volume and relative volume change

As mentioned in the previous chapters, the uptake of lithium during the electrochemical process causes an expansion of the volume of the host lattice. In particular, the variation the molar volume, of a Li-metal alloy ( $Li_xM$ ), for example, can be evaluated as:

$$\Delta V_m = \frac{V_m(Li_xM) - V_m(M)}{V_m(M)} \quad (C.1)$$

where  $V_m(Li_xM)$  is the final molar volume of the reacted metal host and  $V_m(M)$  is the initial molar volume of the host material. The molar volume of a compound can be expressed as:

$$V_m = \frac{N_A \cdot V_{UC}}{Z} \quad (C.2)$$

where  $Z$  is the number of molecules per unit cell,  $N_A$  is Avogadro's number and  $V_{UC}$  is the volume of a unit cell. For an arbitrary lattice structure the volume of a unit cell can be calculated as:

$$V_{UC} = a_l \cdot b_l \cdot c_l \cdot \sqrt{1 - \cos^2 \alpha_l - \cos^2 \beta_l - \cos^2 \gamma_l} \quad (C.3)$$

where  $a_l$ ,  $b_l$  and  $c_l$  are the unit cell parameters, and  $\alpha_l$ ,  $\beta_l$  and  $\gamma_l$  are its fundamental angles.

## C.2 Calculation of energy density for Li-alloys

The volumetric energy density  $\tilde{U}$  (i.e. Whcm<sup>-3</sup>) of a negative electrode material in a Li-ion battery can be calculated by the following expression [1]:

$$\tilde{U} = \frac{- \int_{x=x_f}^0 [V_{(+)}(x) - V_{(-)}(x)] F dx}{v(x_f)} \quad (C.4)$$

where  $x$  is the number of moles of Li per mole of host alloy atoms,  $x_f$  is the number of moles of Li per mole of host alloy at full lithiation,  $V_{(+)}$  is the voltage of the positive material,  $V_{(-)}$  is the voltage of the negative material,  $v$  is the molar volume of

the alloyed negative electrode (calculated per mole of host alloy atoms), and  $F$  is the Faraday's constant ( $F \approx 26.802 \text{ Ahmol}^{-1}$ ).

Equation (C.4) is only valid when the volume changes of positive materials are negligible. Since the volume changes for most of high-energy density positive materials are very small compared to those of negative materials, it can be reasonably assumed that equation (C.4) remains a good approximation for the calculation. Nevertheless, this expression is valid *only* in a particular case: i.e. when the integral is calculated between 0 and  $x = x_f$  and the denominator  $v_f = v_0 + kx_f$  is a known value, so that it can be directly used in the above calculation. However, the relationship described by the following equation (C.5) - i.e. the evolution of the molar volume of the alloyed negative electrode upon increasing Li content in the alloy - shows a linear dependence from  $x$ , which on its turn, is related to the actual cell voltage, e.g. ( $V=V(x)$ ).

$$v(x) = v_0 + kx \quad (\text{C.5})$$

where  $v_0$  is the initial molar volume of the unreacted negative host and  $k$  is a constant, typical for each material.

Therefore a general expression for  $\tilde{U}$ , which can be calculated for *any* value of  $x$  should be conveniently rewritten as follows:

$$\tilde{U}(x) = \int_0^x \frac{[V_{(+)}(x) - V_{(-)}(x)]Fdx}{(v_0 + kx)} \quad (\text{C.6})$$

where the molar volume dependence has been included in the integral, and the property of definite integrals has been applied. (i.e. the change of sign with inversion of the integration limits).

In the case of cells having metallic Li as reference and counter electrode, Li plays the role of the negative material. Besides, the potential is always defined except for an additive constant. Therefore, it is also possible to set  $V_{(-)} = V_{Li} = 0$ , taking the potential of metallic Li as reference (i.e.  $V$  vs.  $Li/Li^+$ ), without losing generality. The resulting expression is then:

$$\tilde{U}(x) = F \int_0^x \frac{V_{mat}(\xi)d\xi}{(v_0 + k\xi)}, \quad 0 \leq x \leq x_f \quad (\text{C.7})$$

where  $V_{mat}(\xi)$  is the voltage profile of the material of interest.  $\tilde{U}(x)$  is then function of the extreme  $x$ . The analytical expression of the voltage profile of the material of interest is not known a priori, but as a first approximation simple shapes can be taken into account and some preliminary considerations can be made:

$$\begin{aligned}
 a. & \begin{cases} V(\xi) = V_0 + s\xi, & s < 0 \\ V(0) = V_0 \\ V(\xi_f) = 0 \end{cases} \\
 b. & \begin{cases} V(\xi) = V_0 & \forall 0 \leq \xi \leq \xi_f \\ V(\xi) = 0 & \forall \xi > \xi_f \end{cases} \\
 c. & \begin{cases} V(\xi_1) = V_1 & \forall 0 \leq \xi \leq \xi_1 \\ V(\xi_2) = V_2 & \forall \xi_1 < \xi \leq \xi_2 \\ \dots\dots\dots \\ V(\xi_f) = V_f & \forall \xi_{f-1} < \xi \leq \xi_f \\ V(\xi) = 0 & \forall \xi > \xi_f \end{cases}
 \end{aligned} \tag{C.8}$$

where  $x(\xi_f) = x_f$ , and a staircase-potential with multi-step plateaus is chosen for sequential reactions of the electrode material with lithium. Keeping these ideas in mind, the simplest case of a constant voltage can be considered (i.e. equation. C.8b). In this case, the expression becomes:

$$\tilde{U}(x) = FV_0 \int_0^x \frac{d\xi}{(v_0 + k\xi)}, \quad 0 \leq x \leq x_f \tag{C.9}$$

It can be noted that  $v_0$  and  $k$  are positive constants and that the function contained in the integral is continuous and well-defined. Clearly it is  $\tilde{U}(0) = 0$  and  $\tilde{U}(x_f)$  can be calculated solving the definite integral in the interval  $[0, x_f]$ . The solution of the integral is immediate:

$$FV_0 \int_0^{x_f} \frac{d\xi}{(v_0 + k\xi)} = FV_0 \frac{1}{k} [\ln(v_0 + k\xi)]_0^{x_f} = FV_0 \frac{1}{k} [\ln(v_0 + kx_f) - \ln v_0] \tag{C.10}$$

Moreover, for the fundamental theorem of calculus the first derivative equals:

$$\tilde{U}'(x) = FV_0 \frac{1}{(v_0 + kx)} > 0 \quad \forall 0 \leq x \leq x_f \tag{C.11}$$

and  $\tilde{U}(x)$  monotonically increases in the interval. Besides, the second derivative is:

$$\tilde{U}''(x) = -FV_0 \frac{k}{(v_0 + kx)^2} < 0 \quad \forall 0 \leq x \leq x_f \tag{C.12}$$

meaning that the function  $\tilde{U}(x)$  is strictly concave in the interval.



Therefore, it can be concluded that for a constant potential over the entire range of Li compositions the volumetric energy density assumes its maximum value at full lithiation (i.e. when  $x=x_f$ ), since the function  $\tilde{U}(x)$  increases monotonically.

This approach could be a first attempt to describe the electrochemical lithiation by means of an average constant potential. The same calculations can be also iterated for a multi-step potential (equation C.8c) over the various compositional ranges, where a specific voltage is defined. The result is analogous to the one already found: the curve results from the contributions of the different constant voltages over the various Li compositions. Also in this case, the total volumetric energy density increases monotonically, being the single contributions monotonically increasing over their individual compositional ranges.

Finally, the voltage profile C.8a is considered. As it has been suggested, this sloping voltage profile can be used to describe the electrochemical behavior of many amorphous or nanocrystalline alloy negative electrodes. The voltage drops linearly from an initial value of  $V_0$  and it can eventually reach zero for  $t_f = -V_0/s$ . The expression for the integral is the following:

$$\tilde{U}(x) = F \int_0^x \frac{(V_0 + s\xi)}{(v_0 + k\xi)} d\xi \quad , \quad \begin{cases} 0 \leq x \leq x_f \\ s < 0 \end{cases} \quad (\text{C.13})$$

It can be noticed that  $\tilde{U}(x_f)$  can be calculated as the sum of two terms:

$$\tilde{U}(x) = F \int_0^{x_f} \frac{(V_0 + s\xi)}{(v_0 + k\xi)} d\xi = FV_0 \int_0^{x_f} \frac{d\xi}{(v_0 + k\xi)} + Fs \int_0^{x_f} \frac{\xi d\xi}{(v_0 + k\xi)} \quad (\text{C.14})$$

The first term has for solution the above-mentioned equation (C.10), while the second term can be conveniently rewritten as:

$$Fs \int_0^{x_f} \partial \left( \frac{1}{k} \ln(v_0 + k\xi) \right) \cdot \xi d\xi = Fs \left\{ \frac{1}{k} [\ln(v_0 + k\xi) \cdot \xi]_0^{x_f} - \int_0^{x_f} \frac{d\xi}{(v_0 + k\xi)} \right\} \quad (\text{C.15})$$

where  $\partial$  indicates the derivative of the term between round parenthesis, and the property of integration by parts has been used. Again, the second term of equation (C.15) can be solved by using the expression reported before in (C.10). Therefore, the sum of all the terms gives:

$$FV_0 \frac{1}{k} [\ln(v_0 + kx_f) - \ln v_0] + Fs \frac{1}{k} \left\{ [x_f \cdot \ln(v_0 + kx_f)] - [\ln(v_0 + kx_f) - \ln v_0] \right\} \quad (\text{C.16})$$

and by gathering all the common factors in (C.16),  $\tilde{U}(x_f)$  can be rewritten as:

$$\tilde{U}(x_f) = F \frac{1}{k} \left\{ \left[ \ln(v_0 + kx_f) - \ln v_0 \right] \cdot (V_0 - s) + s \cdot \left[ x_f \cdot \ln(v_0 + kx_f) \right] \right\} \quad (\text{C.17})$$

Moreover, the first derivative of the expression in equation (C.13) results:

$$\tilde{U}'(x) = F \frac{(V_0 + sx)}{(v_0 + kx)} > 0 \quad \forall 0 \leq x < x_f \quad (\text{C.18})$$

Also in this case, the values of the derivative are positive, and it can eventually assume a zero value for  $x_f = -V_0/s$ . Moreover, its second derivative yields:

$$\tilde{U}''(x) = F \frac{(sv_0 - kV_0)}{(v_0 + kx)^2} < 0 \quad \forall 0 \leq x \leq x_f \quad (\text{C.19})$$

Hence, it results that the volumetric energy density increases monotonically, reaching its maximum value in correspondence of full lithiation.

On the basis of the above considerations it can be concluded that for the approximations adopted so far for the voltage profile, the volumetric energy density increases monotonically together with the amount of Li stored in the alloy. Consequently, there are no points of local maxima, where a tradeoff between the volume expansion and the charge stored could be eventually reached. On the one hand, increasing the content of lithium incorporated into the alloy results in an enhancement of the energy density, on the other hand this fact intrinsically implies a larger volume change for the host lattice, which therefore is more prone to be damaged upon successive cycles of reaction.

In conclusion, although this theoretical analysis shows evident restrictions for the ideal behavior of the Li-alloys, i.e. when it comes to optimize their energy densities and limit the related volume changes, it provides some rough guidelines for a convenient approach to the fabrication of advanced electrodes. Indeed, these considerations are a starting point to develop composite electrodes, where both the overall energy densities and the mechanical properties are directly affected by the presence of additional components (i.e. binders, additives).

### C.3 Reference

- [1] M. N. Obrovac, L. Christensen, D. B. Le, J. R. Dahn, *Journal of the Electrochemical Society* **2007**, 154.

# Acknowledgements

*...E tu certo comprendi  
Il perchè delle cose, e vedi il frutto  
Del mattin, della sera,  
Del tacito, infinito andar del tempo...*  
(Canto notturno di un pastore errante dell'Asia – Giacomo Leopardi)

And silently the time has come for the PhD to find its natural ending with the completion of the present work. I see sometimes this thesis a bit as a signpost in a certain way similar to the blue sign “Delft” that appeared to me through the train window almost five and a half years ago when I first arrived in this city. At that time I was hardly aware of my journey. The sign was there, indicating the destination. Still, “...How does Delft look like?...” A lot of similar thoughts came up to my mind, as it happens to the newcomer, who has never visited a place before. Hopefully this thesis can be for the readers a bit more than a signpost: a booklet with a colored cover, a name and a title indicating the destination. Indeed, I hope that as Delft proved to be a nice city with gorgeous spots and characteristic architecture, this piece of work has eventually some (interesting?) features to offer to those who want to explore it a bit.

This thesis would not exist if Erik did not give me the chance at the beginning of 2006 to continue working in his group as a PhD. Erik, I would like to express my profound gratitude for your great hospitality and the way you welcomed me in your group from the very first moment. You directly came to pick me up at “station Delft” when I first arrived on a rainy day at the beginning of July 2005 to start my internship in the battery group, which was at that time part of the Inorganic Chemistry section led by Prof. Schoonman (thanks a lot for giving me this opportunity!!)...and that was only the beginning of this unforgettable journey that has now produced fruits of its own... Thank you very much for the constant patience, assistance and empathy that you showed me through all these years. I am particularly grateful for your human, open approach and for all the support, trust and freedom you always gave me. Many thanks for your continuous feedbacks and help, particularly during these last

months to correct and improve all the work, not last for your aid with the samenvatting and stellingen!

I would like to express my gratitude to Stephen, for his valuable help in critically revising the thesis contents and further enhancing the quality of the final manuscript. Thank you very much for your great expertise, availability, wit and sense of humor.

I would also like to thank all the committee members for their willingness to participate in this defence and allowing me to defend this thesis. I would like to express my gratitude to Jan Marijnissen. Jan, I am really grateful that I had the chance to follow the Electrospray workshop in Florida: it was simply great. Indeed, you and Rein added an extra dimension to the description of this fascinating phenomenon. I am indebted to both of you, not only for giving me a wide perspective of this technique and its applications in a very clear and enthusiastic way, but also for your precious advice and prompt help in troubled periods. I would like to thank Caner for his valuable help and kind assistance. Thank you very much for your availability and willingness to discuss practical aspects of electrospraying and helping me in finding proper approaches to tackle experimental hurdles. Thanks also to Gabriele for his empathy and help in moments of uncertainty.

I would then like to thank Asun Quintanilla and Freek Kapteijn for their important contribution to this thesis and their willingness to use electrospraying to generate Au nanoparticles for catalysis purposes.

A huge “thank you!” goes to the secretaries, Wil and Karin, who helped me a lot with the bureaucracy in these years. Wil, probably the entire organization of the defence would have not been possible on this date without your constant help and collaboration...

Many thanks also to Ben, Gerard, Marcel, Piet, Nico, Valerie, Alex and Ruben for their important technical assistance, as well as to the people of the technical service and workshop. A special thanks also to Ricardo and all the people of the IT group for their prompt help and assistance.

I would like then to thank all the NanoStructured Materials (NSM) section for the friendly atmosphere that I enjoyed during these years. Thanks for all the nice time we had at the BBQs, borrels, lunches, excursions, celebrations and other activities.

I would like to thank Tony Terrasi for his kind invitation to attend the International summer school on materials for renewable energies in Erice. I would like to compliment you on the success of such event. It was great and I enjoyed it a lot! It was really important for me to be there! Grazie!

A special “thank you” goes to Maaïke Belien for her enthusiasm and great expertise in teaching English. I would like to thank you for your important inputs and assisting me in the preparation of the final examination. I would also like to thank all my colleagues of the English course for their nice and friendly company during the

lessons. Moreover, I would like to thank my Dutch teachers Karin and Maria for their help in giving me the basis of the Dutch language, thus enabling me to proceed with further learning. Thanks also to all my former classmates voor de gezellige sfeer. A big thanks also to my saxophone teacher, Wim who introduced me to this wonderful instrument! Thanks also to the salsa teachers Jan and Viviane, it was really funny!

A “hyper-thank you!” goes to all my dear friends and colleagues of the office/section/department/university/... You accompanied, supported and rescued me in this incredible journey, and above all you tolerated my useless complaints. I really enjoyed all the time we spent together and if I would have to thank you for all the various contributions to this work, my mental (in)sanity, as well as all the incredible experiences of these years...I need to write another thesis - or better - a tale! Still, I will try to thank you, being also conscious that due to my random (access?) memory there is a high risk of forgetting to mention people that contributed to this work. Therefore, I would like to sincerely apologize for all my eventual mistakes and forgetfulness.

Corrado, I have really no words to thank you enough for your help, support, patience and for all the fun we had in this crazy adventure! Thank you Boccolo for your cherub-like hair style, your ‘80s soul, your peculiar views on entropy, phase and cosmology, as well as your proven ability to follow improbable (Russian?) dances at 5 a.m. David, you are GREAT (in increasing entropy, too!!)...it’s really a lot of fun working and travelling with you!! Thanks for your eagerness to play with electrospaying suspensions with Si np’s & polymer binders and contributing to this thesis. Ugo, thank you very much for your precious assistance and encouragement all through these years! You carried out very important TEM analyses (thanks also to Patricia Kooijman, for the very last analysis!), without which this work would have been practically shapeless. I really enjoyed your great company and your extremely funny, generous character! You & Natacha are extraordinary...I wish you all the best for your (growing) family!! Loic, thank you very much for your first introduction to the Li-lab and teaching me the technical work with Li batteries. Thanks a lot for all the fun we had and for bringing me to the music shop to buy a saxophone: for the joy of the neighbours, first...and the department, after!! I wish all the best for you, Agnes and (le petit?) Ruben. Giacomo, thanks a lot for your great support (...‘ngna fa!!) and all the loud laughs we had in these years...not last, for being sensible to the small ‘dramas’ that can occur in a conference...pangafilet!!! All the best for you, Silvia and Siria!! Jan, detto Gianni per gli amici, thank you very much for your HUGE hospitality and your assistance, not last for the high-quality Si np’s produced by your flaming creature ‘Silizia’. Thank you for all the laughter we had during delicious dinners, BBQs, degustations of ‘hyper-space’ bieren in Hilvarenbeek, not last for meeting the gnomes in Achouffe 6666. Tobias you’re one of the most enthusiastic people I’ve ever met. Your style, wit and sense of humor are really special. Thank

you very much for your prompt help and assistance, your spark(l)ing jokes on any subject and all the laughs during lunches, dinners, borrels, concerts and...conferences, of course!! Esteban, thanks a lot for your precious help and efforts with experiments, data & drafts. The results you obtained constitute an important part of this thesis. Thanks a lot for sharing and increasing the fun...not last for laughing loud together for the n<sup>th</sup> time to the Italian man who went to Malta! Grazie Stefano!...( & Stefy, too!). Thanks Julien, you also significantly contributed to enhance the fun...you are cool and an active 'dancing catalyst' at conferences, too!! (i.e. Nürnberg). Thank you very much for carefully documenting that music & musicians (Miss Fizz – music for friends, you're terrific!) can induce sudden transformations in most of the people... Thank you very much Anca & Joost for the nice time, discussions, parties, BBQs and all the fun we had in these years! Thanks a lot also for your immediate help in the lab and with equipments. I wish you all the best! Thanks a lot Yen for your continuous support and the kindness you showed me in these years. I really enjoyed our nice talks! Sheida and Zohre, I would like to thank you for your nice company in Nürnberg, for your encouragements and the great time in these months. I wish you success with your new jobs! And then, thanks a lot Marco!!! You wanted to spend more time in Helsinki and indeed it was great fun there! I really enjoyed your cool company and all the laughs we had! I wish your vivid passion for science and culture could bring you soon to the place of your dreams (Helsinki?). Thanks a lot Vincent for your enthusiasm and the fun in the last conferences. Thanks for your eagerness to regularly organize the Friday borrels and promoting interactions between NSM'ers. I wish you a pleasant holiday in Africa together with Hanneke! I would like then to thank Yonsuang and Lewton, I really enjoyed your company in Florida and during conferences! Thank you very much for the interesting discussions and the nice time we spent travelling together. Thanks also to Gerrit and Sybrand, it was a great pleasure to meet you in Florida as well as travelling with you...thanks for your great enthusiasm and the nice discussions!

A big thanks goes also to all the current and previous students of the battery group: Dion, Sander, Marilena, Claudia, Maria, Karol, Alper, Sergei, Sharon, Michael...thanks for all the nice time and fun in these years! Special thanks to Frans, Dan & Silvia for your valuable help, expertise and advice. Thanks a lot also for the great jazz gigs and the nice discussions I enjoyed with you guys!

Thanks also to Cristian, Bas, Ineke, Parisa, I enjoyed a lot your company and the nice time at BBQs and dinners. And then, thanks to Daniela, Maria, Aurelie, Job, Esson, Cristhoff, Elise & Max, Lennard, Sameer, Krishna, Judith, George, Ula, Plamen and Chris, for your encouragement.

Cristian & Jealemy, I cannot thank you enough for your incredible help, empathy and continuous encouragements. Needless to say, we had a lot of fun...and even the darkest moments with you guys, became suddenly bearable if not a source of

laughs...I am indebted to both of you for all the care you took of me in these years and the kindness you showed me.

Salvo, Turyddu, your hospitality, help, advice and continuous support are the milestones of this amazing journey. Thanks A LOT for all the fun!! Arance, Studio K, Windmill, exhibitions, concerts, festivals, feste di compleanno/dottorato(!), Oosterpark, Parijs (thanks Nacho!), Pathe', fiordi, koop(en)avond, orsi norvegesi...just to mention some key words. I will try to keep it short otherwise I am going to generate randomly commonplaces and nonsense's and then it will be hard to stop...E poi Paolo, veramende, grazie mille per la tua estrema pazienza, ospitalita' ed incoraggiamento, nonche' per la tua puntualita' nel sottolineare la ricchezza avverbiale nelle nostre conversazioni e...per il tuo spiccato accento Siculo! I would like to thank you for spurring me to buy an umbrella during our holiday in the Scandinavian countries and for all the energy and enthusiasm you put in organizing this memorable road trip (thnx also to Daniele!)!! All the best for you & Jenny! Alessia, Ale, perche' alla fine...ci abbiamo creduto...Grazie per l'affetto che mi hai dimostrato in questi anni e per il tuo grandissimo aiuto ed incoraggiamento in questo periodo caotico e di transizione. Thanks a lot for all the short trips, excursions, lekkere dinnertjes, BBQs, the Original Spritz con la "O" maiuscola, not last for yours & Fendy great hospitality! Yenny, thanks a lot for your precious help and your great sympathy! Irene, grazie per avermi incoraggiato e per le tue parole. Thanks Sandra for your dancing mood and the fun at birthdays! I would also like to thank Wojciech, Christos, Esteban & Loesje, I had really good time with you guys! I wish you all the best! Many thanks also to Simone, Radek, Marwan, Mariana, Phil, Silvano, Seb, Tangy, Matias, Javier, Viviana, Giuliana, Julie, Andy, Marco, Sara, Andrea, Nico, Mauro, Maristella, Alessandro, Enrico & Fra, Amelia for your company and support. Thanks Julia for your important "keep on going..." and your entropic contribution. Grazie mille Salvo & Nadia, per il vostro affetto, aiuto e le varie risate... in bocca al lupo per tutto! Grazie mille a Paolo & Silvia e la piccola Irene, Luca & Ilaria, Daniela & Francesco, Ivan & Irene ed Alex...grazie per il vostro grande affetto, ospitalita' ed importante supporto, far away so close!! A special thanks to Francesco. Thank you very much Ciccio for your enthusiasm and your great support!! Grazie per le belle giornate che abbiamo trascorso viaggiando tra Delft, R'dam, Kinderdijk...e per esserci goduti il sole primaverile da balconi fioriti e terrazze. E poi...grazie infinite Mario...per la tua grande ospitalita'...per le risate che ci siamo fatti, per la tua strenua difesa di Cartesio, per aver rivalutato un venditore di batterie ed aver averne distillato l'essenza. Auguroni per te e la piccola Alicetta!! Grazie Luca per il tuo grande entusiasmo, il tuo strenuo incoraggiamento in questi anni e le grasse risate, naturalmente! A presto...ed in bocca al lupo per te & Elena!!

Infine voglio ringraziare i miei genitori per essermi stati costantemente vicini, per non aver mai dubitato delle mie scelte ed avermi lasciato libero di seguire il mio

percorso incoraggiandomi ad andare avanti, sempre. Mamma & Papa', grazie per avermi sempre sostenuto, soprattutto nei momenti piu' critici. La luce del vostro immenso affetto ha rischiarato il mio cammino e mi ha mostrato la via verso porti sicuri, come un faro che brilla nelle notti buie e tempestose. La tesi e' dedicata a voi e a tutta la nostra famiglia: ai miei nonni Maria ed Eduardo, Giuseppina e Mario, ai miei zii Giovanni e Laura, ad Ilaria ed Ivan, Marinella, Giovanni e Saveria, Enrico, Angelo, Antonio, Gaetano, Concetta e Luigi. Grazie.

Last but not least, Lua, words are not enough to thank you for all the care and dedication you took of me, for your incredible help and enthusiasm, not last the way you patiently rescued me during these months, despite my lousy mood. Grazie.



# Publications

## Papers by the author related to this thesis:

**“Synthesis of anisotropic gold nanoparticles by electro spraying into a reductive-surfactant solution”** – *Chemistry of Materials* Vol. 22, (2010), 1656.

A. Quintanilla, M. Valvo, U. Lafont, E. Kelder, M. Kreuzer, F. Kapteijn.

**“An aerosol-based route to nanostructured powders synthesis in liquids”** – *Journal of Nanoscience and Nanotechnology*, Vol. 10, (2010), pp. 5800.

M. Valvo, U. Lafont, E.M. Kelder.

**“Electro spraying-assisted synthesis of tin nanoparticles for Li-ion battery electrodes”** – *Journal of Power Sources*, Vol. 189, (2009), pp. 297.

M. Valvo, U. Lafont, D. Munao', E.M. Kelder.

**“Sn-Co compound for Li-ion battery made via advanced electro spraying”** – *Journal of Power Sources*, Vol. 174, (2007), pp. 428.

M. Valvo, U. Lafont, L.Simonin, E.M. Kelder.

**“Synthesis of silicon nano-particles for thin film electrodes preparation”**  
2010 MRS Spring Meeting Symposium A proceedings – *In press*.

D. Munao', J. van Erven, M. Valvo, V. Vons, A. Evirgen, E. Kelder.

## Other papers by the author:

**“Sol-gel and hard template-assisted synthesis of 3D nanostructured SnO<sub>2</sub> Electrodes”** – *Journal of Nanoscience and Nanotechnology*, Vol. 10, (2010), pp. 4273.

U. Lafont, S. Waichman, M. Valvo, E.M. Kelder.

**“New insight on the failure mechanism of nano-Si based anodes for Li-ion batteries”** – *submitted to Journal of Power Sources*.

D. Munao', J.W.M van Erven, M. Valvo, E. Garcia-Tamayo, E.M. Kelder.

# Curriculum vitae

- Name** : **Mario Valvo**
- Date of birth** : **21 August 1979**
- Place of birth** : **Enna, Italy**
- 
- 1994 – 1998** : **Undergraduate degree in classical studies – Liceo Ginnasio statale “Napoleone Colajanni”, (Enna, Italy).**
- 1998 – 2004** : **Bachelor and Master Degree in Physics Universita’ degli Studi di Catania, (Catania, Italy).**
- 2005 – 2006** : **International Degree in Micro and Nano-Technologies – (European School of Advanced Studies in Materials Science), Istituto Universitario di Studi Superiori di Pavia, (Pavia, Italy).**
- 2006 – 2010** : **PhD student in Chemical Engineering Nanostructured Materials, ChemE, TU Delft – Delft University of Technology, (Delft, The Netherlands).**